Helping Observe and Tune Diffusion Using Mn^{2+} Photophysics in Inorganic Nanocrystals after Growth

Charles J. Barrows

A dissertation

submitted in partial fulfillment of the

requirements for the degree of

Doctor of Philosophy

University of Washington

2017

Reading Committee:

Daniel R. Gamelin, Chair

Brandi M. Cossairt

Xiaosong Li

Program Authorized to Offer Degree:

Chemistry

University of Washington

Abstract

Helping Observe and Tune

Diffusion Using Mn^{2+} Photophysics in Inorganic Nanocrystals after Growth

Charles J. Barrows

Chair of the Supervisory Committee:

Professor Daniel R. Gamelin

Department of Chemistry

Doped inorganic crystals exhibit attractive optical, electrical, and magnetic properties that enabled the development of important modern technologies including ruby lasers and silicon microelectronics. The next frontier of doping chemistry is taking place on the nanoscale, where quantum confinement effects dramatically change the photophysical properties of semiconductors. This thesis describes recent advances in the doping of colloidal II–VI semiconductor nanocrystals known as “quantum dots.” Interactions between excitonic excited states and Mn^{2+}, a model magnetic dopant, are investigated, primarily by magnetic circular dichroism (MCD) spectroscopy. These data reveal a new mechanism of nanocrystal doping characterized by thermodynamic addition of cation + anion pairs,

followed by diffusional mixing. A broad range of equilibrium compositions are achieved, from less than one to hundreds of impurities per quantum dot, and subsequent cation exchange reactions are utilized to develop a model for dopant diffusion in these nanocrystals. Unique spectroscopic signatures are demonstrated, including nonmonotonic magnetization in the low-doping regime and extraordinarily large (whopping) Zeeman splittings in more highly doped quantum dots. Collectively, these studies provide insight into the fundamental processes of diffusion and magnetic exchange on the nanoscale, and may be useful for future spintronics, spin-photonics, and solar energy conversion technologies.

In loving memory of
William H. Barrows, M.D.
1954–2014

ACKNOWLEDGMENTS

I would like to start by thanking all the teachers who inspired me to study chemistry and pursue a Ph.D. at the University of Washington. This includes, but is not limited to, (1) my 8th grade science teacher, Mr. Seth Robey, who taught me Lewis Dot diagrams and opened up an exciting world to me, (2) my high school chemistry teacher, Ms. Cheryl Rulis, who taught me the power of dimensional analysis and the joy of Mole Day, (3) Professor Steve Kinsley, who showed me that professors can make a fulfilling career out of teaching at the college level, (4) Professor Amy Walker for making it her mission that I not quit the chemistry major just because organic chemistry was not as fun to learn as physical or inorganic chemistry, (5) Professor Dan Giammar for showing how a chemist can play a vital role in interdisciplinary research, and (6) Professor Bill Buhro for suggesting UW would be a great place to study and for introducing me to the man who would become my advisor.

Speaking of whom, I would like to thank Professor Daniel Gamelin for all of his guidance and assistance over the last 5.5 years. He pushed me academically and scientifically, and made me a better writer and researcher. This thesis would not be possible without him. I would also like to thank my committee members Professors Brandi Cossairt, Xiaosong Li, and Peter Pauzauskie for all their valuable feedback and advice.

The Gamelin Lab has been a supportive place to tackle complex projects. I have learned valuable skills and concepts from every member of the lab and their combined expertise in synthesis and spectroscopy is exceptional. I'd especially like to thank a few colleagues who made a significant impact on my experience in grad school. This section of acknowledgments is made in roughly chronological order for narrative purposes.

Dr. Vladimir Vlaskin taught me everything I needed to know about synthesis of nanocrystals, including passing on his wisdom for washing quantum dots: "Reach for the TOP, but oleic acid is also a miracle worker." Our philosophical discussions encouraged me to ask big questions, both in research and in life, and he pushed me to believe "all impossibilities are only inside our own minds."

Christian Erickson, who was working with Vlad as an undergraduate researcher at the time I joined the lab, taught me the beta version of nanocrystal diffusion doping. Now that he is back in the lab as a Ph.D. student, I have had the pleasure of working alongside him on new frontiers of NC synthesis and I know its future is in his good hands.

Rob Johns was also an undergraduate researcher when we met and our friendship has meant a lot to me, even after he moved to Berkeley to pursue his Ph.D. He always

pushes me to do better and not to accept the status quo. It was an honor to co-chair the first GRS for the colloidal semiconductor nanocrystals GRC with him.

Dr. Liam Bradshaw became a good friend and mentor and I'd like to thank him for sharing Donut Time, Cookie Time, Avocado (with salt) Time, Frisbee Time, Venting Time, and just about any other Time. His ability to tinker and engineer solutions to hardware issues was instrumental to the success of many of my projects. For example, he built me a heated aluminum block in which I could run up to 16 parallel reactions, which we named the Workstation for Exciting Nanoparticle Development and Innovation (WENDI), the younger (and cheaper, less automated) sister of WANDA at Lawrence Berkeley National Laboratory.

Dr. Jeffrey Rinehart and I worked together on what was perhaps simultaneously both the most frustrating and most rewarding project of my graduate career: the "voltage booster." In addition to teaching me how to take charge of a collaboration by uniting the Super Friends, he became a super friend to me and I will always appreciate his mentorship and sense of humor. I would be most appreciative if he and Dr. Alina Schimpf could recover my belt of minor gender change in the crypts of Waterdeep some day soon.

Kimberly Hartstein and I visited the lab together as prospective students, but she deferred a year to complete a research fellowship in Germany. This proved to work out well for both of us, as I did not have to compete with her for a spot in the lab! After she joined however, she was a pleasure to work with, even when I was being difficult. She also makes a mean batch of bacon and was a fantastic roommate.

Dr. Rachel Fainblat has been my long-standing collaborative partner, beginning when she was a Ph.D. student in the lab of Professor Gerd Bacher at the University of Duisburg-Essen. Since joining the Gamelin Lab as a postdoc, I have had the pleasure of working even more closely and productively with her, and I am grateful for her eagerness to help whenever and wherever she can. I will miss our weekly burrito trips.

One of the highlights of my role as a graduate student has been working with talented undergraduate researchers. I enjoyed mentoring Lindsey Kornowske, Michael James, and Atchuthan Gopalan, and look forward to following their careers in STEM. I already miss playing viola with Lindsey, discussing Game of Thrones with Michael, and debating the difference between cookies and biscuits with Atch.

I'd like to thank all of my office mates (Dr. Emily McLaurin, Dr. Kathryn Knowles, Troy Kilburn, Professor Andries Meijerink, Stijn Hinterding, Kira Hughes, Tyler Milstein, and others I have already mentioned) with whom I have shared many fantastic conversations,

both science-related and not, while “working” from the couch, and who somehow put up with me whenever I got hangry.

Throughout my Ph.D. I had the privilege of working closely with a number of fantastic collaborators in other groups at UW, including Professor David Ginger, Professor Scott Dunham, Dr. Hiro Nagaoka, Dane DeQuilettes, Yu Jin, and Ellen Hayes. Towards the end of my studies, I was afforded the opportunity to go work in Professor Bacher’s lab in Duisburg, Germany for two months. Their hospitality was much appreciated and I had both a productive and enjoyable trip. I’d especially like to thank Professor Bacher, Severin Lorenz, and Franziska Muckel for all their help, encouragement, and wisdom.

Next I would like to thank all of my friends from outside the lab who helped make Seattle my home. To start, thank you to Michael Freeman, Scott Ventrudo, and Emily Brosius for taking me out for pizza and convincing me to move to Seattle. To Victor (Jake) Kessler and Zach Fox, you are two of the best friends I could ever ask for. Your shared love of cheese, camping, and Fancy Feasting put a smile on my face every time I walked in the door of our apartment. I also want to thank Jaime Hensel for her invaluable friendship and unwavering support, and for asking the tough questions in our conversations about life. Chris Steckler, I cannot express how much your love and patience has meant to me as I tried to balance work with getting to know you better. Thank you for accepting me for who I am and teaching me to accept myself.

Finally, I thank my family for all of their love and support for the last 27 years. I appreciate how you have always encouraged me to pursue my passions, even when they have taken me far away from home. Without you, none of my successes would have been possible. I know dad would be proud of who I have become and what I have accomplished, just as I am proud of my mother (Donna, the “Mother of Dragons”) and brothers Sam (the “Short, Fat One”) and Ted (“Teddy-For-Short-But-Not-For-Long”).

TABLE OF CONTENTS

List of Figures

List of Schemes

List of Tables

List of Publications at UW

2017

12. Barrows, C. J.; Fainblat, R.; Gamelin, D. R. Colloidal Zero-Dimensional Nanostructures Doped with Single Magnetic Impurities. *in preparation*.
11. Barrows, C. J.; Fainblat, R.; Gamelin, D. R. Excitonic Zeeman Splittings in Colloidal CdSe Quantum Dots Doped with Single Magnetic Impurities. *submitted*.
10. Muckel, F.; Barrows, C. J.; Graf, A.; Schmitz, A.; Gamelin, D. R.; Bacher, G. Current-Induced Magnetism in a Colloidal Quantum-Dot Device. *submitted.*
9. Barrows, C. J.; Rinehart, J. D.; Nagaoka, H.; deQuilettes, D. W.; Salvador, M.; Chen, J. I. L.; Ginger, D. S.; Gamelin, D. R. Electrical Detection of Quantum Dot Hot Electrons Generated via a Mn^{2+}-Enhanced Auger Process. *J. Phys. Chem. Lett.* **2017**, *8*, 126–130.

2016

8. Fainblat, R.; Barrows, C. J.; Hopmann, E.; Siebeneicher, S.; Vlaskin, V. A.; Gamelin, D. R.; Bacher, G. Giant Excitonic Exchange Splittings at Zero Field in Single Colloidal CdSe Quantum Dots Doped with Individual Mn^{2+} Impurities. *Nano Lett.* **2016**, *16*, 6371–6377.
7. Chakraborty, P.; Jin, Y.; Barrows, C. J.; Dunham, S.; Gamelin, D. R. Kinetics of Isovalent (Cd^{2+}) and Aliovalent (In^{3+}) Cation Exchange in $Cd_{1-x}Mn_xSe$ Nanocrystals. *J. Am. Chem. Soc.* **2016**, *138*, 12885–12893.
6. Hayes, E. C.; Porter, T. R.; Barrows, C. J.; Kaminsky, W.; Mayer, J. M.; Stoll, S. Electronic Structure of a Cu^{II}-Alkoxide Complex Modeling Intermediates in Copper-Catalyzed Alcohol Oxidations. *J. Am. Chem. Soc.* **2016**, *138*, 4132–4145.
5. Barrows, C. J.; Chakraborty, P.; Kornowske, L. M.; Gamelin, D. R. Tuning Equilibrium Compositions in Colloidal $Cd_{1-x}Mn_xSe$ Nanocrystals Using Diffusion Doping and Cation Exchange. *ACS Nano* **2016**, *10*, 910–918.

2015

4. Nelson, H. D.; Bradshaw, L. B.; Barrows, C. J.; Vlaskin, V. A.; Gamelin, D. R. Picosecond Dynamics of Excitonic Magnetic Polarons in Colloidal Diffusion-Doped $Cd_{1-x}Mn_xSe$ Quantum Dots. *ACS Nano* **2015**, *9*, 11177–11191.
3. Barrows, C. J.; Vlaskin, V. A.; Gamelin, D. R. Absorption and Magnetic Circular Dichroism Analyses of Giant Zeeman Splittings in Diffusion-Doped Colloidal $Cd_{1-x}Mn_xSe$ Quantum Dots. *J. Phys. Chem. Lett.* **2015**, *6*, 3076–3081.

2014

2. Fainblat, R.; Muckel, F.; Barrows, C. J.; Vlaskin, V. A.; Gamelin, D. R.; Bacher, G. Valence-Band Mixing Effects in the Upper-Excited-State Magneto-Optical Responses of Colloidal Mn^{2+}-Doped CdSe Quantum Dots. *ACS Nano* **2014**, *8*, 12669–12675.

2013

1. Vlaskin, V. A.; Barrows, C. J.; Erickson, C. S.; Gamelin, D. R. Nanocrystal Diffusion Doping. *J. Am. Chem. Soc.* **2013**, *135*, 14380–14389.

Chapter 1. Colloidal Zero-Dimensional Nanostructures Doped with Single Magnetic Impurities

1.1 Overview

Magnetic impurity doping dramatically alters the photophysical properties of semiconductors. The development of diluted magnetic semiconductors (DMSs) is critical for technologies requiring spin manipulation, such as spintronics and quantum computing. Singly doped quantum dots (SDQDs) represent a promising class of materials for the implementation of these technologies, and also provide model systems for the investigation of fundamental properties related to *sp–d* exchange. This Chapter reviews recent progress towards the development of colloidal zero-dimensional nanoclusters and quantum dots, doped with individual magnetic impurities. We summarize (magneto-)optical investigations of these materials on both the ensemble and single-particle level. Comparisons to the bulk materials and self-assembled quantum dots (QDs) are drawn, and advantages of the colloidal counterparts are discussed, including highly tunable compositions and enhanced *sp–d* exchange due to strong quantum confinement.

1.2 Introduction

Historically, impurity centers were viewed as a nuisance that inhibited the study of semiconductors,[1] but controlled doping of materials enabled the development of modern technologies such as the ruby laser and silicon microelectronics. The detection and manipulation of single spins in semiconductors underpins the ability to perform logic, communications, and storage operations in spin-based solid-state devices.[2, 3] Transition-metal doped semiconductors, known as "diluted magnetic semiconductors" (DMSs), are promising candidates for spintronics applications because they combine magnetic and semiconductor properties into a single material. Spin–spin (*sp–d*) exchange interactions between host semiconductor charge carriers and unpaired electrons localized around impurities lead to extraordinary magneto-optical responses in DMSs, such as giant Zeeman splittings,[4] giant Faraday rotation[5-7] and excitonic magnetic polaron formation.[8, 9] Because these effects are so large, they provide a rich field for the investigation of fundamental science and harnessing these effects allows us to add spin as a degree of freedom we can control in devices. For example, the ability to manipulate charge carriers based on spins in bulk DMSs has already been implemented in spin LEDs[10] and spin filters.[11, 12]

Advances in both the fabrication of epitaxially grown quantum dots (QDs)[13-17] and the synthesis of their colloidal analogues[18-23] over the last two decades have begun to overcome the longstanding challenge of controlled impurity doping in nanomaterials. Although most research has focused on achieving larger and larger dopant

concentrations, the emerging field of "solotronics" seeks to harness the properties of singly doped semiconductors for applications in quantum computation, quantum information science, and non-classical light sources.[24] There are certain advantages to preparing materials with precisely *one* magnetic dopant, such as the optical or electrical manipulation of a single defined spin state[24-28] and single-photon emission.[24, 29] Isolated transition-metal impurities can exhibit long spin coherence lifetimes (ms) necessary for durably storing information due to the absence of dopant–dopant interactions.[30-33] Theoretical predictions show quantum dots with single magnetic dopants could be utilized in single-electron transistors and spin filters,[34-36] but such devices fabricated from QDs have not yet been demonstrated.

Colloidal nanomaterials offer exquisite control over carrier wavefunctions through synthetic engineering of sizes, shapes, compositions, and heterointerfaces.[37] Recent advances in synthetic techniques have enabled unprecedented control over dopant incorporation, concentration, and location, thereby tuning the *sp–d* exchange interaction, which is affected by the overlap between the impurities and the confined wavefunctions of the semiconductor charge carriers.[38] Due to stronger quantum confinement in smaller volumes, giant magneto-optical responses in colloidal DMS nanostructures are strongly enhanced relative to their bulk and self-assembled counterparts, allowing the observation of *sp–d* exchange interactions even up to room temperature.[39-42]

In this Chapter, we review recent progress toward intentional doping of colloidal zero-dimensional semiconductor nanostructures with individual magnetic impurities. We

start by describing the mechanism responsible for the giant magneto-optical response of DMS materials: the *sp–d* exchange interaction. After this, we give an overview of the spectroscopic techniques commonly used to characterize magnetically doped semiconductors. Then we summarize ensemble measurements of singly doped DMS nanostructures, including both nanoclusters and quantum dots. Finally, we describe advances in single-particle measurements showing enhanced sensitivity to dopant location in singly doped quantum dots (SDQDs). Remaining challenges for harnessing the properties of colloidal SDQDs for new spin-based technologies are discussed.

1.2.1 sp–d Exchange

The incorporation of magnetic transition-metal (TM^{n+}) impurities to semiconductors introduces *sp–d* exchange interactions between unpaired spins of the impurity and charge carriers in the valence band and conduction band. *sp–d* exchange is the most characteristic feature of DMSs. The *s–d* and *p–d* exchange energies (related to the exchange constants $N_0\alpha$ and $N_0\beta$, respectively) in DMS nanostructures depend on wavefunction overlap between the dopant ion and the spatially confined carriers.[43] Mn^{2+} is by far the most commonly studied impurity in DMS systems, so we will use it as a model example to describe the origin of both *s–d* and *p–d* exchanges below. In Mn^{2+}-doped semiconductors, Mn^{2+} interactions with conduction band electrons (e^-_{CB}) are dominated by ferromagnetic kinetic exchange involving semiconductor cation *s* and Mn^{2+} 4*s* orbitals ($N_0\alpha > 0$).[44, 45] Mn^{2+} interactions with valence band holes (h^+_{VB}) are characterized by antiferromagnetic kinetic exchange involving hybridization of Mn 3*d* orbitals with

semiconductor anion *p* orbitals in the valence band. These interactions are typically stronger than TM^{n+}–e^-_{CB} interactions because the impurity is directly bound to anions. Because the 3*d* shell is half-occupied for Mn^{2+}, these interactions are always antiferromagnetic ($N_0\beta$ <0), including in bulk DMSs.[46] Similar orbital pathways apply for Co^{2+} and other transition-metal dopants.

In a magnetic field, excitonic states are split according to the Zeeman effect, as described in Equation 1.1. The first term describes the relatively small intrinsic Zeeman splitting (ΔE_{Int}), where g_{Int} is the intrinsic *g* value of the exciton (generally ~ +1), μ_B is the Bohr magneton, and *B* is the magnetic field. The so-called "giant Zeeman effect" is enabled by *sp–d* exchange contributions (ΔE_{sp-d}) to excitonic Zeeman splittings (ΔE_Z) according to the second term in Equation 1.1, where *x* is the dopant concentration and *γ* describes the exciton–impurity wavefunction overlap. $\langle S_Z \rangle$ is the spin expectation value of the magnetic ion spin along the magnetic field axis (*Z* component) at the experimental temperature (*T*) and magnetic field as described by the Brillouin function (Equation 1.2) for magnetic ions with spin-only ground states, such as Mn^{2+}. Following the sign convention of Piepho and Schatz,[47] S = –5/2 and $N_0(\alpha - \beta)$ is positive. The *sp–d* exchange term therefore opposes the positive sign of the relatively weak intrinsic Zeeman splitting, usually leading to an overall Zeeman splitting that is negative.

$$\Delta E_Z = g_{Int}\mu_B B + x\gamma N_0(\alpha - \beta)\langle S_Z \rangle \tag{1.1}$$

$$S_Z = \frac{2S+1}{2}\coth\left(\frac{2S+1}{2} \bullet \frac{g_{TM}\mu_B B}{k_B T}\right) - \frac{1}{2}\coth\left(\frac{g_{TM}\mu_B B}{k_B T}\right) \tag{1.2}$$

1.2.2 Spectroscopic Signatures of Magnetic Dopants

Many common spectroscopic and analytical techniques can detect the presence of a dopant associated with a nanocrystal, including nuclear magnetic resonance (NMR), energy dispersive X-ray spectroscopy (EDX), mass spectrometry (MS), and inductively coupled plasma atomic emission spectrometry (ICP-AES).[48, 49] Optically detected magnetic resonance (ODMR)[19] and electron paramagnetic resonance (EPR)[19, 50] can both detect the incorporation of magnetic dopants, and in the limit of low dopant concentrations can be used to distinguish between surface and core sites for magnetic dopants in semiconductor nanocrystals.[51] Depending on the host lattice's bandgap energy, dopants may introduce sub-bandgap ligand to metal charge transfer (LMCT) transitions or *d*–*d* excited states which can be observed by absorption or PL spectroscopies. The characteristic *sp*–*d* exchange interaction in magnetically doped semiconductor nanocrystals can be probed by Faraday rotation, magnetic circular dichroism (MCD) and magnetic circularly polarized luminescence (MCPL; when excitonic luminescence is present) spectroscopies, providing unambiguous confirmation of doping.[19, 52-55] Single-QD photoluminescence (PL) can also reveal magnetic-dopant–host exchange interactions, even in the absence of a magnetic field.[25]

Most of the investigations of DMS properties in this Chapter rely on a combination of EPR, MCD, and PL spectroscopies. Scheme 1.1 displays different optical transitions probed by these methods in zero-dimensional semiconductor nanostructures doped with

a single Mn^{2+} ion. The $^6A_1$ ground state of Mn^{2+} has a total spin $S = -5/2$ and splits into six Zeeman components ($m_S = \pm 1/2, \pm 3/2, \pm 5/2$) in a magnetic field (Scheme 1.1A). EPR spectroscopy probes transitions between these states (corresponding to different spin projections along the magnetic field axis) with the selection rule of $\Delta M_J = \pm 1$ for the typical transverse experimental configuration. EPR spectra of Mn^{2+}-doped nanocrystals usually show one resonance split into six major hyperfine features due to coupling of the $m_S = 5/2$ electron spins and the $I = 5/2$ Mn^{2+} nuclear spins.[19, 50] Covalency of the Mn^{2+}–anion bond affects the magnitude of this coupling, and therefore EPR spectroscopy can allow determination of the Mn^{2+} coordination environment (e.g. Mn^{2+} bound to O^{2-} of surface-passivating ligands vs. core Mn^{2+} bound to lattice anions in a nanocrystal).[51] When the dopant concentration increases, dopant–dopant interactions contribute to inhomogeneous broadening of the hyperfine splittings, resulting in a single broad derivative-shaped feature. Figure 1.1A shows a representative EPR spectrum of colloidal Mn^{2+}-doped CdS nanocrystals.[19] Six hyperfine lines are observed and additional weaker peaks between the six hyperfine lines come from second-order zero-field splitting of the $^6A_1$ ground state. The hyperfine coupling constant, $|A| = 64.5 \times 10^{-4}$ is consistent with Mn^{2+} in a tetrahedral S^{2-} environment.

The band-edge exciton ($1S_{3/2}1S_e$) of zero-dimensional, isotropic nanostructures is eight-fold degenerate. Due to shape and crystal lattice anisotropies however, this degeneracy is lifted and the $1S_{3/2}1S_e$ state splits into five excitonic sublevels,[56] three of which can be further split by the Zeeman splitting with an applied magnetic field (Scheme

1.1B). The Zeeman splitting of the $\pm1^U$ states (ΔE_Z) leads to preferential absorption of left (σ^-) or right (σ^+) circularly polarized light, which can be detected in MCD ($\Delta E_Z = E_L - E_R$). The sign of the MCPL polarization ratio $((I_L - I_R)/(I_L + I_R)$, where I is the intensity of emitted light) reflects the sign of the Zeeman splitting of the $\pm1^L$ state. The ±2 level is the so-called "dark exciton," which also splits in a magnetic field, but due to its low oscillator strength is not probed directly by these spectroscopies. It can however, pick up some intensity *via* field-induced mixing with higher-energy states, leading to a longer observed PL lifetime.[56] Negative Zeeman splittings (using the sign convention of Piepho and Schatz[47]) are observed in the MCD of Mn^{2+}-doped ZnSe (Figure 1.1B)[50] and the MCPL of Mn^{2+}-doped CdSe (Figure 1.1C).[54] Both sets of spectra exhibit signs of magnetic saturation at low temperature, characteristic of dominant *sp–d* exchange interactions.

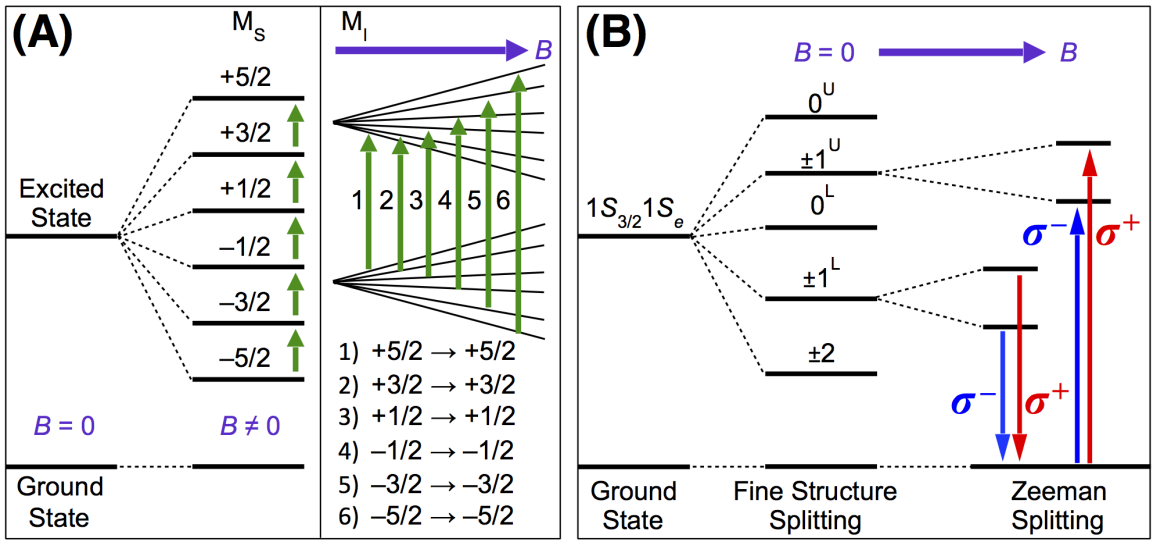

Scheme 1.1. **(A)** Electronic transitions in Mn^{2+}-doped semiconductors probed by EPR. Hyperfine transitions are shown on the right side of the panel. **(B)** Excitonic transitions probed by MCD and MCPL spectroscopies.

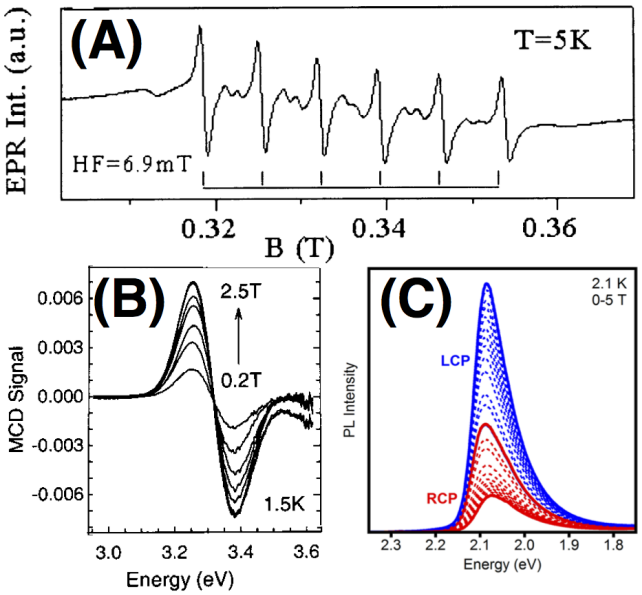

Figure 1.1. Representative magneto-optical spectra of colloidal nanocrystals doped with Mn^{2+}. (A) EPR of Mn^{2+}-doped CdS.[19] (B) MCD of Mn^{2+}-doped ZnSe.[50] (C) MCPL of Mn^{2+}-doped CdSe.[54] All three panels were adapted with permission from the noted references.

1.3 Ensemble Measurements of Singly Doped Nanostructures

1.3.1 Clusters

A fundamental challenge in nanocrystal doping has been overcoming self-purification processes, i.e. the exclusion of dopants from the quantum dot nucleus.[20, 21, 57, 58] Doping studies in nanoclusters may provide insight into doping mechanisms of nanocrystals via kinetic-trapping or cation-exchange processes. It has also been proposed that singly doped clusters could be used as seeds for larger nanocrystals for use in spintronics, overcoming the problem of the undoped core.[59]

The incorporation of a very small number of magnetic impurities in nanoclusters was first reported by the Meijerink group, who doped preformed magic-sized ZnTe with Mn^{2+} by cation exchange (Scheme 1.2).[59] They observed PL associated with the $^4T_1 \rightarrow {}^6A_1$ Mn^{2+} transition that was sensitized by the magic-sized nanoclusters and decayed with a 45 μs lifetime, similar to the PL lifetime in bulk Mn^{2+}:ZnTe. The lifetime in the cluster would likely be shorter if the Mn concentration was large, due to Mn^{2+}–Mn^{2+} cross-relaxation.[60] A low Mn^{2+} concentration is also consistent with the observation of a higher energy luminescence band associated with undoped ZnTe.

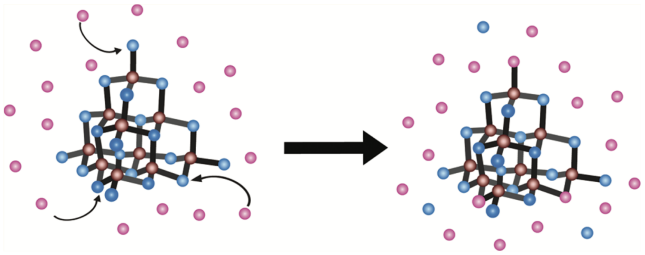

Scheme 1.2. Doping of magic-sized nanoclusters by cation exchange. Reproduced with permission from reference 59.

Early success in preparing Mn^{2+}-doped ZnTe magic-sized nanoclusters generated interest in the doping of other chalcogenide clusters. For example, Ling et al. employed a similar strategy of doping preformed clusters by engineering $[Cd_6In_{28}S_{52}(SH)_4]$ clusters with vacant core sites, enabling the incorporation of Mn^{2+} ions into specifically directed sites.[61] Reports of another molecular cluster cation-exchange reaction demonstrate the incorporation of Co^{2+} ions into metal benzene-thiolate clusters ($[M_4(SPh)_{10}]^{2-}$ (M = Zn, Cd)) containing only 4 cation sites.[62] Figure 1.2 shows room-temperature electronic absorption spectra of $[(Zn_{1-x}Co_x)_4(SPh)_{10}]^{2-}$ (labeled in the figure as "**$(Zn_{1-x}Co_x)$-4**") and $[(Cd_{1-x}Co_x)_4(SPh)_{10}]^{2-}$ ("**$(Cd_{1-x}Co_x)$-4**") clusters, as well as an analogous $[(Co)_4(SPh)_{10}]^{2-}$ ("**Co-4**") cluster and $[Co(SPh)_4](NMe_4)_2$ ("**Co-1**"). The Co^{2+} $^4A_2$ (F) $\rightarrow$ $^4T_1$(P) ligand field transition at ~1.8 eV is clearly observed in both the Zn and Cd clusters, providing evidence of successful doping.[63] Co^{2+}-doping also activates ligand-to-metal (3*d*) charge transfer ($LM_{Co}CT$) transitions at ~2.6–3.8 eV from ligand-based π-orbitals of the thiolates to the partially filled t_2 orbitals of the Co^{2+}. Higher energy transitions (>3.8 eV) in the Zn and Cd clusters are associated with host-based LMCT transitions and are relatively unchanged by Co^{2+} doping. Additional studies have shown that the incorporation of Co^{2+} impurities in the smaller $[Cd_4(SPh)10]^{2-}$ clusters is more thermodynamically favored than in its larger $[Cd_{10}S_4(SPh)16]^{4-}$ and $[Cd_{17}S_4(SPh)_{28}]^{2-}$ counterparts.[64] A combination of electrospray ionization mass spectrometry (ESI-MS) and ^{1}H-NMR and electronic absorption spectroscopies suggest a specific site (M-(μ-$SPh)_3$(SPh)) on the $(Cd_{1-x}Co_x)_{10}$ and $(Cd_{1-x}Co_x)_{17}$ clusters has the lowest energy barrier for single Co^{2+} cation exchange.

Although these clusters were used in the first successful doping of CdSe QDs with Co^{2+},[65] and they provide a clear molecular model for investigating cation exchange mechanisms in QDs, no semiconducting properties have been reported for these clusters.

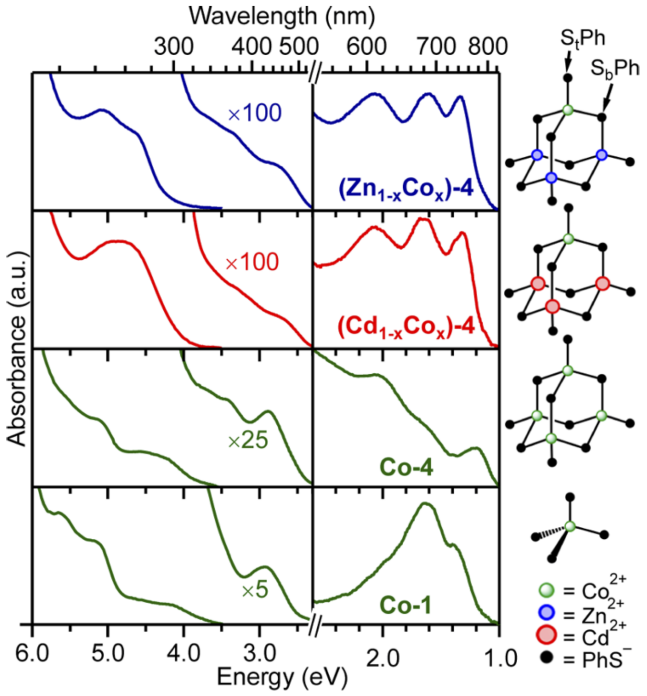

Figure 1.2. Room-temperature electronic absorption spectra of $[(Zn_{1-x}Co_x)_4(SPh)_{10}]^{2-}$ (blue), $[(Cd_{1-x}Co_x)_4(SPh)_{10}]^{2-}$ (red), $[(Co)_4(SPh)_{10}]^{2-}$ (green; upper), and $[Co(SPh)_4](NMe_4)_2$ (green; lower) clusters in acetonitrile. x_{nom} = 0.25 for the two doped clusters. The spectra are separated into three regions: >3.8 eV are intense host-based LMCT transitions; between 2.5 and ~3.9 eV are weaker Co^{2+}-related transitions; <2.3 eV are ligand-field transitions associated with Co^{2+}. The optical densities in the visible region are scaled by 1–2 orders of magnitude to be on the same scale as the UV transitions. Note the change in energy scaling changes at 2.3 eV denoted by the vertical line and "//" on the axes. Far right: schematic representations of the cluster and coordination environment of the Co^{2+} ions (phenyl groups omitted). Reproduced with permission from reference 62.

Absorption and MCD spectra of $Cd_{13-x}Mn_xSe_{13}$ clusters however, have revealed magneto-optical behavior consistent with the smallest known doped semiconductor (Figure 1.3A).[66] Because the energy differences between the five fine-structure-related excitonic states (Scheme 1.1B) scale inversely with volume, each of these transitions are easily resolved in the electronic absorption spectrum of the clusters. Using MCD spectroscopy, Yang et al. demonstrated the theoretically predicted magneto-optical activity of $\pm1^L$ and $\pm1^U$ (red and yellow regions of Figure 1.3A, respectively) and showed that the remaining 0^L and 0^U states (shown as dashed curves in the absorption spectrum) of the excitonic fine structure are magneto-optically passive.[66] Due to their extremely small size, the replacement of a single atom in magic-sized nanocrystals results in a very high doping concentration. Indeed, the large Mn^{2+} concentration (up to 10%) in the $Cd_{13-x}Mn_xSe_{13}$ clusters was confirmed by ICP-AES and laser desorption/ionization time-of-flight mass spectrometry (LDI-TOF MS). In temperature-dependent MCD studies on these clusters, the Zeeman splitting of the $\pm1^L$ state was always negative, indicating the *sp–d* exchange interaction with a single dopant is stronger than the intrinsic Zeeman splitting in clusters.[42]

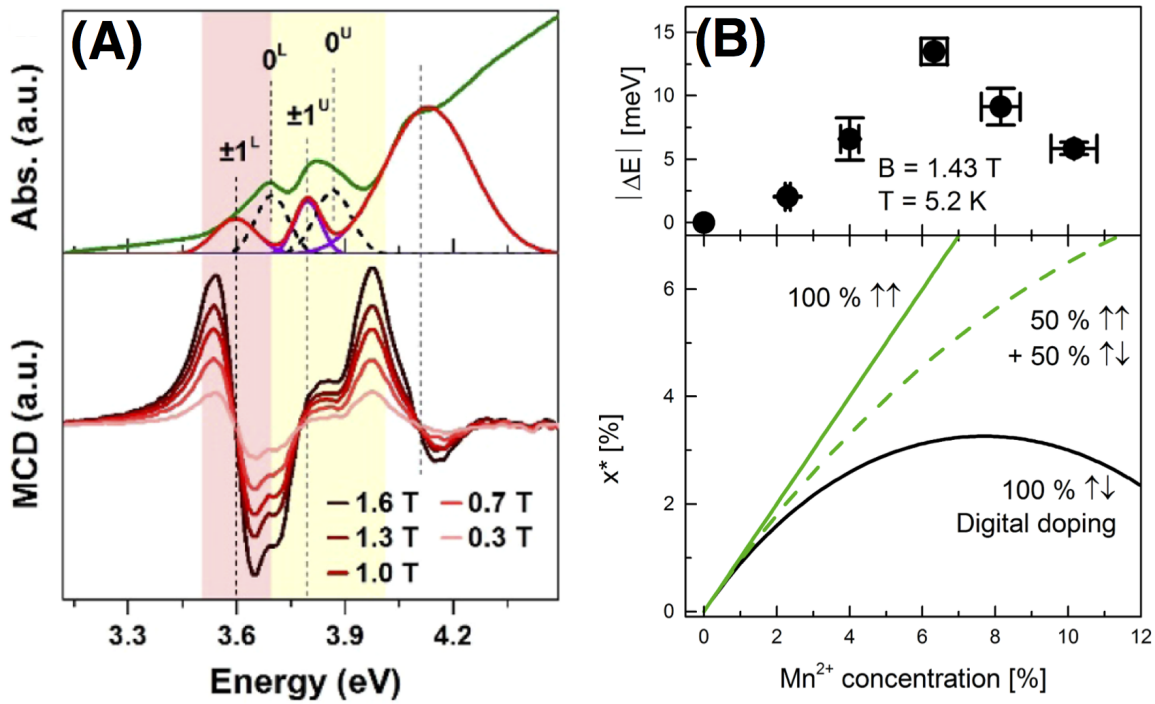

Figure 1.3. (A) Electronic absorption (top) and variable-field MCD (bottom) spectra of 4% Mn^{2+}-doped $(CdSe)_{13}$ clusters at 4.2 K. In the upper panel, green, violet, and black dashed lines indicate measured data, magneto-optically active, and inactive peaks, respectively. The red curve is the sum of the magneto-optically active transitions. (B) Digital doping in similar Mn^{2+}-doped $(CdSe)_{13}$ clusters. Top: Extracted Zeeman splittings of the $\pm 1^L$ state for different x_{nom}. The error bars for the Zeeman splitting take into account the uncertainty due to the fitting procedure. Bottom: Relation between the concentration of magneto-optically active Mn^{2+} ions and x_{nom} for two limiting cases: Mn^{2+} ions in $Cd_{11}Mn_2Se_{13}$ align either ferromagnetically (green continuous line) or antiferromagnetically (black line, the digital doping case). The dashed green line represents the case in which only 50% of the Mn^{2+} ions are antiferromagnetically coupled. Adapted with permission from references 42, 66.

$Cd_{13-x}Mn_xSe_{13}$ clusters were also used to reveal the type of coupling between two magnetic dopants within the same cluster. Using LDI-TOF MS, Muckel et al. demonstrated the presence of only undoped, mono- and bi-doped clusters, which seem to be the only energetically stable species under the synthesis conditions.[42] The relative amount of each $Cd_{13-x}Mn_xSe_{13}$ with x = 0, 1, and 2 species in an ensemble was extracted from the relative intensities of the features observed in the mass spectra. The authors proposed that only clusters containing a single impurity would exhibit a giant magneto-optical response. Clusters containing two Mn^{2+} ions should exhibit the same magneto-optical response as undoped species because the impurities align antiferromagnetically, nullifying their total spin. This proposed theory, called "digital doping," was verified by studying a series of clusters with different dopant concentrations (see Figure 1.3B). As the dopant concentration was increased, the Zeeman splitting increased in magnitude, but then began to decrease above ~7%, consistent with the prediction of digital doping. An outstanding question in these clusters is determining their molecular structure and the precise location of the dopants. Differentiation between a surface-bound dopant and a dopant in a "caged" core site could provide insight into structure–property relationships in doped nanostructures.

1.3.2 Quantum Dots

The synthesis of colloidal doped semiconductor nanocrystals has developed in parallel with the synthesis of clusters. Early doping strategies in colloidal QDs relied on kinetic trapping of dopants during NC growth, enabling studies of a wide range of DMS NCs.[20, 21] A second technique, cation exchange, allows post-synthetic control over dopant incorporation in a thermodynamically governed process.[67-72] Cation exchange is a versatile and robust strategy that often leads to large dopant concentrations, either by alloying or formation of core/shell heterointerfaces. Complete phase transformations are also possible. Recently, a second thermodynamically governed process, known as "diffusion doping," was developed for ions of relatively low mobility, such as Mn^{2+} and Co^{2+}.[41] Diffusion doping allows for exquisite tuning of the dopant concentration, from one impurity up to ~30%.[73, 74] Here, we review EPR and MCD studies of colloidal singly doped quantum dots (SDQDs).

Certain spintronics applications, such as quantum computing devices, will require long spin coherence lifetimes. The spins of single dopants within colloidal QDs are even more isolated than dopants inside bulk materials with the same dopant concentration due to the potential barriers formed by insulating ligand shells on colloidal QD surfaces. Isolation of these spins reduces the number of spin–spin relaxation pathways and consequently lengthens spin coherence lifetimes. Spin dephasing in colloidal QD ensembles doped with single magnetic impurities have been studied by pulsed EPR spectroscopy.[30-32] 2-pulse and 3-pulse electron spin echo envelope modulation (ESEEM)

experiments produce time-domain spectra with modulation frequencies that depend on electron–nuclear coupling. Fourier transforms of these spectra reveal which nuclei are coupled to the electron and therefore provide insight into spin relaxation processes. 2-pulse ESEEM measures T_2 (spin–spin relaxation) times and 3-pulse ESEEM measures T_1 (spin–lattice relaxation) times. More details about these techniques are provided elsewhere.[75, 76]

Figure 1.4A shows the pulse sequence (τ_0 = 3 μs; τ = 400 ns) used in nutation experiments performed at 5 K on colloidal d = 4.2 nm $Zn_{0.9995}Mn_{0.0005}O$ QDs.[30] Figure 1.4B shows the microwave power dependence of the average magnetization along the magnetic field axis (z). The oscillation period increases with decreasing power, depicting the first manipulation of spin coherence in colloidal DMS NCs. The Fourier transformed spectra of time decay curves are plotted in Figure 1.4C. A power-independent sharp peak at ~15 MHz corresponds to the ^{1}H ESEEM frequency. The power dependence of two additional frequencies is plotted in Figure 1.4D. The linear relationship between these two frequencies and the magnetic field amplitude of the microwave radiation ($B_1 = 1.04 \times P^{½}$) confirms these are the first observed Rabi oscillations in colloidal QDs.[76] The Rabi frequency (Ω_R) of an EPR transition from state i to state f is proportional to the matrix element of its magnetic dipole $\hat{S}_+$, defined by $\langle i \mid \hat{S}_+ \mid f \rangle$.[76] The observation of more than one frequency is a sign of the simultaneous excitation of multiple transitions, likely from Mn^{2+} ions in different QDs. Long-lasting Rabi oscillations in colloidal QDs could potentially be used as optically generated spin qubits in quantum computing applications.[77]

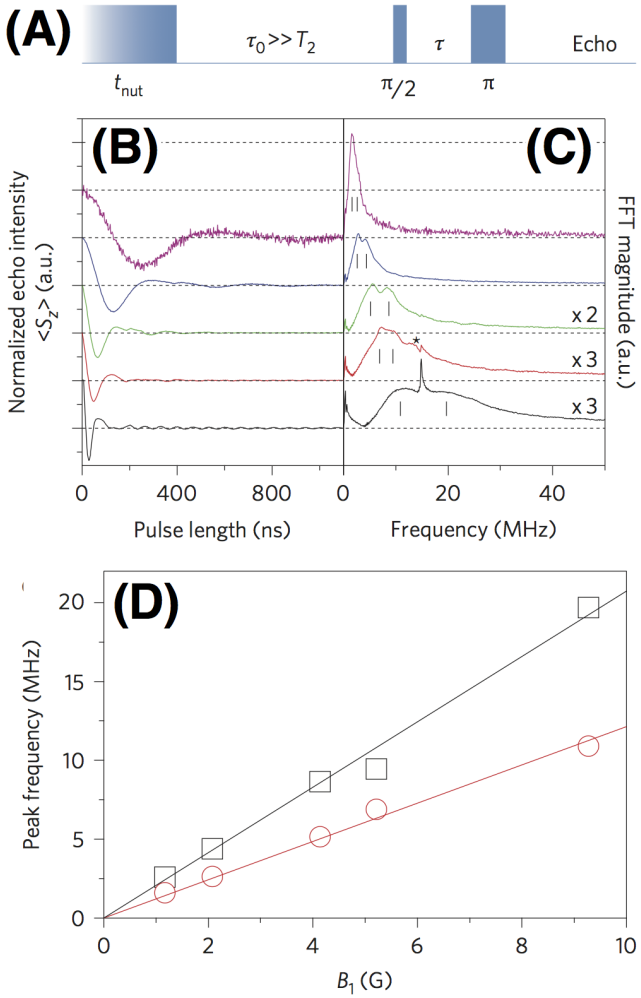

Figure 1.4. **(A)** Scheme of pulse sequence used to measure Rabi oscillations. **(B)** Echo intensity versus nutation pulse length (t_{nut}) measured for $Zn_{0.9995}Mn_{0.0005}O$ QDs at 3,479 G with microwave powers P of 1.25, 4.0, 15.8, 25.1, and 79.4 mW (top to bottom). **(C)** Fourier transform of panel B. The tick marks indicate the peak positions derived from Gaussian fits. The asterisk denotes the ^{1}H ESEEM frequency, which is independent of power (unlike the Rabi frequencies). **(D)** Peak frequencies from panel C as a function of the magnetic field component of the microwave radiation, B_1 (B_1 = 1.04 x $P^{1/2}$). The error of the peak position is approximately the size of the symbols. Adapted with permission from reference 30.

Dipole–dipole coupling between a magnetic dopant and spins on other nearby atoms reduces spin coherence times. Because the dopant concentration was so small, Mn^{2+}–Mn^{2+} spin dephasing was minimized in these $Zn_{0.9995}Mn_{0.0005}O$ QDs and T_2 was ~0.9 μs,[30] orders of magnitude longer than T_2 in bulk systems and quantum wells (<1 ns).[78, 79] Another strategy for minimizing dipole–dipole coupling in colloidal SDQDs is to insulate the magnetic impurity from the surface and solvent. Schimpf et al. studied QD relaxation process involving surfaces by growing a CdSe shell on d = ~2.9 nm $Cd_{0.996}Mn_{0.004}Se$ QDs and measuring the T_1 and T_2 relaxation times by pulsed EPR techniques (Figure 1.5A–B).[31] They found both the spin–spin and spin–lattice relaxation times in the core/shell nanocrystals were lengthened by more than a factor of 2 compared to the core-only QDs, corresponding to reduced dipole–dipole coupling expected due to the increased shell thickness. Fourier transforms of 3-pulse ESEEM data are plotted in Figure 1.5C and show the ^{1}H peak height decreases relative to the $^{111,113}Cd$ peak with shell growth, confirming reduced Mn^{2+}–surface H^{+} coupling in the core/shell QDs. Deuteration of the solvent and ligands reduced the Larmor frequency and also increased T_1 and T_2 times in Mn^{2+}-doped ZnO, implying long-range dipolar coupling, even to nuclear spins outside the QDs, can directly affect our ability to control dopant spins in colloidal systems.[31] Further work to isolate single magnetic impurities within colloidal QDs from other dipoles or nuclear spins could improve on this progress in understanding and manipulating spin coherence. For example, singly doped Fe^{3+}:ZnO should display longer spin-relaxation times because there is no nuclear spin to which the unpaired electrons can couple.[80, 81]

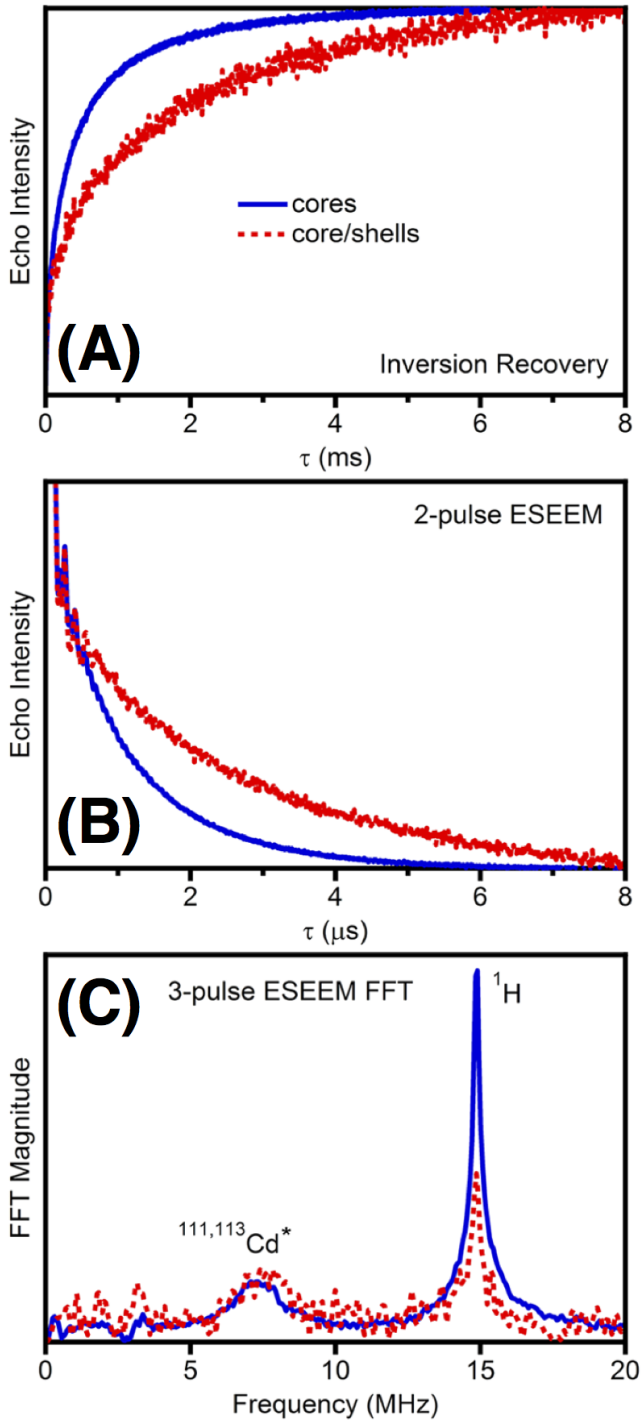

Figure 1.5. 4.5 K pEPR data collected on d = ~2.9 nm $Cd_{0.996}Mn_{0.004}Se$ QDs before and after CdSe shell growth (d = ~5.0 nm). **(A)** Echo-detected inversion recovery (T_1), **(B)** two-pulse spin–echo decay (T_2), and **(C)** Fourier transform plot of three-pulse ESEEM data. Adapted with permission from reference 31.

Because QDs are significantly larger than nanoclusters, they have much smaller values of *x* in the low-doping limit, leading to different behavior in MCD experiments. Although the exciton fine structure is not resolved in ensemble absorption measurements of QDs, low doping concentrations maintain the narrow and resolved excitonic absorption bands, allowing for the investigation of rich spectroscopic features by MCD, including the demonstration of valence-band mixing in the upper excited states of $Cd_{1-x}Mn_xSe$.[82] Figure 1.6 shows absorption and variable-temperature MCD spectra of colloidal $Cd_{0.995}Mn_{0.005}Se$ and $Cd_{0.995}Co_{0.005}Se$ QDs.[83] At low temperatures giant excitonic Zeeman splittings are observed. As the temperature increases, these splittings decrease in magnitude and eventually flip sign, approaching the intrinsic Zeeman splitting of undoped CdSe in the high-temperature limit. These results clearly illustrate the competition between intrinsic and exchange contributions to excitonic Zeeman splittings and demonstrate the *sp–d* exchange interactions are thermally tunable. This finding has important ramifications for the development of spintronics technologies where manipulation of exciton spin polarization is crucial.

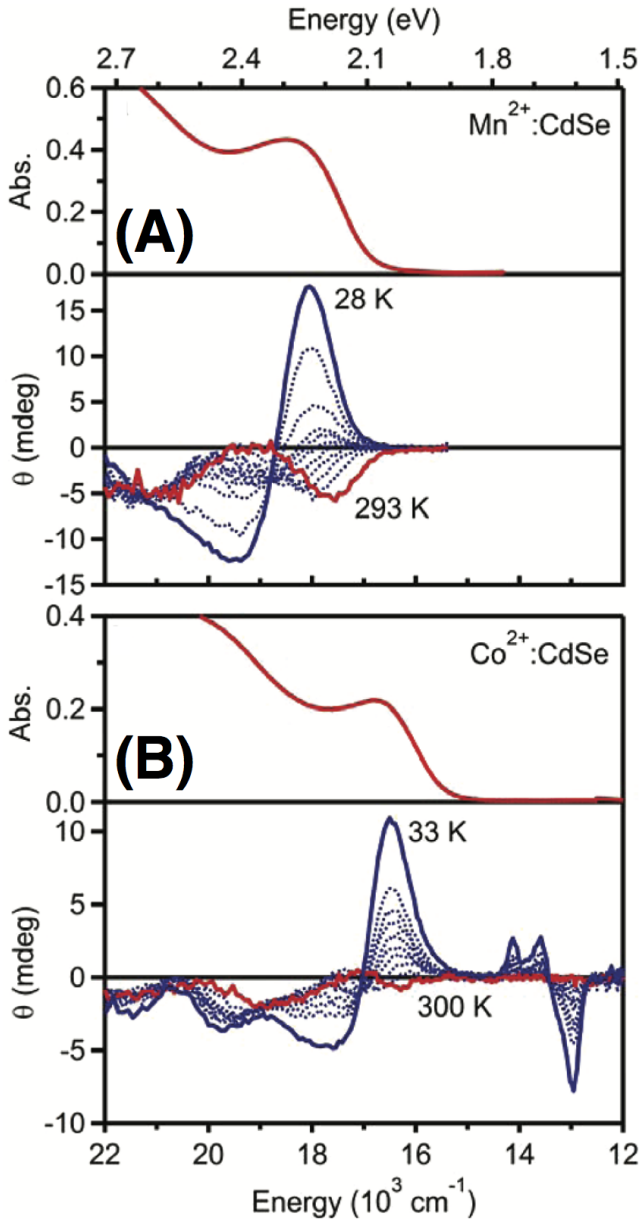

Figure 1.6. Representative absorption and variable-temperature MCD spectra of colloidal (A) $Cd_{0.995}Mn_{0.005}Se$ and (B) $Cd_{0.995}Co_{0.005}Se$ QDs, collected at B = 0.63 T. The bold red and blue MCD spectra represent the highest and lowest temperatures, respectively. Absorption spectra were collected on colloidal suspensions, and MCD spectra were collected on films drop-coated from these suspensions. Adapted with permission from reference 83.

Diluting the impurity concentration even further to the limit of less than one Mn^{2+} per CdSe QD reveals nonmonotonic evolution of MCD spectra with magnetic field at 1.7 K (Figure 1.7).[74] Figure 1.7A–B shows the zero-field 1.7 K electronic absorption spectrum collected simultaneously with variable-field (0–6 T) MCD spectra of colloidal d = 5.1 nm $Cd_{0.9997}Mn_{0.0003}Se$ QDs. The first two excitonic transitions ($1S_{3/2}1S_e$ and $2S_{3/2}1S_e$, respectively) are well-resolved. Instead of tuning ΔE_Z thermally,[83] here the competition between intrinsic and *sp–d* exchange contributions to ΔE_Z is achieved by changing the magnetic field.[74] At low magnetic fields, the low-energy leading edge of the MCD spectrum grows increasingly positive ($\Delta E_Z < 0$) with increasing field, consistent with Mn^{2+}-doped CdSe and a dominant *sp–d* exchange interaction.[65, 84, 85] This intensity reaches a maximum at ~1.5 T and then decreases and changes sign at higher fields ($\Delta E_Z > 0$), indicative of a dominant intrinsic Zeeman splitting. The temperature- and field-dependent Zeeman splitting of the $1S_{3/2}1S_e$ transition is plotted in Figure 1.7C. As the temperature increases, ΔE_Z approaches the intrinsic Zeeman splitting of undoped CdSe. Spectral deconvolution of the intrinsic and *sp–d* exchange contributions demonstrated that the origin of this turnover behavior was indeed due to the intrinsic term dominating at high fields after magnetic saturation of the *sp–d* exchange term.[74] From these data, the MCD spectra of undoped, singly doped, and bi-doped QDs were also extracted, revealing negative Zeeman splittings at all (positive) magnetic fields even in the limit of one dopant per QD.[74] This finding suggests the strength of the ensemble *sp–d* exchange in SDQDs is sufficient to produce giant magneto-optical responses necessary for viable spintronics applications.

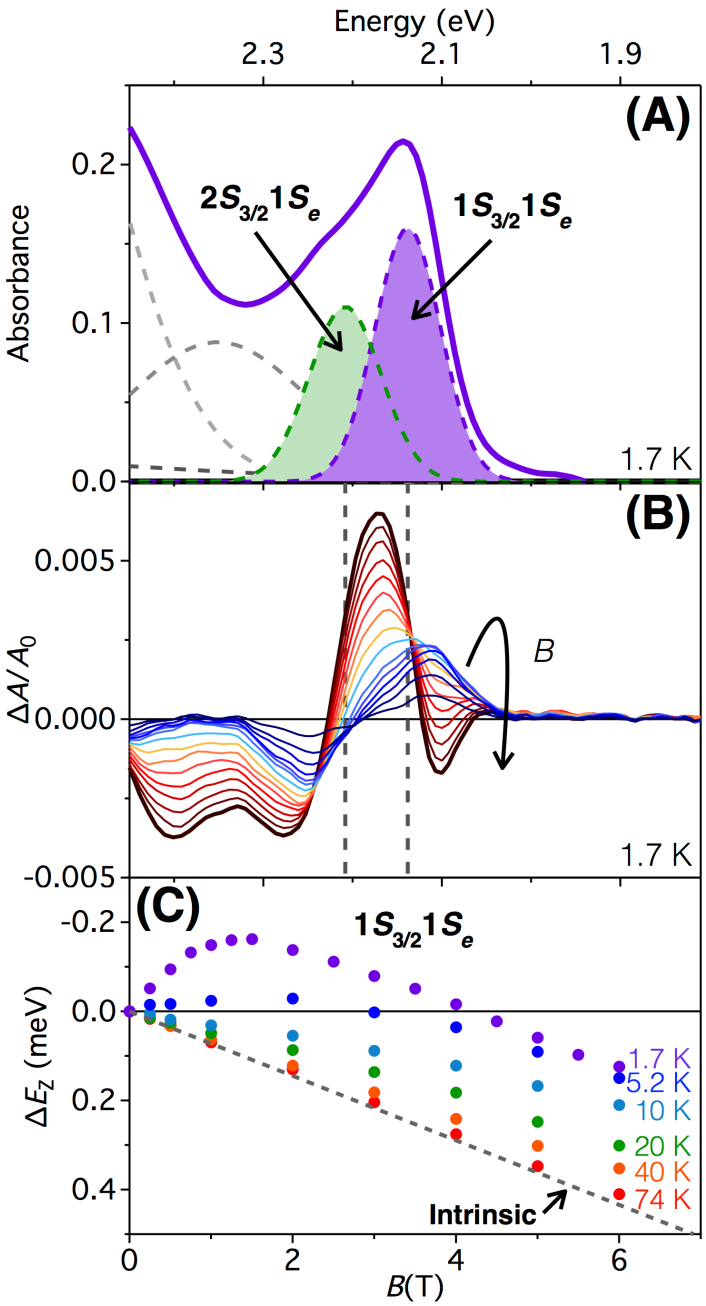

Figure 1.7. **(A)** 1.7 K electronic absorption spectrum (purple line) and multi-peak Gaussian fit of d = 5.1 nm $Cd_{0.9997}Mn_{0.0003}Se$ QDs. **(B)** Corresponding variable field (0–6 T; blue to red lines) MCD spectra of the same QDs at 1.7 K. The arrow indicates the direction of increasing magnetic field. Vertical dashed lines indicate the average energies of the first two excitonic transitions. **(C)** Field-dependent Zeeman splitting energies of the first excitonic band, determined from analysis of variable-temperature, variable-field MCD spectra. The intrinsic component (which is temperature-independent) is plotted as a grey dashed line. Adapted from Chapter 5.[74]

1.4 Measurements of Single Quantum Dots

Although the synthesis of colloidal zero-dimensional nanostructures has improved tremendously over the last two decades, ensemble inhomogeneities inevitably remain. Distributions in QD size, dopant concentration, and dopant location directly affect the photophysical properties of DMSs. Studies of single QDs (SQDs) can reveal effects that are attenuated by inhomogeneous broadening in ensembles. Isolation of single-magnetic-dopant–single-particle interactions provides insight into the photophysical properties of DMS QDs and advances our understanding of *sp–d* exchange on the nanoscale.

1.4.1 Imaging Single Dopants in Single QDs

Developments in microscopy now allow atomic-scale visualization of NC lattices. Identification of single dopants inside QD lattices can be achieved by annular dark-field scanning transmission electron microscopy (ADF-STEM), but only when the atomic number (Z) of the dopant is in large contrast to the host atoms.[86-90] Gunawan et al. recently overcame this limitation by combining ADF-STEM with electron energy loss spectroscopy (EELS), which detects atom-specific signals, regardless of Z-contrast.[91] Figure 1.8 shows an EELS map correlated with ADF-STEM measurements of colloidal Mn^{2+}-doped ZnSe nanocrystals. At specific points in the map, the characteristic two-peaked EELS spectrum of the Mn $L_{2,3}$-edge appears, providing precise measurements of which atomic columns of the NC contain the dopant. Detection of Mn^{2+} down to one dopant per d = 2.9 nm nanocrystal was achieved. Further development of this technique, perhaps in tandem with

modeling of MCD data,[92] could allow atomic-scale studies of dopant diffusion in nanocrystals and provide insight into dopant location–photophysical property correlations.

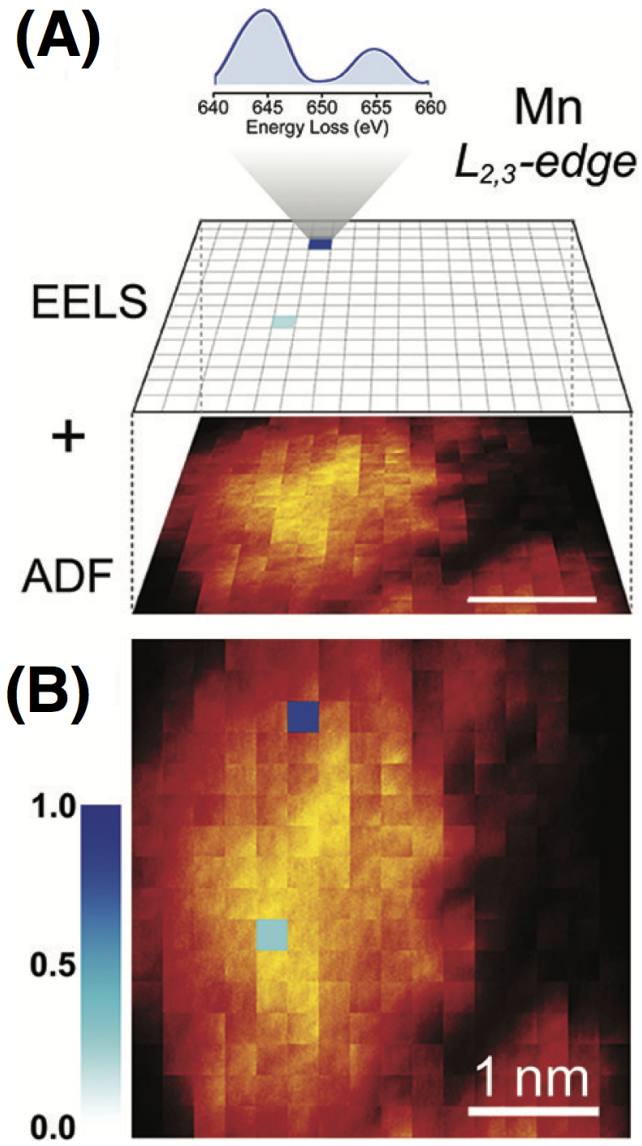

Figure 1.8. (A) Extracted core-level EELS map (shown as pixels on a grid) for the Mn $L_{2,3}$-edge along with the corresponding ADF-STEM image of a Mn^{2+}-doped ZnSe nanocrystal (d = 3.7 nm, 6.2 ± 1.5 Mn^{2+}/NC). The energy loss spectrum for one of the pixels where Mn was detected is shown. The characteristic double-peaked EELS spectrum for the Mn $L_{2,3}$-edge is seen. (B) Overlap of the Mn $L_{2,3}$-edge intensity map and the ADF-STEM image, both shown in panel A. Adapted with permission from reference 91.

1.4.2 Single-Particle Spectroscopy of SDQDs

The development of both self-assembled (epitaxially grown) QD synthesis and spectroscopic techniques with high spatial resolution enabled the investigation of (undoped) single self-assembled QDs using photoluminescence (PL) spectroscopy.[93-102] Spectroscopic investigations of single DMS QDs (grown by molecular beam epitaxy) containing a very small number of magnetic impurities soon followed, revealing that the observed PL linewidth is affected by magnetic fluctuations of the dopant spins.[13, 103] Shortly after this, Besombes et al. reported the first observation of spin–spin exchange interactions between a single Mn^{2+} impurity and the charge carriers of an individual CdTe QD.[25] PL spectra of undoped SQDs typically exhibit a sharp emission feature related to excitonic recombination, which in some cases is accompanied by relatively weak peaks at lower energy that are attributed to phonon replicas.[95, 104] Contrary to the commonly observed and relatively simple emission spectra of undoped QDs, a SQD containing only one Mn^{2+} impurity displays six lines related to the projection of its spin onto the exciton (Scheme 1.3). Although Mn^{2+} is by far the most studied single magnetic dopant,[26-28, 105-108] recently the incorporation of cobalt,[17] chromium,[33] and iron[109] as single impurities in individual self-assembled quantum dots have been reported.

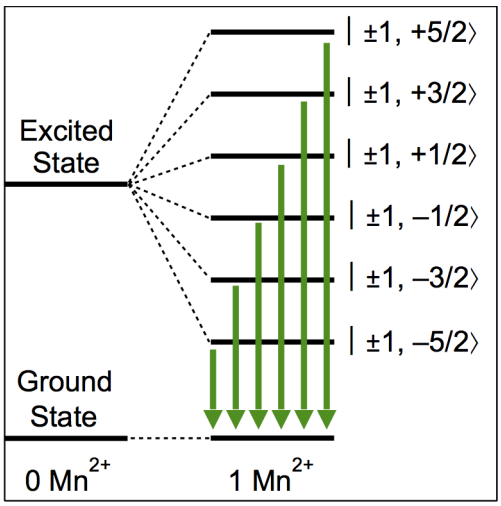

Scheme 3.3. Excitonic photoluminescence in QDs doped with a single Mn^{2+} impurity. The interaction between the spin of a photo-generated electron-hole pair ("Excited State"; $m_s = \pm 1$) with the different spin projections of a single impurity leads to the observation of multiple emission features. Mn^{2+} has five unpaired *d*-electrons, thus leading to a total spin of 5/2 and six possible projections (±5/2, ±3/2, and ±1/2).

The study of the PL of SDQDs was recently extended to colloidal systems for the first time.[110] Fainblat et al. investigated the single-particle emission spectra of CdSe QDs (d = 5.1–5.9 nm), each containing a very small number of Mn^{2+} ions. Spectra corresponding to 3 different kinds of single particles were observed: undoped QDs (single sharp emission features with phonon replicas, similar to literature reports), QDs containing two or more dopants (broad emission with no distinguishable sharp emission features) and QDs containing single dopants (spectrally well resolved features). A representative spectrum of a single colloidal CdSe nanocrystal containing a single Mn^{2+} impurity is depicted in Figure 1.9A. The energy splitting of the peaks was analyzed and is summarized in Figure 1.9B. The low-energy side of the spectrum displays features with an energy spacing of ~27 meV, consistent with the exciton–phonon coupling energy in undoped

CdSe.[95, 111] The splitting between neighboring emission peaks in the high-energy part of the spectrum originates from the exchange between the exciton spin with the different projections of Mn^{2+} spins (Scheme 1.3). Because the *sp–d* exchange interaction strongly depends on the overlap of the excitonic wavefunction and the dopant, the exact splitting energy provides a spectroscopic fingerprint for determining the dopant location within the nanocrystal, with larger splittings coming from dopants located closest to the core. Calculations confirm that due to the smaller volume of the colloidal QDs this splitting can be more than an order of magnitude larger than in epitaxially grown QDs. Indeed, splittings of up to ~80 meV were observed for these colloidal SDQDs, even in the absence of an applied magnetic field. Such "whopping" Zeeman splittings have only been observed previously in heavily-doped ensembles[39, 41, 54, 73, 85, 92] and could be used to prepare spin-polarized currents in future spintronics devices. More experiments are necessary to understand the relative intensities of the peaks. Time-resolved PL and MCPL could provide further insight into SDQD relaxation processes.

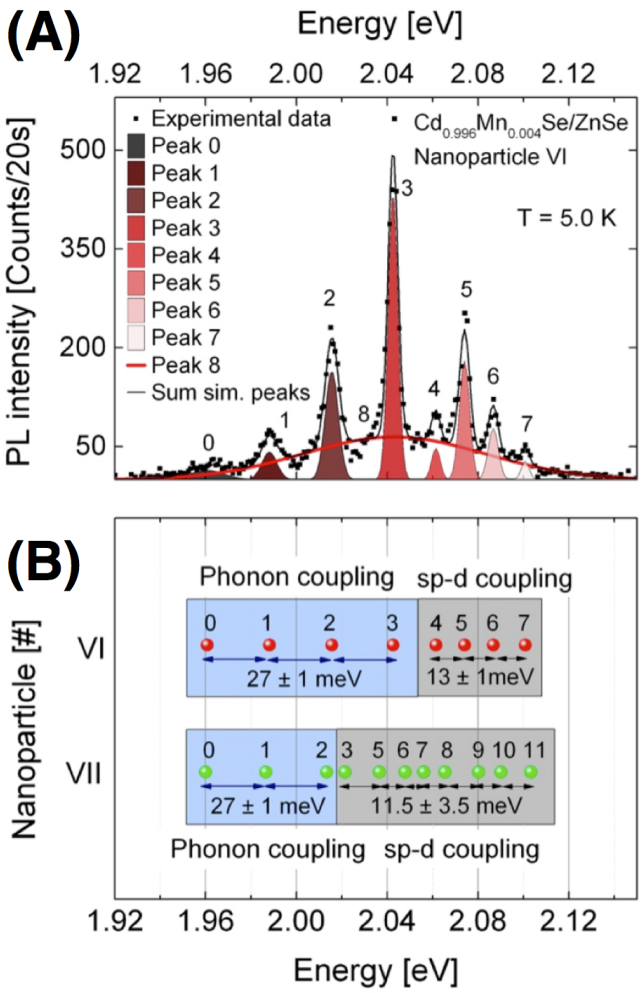

Figure 1.9. (A) PL spectrum of a single $Cd_{0.996}Mn_{0.004}Se/ZnSe$ nanocrystal collected at 5 K. The dots depict the experimental data, while the colored shaded peaks represent the fitted peaks. The sum of the fitted peaks is represented by the black line. The red curve accounts for the broad luminescence background, attributed to the multiple weak phonon replicas of the various purely electronic transitions. (B) Energy position of fitted peaks for two different single nanoparticles, including the nanoparticle analyzed in panel A. Adapted with permission from reference 110.

1.5 Conclusion

The preparation of colloidal semiconductor nanocrystals with single magnetic impurities represents a long-standing challenge in nanoscience. Our recent ability to access these structures opens the door for questions in fundamental research and potential technological applications. This Chapter highlights advances in this field and presents new challenges for studies of spintronics. Harnessing the advantages of thermodynamically controlled doping processes such as diffusion doping and cation exchange will contribute to our ability to perform atomically precise ion implantation. Single dopants are extremely sensitive to perturbations in nanocrystal size, shape, strain, or anisotropy, and can therefore be utilized as probes of electronic structure. Development of colloidal SDQDs represents the next logical step for implementing new solotronics technologies and future work in colloidal nanocrystal doping (e.g., in III–V materials and/or with lanthanide dopants) will provide new opportunities for this rich and growing field.

1.6 Acknowledgments

I thank Dr. Rachel Fainblat for many useful discussions.

1.7 References

1. Pauli, W. *Wissenschaftlicher Briefwechsel mit Bohr, Einstein, Heisenberg u.a. Band II: 1930–1939*. Springer: Berlin, 1985; Vol. 6.
2. Awschalom, D. D.; Flatté, M. E. Challenges for Semiconductor Spintronics. *Nat. Phys.* **2007**, *3*, 153–159.
3. Dietl, T.; Ohno, H. Dilute Ferromagnetic Semiconductors: Physics and Spintronic Structures. *Rev. Mod. Phys.* **2014**, *86*, 187–251.
4. Aggarwal, R. L.; Jasperson, S. N.; Stankiewicz, J.; Shapira, Y.; Foner, S.; Khazai, B.; Wold, A. Magnetoreflectance at the Band Edge in $Cd_{1-x}Mn_xSe$. *Phys. Rev. B* **1983**, *28*, 6907–6913.
5. Bartholomew, D. U.; Furdyna, J. K.; Ramdas, A. K. Interband Faraday-Rotation in Diluted Magnetic Semiconductors: $Zn_{1-x}Mn_xTe$ and $Cd_{1-x}Mn_xTe$. *Phys. Rev. B* **1986**, *34*, 6943–6950.
6. Yasuhira, T.; Uchida, K.; Matsuda, Y. H.; Miura, N.; Twardowski, A. Magnetic and Non-Magnetic Faraday Rotation in ZnMnSe in High Magnetic Fields. *Semicond. Sci. Technol.* **1999**, *14*, 1161–1164.
7. Yasuhira, T.; Uchida, K.; Matsuda, Y. H.; Miura, N.; Twardowski, A. Giant Faraday Rotation Spectra of $Zn_{1-x}Mn_xSe$ Observed in High Magnetic Fields Up To 150 T. *Phys. Rev. B* **2000**, *61*, 4685–4688.
8. Golnik, A.; Ginter, J.; Gaj, J. A. Magnetic Polarons in Exciton Luminescence of $Cd_{1-x}Mn_xTe$. *J. Phys. C.: Sol. State Phys.* **1983**, *16*, 6073–6084.
9. Mackh, G.; Ossau, W.; Yakovlev, D. R.; Waag, A.; Landwehr, G.; Hellmann, R.; Göbel, E. O. Localized Exciton Magnetic Polarons in $Cd_{1-x}Mn_xTe$. *Phys. Rev. B* **1994**, *49*, 10248.
10. Fiederling, R.; Keim, M.; Reuscher, G.; Ossau, W.; Schmidt, G.; Waag, A.; Molenkamp, L. W. Injection and Detection of a Spin-Polarized Current in a Light-Emitting Diode. *Nature* **1999**, *402*, 787–790.
11. Ohno, H.; Matsukura, F.; Omiya, T.; Akiba, N. Spin-Dependent Tunneling and Properties of Ferromagnetic (Ga,Mn)As. *J. Appl. Phys.* **1999**, *85*, 4277–4282.
12. Ohno, Y.; Young, D. K.; Beschoten, B.; Matsukura, F.; Ohno, H.; Awchalom, D. D. Electrical Spin Injection in a Ferromagnetic Semiconductor Heterostructure. *Nature* **1999**, *402*, 790–792.
13. Hundt, A.; Puls, J.; Henneberger, F. Spin Properties of Self-Organized Diluted Magnetic $Cd_{1-x}Mn_xSe$ Quantum Dots. *Phys. Rev. B* **2004**, *69*, 121309(R).
14. Bacher, G.; Schömig, H.; Scheibner, M.; Forchel, A.; Maksimov, A. A.; Chernenko, A. V.; Dorozhkin, P. S.; Kulakovskii, V. D.; Kennedy, T.; Reinecke, T. L. Spin–Spin Interaction in Magnetic Semiconductor Quantum Dots. *Phys. E* **2005**, *26*, 37–44.
15. Gaj, J. A.; Kossut, J. *Introduction to the Physics of Diluted Magnetic Semiconductors*. Springer: Berlin, 2010; Vol. 144.
16. Tartakovskii, A. *Quantum Dots: Optics, Electron Transport, and Future Applications*. Cambridge University Press: Cambridge, UK, 2012.

17. Kobak, J.; Smoleński, T.; Goryca, M.; Papaj, M.; Gietka, K.; Bogucki, A.; Koperski, M.; Rousset, J.-G.; Suffczyński, J.; Janik, E.; Nawrocki, M.; Golnik, A.; Kossacki, P.; Pacuski, W. Designing Quantum Dots for Solotronics. *Nat. Commun.* **2014**, *5*, 3191.
18. Bhargava, R. N.; Gallagher, D.; Hong, X.; Nurmikko, A. Optical Properties of Manganese-Doped Nanocrystals of ZnS. *Phys. Rev. Lett.* **1994**, *72*, 416–419.
19. Hoffman, D. M.; Meyer, B. K.; Ekimov, A. I.; Merkulov, I. A.; Efros, A. L.; Rosen, M.; Couino, G.; Gacoin, T.; Boilot, J. P. Giant Internal Magnetic Fields in Mn Doped Nanocrystal Quantum Dots. *Solid State Commun.* **2000**, *114*, 547–550.
20. Erwin, S. C.; Zu, L.; Haftel, M. I.; Efros, A. L.; Kennedy, T. A.; Norris, D. J. Doping Semiconductor Nanocrystals. *Nature* **2005**, *436*, 91–94.
21. Norris, D. J.; Efros, A. L.; Erwin, S. C. Doped Nanocrystals. *Science* **2008**, *319*, 1776–1779.
22. Beaulac, R.; Archer, P. I.; Ochsenbein, S. T.; Gamelin, D. R. Mn^{2+}-Doped CdSe Quantum Dots: New Inorganic Materials for Spin-Electronics and Spin-Photonics. *Adv. Funct. Mater.* **2008**, *18*, 3873–3891.
23. Buonsanti, R.; Milliron, D. J. Chemistry of Doped Colloidal Nanocrystals. *Chem. Mater.* **2013**, *25*, 1305–1317.
24. Koenraad, P. M.; Flatté, M. E. Single Dopants in Semiconductors. *Nat. Mater.* **2011**, *10*, 91–100.
25. Besombes, L.; Léger, Y.; Maingault, L.; Ferrand, D.; Mariette, H.; Cibert, J. Probing the Spin State of a Single Magnetic Ion in an Individual Quantum Dot. *Phys. Rev. Lett.* **2004**, *93*, 207403.
26. Kudelski, A.; Lemaître, A.; Miard, A.; Voisin, P.; Graham, T. C. M.; Warburton, R. J.; Krebs, O. Optically Probing the Fine Structure of a Single Mn Atom in an InAs Quantum Dot. *Phys. Rev. Lett.* **2007**, *99*, 247209.
27. Goryca, M.; Kazimierczuk, T.; Nawrocki, M.; Golnik, A.; Gaj, J. A.; Kossacki, P.; Wojnar, P.; Karczewski, G. Optical Manipulation of a Single Mn Spin in a CdTe-Based Quantum Dot. *Phys. Rev. Lett.* **2009**, *103*, 087401.
28. Baudin, E.; Benjamin, E.; Lemaître, A.; Krebs, O. Optical Pumping and a Nondestructive Readout of a Single Magnetic Impurity Spin in an InAs/GaAs Quantum Dot. *Phys. Rev. Lett.* **2011**, *107*, 197402.
29. Besombes, L.; Leger, Y.; Bernos, J.; Boukari, H.; Mariette, H.; Poizat, J. P.; Clement, T.; Fernández-Rossier, J.; Aguado, R. Optical Probing of Spin Fluctuations of a Single Paramagnetic Mn Atom in a Semiconductor Quantum Dot. *Phys. Rev. B* **2008**, *78*, 125324.
30. Ochsenbein, S. T.; Gamelin, D. R. Quantum Oscillations in Magnetically Doped Colloidal Nanocrystals. *Nature Nanotech.* **2011**, *6*, 112–115.
31. Schimpf, A. M.; Ochsenbein, S. T.; Gamelin, D. R. Surface Contributions to Mn^{2+} Spin Dynamics in Colloidal Doped Quantum Dots. *J. Phys. Chem. Lett.* **2015**, *6*, 457–463.
32. Moro, F.; Turyanska, L.; Wilman, J.; Fielding, A. J.; Fay, M. W.; Granwehr, J.; Patanè, A. Electron Spin Coherence Near Room Temperature in Magnetic Quantum

Dots. *Sci. Rep.* **2015**, *5*, 10855.
33. Lafuente-Sampietro, A.; Utsumi, H.; Boukari, H.; Kuroda, S.; Besombes, L. Spin Dynamics of an Individual Cr Atom in a Semiconductor Quantum Dot Under Optical Excitation. *Appl. Phys. Lett.* **2016**, *109*, 053107.
34. Qu, F.; Vasilopoulos, P. Spin Transport Across a Quantum Dot Doped with a Magnetic Ion. *Appl. Phys. Lett.* **2006**, *89*, 122512.
35. Fernández-Rossier, J.; Aguado, R. Single-Electron Transport in Electrically Tunable Nanomagnets. *Phys. Rev. Lett.* **2007**, *98*, 106805.
36. Efros, A. L.; Rashba, E. I.; Rosen, M. Paramagnetic Ion-Doped Nanocrystal as a Voltage-Controlled Spin Filter. *Phys. Rev. Lett.* **2001**, *87*, 206601.
37. Kovalenko, M. V.; Manna, L.; Cabot, A.; Hens, Z.; Talapin, D. V.; Kagan, C. R.; Klimov, V. I.; Rogach, A. L.; Reiss, P.; Milliron, D. J.; Guyot-Sionnest, P.; Konstantatos, G.; Parak, W. J.; Hyeon, T.; Korgel, B. A.; Murray, C. B.; Heiss, W. Prospects of Nanoscience with Nanocrystals. *ACS Nano* **2015**, *9*, 1012–1057.
38. Bhattacharjee, A. K.; Pérez-Conde, J. Confinement-Induced Enhancement of Spin Interaction in Mn-Doped II–VI Semiconductor Nanocrystals. *Phys. Stat. Sol. (B)* **2004**, *241*, 672–675.
39. Beaulac, R.; Schneider, L.; Archer, P. I.; Bacher, G.; Gamelin, D. R. Light-Induced Spontaneous Magnetization in Doped Colloidal Quantum Dots. *Science* **2009**, *325*, 973–976.
40. Fainblat, R.; Frohleiks, J.; Muckel, F.; Yu, J. H.; Yang, J.; Hyeon, T.; Bacher, G. Quantum Confinement-Controlled Exchange Coupling in Manganese(II)-Doped CdSe Two-Dimensional Quantum Well Nanoribbons. *Nano Lett.* **2012**, *12*, 5311–5317.
41. Vlaskin, V. A.; Barrows, C. J.; Erickson, C. S.; Gamelin, D. R. Nanocrystal Diffusion Doping. *J. Am. Chem. Soc.* **2013**, *135*, 14380–14389.
42. Muckel, F.; Yang, J.; Lorenz, S.; Baek, W.; Chang, H.; Hyeon, T.; Bacher, G.; Fainblat, R. Digital Doping in Magic-Sized CdSe Clusters. *ACS Nano* **2016**, *10*, 7135–7141.
43. Bhattacharjee, A. K. Nanocrystals of Diluted Magnetic Semiconductors: Model for Magnetic Polaron. *Phys. Rev. B* **1995**, *51*, 9912.
44. Beaulac, R.; Gamelin, D. R. Two-Center Formulation of Mn^{2+}–Electron *s–d* Exchange Coupling in Bulk and Quantum-Confined Diluted Magnetic Semiconductors. *Phys. Rev. B* **2010**, *82*, 224401.
45. Beaulac, R.; Feng, Y.; May, J.; Badeva, E.; Gamelin, D. R.; Li, X. Orbital Pathways for Mn^{2+}–Carrier *sp–d* Exchange in Magnetic Semiconductor Quantum Dots. *Phys. Rev. B* **2011**, *84*, 195324.
46. Gaj, J. A.; Kossut, J. Basic Consequences of *sp–d* and *d–d* Interactions in DMS. In *Introduction to the Physics of Diluted Magnetic Semiconductors*, Gaj, J. A.; Kossut, J., Eds; Springer: Berlin, 2010; Vol. 144.
47. Piepho, S. B.; Schatz, P. N. *Group Theory in Spectroscopy with Applications to Magnetic Circular Dichroism*. Wiley: New York, 1983.

48. Bryan, J. D.; Gamelin, D. R. Doped Semiconductor Nanocrystals: Synthesis, Characterization, Physical Properties, and Applications. *Prog. Inorg. Chem.* **2005**, *54*, 47–126.
49. Ladizhansky, V.; Vega, S. Doping of CdS Nanoparticles by Co2+ Ions Studied by NMR. *J. Phys. Chem. B* **2000**, *104*, 5237–5241.
50. Norris, D. J.; Yao, N.; Chamrock, F. T.; Kennedy, T. A. High-Quality Manganese-Doped ZnSe Nanocrystals. *Nano Lett.* **2001**, *1*, 3–7.
51. Zheng, W.; Wang, Z.; Wright, J.; Goundie, B.; Dalal, N. S.; Meulenberg, R. W.; Strouse, G. F. Probing the Local Site Environments in Mn:CdSe Quantum Dots. *J. Phys. Chem. C* **2011**, *115*, 23305–23314.
52. Beaulac, R.; Archer, P. I.; Liu, X.; Lee, S.; Salley, G. M.; Dobrowolska, M.; Furdyna, J. K.; Gamelin, D. R. Spin-Polarizable Excitonic Luminescence in Colloidal Mn^{2+}-Doped CdSe Quantum Dots. *Nano Lett.* **2008**, *8*, 1197–1201.
53. Viswanatha, R.; Pietryga, J. M.; Klimov, V. I.; Crooker, S. A. Spin-Polarized Mn^{2+} Emission from Mn-Doped Colloidal Nanocrystals. *Phys. Rev. Lett.* **2011**, *107*, 067402.
54. Nelson, H. D.; Bradshaw, L. R.; Barrows, C. J.; Vlaskin, V. A.; Gamelin, D. R. Picosecond Dynamics of Excitonic Magnetic Polarons in Colloidal Diffusion-Doped $Cd_{1-x}Mn_xSe$ Quantum Dots. *ACS Nano* **2015**, *9*, 11177–11191.
55. Rice, W. D.; Liu, W.; Baker, T. A.; Sinitsyn, N. A.; Klimov, V. I.; Crooker, S. A. Revealing Giant Internal Magnetic Fields Due to Spin Fluctuations in Magnetically Doped Colloidal Nanocrystals. *Nat. Nanotechnol.* **2016**, *11*, 137–142.
56. Efros, A. L.; Rosen, M.; Kuno, M.; Nirmal, M.; Norris, D. J.; Bawendi, M. G. Band-edge Exciton in Quantum Dots of Semiconductors with a Degenerate Valence Band: Dark and Bright Exciton States. *Phys. Rev. B* **1996**, *54*, 4843–4856.
57. Mikulec, F. V.; Kuno, M.; Bennati, M.; Hall, D. A.; Griffin, R. G.; Bawendi, M. G. Organometallic Synthesis and Spectroscopic Characterization of Manganese-Doped CdSe Nanocrystals. *J. Am. Chem. Soc.* **2000**, *122*, 2532–2540.
58. Dalpian, G. M.; Chelikowsky, J. R. Self-Purification in Semiconductor Nanocrystals. *Phys. Rev. Lett.* **2006**, *96*, 226802.
59. Eilers, J.; Groenveld, E.; de Mello Donegá, C.; Meijerink, A. Optical Properties of Mn-Doped ZnTe Magic Size Nanocrystals. *J. Phys. Chem. Lett.* **2012**, *3*, 1663–1667.
60. Suyver, J. F.; Wuister, S. F.; Kelly, J. J.; Meijerink, A. Luminescence of Nanocrystalline ZnSe:Mn^{2+}. *Phys. Chem. Chem. Phys.* **2000**, *2*, 5445–5448.
61. Lin, J.; Zhang, Q.; Wang, L.; Liu, X.; Yan, W.; Wu, T.; Bu, X.; Feng, P. Atomically Precise Doping of Monomanganese Ion into Coreless Supertetrahedral Chalcogenide Nanocluster Inducing Unusual Red Shift in Mn^{2+} Emission. *J. Am. Chem. Soc.* **2014**, *136*, 4769–4779.
62. Pittala, S.; Kittilstved, K. R. Cation Exchange in Small ZnS and CdS Molecular Analogues. *Inorg. Chem.* **2015**, *54*, 5757–5767.

63. Dance, I. G. Synthesis, Crystal Structure, and Properties of the Hexa(.mu.-benzenethiolato)tetra(benzenethiolatocobaltate(II)) Dianion, the Prototype Cobalt(II)-thiolate Molecular Cluster. *J. Am. Chem. Soc.* **1979**, *101*, 6264–6273.
64. Pittala, S.; Mortelliti, M. J.; Kato, F.; Kittilstved, K. R. Substitution of Co2+ Ions into CdS-Based Molecular Clusters. *Chem. Commun.* **2015**, *51*, 17096–17099.
65. Archer, P. I.; Santangelo, S. A.; Gamelin, D. R. Direct Observation of sp–d Exchange Interactions in Colloidal Mn^{2+}- and Co^{2+}-Doped CdSe Quantum Dots. *Nano Lett.* **2007**, *7*, 1037–1043.
66. Yang, J.; Fainblat, R.; Kwon, S. G.; Muckel, F.; Yu, J. H.; Terlinden, H.; Kim, B. H.; Iavarone, D.; Choi, M. K.; Kim, I. Y.; Park, I.; Hong, H.-K.; Lee, J.; Son, J. S.; Lee, Z.; Kang, K.; Hwang, S.-J.; Bacher, G.; Hyeon, T. Route to the Smallest Doped Semiconductor: Mn^{2+}-Doped $(CdSe)_{13}$ Clusters. *J. Am. Chem. Soc.* **2015**, *137*, 12776–12779.
67. Son, D. H.; Hughes, S. M.; Yin, Y.; Alivisatos, A. P. Cation Exchange Reactions in Ionic Nanocrystals. *Science* **2004**, *306*, 1009–1012.
68. de Mello Donegá, C. Synthesis and Properties of Colloidal Heteronanocrystals. *Chem. Soc. Rev.* **2011**, *40*, 1512–1546.
69. Beberwyck, B. J.; Surendranath, Y.; Alivisatos, A. P. Cation Exchange: A Versatile Tool for Nanomaterials Synthesis. *J. Phys. Chem. C* **2013**, *117*, 19759–19770.
70. Rivest, J. B.; Jain, P. K. Cation Exchange on the Nanoscale: An Emerging Technique for New Material Synthesis, Device Fabrication, and Chemical Sensing. *Chem. Soc. Rev.* **2013**, *42*, 89–96.
71. Gupta, S.; Kershaw, S. V.; Rogach, A. L. 25th Anniversary Article: Ion Exchange in Colloidal Nanocrystals. *Adv. Mater.* **2013**, *25*, 6923–6944.
72. De Trizio, L.; Manna, L. Forging Colloidal Nanostructures via Cation Exchange Reactions. *Chem. Rev.* **2016**, *116*, 10852–10887.
73. Barrows, C. J.; Chakraborty, P.; Kornowske, L. M.; Gamelin, D. R. Tuning Equilibrium Compositions in Colloidal $Cd_{1-x}Mn_xSe$ Nanocrystals Using Diffusion Doping and Cation Exchange. *ACS Nano* **2016**, *10*, 910–918.
74. Barrows, C. J.; Fainblat, R.; Gamelin, D. R. Excitonic Zeeman Splittings in Colloidal CdSe Quantum Dots Doped with Single Magnetic Impurities. *submitted*.
75. Hahn, E. L. Spin Echoes. *Phys. Rev.* **1950**, *80*, 580.
76. Schweiger, A.; Jeschke, G. *Principles of Pulse Electron Paramagnetic Resonance*. Oxford University Press: Oxford, 2001.
77. Loss, D.; DiVincenzo, D. P. Quantum Computation with Quantum Dots. *Phys. Rev. A* **1998**, *57*, 120–126.
78. Crooker, S. A.; Baumberg, J. J.; Flack, F.; Samarth, N.; Awchalom, D. D. Terahertz Spin Precession and Coherent Transfer of Angular Momenta in Magnetic Quantum Wells. *Phys. Rev. Lett.* **1996**, *77*, 2814–2817.
79. Dietl, T.; Peyla, P.; Grieshaber, W.; Merle d'Aubigné, Y. Dynamics of Spin Organization in Diluted Magnetic Semiconductors. *Phys. Rev. Lett.* **1995**, *74*, 474–477.

80. Tribollet, J.; Behrends, J.; Lips, K. Ultra Long Spin Coherence Time for Fe^{3+} in ZnO: A New Spin Qubit. *EPL* **2008**, *84*, 20009.
81. Zhou, D.; Kittilstved, K. R. Control Over Fe^{3+} Speciation in Colloidal ZnO Nanocrystals. *J. Mater. Chem. C* **2015**, *3*, 4352–4358.
82. Fainblat, R.; Muckel, F.; Barrows, C. J.; Vlaskin, V. A.; Gamelin, D. R.; Bacher, G. Valence-Band Mixing Effects in the Upper-Excited-State Magneto-Optical Responses of Colloidal Mn^{2+}-Doped CdSe Quantum Dots. *ACS Nano* **2014**, *8*, 12669−12675.
83. Schimpf, A. M.; Gamelin, D. R. Thermal Tuning and Inversion of Excitonic Zeeman Splittings in Colloidal Doped CdSe Quantum Dots. *J. Phys. Chem. Lett.* **2012**, *3*, 1264–1268.
84. Beaulac, R.; Ochsenbein, S. T.; Gamelin, D. R. Colloidal Transition-Metal-Doped Quantum Dots. In *Nanocrystal Quantum Dots*, 2nd ed.; Klimov, V. I., Ed; CRC Press: Boca Raton, FL, 2010; pp 397–453.
85. Barrows, C. J.; Vlaskin, V. A.; Gamelin, D. R. Absorption and Magnetic Circular Dichroism Analyses of Giant Zeeman Splittings in Diffusion-Doped Colloidal $Cd_{1-x}Mn_xSe$ Quantum Dots. *J. Phys. Chem. Lett.* **2015**, *6*, 3076–3081.
86. Voyles, P. M.; Muller, D. A.; Grazul, J. L.; Citrin, P. H.; Gossmann, H.-J. L. Atomic-Scale Imaging of Individual Dopant Atoms and Clusters in Highly *n*-Type Bulk Si. *Nature* **2002**, *416*, 826–829.
87. Voyles, P. M.; Muller, D. A.; Kirkland, E. J. Depth-Dependent Imaging of Individual Dopant Atoms in Silicon. *Microsc. Microanal.* **2004**, *10*, 291–300.
88. Shibata, N.; Findlay, S. D.; Azuma, S.; Mizoguchi, T.; Yamamoto, T.; Ikuhara, Y. Atomic-Scale Imaging of Individual Dopant Atoms in a Buried Interface. *Nat. Mater.* **2009**, *8*, 654–658.
89. Krivanek, O. L.; Chisholm, M. F.; Nicolosi, V.; Pennycook, T. J.; Corbin, G. J.; Dellby, N.; Murfitt, M. F.; Own, C. S.; Szilagyi, Z. S.; Oxley, M. P.; Pantelides, S. T.; Pennycook, S. J. Atom-by-Atom Structural and Chemical Analysis by Annular Dark-Field Electron Microscopy. *Nature* **2010**, *464*, 571–574.
90. Mittal, A.; Mkhoyan, K. A. Limits in Detecting an Individual Dopant Atom Embedded in a Crystal. *Ultramicroscopy* **2011**, *111*, 1101–1110.
91. Gunawan, A. A.; Mkhoyan, K. A.; Wills, A. W.; Thomas, M. G.; Norris, D. J. Imaging "Invisible" Dopant Atoms in Semiconductor Nanocrystals. *Nano Lett.* **2011**, *11*, 5553–5557.
92. Chakraborty, P.; Jin, Y.; Barrows, C. J.; Dunham, S.; Gamelin, D. R. Kinetics of Isovalent (Cd^{2+}) and Aliovalent (In^{3+}) Cation Exchange in $Cd_{1-x}Mn_xSe$ Nanocrystals. *J. Am. Chem. Soc.* **2016**, *138*, 12885–12893.
93. Brunner, K.; Bockelmann, U.; Abstreiter, G.; Walther, M.; Böhm, G.; Tränkle, G.; Weimann, G. Photoluminescence from a Single GaAs/AlGaAs Quantum Dot. *Phys. Rev. Lett.* **1992**, *69*, 3216.

94. Grundmann, M.; Christen, J.; Ledentsov, N. N.; Böhrer, J.; Binberg, D.; Ruvimov, S. S.; Werner, P.; Richter, U.; Gösele, U.; Heydenreich, J.; Ustinov, V. M.; Egorov, A. Y.; Zhukov, A. E.; Kop'ev, P. S.; Alferov, Z. I. Ultranarrow Luminescence Lines from Single Quantum Dots. *Phys. Rev. Lett.* **1995**, *74*, 4043.
95. Empedocles, S. A.; Norris, D. J.; Bawendi, M. G. Photoluminescence Spectroscopy of Single CdSe Nanocrystallite Quantum Dots. *Phys. Rev. Lett.* **1996**, *77*, 3873–3876.
96. Gammon, D.; Snow, E. S.; Shanabrook, B. V.; Katzer, D. S.; Park, D. Homogeneous Linewidths in the Optical Spectrum of a Single Gallium Arsenide Quantum Dot. *Science* **1996**, *273*, 87–90.
97. Nirmal, M.; Dabbousi, B. O.; Bawendi, M. G.; Macklin, J. J.; Trautman, J. K.; Harris, T. D.; Brus, L. E. Fluorescence Intermittency in Single Cadmium Selenide Nanocrystals. *Nature* **1996**, *383*, 802–804.
98. Tittel, J.; Göhde, W.; Koberling, F.; Basché, T.; Kornowski, A.; Weller, H.; Eychmüller, A. Fluorescence Spectroscopy on Single CdS Nanocrystals. *J. Phys. Chem. B* **1997**, *101*, 3013–3016.
99. Bonadeo, N. H.; Erland, J.; Gammon, D.; Park, D.; Katzer, D. S.; Steel, D. G. Coherent Optical Control of the Quantum State of a Single Quantum Dot. *Science* **1998**, *282*, 1473–1476.
100. Banin, U.; Bruchez, M.; Alivisatos, A. P.; Ha, T.; Weiss, S.; Chemla, D. S. Evidence for a Thermal Contribution to Emission Intermittency in Single CdSe/CdS Core/Shell Nanocrystals. *J. Chem. Phys.* **1998**, *110*, 1195–1201.
101. Kümmell, T.; Weigand, R.; Bacher, G.; Forchel, A.; Leonardi, K.; Hommel, D.; Selke, H. Single Zero-Dimensional Excitons in CdSe/ZnSe Nanostructures. *Appl. Phys. Lett.* **1998**, *73*, 3105.
102. Michler, P.; Kiraz, A.; Becher, C.; Schoenfeld, W. V.; Petroff, P. M.; Zhang, L.; Hu, E.; Imamoglu, A. A Quantum Dot Single-Photon Turnstile Device. *Science* **2000**, *290*, 2282–2285.
103. Mackowski, S.; Jackson, H. E.; Smith, L. M.; Kossut, J.; Karczewski, G.; Heiss, W. Tuning the Properties of Magnetic CdMnTe Quantum Dots. *Appl. Phys. Lett.* **2003**, *83*, 3575.
104. Nguyen, T. A.; Mackowski, S.; Jackson, H. E.; Smith, L. M.; Karczewski, G.; Kossut, J.; Dobrowolska, M.; Furdyna, J. K.; Heiss, W. Exciton-LO Phonon Interaction in II–VI Self-Assembled Quantum Dots. *Phys. Stat. Sol. (C)* **2004**, *1*, 767–770.
105. Mariette, H.; Besombes, L.; Bougerol, C.; Ferrand, D.; Léger, Y.; Maingault, L.; Cibert, J. Control of Single Spins in Individual Magnetic Quantum Dots. *Phys. Stat. Sol. (B)* **2006**, *243*, 3709–3718.
106. Maingault, L.; Besombes, L.; Léger, Y.; Bougerol, C.; Mariette, H. Inserting One Single Mn Ion Into a Quantum Dot. *Appl. Phys. Lett.* **2006**, *89*, 193109.

107. Le Gall, C.; Besombes, L.; Boukari, H.; Kolodka, R.; Cibert, J.; Mariette, H. Optical Spin Orientation of a Single Manganese Atom in a Semiconductor Quantum Dot Using Quasiresonant Photoexcitation. *Phys. Rev. Lett.* **2009**, *102*, 127402.
108. Besombes, L.; Boukari, H.; Le Gall, C.; Brunetti, A.; Cao, C. L.; Jamet, S.; Varghese, B. Optical Control of the Spin of a Magnetic Atom in a Semiconductor Quantum Dot. *Nanophotonics* **2015**, *4*, 75–89.
109. Smoleński, T.; Kazimierczuk, T.; Kobak, J.; Goryca, M.; Golnik, A.; Kossacki, P.; Pacuski, W. Magnetic Ground State of an Individual Fe^{2+} Ion in Strained Semiconductor Nanostructure. *Nat. Commun.* **2016**, *7*, 10484.
110. Fainblat, R.; Barrows, C. J.; Hopmann, E.; Siebeneicher, S.; Vlaskin, V. A.; Gamelin, D. R.; Bacher, G. Giant Excitonic Exchange Splittings at Zero Field in Single Colloidal CdSe Quantum Dots Doped With Individual Mn^{2+} Impurities. *Nano Lett.* **2016**, *16*, 6371–6377.
111. Fernée, M. J.; Littleton, B. N.; Cooper, S.; Rubinsztein-Dunlop, H.; Gómez, D. E.; Mulvaney, P. Acoustic Phonon Contributions to the Emission Spectrum of Single CdSe Nanocrystals. *J. Phys. Chem. C* **2008**, *112*, 1878–1884.

Chapter 2. Nanocrystal Diffusion Doping*

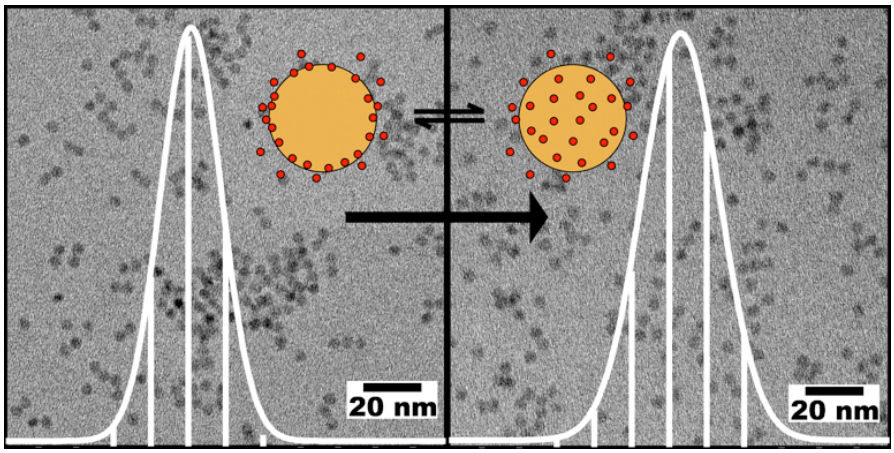

*Reproduced with permission from Vlaskin, V. A.; Barrows, C. J.; Erickson, C. S.; Gamelin, D. R. *J. Am. Chem. Soc.* **2013**, *135*, 14380–14389. Copyright 2013 American Chemical Society.

2.1 Overview

A diffusion-based synthesis of doped colloidal semiconductor nanocrystals is demonstrated. This approach involves thermodynamically controlled addition of both impurity cations and host anions to preformed seed nanocrystals under equilibrium conditions, rather than kinetically controlled doping during growth. This chemistry allows thermodynamic crystal compositions to be prepared without sacrificing other kinetically trapped properties such as shape, size, or crystallographic phase. This doping chemistry thus shares some similarities with cation-exchange reactions, but proceeds without the loss of host cations and excels at the introduction of relatively unreactive impurity ions that have not been previously accessible using cation exchange. Specifically, we demonstrate the preparation of $Cd_{1-x}Mn_xSe$ ($0 \leq x \leq \sim 0.2$) nanocrystals with narrow size distribution, unprecedentedly high Mn^{2+} content, and very large magneto-optical effects by diffusion of Mn^{2+} into seed CdSe nanocrystals grown by hot injection. Controlling the solution and lattice chemical potentials of Cd^{2+} and Mn^{2+} allows Mn^{2+} diffusion into the internal volumes of the CdSe nanocrystals with negligible Ostwald ripening, while retaining the crystallographic phase (wurtzite or zinc blende), shape anisotropy, and ensemble size uniformity of the seed nanocrystals. Experimental results for diffusion doping of other nanocrystals with other cations are also presented that indicate this method may be generalized, providing access to a variety of new doped semiconductor nanostructures not previously attainable by kinetic routes or cation exchange.

2.2 Introduction

The physical properties of inorganic crystals can be changed dramatically by the introduction of impurities. The development of synthetic methods for growing high-quality doped inorganic crystals has consequently been a perennial frontier of materials science, laying the foundation for such technological milestones as the ruby laser and silicon microelectronics. The past two decades have seen the emergence of another frontier in crystal growth that exploits the ability to isolate kinetically trapped semiconductor nanocrystals (NCs), often with anisotropic shapes, before they evolve into their macroscopic thermodynamic end products. Colloidal CdSe nanocrystals have played a central role in the advancement of this field,[1-5] serving as a model system for the development of optimized syntheses controlling structural quality, nanocrystal uniformity, and shape anisotropies, and ultimately translating these features into powerful physical properties.[6, 7] For almost as long, however, it has also been recognized that traditional methods for doping macroscopic crystals are generally incompatible with the syntheses of such kinetically trapped nanostructures.[8-13] For example, a traditional method for preparation of high-quality crystals of II–VI semiconductor solid solutions is the Bridgman technique, in which the crystal growth front is in equilibrium with the melt reservoir and hence the crystal is formed at its thermodynamically favored composition. Heating colloidal nanocrystals to drive such equilibria usually results in severe Ostwald ripening and loss of the desired properties obtained from size or shape control. Consequently, efforts to dope nanocrystals have largely focused on impurity incorporation during growth, where doping is governed kinetically. Under these conditions, dopants must compete with host cations

for available surface binding sites, and nanocrystal surfaces must compete against surfactant ligands for impurity binding. These surface competition reactions are biased against impurities that have mismatches in charge, size, geometry, iconicity, or other physical attributes and hence typically disfavor doping. For example, whereas bulk $Cd_{1-x}Mn_xSe$ crystals have been grown from the melt with x as high as 0.5,[14] synthesis of comparable colloidal $Cd_{1-x}Mn_xSe$ nanocrystals by state-of-the-art hot-injection methods has proven tremendously challenging.[11] Figure 2.1A adapts the Sugimoto model[15] of nutrient concentration gradients during crystal growth to describe the scenario of a small nanocrystal growing in the presence of both lattice nutrient and impurity ions. For $Cd_{1-x}Mn_xSe$ growth under normal hot-injection conditions, Cd^{2+} deposition is diffusion limited, resulting in depletion at the surfaces. Because of unfavorable hard/soft acid/base conditions, however, Mn^{2+} depletion at the same surface is negligible. The synthesis of colloidal $Cd_{1-x}Mn_xSe$ nanocrystals has therefore long served as a testing ground for the development of innovative nanocrystal doping chemistries intended to overcome these general challenges.

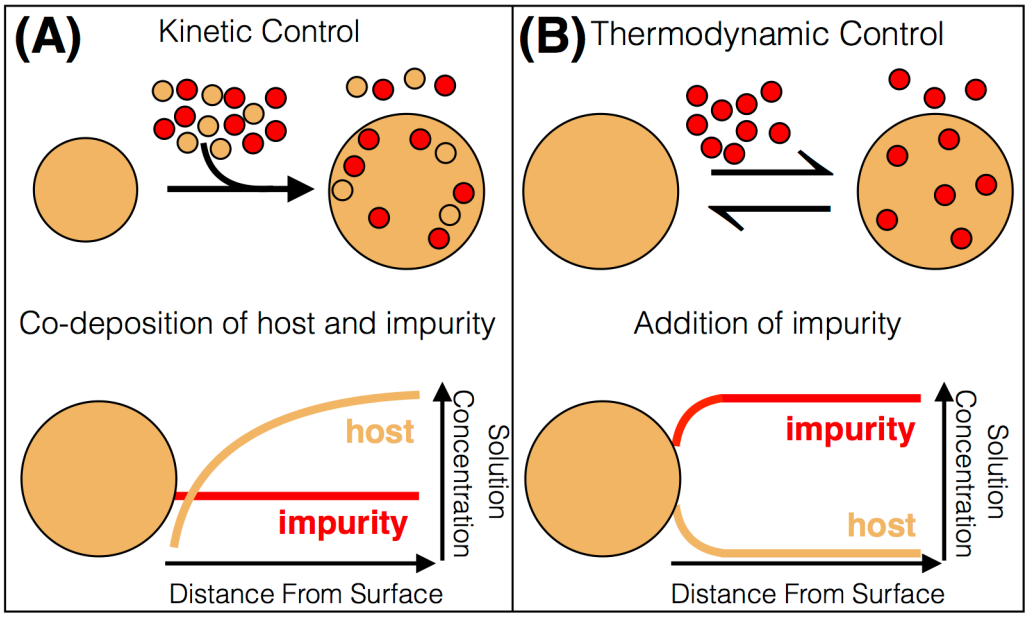

Figure 2.1. Incorporation of impurities into nanocrystals under (A) kinetic or (B) thermodynamic control. Under kinetic control, impurities compete with host nutrients for surface binding sites and are internalized via subsequent crystal lattice overgrowth. Under thermodynamic control, impurities enter the nanocrystal lattice under quasi-equilibrium conditions, driven by entropy, and are internalized via diffusion of the crystal ions.

In specific cases, fast-diffusing ions can be introduced into colloidal nanocrystals at temperatures that are too low for substantial Ostwald ripening, allowing thermodynamic nanocrystal composition control.[16-25] The most thoroughly investigated of such chemistries is so-called "cation exchange."[16-22] A defining feature of cation-exchange reactions that makes them extremely powerful is that the anion sublattice remains invariant, allowing retention of crystallite shape anisotropies and phases despite dramatic changes in crystal composition. Under thermodynamic control, cation exchange is governed by the differences between crystal and solution chemical potentials (μ^{NC} vs $\mu^{solution}$) of the impurity and host ions. Unfortunately, such reactions are limited to a relatively small set of cation combinations for which diffusion is rapid. Raising temperatures to drive diffusion of less reactive cations such as Mn^{2+} can cause severe Ostwald ripening and sacrifice nanostructuring.[26] Mn^{2+} incorporation into magic-size ZnTe nanoclusters via cation exchange has been successful,[27] as has cation exchange in even smaller clusters,[28, 29] but successful synthesis of $Cd_{1-x}Mn_xSe$ or related nanocrystals by cation exchange has not been reported. For example, deliberate attempts to introduce Mn^{2+} into preformed colloidal ZnSe nanocrystals at elevated temperatures were either unsuccessful[30] or accompanied by severe ripening and collapse of shape anisotropy.[26] Indeed, it has been a long-standing tenet of nanocrystal doping that Mn^{2+} diffusion in II–VI nanocrystals is negligible at normal colloid growth or handling temperatures and that equilibrium compositions are therefore inaccessible.[9, 10, 31, 32] Researchers wishing to access the unique luminescent, magnetic, magneto-optical, or magneto-electronic properties of Mn^{2+}-doped II–VI semiconductor nanocrystals, or of other doped nanocrystals that do not involve fast diffusers, are thus to

date primarily restricted to samples synthesized under kinetic control.

To achieve thermodynamically controlled Mn^{2+} doping of semiconductor nanocrystals, two seemingly incommensurate criteria must be met: the nanocrystals must be allowed to progress toward their equilibrium solid-solution composition without approaching their equilibrium morphology. In other words, the lattice must be sufficiently fluid to allow mixing rather than just heterostructures formation, but at the same time, interparticle (and in anisotropic crystals, also intraparticle) mass transfer must be avoided. Figure 2.1B illustrates the desired thermodynamically suppressed doping process, in this example via impurity addition to a preformed spherical nanocrystal. To be successful, the solution and lattice chemical potentials of both host and impurity ions must be tuned such that impurity addition is thermodynamically favorable and ripening is minimized. Simultaneously, it must provide sufficient thermal energy for impurity diffusion from the surfaces into the nanocrystal internal volumes.

Here we report development of a successful synthesis of high-quality colloidal $Cd_{1-x}Mn_xSe$ nanocrystals performed under thermodynamic rather than kinetic control, based on addressing the above challenges in a systematic way. Beginning with colloidal CdSe quantum dots prepared by state-of-the-art hot-injection methods, we demonstrate thermally activated diffusion of Mn^{2+} into the nanocrystal internal volumes. In contrast with cation-exchange processes described previously, we show that this diffusion doping involves stoichiometric cation + anion *addition*, without the loss of host cations, and hence increases the nanocrystal volume in proportion to x. In common with cation-exchange reactions, we show that this diffusion doping allows retention of the original nanocrystal

size distributions, crystallographic phases, and even shape anisotropies. The resulting nanocrystals show Mn^{2+} concentrations exceeding any reported previously for colloidal $Cd_{1-x}Mn_xSe$ nanocrystals, while simultaneously showing size and shape uniformity unparalleled in doped CdSe nanocrystals to date. We then illustrate the generality of this method by describing doping of CdSe nanocrystals with other cationic impurities, sequential tandem doping of two impurities into the same CdSe nanocrystals, and preliminary results for diffusion doping of CdTe, CdS, and ZnSe nanocrystals. The materials reported here represent a new benchmark for high-quality doped CdSe nanocrystals in particular, and in general illustrate the value of diffusion doping for preparing complex doped nanostructures under thermodynamic control.

2.3 Experimental Methods

2.3.1 Chemicals

Trioctylphosphine oxide (TOPO; 99%), 1-octadecene (ODE; 90%), hexadecylamine (HDA; 90%), Super-Hydride (1 M triethylborohydride in THF), tributylphosphine (TBP; 97%), oleylamine (70%), oleic acid (OA; 90%), selenium metal (99.99+%), tellurium metal (99.8%), CdO (99.99+%), $Cd(OAc)_2•2H_2O$ (99.99+%), and $Fe(SO_4)•7H_2O$ (99+%) were purchased from Aldrich. Octadecylphosphonic acid (ODPA; 97%), trioctylphosphine (TOP; 97%), and $Mn(OAc)_2•4H_2O$ (99.999+%) were purchased from Strem. Stearic acid (SA; 97%) was purchased from Acros. $Co(OAc)_2•4H_2O$ was purchased from GFS chemicals. All chemicals were used as received.

2.3.2 Nanocrystal Synthesis and Diffusion Doping

Seed CdSe nanocrystals of different crystallographic phases, shapes, and sizes, as well as seed ZnSe, CdS, and CdTe nanocrystals, were all prepared by methods adapted from various literature sources[33-36] as described in detail in Appendix A. All nanocrystals were capped with oleate prior to diffusion doping, but the complete elimination of the native ligands employed in the various syntheses was not assumed.

Diffusion doping of CdSe nanocrystals with Mn^{2+} was performed as follows: CdSe nanocrystals (~0.13 mmol in terms of CdSe units) were dried and added to 0.17 g (2.1 mmol) of selenium powder, 1 mL of ODE, and 1 mL of TBP in a septum-capped 5 mL round-bottom flask in a nitrogen-atmosphere glovebox. Separately, 12 g of ODE, 0.5 g of SA, and 1 g of HDA were added to a 100 mL three-neck round-bottom flask. Following heating of the latter solution for 30 min at 100 ºC under vacuum, 0.03 g (0.1 mmol) of $Mn(OAc)_2 \bullet 4H_2O$ was added against a nitrogen overpressure in a method known colloquially in the Gamelin lab as the "hot dump." The flask was then placed under vacuum to remove acetic acid and water and then heated under nitrogen to 300 ºC, at which point the CdSe/selenide solution was injected rapidly. This reaction mixture was held at temperatures between 290 and 300 ºC for between a few seconds and 29 h. The reaction is aided by the greater activity of TBP than the more common TOP. As the solution was cooled to room temperature, 3 mL of toluene was added at ~120 ºC to prevent SA solidification. Parallel experiments in which the samples were heated to only 200 ºC failed to incorporate Mn^{2+} (see Appendix A). The synthetic procedures for Co^{2+} or Fe^{2+} diffusion doping were identical, but with Co^{2+} added as $Co(OAc)_2 \bullet 4H_2O$ or Fe^{2+} added as $Fe(SO_4) \bullet 7H_2O$.

Diffusion doping of CdTe nanocrystals with Mn^{2+} was performed as follows: A 12 g portion of ODE, 1 g of HDA, and 0.5 g of SA were added to a 100 mL three-neck round-bottom flask. The solution was degassed for 30 min under vacuum at 100 ºC and brought back under nitrogen. Under a nitrogen overpressure, 0.03 g (0.1 mmol) of $Mn(OAc)_2 \bullet 4H_2O$ was added, followed by a brief pump/purge cycle, before the solution was heated to

170 ºC for the nanocrystal injection. In a separate, septum-capped 5 mL round-bottom flask, 0.32 g (2.5 mmol) of tellurium, 1 mL of TBP, 0.5 mL of 1 M Super-Hydride solution in THF, 1 mL of oleylamine, and CdTe nanocrystals (~0.1 mmol in terms of CdTe units) were mixed in a nitrogen-atmosphere glovebox. This solution was injected into the Mn^{2+} solution at 170 ºC and stirred for 30 min at this temperature.

All nanocrystals were washed using the same procedures: The nanocrystals were precipitated from solution by addition of ethanol and washed by repeated suspensions in toluene and flocculation with ethanol. In some cases, TOPO, HDA, OA, or TOP was added to improve nanocrystal solubility.

2.3.3 Physical Characterization

Room-temperature electronic absorption spectra were collected for colloidal toluene suspensions of nanocrystals in 0.1 cm path length cuvettes using a Cary 500 spectrophotometer (Varian). X-ray diffraction (XRD) data were collected from evaporated nanocrystal films on glass slides using a Bruker D8 Discover spectrometer at the University of Washington (UW) NanoTech User Facility (NTUF). TEM samples were prepared by submerging a 200 mesh copper grid (Ted Pella, Inc.) in a 1 μM colloidal suspension of nanocrystals in toluene and allowing this substrate to dry in air. TEM images were obtained on an FEI TECNAI F20, 200 kV microscope at the UW NTUF. Nanocrystal sizes and size distributions were determined by analysis of the images of >100 individual nanocrystals for each value reported. Relative atomic concentrations were obtained by analysis of dried nanocrystals digested in ultrapure nitric acid (EMD Chemicals) using inductively coupled plasma atomic emission spectrometry (ICP-AES; Perkin-Elmer). Room-temperature magnetic circular dichroism (MCD) spectra were collected on colloidal nanocrystal suspensions in a 0.1 cm path length cuvette placed in a 1.5 T electromagnet oriented in the Faraday configuration. Low-temperature absorption and MCD spectra were collected on nanocrystal films prepared by depositing dilute toluene suspensions between two quartz disks. These samples were placed in a superconducting magneto-optical cryostat

(Cryo-Industries SMC-1659 OVT) oriented in the Faraday configuration. At helium temperature, each sample was screened for depolarization by matching the CD spectra of a chiral molecule placed before and after the sample. In all cases, depolarization was <5%. Electronic absorption and MCD spectra were collected simultaneously using an Aviv 40DS spectropolarimeter. The differential absorption collected in the MCD experiment is reported as $\Delta A = A_L - A_R$, where A_L and A_R refer to the absorption of left and right circularly polarized photons in the sign convention of Piepho and Schatz.[37, 38] From these data, values of ΔE_{Zeeman} and g_{Exc} can be obtained.[12, 39]

2.4 Results and Analysis

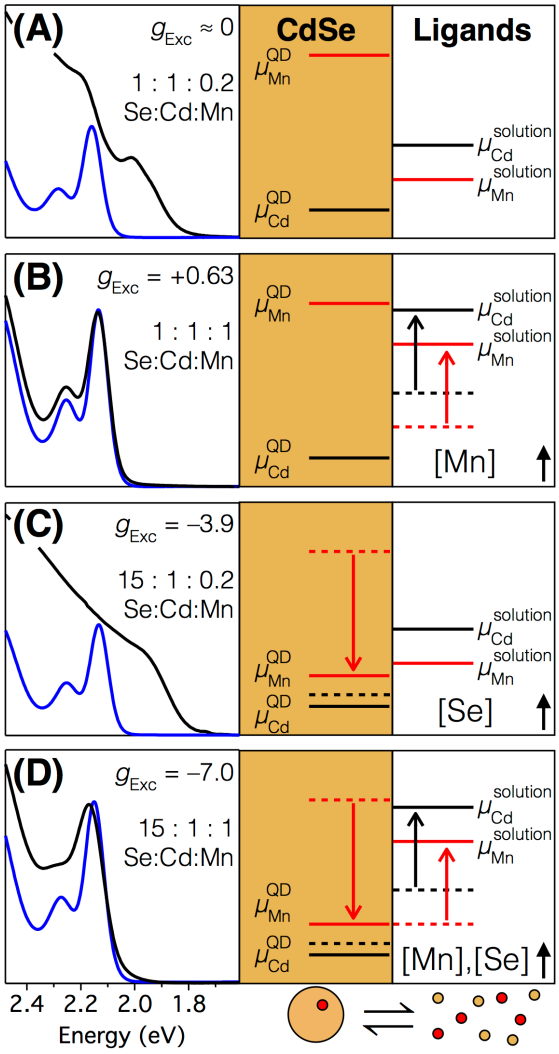

Figure 2.2. (A) (Left) Room-temperature electronic absorption spectra of the first excitonic feature of zb-CdSe nanocrystals before (blue) and after (black) 30 min at 300 °C under the conditions described in the text and with the ion ratios indicated. Undoped zb-CdSe nanocrystals are injected into reaction solutions with **(A)** Mn^{2+} in a 0.2:1 ratio to the Cd^{2+} contained in the nanocrystals, **(B)** Mn^{2+} in solution in a 1:1 ratio with the Cd^{2+} contained in the nanocrystals, **(C)** Se^{2-} and Mn^{2+} in 15:1 and 0.2:1 ratios, respectively, to the Cd^{2+} contained in the nanocrystals, and **(D)** Se^{2-} and Mn^{2+} in a 15:1:1 ratio to the Cd^{2+} contained in the nanocrystals. The excitonic *g* values of the resulting nanocrystals, determined from room-temperature MCD spectroscopy, are given in each panel and indicate negligible-to-weak Mn^{2+}–exciton exchange coupling in panels **A** and **B** and strong exchange coupling in panels **C** and **D**. (Right) Relative free energies of the Mn^{2+} and Cd^{2+} cation chemical potentials on either side of the nanocrystal/solution interface for identical reaction conditions with the exception of relative ionic ratios.

Figure 2.2 summarizes results from a series of experiments performed to elucidate the roles of Mn^{2+} and Se^{2-} concentrations in diffusion doping. Room-temperature absorption and MCD spectra were used as convenient probes for monitoring sample evolution under various diffusion-doping conditions. For the baseline experiment, presented in Figure 2.2A, experimental conditions resemble those of a typical hot-injection synthesis during postnucleation growth, in which the ratio of Mn^{2+} (solvated) to Cd^{2+} (as CdSe seed nanocrystals) is relatively small (0.2:1) and no excess Se^{2-} has been added. Prior to heating, the seed nanocrystals show a narrow exciton peak at ~2.17 eV. After heating, the absorption spectrum is broadened substantially and shifted to lower energy, indicative of severe Ostwald ripening and loss of size uniformity. The room-temperature MCD spectrum shows no evidence of substantial Mn^{2+} incorporation. As detailed previously,[11, 12, 40, 41] doping CdSe nanocrystals with Mn^{2+} results in MCD intensity inversion and enhancement at the CdSe absorption edge. These changes arise from the introduction of strong *sp–d* exchange contributions to excitonic Zeeman splittings upon Mn^{2+} doping, as described by Equation 2.1.[12, 39] The first term in Equation 2.1 describes the intrinsic contribution to the excitonic Zeeman splitting energies (ΔE_{Zeeman}) of CdSe nanocrystals. This contribution is small, temperature independent, and linearly dependent on the magnetic field (B, where μ_B is the Bohr magneton). Experimental measurements have yielded $g_{Int} \approx +1$ for undoped pseudospherical CdSe nanocrystals.[40, 42] The second term in Equation 2.1 describes the dopant–exciton *sp–d* exchange coupling contribution to ΔE_{Zeeman}, where $\langle S_Z \rangle$ is the spin expectation value of the dopant at the experimental temperature and magnetic field (as described by the Brillouin function for magnetic ions

with spin-only ground states, such as Mn^{2+}), $N_0(\alpha - \beta)$ is the mean-field *sp–d* exchange energy, and x_{Eff} represents the effective amount of paramagnetic Mn^{2+} exchange coupled with the exciton. $\langle S_Z \rangle$ is strongly temperature dependent, increasing as $1/T$ for simple paramagnets such as Mn^{2+}. x_{Eff} is generally smaller than x because of Mn^{2+}–Mn^{2+} pair formation,[14, 43] reaching its maximum of ~3.3% when x is ~8.2%. In nanocrystals, x_{Eff} is typically also smaller than x because of undoped cores.[44, 45] For the cases studied here, the *sp–d* exchange term has the opposite sign compared to the intrinsic term. In the limit of small B, $\langle S_Z \rangle$ is also linearly proportional to B (the Curie limit). In this regime, the proportionality constant $g_{Exc} = \Delta E_{Zeeman}/\mu_B B$ provides a measure of these two competing contributions to ΔE_{Zeeman}. For the purposes of this study we consider negative g_{Exc} values to be indicative of substantial Mn^{2+} incorporation and positive g_{Exc} values as indicative of an absence of such incorporation, although positive g_{Exc} values can be obtained at high temperatures in doped nanocrystals with low doping concentrations.[46] Room-temperature MCD spectroscopy of the nanocrystals in Figure 2.2A shows little or no intensity at the first exciton, $g_{Exc} \approx 0$, and hence little or no success in doping.

$$\Delta E_{Zeeman} = g_{Int}\mu_B B + x_{Eff}\langle S_Z \rangle N_0(\alpha - \beta) \quad (2.1)$$

Figure 2.2A (right) illustrates why doping fails here, in terms of Cd^{2+} and Mn^{2+} chemical potentials. Under these experimental conditions, the soft Cd^{2+} Lewis acid preferentially binds to the soft Se^{2-} rather than to the hard Lewis bases present in solution as surfactants (stearate and hexadecylamine). Conversely, Mn^{2+} prefers these harder ligands. The resulting imbalance in chemical potentials favors Mn^{2+} solvation and is responsible for the unsuccessful exchange of Cd^{2+} by Mn^{2+} under these conditions.

Moreover, the relatively small imbalance between $\mu_{Cd,NC}$ and $\mu_{Cd,solution}$ allows large Cd^{2+} diffusion lengths in solution and hence Ostwald ripening.

To encourage doping, the Mn^{2+} concentration in solution was increased massively relative to the conditions of Figure 2.2A so that it equaled the total Cd^{2+} content of the seed CdSe nanocrystals. These levels more closely resemble conditions in cation-exchange reactions than in kinetic doping reactions. Figure 2.2B (left) shows absorption spectra collected before and after heating CdSe nanocrystals in the presence of such an excess of Mn^{2+}. A positive value of g_{Exc} = +0.63 is observed by MCD spectroscopy following heating at 300 ºC for 30 min, again indicating little or no successful doping. Although Mn^{2+} is not incorporated, the nanocrystals remarkably preserve their average size and narrow size distribution despite prolonged heating. These observations can be understood by considering the effects of increased Mn^{2+} concentration illustrated in Figure 2.2B (right). When Mn^{2+} is added as $Mn(OAc)_2$, its ligands can be exchanged by pumping off acetic acid, such that Mn^{2+} in the reaction solution is coordinated by the surfactant ligands, stearate and hexadecylamine. Such a large increase in Mn^{2+} concentration thus increases the chemical potentials of both Mn^{2+} and Cd^{2+} ions in solution because the free ligand concentration decreases (analogous to the common-ion effect). Supporting this interpretation, control experiments confirm that adding more HDA increases Ostwald ripening again. The added driving force for Cd^{2+} binding to the CdSe surfaces offsets any increased driving force for Mn^{2+} incorporation into the crystals, and consequently, doping does not proceed. At the same time, the increased chemical potential of Cd^{2+} in solution attenuates CdSe diffusion and thereby suppresses Ostwald ripening.

For successful doping, the CdSe nanocrystal surface must be made more attractive for Mn^{2+} binding. Figure 2.2C (left) shows absorption spectra collected before and after heating when excess Se^{2-} (instead of excess Mn^{2+}) is added at a 15:1 ratio to total Cd^{2+}, with other conditions the same as in Figure 2.2A. Upon heating, the CdSe absorption edge red shifts by ~186 meV and broadens considerably, indicating extensive ripening, but room-temperature MCD spectra of the resulting nanocrystals show sign inversion and yield g_{Exc} = –3.9, indicating dominance of Mn^{2+}–exciton *sp*–*d* exchange and hence successful Mn^{2+} incorporation. Figure 2.2C (right) illustrates the origins of these changes. With excess Se^{2-}, the Mn^{2+} chemical potential inside the lattice drops to a level where solid-solution formation is thermodynamically favorable. Mn^{2+} adds to the lattice not by expulsion of Cd^{2+}, but via incorporation of new Mn–Se units instead. This feature constitutes an essential distinction between the diffusion-doping process reported here and previous cation-exchange chemistries.

By combining the suppression of Ostwald ripening at high Mn^{2+} concentrations (Figure 2.2B) with the elimination of cation competition for Se^{2-} at high Se^{2-} concentrations (Figure 2.2C), diffusion doping of CdSe nanocrystals to form $Cd_{1-x}Mn_xSe$ nanocrystals could be optimized. Figure 2.2D (left) shows absorption spectra collected before and after heating CdSe seed nanocrystals at 300 ºC for 30 min in the presence of high concentrations of excess Se^{2-} and excess Mn^{2+}. Instead of a red shift from Ostwald ripening, the first CdSe excitonic maximum blue shifts and broadens slightly. Furthermore, room-temperature MCD spectroscopy yields g_{Exc} = –7.0 for these nanocrystals after heating, indicative of very strong *sp*–*d* exchange and hence of even more successful

doping than in Figure 2.2C. As illustrated in figure 2.2D (right), the chemical potentials of both Cd^{2+} and Mn^{2+} decrease inside the CdSe nanocrystals and increase in solution when both are added in excess. Importantly, neither XRD nor TEM shows any suggestion of MnSe formation under the conditions of Figure 2.2D (*vide infra*), from which we conclude that this phase either does not form at all or exists only as an intermediate. Control experiments performed in the absence of seed CdSe nanocrystals also fail to produce MnSe.

The data in Figure 2.2D are interpreted as reflecting Mn–Se addition to and diffusion into the seed CdSe nanocrystals. To explore the chemistry of Figure 2.2D in more depth, a reaction was performed under the same optimized conditions and aliquots were removed periodically. Figure 2.3A shows the evolution of the CdSe absorption spectrum with the reaction time at 300 ºC. The first excitonic feature broadens and shifts to higher energy as the reaction proceeds. Figure 2.3B shows that this trend is accompanied by an inversion and progressive increase in MCD intensity at the CdSe absorption edge. g_{Exc} becomes dominated by *sp–d* exchange within only ~2 min. These data are consistent with rapid Mn^{2+} incorporation into the CdSe nanocrystals and a growing x_{Eff} (Equation 2.1) throughout the entire reaction.

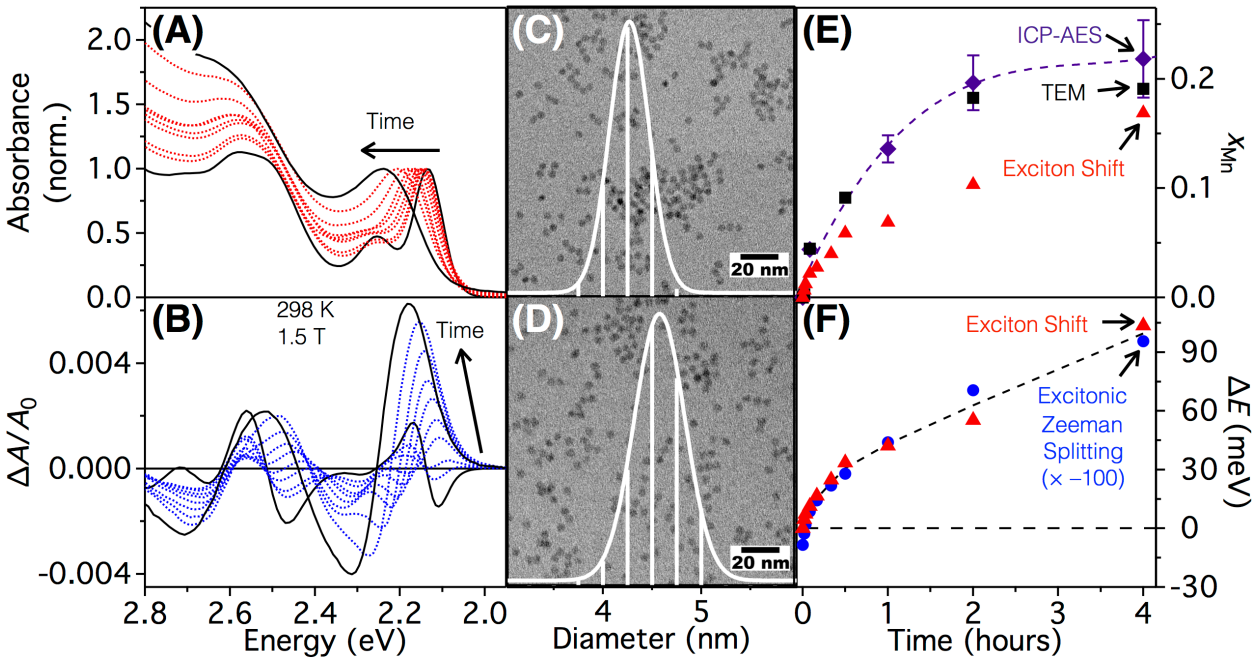

Figure 2.3. (A) Room-temperature electronic absorption spectra of reaction aliquots taken at different times during w-CdSe nanocrystal diffusion doping at 300 ºC, normalized at the first excitonic maximum. (B) Corresponding MCD spectra showing a sign inversion and signal growth with increased reaction time, indicative of growing *sp–d* exchange coupling strengths. (C) TEM image and corresponding diameter histogram from analysis of undoped CdSe (d = 4.37 ± 0.18 nm) precursor nanocrystals. (D) TEM image and corresponding diameter histogram from analysis of $Cd_{1-x}Mn_xSe$ nanocrystals after 240 min of diffusion doping at 300 ºC (d = 4.69 ± 0.24 nm). (E) Mn^{2+} cation mole fraction (x_{Mn}) determined by ICP-AES (purple tilted squares, with error bars from three measurements of each aliquot), analysis of nanocrystal volumes from TEM (black squares), and analysis of the excitonic absorption energy shifts (red triangles). The dashed line is a guide to the eye. In order of increasing reaction time, the standard deviations of the average nanocrystal diameters from TEM are 4.1% (seed), 3.4%, 4.1%, 3.8%, 3.6%, and 5.1% (see Appendix A). (F) Excitonic absorption energy shifts (red triangles, from analysis of panel A data) and excitonic Zeeman splittings (blue circles, from analysis of panel B data, multiplied by –100) plotted vs the diffusion-doping time. The dashed line is a guide to the eye. See the text and Appendix A for additional details.

Figure 2.3C shows a TEM image of the seed CdSe nanocrystals used in the experiments of Figure 2.3A,B. These nanocrystals have a diameter of 4.37 ± 0.18 nm (σ = 4.1%). Figure 2.3D shows a TEM image of the same nanocrystals after 240 min of heating at 300 ºC in the presence of excess Mn^{2+} and Se^{2-}. The average diameter increases to 4.69 ± 0.24 nm (σ = 5.1%). We attribute this growth entirely to addition of Mn–Se units to the seed CdSe nanocrystal. From this volume increase, a value of $x_{Mn} \approx 0.19$ can be inferred in the maximally doped nanocrystals, corresponding to ~195 Mn^{2+} ions/nanocrystal. Similar analyses were performed for other aliquots (Appendix A). Figure 2.3E summarizes the TEM results, plotting the data as x_{Mn} vs diffusion-doping time under the assumption that growth derives solely from addition of Mn–Se units. These data show an initial increase and subsequent plateau at $x_{Mn} \approx 0.19$ over the course of 4 hours. This curvature is indicative of an equilibrium process. For comparison, x_{Mn} was also determined analytically for each aliquot using ICP-AES following careful washing to remove adventitious Mn^{2+}. Figure 2.3E plots these analytical concentrations on the same axes as the concentrations estimated from TEM. The analytical x_{Mn} data agree very well with the values deduced from the TEM data, again increasing over the first 2 hours before plateauing at $x_{Mn} \approx 0.22$. The agreement between these two data sets confirms that this synthesis introduces Mn^{2+} into seed CdSe nanocrystals by addition of Mn–Se units. Beyond this unprecedentedly large Mn^{2+} concentration in colloidal CdSe nanocrystals, the remarkable feature of these data is that the nanocrystal size distribution remains essentially unchanged following such prolonged heating.

The TEM results show that the exciton broadening seen in Figures 2.2D and 2.3A does not come from a loss of the size uniformity. Instead, this broadening reflects a perturbation of the transition energy due to Mn^{2+} addition. Figure 2.3F plots the energy of the first excitonic maximum (E_g) vs Mn^{2+} diffusion-doping time for the same aliquots. E_g *increases* with Mn^{2+} addition, despite the increasing nanocrystal volumes. This increase starts immediately and proceeds for the first 2 hours before leveling somewhat, but a terminal plateau is not reached within 4 hours. These data demonstrate that Mn–Se does not simply deposit onto the CdSe NC surfaces to form CdSe/MnSe core/shell structures. Like CdSe/ZnSe core/shell nanocrystals, such structures would show exciton relaxation into the shell layer and hence a small decrease in E_g. Instead, the data confirm $Cd_{1-x}Mn_xSe$ solid-solution formation. To understand these data, we recall that E_g in bulk CdSe displays a well-defined dependence on x_{Mn}, shifting to higher energy linearly with a slope of ~11.4 meV/x_{Mn} (%) (or +92 cm^{-1}/x_{Mn} (%)).[39] This shift is largely attributable to the fact that the empty Mn^{2+} 4*s* orbitals are in poor energetic alignment with the Cd^{2+} 5*s* orbitals,[47, 48] and consequently, Mn^{2+} inclusion into the lattice disrupts the CdSe conduction band. The blue shift in E_g with increasing nanocrystal volume shown in Figure 2.3 thus results from the dependence of E_g on x_{Mn}. An estimate of x_{Mn} from E_g was attempted but is made difficult by the fact that these nanocrystals are quantum confined, and addition of Mn–Se units simultaneously relaxes the exciton spatial confinement. If we assume that E_g simply scales linearly with x_{Mn} as in the bulk, but now starts from E_g of the undoped CdSe NCs and finishes at the bulk band gap energy of the hypothetical wurtzite MnSe (i.e., assuming no MnSe quantum confinement at these diameters and no relaxation of confinement with

Mn–Se addition to CdSe nanocrystals), then the excitonic blue shift in Figure 2.3F implies a value of $x_{Mn} \approx 0.14$. Taking into account the increasing nanocrystal volumes determined by TEM, the excitonic shift data can be corrected for the relaxation of quantum confinement in the CdSe host[35, 49] to yield a final $x_{Mn} \approx 0.17$ (Figure 2.3E), which agrees well with the values determined by ICP-AES and from TEM volume increases. For comparison with the absorption data, Figure 2.3F also shows the room-temperature excitonic Zeeman splitting energies (ΔE_{Zeeman}) determined from analysis of the MCD intensities in Figure 2.3B, plotted vs diffusion-doping time. These data behave in essentially the same way as E_g. The fact that Mn^{2+} addition plateaus (Figure 2.3E) but the spectroscopic effects of Mn^{2+} continue to increase (Figure 2.3F) provides strong evidence for a mechanism involving initial Mn–Se deposition within an active surface volume, followed by slower homogenization of the $Cd_{1-x}Mn_xSe$ solid solution.

To test whether diffusion doping retains the crystallographic phase, samples of predominantly hexagonal wurtzite (w) or cubic zinc blende (zb) CdSe nanocrystals were reacted with Mn^{2+} under identical conditions. The different crystal phases of these samples derive from different synthesis conditions (see Appendix A), but under the identical diffusion-doping reaction conditions, both samples should have the same thermodynamically favored crystal phase.

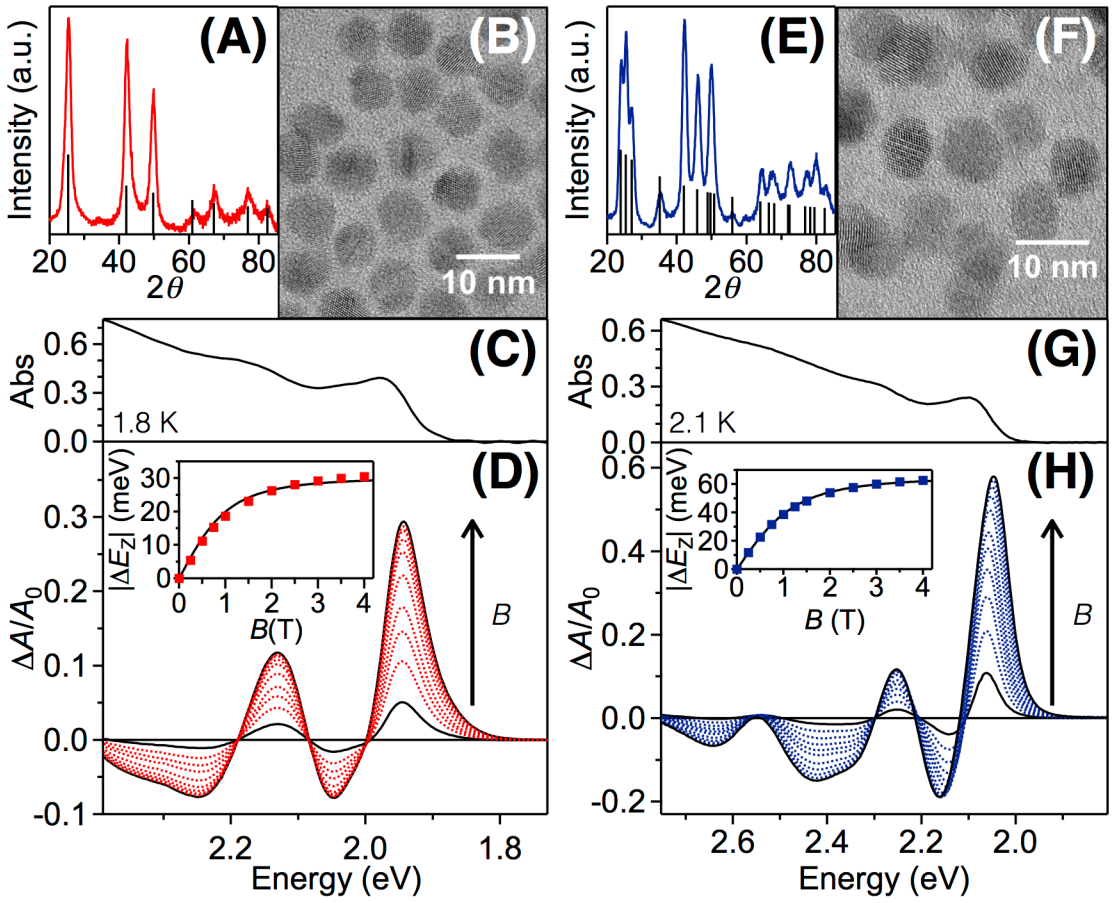

Figure 2.4. (A) XRD and (B) TEM data for the d = 8.8 ± 0.8 nm zb-$Cd_{1-x}Mn_xSe$ nanocrystal product obtained from diffusion doping of d = 8.4 nm zb-CdSe seed nanocrystals for 30 min as in Figure 2.2D. (C,D) Electronic absorption (C) and variable-field MCD (D) spectra (1.8 K) of d = 8.8 nm zb-$Cd_{1-x}Mn_xSe$ nanocrystals. (E) XRD and (F) TEM data for the d = 7.9 ± 0.5 nm w-$Cd_{1-x}Mn_xSe$ nanocrystal product obtained from diffusion doping of d = 6.8 nm w-CdSe seed nanocrystals for 60 min. (G,H) Electronic absorption (G) and variable-field MCD (H) spectra (2.1 K) of d = 7.9 nm w-$Cd_{1-x}Mn_xSe$ nanocrystals. The insets to (D) and (H) plot the excitonic Zeeman splittings vs magnetic field, deduced from the MCD spectra. The solid curves plot S = 5/2 Brillouin functions calculated using g_{Mn} = 2.0 and the experimental temperatures. At saturation, ΔE_{Zeeman} = –31 and –65 meV for these zinc blende and wurtzite $Cd_{1-x}Mn_xSe$ nanocrystals, respectively. The excitonic g values in the limit of small magnetic fields are g_{Exc} = –376 and –815 for the zinc blende and wurtzite $Cd_{1-x}Mn_xSe$ nanocrystals, respectively.

Figure 2.4A–D shows data collected following 30 minutes of diffusion doping of d = 8.4 nm zb-CdSe seed nanocrystals under the same optimized conditions as in Figure 2.2D. The TEM data of Figure 2.4B show growth to d = 8.8 nm, and the XRD data of Figure 2.4A show retention of the cubic lattice structure. Likewise, Figure 2.4E–H show data collected following 60 minutes of diffusion doping of d = 6.8 nm w-CdSe seed nanocrystals under the same conditions. The TEM data of Figure 2.4F show growth to d = 7.9 nm, and the XRD data of Figure 2.4E show retention of the wurtzite lattice structure. From the XRD peak positions and bulk relationships between x_{Mn} and XRD peak positions, x_{Mn} values of 0.12 ± 0.02 and 0.19 ± 0.01 are estimated for the zinc blende and wurtzite $Cd_{1-x}Mn_xSe$ nanocrystals, respectively, consistent with the results of Figure 2.3.[14]

Panels C and D and panels G and H of Figure 2.4 plot low-temperature absorption and variable-field MCD spectra of these nanocrystals after diffusion doping. In both cases, the MCD signals are very strong and show the hallmark signatures of successful Mn^{2+} doping. Plots of ΔE_{Zeeman} vs magnetic field (insets) show the S = 5/2 saturation magnetization expected for $Cd_{1-x}Mn_xSe$. For the zb-$Cd_{1-x}Mn_xSe$ nanocrystals, ΔE_{Zeeman} saturates at –31 meV and g_{Exc} = –376 in the low-field limit (1.8 K). For the w-$Cd_{1-x}Mn_xSe$ nanocrystals, ΔE_{Zeeman} saturates at –65 meV and g_{Exc} = –815 in the low-field limit (2.1 K), consistent with their greater x_{Mn}. The largest ΔE_{Zeeman} we have achieved using diffusion doping is ΔE_{Zeeman} = –100 meV, with an extraordinarily large value of g_{Exc} = –907 (at 1.8 K; see Appendix A). This ΔE_{Zeeman} value is close to the maximum of –120 meV anticipated from bulk *sp–d* exchange parameters and the maximum x_{Eff} of ~3.3%.[43] Comparison with the literature shows these to be the largest magneto-optical effects achieved for

$Cd_{1-x}Mn_xSe$ nanocrystals of any type to date, for example, exceeding the next largest ΔE_{Zeeman} and g_{Exc} values by nearly a factor of 2.[11, 12] Such strong magneto-optical responses, and the magneto-electronic properties they report upon, constitute one of the main motivations for synthesis of this class of materials. Beyond showing that diffusion doping yields high-quality $Cd_{1-x}Mn_xSe$ nanocrystals with record large magneto-optical effects, the results in Figure 2.4 demonstrate that diffusion doping retains the crystallographic phases of the seed nanocrystals, a key finding.

To test whether diffusion doping also retains the nanocrystal shape, experiments were performed using anisotropic seed nanocrystals. Figure 2.5A shows TEM data of CdSe nanorods prepared by seeded growth and having $d \approx 6–8$ nm with ~6:1 aspect ratios and distinct bulges that are characteristic of seeded-growth nanorods.[34] The shapes, sizes, and even bulges of these nanorods are retained following 30 minutes of diffusion doping with Mn^{2+} at 300 ºC under the optimized conditions of Figure 2.2D, with successful doping confirmed by MCD spectroscopy (see Appendix A). Combined, the above results demonstrate diffusion doping as a new example of nanocrystal composition control without loss of crystallographic phase, size uniformity, or shape anisotropy, placing this method alongside cation exchange in these capacities.

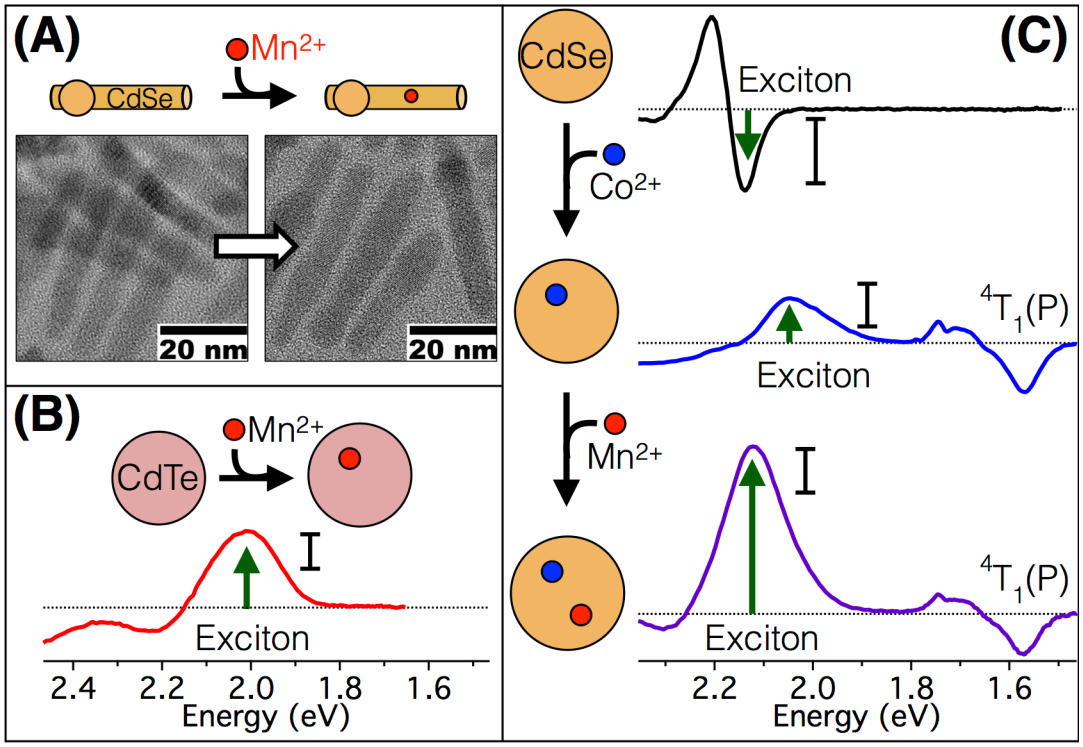

Figure 2.5. **(A)** Diffusion doping of seeded w-CdSe nanorods. TEM images collected before and after diffusion doping of seeded CdSe nanorods ($d \approx 6$–8 nm, aspect ratio ~6:1) with Mn^{2+} at 300 ºC for 30 min. The nanorods retain their shapes. MCD spectra confirm doping (see Appendix A). **(B)** MCD spectrum of CdTe nanocrystals after diffusion doping with Mn^{2+}, showing inversion of the excitonic MCD signal indicative of successful doping. **(C)** Tandem diffusion doping of zb-CdSe nanocrystals with Co^{2+} followed by Mn^{2+}. (*Top*) MCD of undoped CdSe nanocrystal seeds. (*Middle*) MCD spectrum of the same nanocrystals after diffusion doping with Co^{2+}, showing inversion of the excitonic MCD signal and appearance of the characteristic Co^{2+} $^4T_1(P)$ *d*–*d* transition. (*Bottom*) MCD spectrum of the same nanocrystals following diffusion doping with Mn^{2+}, showing increased excitonic Zeeman splitting and retention of the Co^{2+} $^4T_1(P)$ *d*–*d* transition. The vertical scale bars indicate intensities of $\Delta A/A_0 = 0.001$. All MCD spectra were collected at 300 K.

Although the present work has focused primarily on optimization of reaction conditions for the benchmark $Cd_{1-x}Mn_xSe$ nanocrystal system, the principles underpinning the diffusion-doping process described here are general, and the chemistry should therefore also be broadly generalizable. For example, by replacing CdSe nanocrystals and Se^{2-} with CdTe nanocrystals and Te^{2-}, decreasing the injection temperature to 170 ºC, and adding a reductant (Super-Hydride) to accommodate the lower stability of Te^{2-} in solution,[50] successful synthesis of $Cd_{1-x}Mn_xTe$ nanocrystals was achieved (Figure 2.5B) but without satisfactory suppression of Ostwald ripening, as in Figure 2.2C. Similar preliminary results have been obtained for $Cd_{1-x}Mn_xS$ and $Zn_{1-x}Mn_xSe$ nanocrystals (Appendix A). Doping by addition thus appears broadly promising, and we speculate that with optimization it should also be possible to suppress Ostwald ripening to the same extent in these cases as in the $Cd_{1-x}Mn_xSe$ syntheses discussed above. Optimization within each of these large parameter spaces was considered beyond the scope of the present study.

Extension of this diffusion-doping synthesis to other cations has also been preliminarily investigated. Hard Lewis acids such as Al^{3+}, Mg^{2+}, Gd^{3+}, and Er^{3+} were found to bind the capping ligands too strongly and cause sample precipitation. Attempts to codope these ions simultaneously with Mn^{2+}, thereby using a lower concentration of the interfering ion, sacrificed the ability of Mn^{2+} to suppress Ostwald ripening, likely for the same reason. Extension of this method to these hard Lewis acids may be possible with identification of a suitable ligand set, but this parameter space has not yet been thoroughly explored. On the other end of the spectrum, extension to soft Lewis acids such as Cu^{+} and Ag^{+} was not possible because of rapid formation of their respective selenide lattices

separately from the CdSe nanocrystals. Cation-exchange reactions involving these cations avoid such competing side reactions by not including excess anion, and indeed, the new method introduced here can be considered unnecessary for these ions. Borderline hard/soft Lewis acids were also examined: Replacing Mn^{2+} with excess Fe^{2+} without excess Se^{2-} was found to successfully preserve the absorption spectrum of the seed CdSe nanocrystals (see Appendix A), precisely as with Mn^{2+} in Figure 2.2B. Importantly, the nanocrystals also retain their excitonic photoluminescence. Fe^{2+} is a "killer trap" for luminescence in II–VI semiconductors, and this result thus indicates an absence of Fe^{2+} doping in the absence of excess Se^{2-} (as concluded for Mn^{2+} above). Addition of Se^{2-} to this reaction mixture leads to an increase in E_g with reaction time and complete quenching of the CdSe luminescence (see Appendix A), consistent with successful Fe^{2+} incorporation. Fe^{2+} diffusion doping into CdSe nanocrystals thus closely mirrors that of Mn^{2+}. Similarly, using Co^{2+} in place of Mn^{2+} allows the successful synthesis of $Cd_{1-x}Co_xSe$ nanocrystals with high Co^{2+} concentrations (see below and Appendix A).

Finally, the capacity to separate doping from nanocrystal synthesis introduces new opportunities to prepare doped nanostructures that would be difficult to obtain under kinetic trapping conditions. For example, previous work has shown that dopants are excluded from very small semiconductor nanocrystals under kinetic doping conditions.[9, 44, 45, 51] Among other things, this behavior has complicated the analysis of the recently discovered intrinsic dual emission phenomenon in small $Cd_{1-x}Mn_xSe$ nanocrystals because of the coexistence of both doped and undoped nanocrystals.[52] To overcome this problem, $Cd_{1-x-y}Zn_xMn_ySe$ alloys and complex $Zn_{1-x}Mn_xSe$/CdSe and

$Zn_{1-x}Mn_xSe$/ZnS/CdS/ZnS nanocrystal heterostructures were developed.[53-55] By diffusion doping, we have now succeeded in reaching large values of x_{Mn} in CdSe nanocrystals small enough to show pronounced dual emission directly in $Cd_{1-x}Mn_xSe$ for the first time, without signal contamination from undoped nanocrystals (see Appendix A), and have also successfully added both Mn^{2+} and Zn^{2+} into seed CdSe nanocrystals in one simultaneous step, offering a convenient new way to achieve dual-emitting nanocrystals. Furthermore, qualitatively new chemistries are now possible. For example, Figure 2.5C shows excitonic MCD spectra of d = 3.8 nm CdSe seed nanocrystals that are doped sequentially by addition of Co^{2+} and then Mn^{2+}. The undoped CdSe nanocrystals show a negative leading-edge MCD intensity consistent with the absence of *sp–d* exchange. Diffusion doping with Co^{2+} for 30 minutes at 300 ºC inverts the excitonic MCD signal and yields the characteristic Co^{2+} $^4A_2(F) \rightarrow {}^4T_1(P)$ MCD feature centered at 1.66 eV, confirming successful incorporation of Co^{2+} at the tetrahedral cation sites of the CdSe lattice.[40, 41] After subsequent diffusion doping with Mn^{2+} for 40 minutes at 300 ºC, the Co^{2+} $^4A_2(F) \rightarrow {}^4T_1(P)$ transition is retained and the excitonic MCD intensity is further increased. The ratio of excitonic to Co^{2+} ligand-field absorbance varies slowly during Mn^{2+} incorporation (see Appendix A), indicating minimal loss of Co^{2+} during Mn^{2+} addition, consistent with the large difference between lattice and solution chemical potentials for all cations under these conditions.

2.5 Discussion

The data presented here reveal the remarkable ability to introduce Mn^{2+} into high-quality hot-injection CdSe nanocrystals from very low to exceptionally high values of x_{Mn} simply by changing the reaction time, without sacrificing the nanocrystal size or shape uniformity or the crystallographic phase. This process is reminiscent of cation exchange in nanocrystals, but displays a few key differences. First, to date it has been a general requirement of nanocrystal cation-exchange reactions that the participating cations diffuse rapidly. The chemistry demonstrated here involves Mn^{2+}, which shows negligible diffusion into II–VI semiconductor nanocrystals at room temperature. Instead, this diffusion must be activated thermally, requiring long incubation at relatively high temperatures that would normally also cause severe Ostwald ripening. Second, it is a fundamental property of nanocrystal cation-exchange reactions that the number of anions per nanocrystal is invariant,[16] but the results presented above demonstrate that this diffusion doping involves stoichiometric anion and cation addition. The data suggest rapid composition equilibration at the surfaces followed by slower cation randomization within the nanocrystals' internal volumes, precisely how cation exchange proceeds at bulk II–VI semiconductor surfaces,[56] but this stoichiometric cation + anion addition avoids the need to eject Cd^{2+} to form less favorable Mn^{2+}–Se^{2-} bonds. This feature represents a defining characteristic of the diffusion doping presented here that differentiates it from cation-exchange chemistries explored previously.[16-22] Because of this qualitative difference, diffusion doping provides the opportunity to introduce relatively unreactive cations such as Mn^{2+} into semiconductor nanocrystals such as CdSe that have been notoriously difficult to dope under kinetic

control. Sequential tandem doping has been used to illustrate the qualitative difference between this doping by addition and previous cation-exchange or kinetic trapping chemistries. Despite these differences, diffusion doping also offers some of the most attractive features of cation exchange, namely, retention of seed nanocrystal shape anisotropies, sizes and size distributions, and crystallographic phases. These properties identify diffusion doping as a valuable new addition to our current repertoire of methods for controlling crystal composition at the nanoscale.

Scheme 2.1

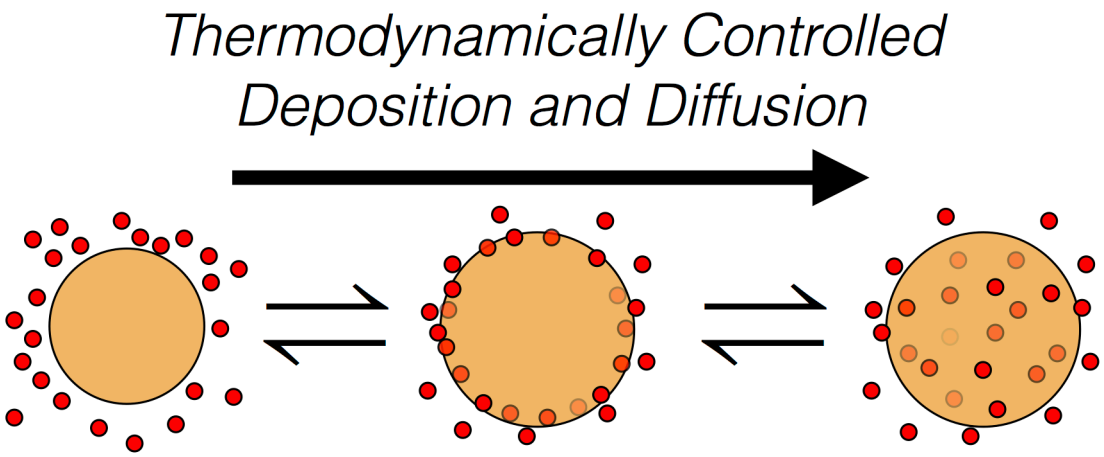

Scheme 2.1 summarizes the diffusion-doping chemistry found here, illustrating a case of doping spherical nanocrystals. Surface binding equilibria, defined by the relative solution vs lattice chemical potentials of the host and impurity cations, allow the thermodynamic solid-solution compositions to be reached within an effective reaction volume at the nanocrystal surfaces (Figure 2.3E). This equilibration is followed on a longer time scale (Figure 2.3F) by impurity randomization within the nanocrystal internal volumes. Ostwald ripening is suppressed despite the long reaction times at high temperatures

because of the limited availability of uncoordinated surfactant ligands and the ample availability of lattice anions. These two factors minimize the solution diffusion length of the host cations.

Although interparticle Cd^{2+} diffusion can be successfully minimized, Cd^{2+} ions continue to diffuse at the nanocrystal surfaces. Surface diffusion is essential for the formation of solid-solution $Cd_{1-x}Mn_xSe$ nanocrystals rather than simple core/shell CdSe/MnSe nanocrystals. As in cation exchange, this reactive surface layer must be small compared to the dimensions of the nanocrystals themselves for the crystallographic phases and shape anisotropies of the seed nanocrystals to be preserved.[16]

The chemical trends in diffusion doping observed here can be understood by considering the surface equilibria as governed by hard/soft acid/base rules. The experimental conditions identified here (including cation, anion, ligand, and nanocrystal concentrations, as well as temperature) were optimized for introduction of Mn^{2+} into CdSe nanocrystals and subsequently found to be suitable for introduction of Fe^{2+} and Co^{2+} as well. These cations share in common that they are all borderline hard Lewis acids. By contrast, more conventional cation-exchange chemistries excel when using soft Lewis acids (e.g., Cu^+, Ag^+, Au^+, Cd^{2+}, Pb^{2+}, and Hg^{2+}), which have a greater affinity for the lattice anions and hence can more easily displace the initial host cations. For the same reason, use of these soft cations under the present diffusion-doping conditions simply leads to nucleation of their independent phases because of the large excess ion concentrations used. Conditions for doping hard Lewis acids (e.g., Al^{3+}, trivalent lanthanides) into II–VI semiconductors via diffusion have so far not been identified but should exist. Under the

present conditions, such hard Lewis acids have too great an affinity for the hard surfactant Lewis bases employed.

Essential to the success of this diffusion-doping strategy in the present case is the fact that MnSe crystallites do not form under the experimental reaction conditions. Formation of MnSe nanoclusters has been reported under conditions similar to those used here,[57] but with the key differences that the present reaction mixtures (i) contain nearly an order of magnitude more stearic acid relative to Mn^{2+} and (ii) also contain CdSe nanocrystals. Both of these additions disfavor MnSe formation by introducing processes that compete for available Mn^{2+} (ligation and surface binding, respectively). The presence of excess stearic acid makes MnSe formation unfavorable.

This synthesis of $Cd_{1-x}Mn_xSe$ nanocrystals is distinct from any reported previously, but its comparison to analogous chemistries is instructive. One interesting analogue is the conversion of CdSe nanocrystals to ZnSe nanocrystals by sequential cation-exchange reactions proceeding via an intermediate $Cu_{2-x}Se$ nanocrystal composition. Whereas the first cation-exchange step (taking CdSe to $Cu_{2-x}Se$) proceeds rapidly at room temperature, the following step ($Cu_{2-x}Se$ to ZnSe) requires elevated temperatures (up to 250 ºC), with trioctylphosphine added as a soft base to assist Cu^{+} removal (and no added Se^{2-}). This transformation reaches completion within a few seconds at 250 ºC.[21] Although less reactive than common Lewis acids used in cation exchange, Zn^{2+} has sufficient affinity for Se^{2-} for this reaction to proceed rapidly, and ripening is not problematic. In principle, a similar approach might possibly allow formation of $Cd_{1-x}Mn_xSe$ or related doped nanocrystals, but such chemistries have not yet been demonstrated.

Perhaps most closely related to the observations here is the synthesis of $Cd_{1-x}Zn_xSe$ alloy nanocrystals by heating core/shell CdSe/ZnSe nanocrystals.[58] In this chemistry, internal diffusion is believed to cause homogeneous alloying within minutes at temperatures above ~290 ºC. Ostwald ripening is evident at temperatures below this alloying point, but the size distribution can be kept relatively narrow ($\sigma \approx$ 5–12%). XRD data suggest a transformation from zinc blende to wurtzite may accompany this alloying.[58] A significant difference between this $Cd_{1-x}Zn_xSe$ nanocrystal synthesis and the present $Cd_{1-x}Mn_xSe$ nanocrystal synthesis is that MnSe is far less stable than ZnSe under the reaction conditions. Because of this instability, the $Cd_{1-x}Mn_xSe$ nanocrystals do not form via core/shell intermediates like the $Cd_{1-x}Zn_xSe$ nanocrystals do, longer times are needed to homogenize the $Cd_{1-x}Mn_xSe$ alloys (hours at 300 ºC, Figure 2.3, compared to <5 min for the $Cd_{1-x}Zn_xSe$ alloys[58]), and $Cd_{1-x}Mn_xSe$ reaches smaller maximum values of x at equilibrium (x_{Mn}(max) ≈ 0.2 vs x_{Zn}(max) ≈ 0.7). The slower alloying in $Cd_{1-x}Mn_xSe$ nanocrystals in particular highlights the importance of suppressing Ostwald ripening, as achieved here. Despite these differences, these two processes may ultimately share a common mechanism. Notable, the $Cd_{1-x}Zn_xSe$ synthesis is also performed in the presence of excess cation and anion precursor, like in the present diffusion doping, and may therefore be assisted by the resulting high chemical potentials of these ions in solution. Given these similarities, it would be of interest to know whether CdSe/ZnSe alloying preserves nanocrystal shape anisotropies and whether conditions can be found under which crystallographic phases are also preserved. The results presented here for $Cd_{1-x}Mn_xSe$ nanocrystals suggest that both should be possible.

2.6 Conclusion

We have demonstrated a successful equilibrium synthesis of doped semiconductor nanocrystals. This method involves cation + anion addition to seed nanocrystals at elevated temperatures followed by diffusive mixing to yield the solid solution, akin to liquid-solid alloying of metals.[59] By suppressing Ostwald ripening, this method allows incorporation of relatively unreactive impurity ions while still retaining anisotropic shapes, size distributions, and crystallographic phases. This diffusion-doping method thus allows the nanocrystals to achieve their thermodynamic compositions without reaching their thermodynamically favored shapes, sizes, or crystallographic phases. Using this strategy, we have demonstrated the successful synthesis of high-quality colloidal $Cd_{1-x}Mn_xSe$ nanocrystals that simultaneously display the narrowest size distributions, the highest values of x, and the largest magneto-optical exciton splittings of any $Cd_{1-x}Mn_xSe$ nanocrystals reported to date. This success motivates the generalization of this strategy to synthesize nanocrystals of various other shapes and compositions under thermodynamic control, particularly compositions that do not involve the few well-known fast-diffusing ions that have dominated cation-exchange chemistries to date, and promising preliminary results for other nanocrystal compositions have been presented. Overall, these findings raise interesting possibilities for the development of new doped nanostructures with complex shapes and compositions, possibly including heterostructures, and may ultimately enable the advancement of new technologies involving this important class of materials.

2.7 Appendix A

Additional synthetic details and experimental data.

2.8 Acknowledgments

This work was supported by the U.S. National Science Foundation (NSF) (Grant DMR-1206221 to D.R.G.). Part of this work was conducted at the University of Washington NanoTech User Facility, a member of the NSF National Nanotechnology Infrastructure Network (NNIN). We thank Prof. Celso de Mello Donegá for fruitful discussions.

2.9 References

1. Murray, C. B.; Norris, D. J.; Bawendi, M. G. Synthesis and Characterization of Nearly Monodisperse CdE (E = Sulfur, Selenium, Tellurium) Semiconductor Nanocrystallites. *J. Am. Chem. Soc.* **1993**, *115*, 8706–8715.
2. Alivisatos, A. P. Perspectives on the Physical Chemistry of Semiconductor Nanocrystals. *J. Phys. Chem.* **1996**, *100*, 13226–13239.
3. Murray, C. B.; Kagan, C. R.; Bawendi, M. G. Synthesis and Characterization of Monodisperse Nanocrystals and Close-Packed Nanocrystal Assemblies. *Annu. Rev. Mater. Sci.* **2000**, *30*, 545–610.
4. Scholes, G. D. Controlling the Optical Properties of Inorganic Nanoparticles. *Adv. Funct. Mater.* **2008**, *18*, 1157–1172.
5. de Mello Donegá, C. Synthesis and Properties of Colloidal Heteronanocrystals. *Chem. Soc. Rev.* **2011**, *40*, 1512–1546.
6. Klimov, V. I., *Nanocrystal Quantum Dots*. 2nd ed.; CRC Press: Boca Raton, FL, 2010.
7. Rogach, A., *Semiconductor Nanocrystal Quantum Dots. Synthesis, Assembly, Spectroscopy and Applications*. Springer: Vienna, 2008.
8. Bryan, J. D.; Gamelin, D. R. Doped Semiconductor Nanocrystals: Synthesis, Characterization, Physical Properties, and Applications. *Prog. Inorg. Chem.* **2005**, *54*, 47–126.
9. Erwin, S. C.; Zu, L. J.; Haftel, M. I.; Efros, A. L.; Kennedy, T. A.; Norris, D. J. Doping Semiconductor Nanocrystals. *Nature* **2005**, *436*, 91–94.
10. Norris, D. J.; Efros, A. L.; Erwin, S. C. Doped Nanocrystals. *Science* **2008**, *319*, 1776–1779.
11. Beaulac, R.; Archer, P. I.; Ochsenbein, S. T.; Gamelin, D. R. Mn^{2+}-Doped CdSe Quantum Dots: New Inorganic Materials for Spin-Electronics and Spin-Photonics. *Adv. Funct. Mater.* **2008**, *18*, 3873–3891.
12. Beaulac, R.; Ochsenbein, S. T.; Gamelin, D. R. Colloidal Transition-Metal-Doped Quantum Dots. In *Semiconductor Quantum Dots*, 2nd ed.; Klimov, V. I., Ed; CRC Press: Boca Raton, FL, 2010; pp 397–453.
13. Buonsanti, R.; Milliron, D. J. Chemistry of Doped Colloidal Nanocrystals. *Chem. Mater.* **2013**, *25*, 1305–1317.
14. Furdyna, J. K.; Kossut, J., *Diluted Magnetic Semiconductors*. Academic: N.Y., 1988; Vol. 25.
15. Sugimoto, T. Preparation of Monodispersed Colloidal Particles. *Adv. Colloid Interfac. Sci.* **1987**, *28*, 65–108.
16. Son, D. H.; Hughes, S. M.; Yin, Y.; Alivisatos, A. P. Cation Exchange Reactions in Ionic Nanocrystals. *Science* **2004**, *306*, 1009–1012.
17. Luther, J. M.; Zheng, H.; Sadtler, B.; Alivisatos, A. P. Synthesis of PbS Nanorods and Other Ionic Nanocrystals of Complex Morphology by Sequential Cation Exchange Reactions. *J. Am. Chem. Soc.* **2009**, *131*, 16851–16857.
18. Jain, P. K.; Amirav, L.; Aloni, S.; Alivisatos, A. P. Nanoheterostructure Cation Exchange: Anionic Framework Conservation. *J. Am. Chem. Soc.* **2010**, *132*, 9997–9999.

19. Casavola, M.; van Huis, M. A.; Bals, S.; Lambert, K.; Hens, Z.; Vanmaekelbergh, D. Anisotropic Cation Exchange in PbSe/CdSe Core/Shell Nanocrystals of Different Geometry. *Chem. Mater.* **2011**, *24*, 294–302.
20. Miszta, K.; Dorfs, D.; Genovese, A.; Kim, M. R.; Manna, L. Cation Exchange Reactions in Colloidal Branched Nanocrystals. *ACS Nano* **2011**, *5*, 7176–7183.
21. Li, H.; Zanella, M.; Genovese, A.; Povia, M.; Falqui, A.; Giannini, C.; Manna, L. Sequential Cation Exchange in Nanocrystals: Preservation of Crystal Phase and Formation of Metastable Phases. *Nano Letters* **2011**, *11*, 4964–4970.
22. Rivest, J. B.; Jain, P. K. Cation Exchange on the Nanoscale: An Emerging Technique for New Material Synthesis, Device Fabrication, and Chemical Sensing. *Chem. Soc. Rev.* **2013**, *42*, 89–96.
23. Mokari, T.; Aharoni, A.; Popov, I.; Banin, U. Diffusion of Gold into InAs Nanocrystals. *Angew. Chem.* **2006**, *45*, 8001–8005.
24. Mocatta, D.; Cohen, G.; Schattner, J.; Millo, O.; Rabani, E.; Banin, U. Heavily Doped Semiconductor Nanocrystal Quantum Dots. *Science* **2011**, *332*, 77–81.
25. Sahu, A.; Kang, M. S.; Kompch, A.; Notthoff, C.; Wills, A. W.; Deng, D.; Winterer, M.; Frisbie, C. D.; Norris, D. J. Electronic Impurity Doping in CdSe Nanocrystals. *Nano Letters* **2012**, *12*, 2587–2594.
26. Acharya, S.; Sarkar, S.; Pradhan, N. Material Diffusion and Doping of Mn in Wurtzite ZnSe Nanorods. *J. Phys. Chem. C* **2013**, *117*, 6006–6012.
27. Eilers, J.; Groeneveld, E.; Donega, C. D.; Meijerink, A. Optical Properties of Mn-Doped ZnTe Magic Size Nanocrystals. *J. Phys. Chem. Lett.* **2012**, *3*, 1663–1667.
28. Hagen, K. S.; Stephan, D. W.; Holm, R. H. Metal Ion Exchange Reactions in Cage Molecules: The Systems $[M_{4-n}M'_n(SC_6H_5)_{10}]^{2-}$ (M, M' = Fe(II), Co(II), Zn(II), Cd(II)) with Adamantane-Like Stereochemistry and the Structure of $[Fe_4(SC_6H_5)_{10}]^{2-}$. *Inorg. Chem.* **1982**, *21*, 3928–3936.
29. Autissier, V.; Henderson, R. A. Mechanism of single metal exchange in the reactions of $[M_4(SPh)_{10}]^{2-}$ (M = Zn or Fe) with CoX_2 (X = Cl or NO_3) or $FeCl_2$. *Inorg. Chem.* **2008**, *47*, 6393–6403.
30. Chen, D.; Viswanatha, R.; Ong, G. L.; Xie, R.; Balasubramaninan, M.; Peng, X. Temperature Dependence of "Elementary Processes" in Doping Semiconductor Nanocrystals. *J. Am. Chem. Soc.* **2009**, *131*, 9333–9339.
31. Du, M.-H.; Erwin, S. C.; Efros, A. L. Trapped-Dopant Model of Doping in Semiconductor Nanocrystals. *Nano Lett.* **2008**, *8*, 2878–2882.
32. Erwin, S. C. Doping PbSe Nanocrystals: Predictions Based on a Trapped-Dopant Model. *Phys. Rev. B* **2010**, *81*, 235433.
33. Qu, L.; Peng, X. Control of Photoluminescence Properties of CdSe Nanocrystals in Growth. *J. Am. Chem. Soc.* **2002**, *124*, 2049–2055.

34. Carbone, L.; Nobile, C.; De Giorgi, M.; Della Sala, F.; Morello, G.; Pompa, P.; Hytch, M.; Snoeck, E.; Fiore, A.; Franchini, I. R.; Nadasan, M.; Silvestre, A. F.; Chiodo, L.; Kudera, S.; Cingolani, R.; Krahne, R.; Manna, L. Synthesis and Micrometer-Scale

Assembly of Colloidal CdSe/CdS Nanorods Prepared by a Seeded Growth Approach. *Nano Letters* **2007**, *7*, 2942–2950.
35. Yu, W. W.; Qu, L.; Guo, W.; Peng, X. Experimental Determination of the Extinction Coefficient of CdTe, CdSe and CdS. *Chem. Mater.* **2003**, *15*, 2854–2860.
36. Yu, W. W.; Peng, X. Formation of High-Quality CdS and Other II–VI Semiconductor Nanocrystals in Noncoordinating Solvents: Tunable Reactivity of Monomers. *Angew. Chem.* **2002**, *41*, 2368–2371.
37. Piepho, S. B.; Schatz, P. N. *Group Theory in Spectroscopy with Applications to Magnetic Circular Dichroism*. Wiley: New York, 1983.
38. Beaulac, R.; Archer, P. I.; Liu, X.; Lee, S.; Salley, G. M.; Dobrowolska, M.; Furdyna, J. K.; Gamelin, D. R. Spin-Polarizable Excitonic Luminescence in Colloidal Mn^{2+}-Doped CdSe Quantum Dots. *Nano Lett.* **2008**, *8*, 1197–1201.
39. Furdyna, J. K. Diluted Magnetic Semiconductors. *J. Appl. Phys.* **1988**, *64*, R29–R64.
40. Archer, P. I.; Santangelo, S. A.; Gamelin, D. R. Direct Observation of sp–d Exchange Interactions in Colloidal Mn^{2+}- and Co^{2+}-doped CdSe Quantum Dots. *Nano Lett.* **2007**, *7*, 1037–1043.
41. Archer, P. I.; Santangelo, S. A.; Gamelin, D. R. Inorganic Cluster Syntheses of TM^{2+}-Doped Quantum Dots (CdSe, CdS, CdSe/CdS): Physical Property Dependence on Dopant Locale. *J. Am. Chem. Soc.* **2007**, *129*, 9808–9818.
42. Kuno, M.; Nirmal, M.; Bawendi, M. G.; Efros, A.; Rosen, M. Magnetic Circular Dichroism Study of CdSe Quantum Dots. *J. Chem. Phys.* **1998**, *108*, 4242–4247.
43. Shapira, Y.; Foner, S.; Ridgley, D. H.; Dwight, K.; Wold, A. Technical Saturation and Magnetization Steps in Diluted Magnetic Semiconductors: Predictions and Observations. *Phys. Rev. B* **1984**, *30*, 4021–4023.
44. Schwartz, D. A.; Norberg, N. S.; Nguyen, Q. P.; Parker, J. M.; Gamelin, D. R. Magnetic Quantum Dots: Synthesis, Spectroscopy, and Magnetism of Co^{2+}- and Ni^{2+}-Doped ZnO Nanocrystals. *J. Am. Chem. Soc.* **2003**, *125*, 13205–13218.
45. Norberg, N. S.; Gamelin, D. R. Giant Zeeman Effects in Colloidal Diluted Magnetic Semiconductor Quantum Dots with Homogeneous Dopant Speciation. *J. Appl. Phys.* **2006**, *99*, 08M104.
46. Schimpf, A. M.; Gamelin, D. R. Thermal Tuning and Inversion of Excitonic Zeeman Splittings in Colloidal Doped CdSe Quantum Dots. *J. Phys. Chem. Lett.* **2012**, *3*, 1264–1268.
47. Beaulac, R.; Gamelin, D. R. Two-Center Formulation of Mn^{2+}-Electron s–d Exchange Coupling in Bulk and Quantum-Confined Diluted Magnetic Semiconductors. *Phys. Rev. B* **2010**, *82*, 224401.
48. Beaulac, R.; Feng, Y.; May, J. W.; Badaeva, E.; Gamelin, D. R.; Li, X. Orbital Pathways for Mn^{2+}-Carrier sp–d Exchange in Diluted Magnetic Semiconductor Quantum Dots. *Phys. Rev. B* **2011**, *84*, 195324.
49. Yu, W. W.; Qu, L.; Guo, W.; Peng, X. Experimental Determination of the Extinction Coefficient of CdTe, CdSe and CdS Nanocrystals. *Chem. Mater.* **2004**, *16*, 560 (erratum).
50. Zhang, J.; Sun, K.; Kumbhar, A.; Fang, J. Shape-Control of ZnTe Nanocrystal Growth in Organic Solution. *J. Phys. Chem. C* **2008**, *112*, 5454–5458.

51. Bryan, J. D.; Schwartz, D. A.; Gamelin, D. R. The Influence of Dopants on the Nucleation of Semiconductor Nanocrystals from Homogeneous Solution. *J. Nanosci. Nanotechnol.* **2005**, *5*, 1472–1479.
52. Beaulac, R.; Archer, P. I.; van Rijssel, J.; Meijerink, A.; Gamelin, D. R. Exciton Storage by Mn^{2+} in Colloidal Mn^{2+}-Doped CdSe Quantum Dots. *Nano Lett.* **2008**, *8*, 2949–2953.
53. Vlaskin, V. A.; Janßen, N.; van Rijssel, J.; Beaulac, R.; Gamelin, D. R. Tunable Dual Emission in Doped Semiconductor Nanocrystals. *Nano Lett.* **2010**, *10*, 3670–3674.
54. McLaurin, E. J.; Vlaskin, V. A.; Gamelin, D. R. Water-Soluble Dual-Emitting Nanocrystals for Ratiometric Optical Thermometry. *J. Am. Chem. Soc.* **2011**, *133*, 14978–14980.
55. McLaurin, E. J.; Fataftah, M. S.; Gamelin, D. R. One-Step Synthesis of Alloyed Dual-Emitting Semiconductor Nanocrystals. *Chem. Commun.* **2013**, *49*, 39–41.
56. Fedorov, V. A.; Ganshin, V. A.; Korkishko, Y. N. Ion Exchange in II–VI Crystals: Thermodynamics, Kinetics, and Technology. *Phys. Stat. Sol. A* **1993**, *139*, 9–65.
57. Pradhan, N.; Peng, X. Efficient and Color-Tunable Mn-Doped ZnSe Nanocrystal Emitters: Control of Optical Performance via Greener Synthetic Chemistry. *J. Am. Chem. Soc.* **2007**, *129*, 3339–3347.
58. Zhong, X.; Han, M.; Dong, Z.; White, T. J.; Knoll, W. Composition-Tunable $Zn_xCd_{1-x}Se$ Nanocrystals with High Luminescence and Stability. *J. Am. Chem. Soc.* **2003**, *125*, 8589–8594.
59. Larsson, L.-E. Homogenization During Liquid-Solid Alloying of a Fe-1Cu-1Mn-0.3C Powder-Forged Steel. *Mat. Sci. Engin.* **1975**, *19*, 231–240.

Chapter 3. Tuning Equilibrium Compositions in Colloidal $Cd_{1-x}Mn_xSe$ Nanocrystals Using Diffusion Doping and Cation Exchange*

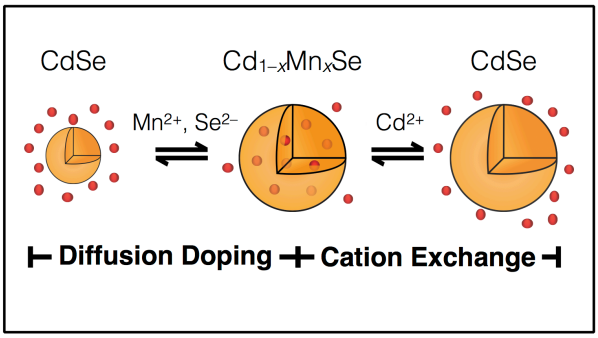

*Reproduced with permission from Barrows, C. J.; Chakraborty, P.; Kornowske, L. M.; Gamelin, D. R. *ACS Nano* **2016**, *10*, 910-918. Copyright 2016 American Chemical Society.

3.1 Overview

The physical properties of semiconductor nanocrystals can be tuned dramatically *via* composition control. Here, we report a detailed investigation of the synthesis of high-quality colloidal $Cd_{1-x}Mn_xSe$ nanocrystals by diffusion doping of preformed CdSe nanocrystals. Until recently, $Cd_{1-x}Mn_xSe$ nanocrystals proved elusive because of kinetic incompatibilities between Mn^{2+} and Cd^{2+} chemistries. Diffusion doping allows $Cd_{1-x}Mn_xSe$ nanocrystals to be prepared under thermodynamic rather than kinetic control, allowing access to broader composition ranges. We now investigate this chemistry as a model system for understanding the characteristics of nanocrystal diffusion doping more deeply. From the present work, a Se^{2-}-limited reaction regime is identified, in which Mn^{2+} diffusion into CdSe nanocrystals is gated by added Se^{2-}, and equilibrium compositions are proportional to the amount of added Se^{2-}. At large added Se^{2-} concentrations, a solubility-limited regime is also identified, in which $x = x_{max} = \sim 0.31$, independent of the amount of added Se^{2-}. We further demonstrate that Mn^{2+} in-diffusion can be reversed by cation exchange with Cd^{2+} under exactly the same reaction conditions, purifying $Cd_{1-x}Mn_xSe$ nanocrystals back to CdSe nanocrystals with fine tunability. These chemistries offer exceptional composition control in $Cd_{1-x}Mn_xSe$ nanocrystals, providing opportunities for fundamental studies of impurity diffusion in nanocrystals and for development of compositionally tuned nanocrystals with diverse applications ranging from solar energy conversion to spin-based photonics.

3.2 Introduction

Nanocrystal (NC) composition control represents a central challenge in nanoscience. Although there has been tremendous progress in recent years,[1-10] many desirable compositions still remain unattainable in colloidal NCs, motivating the development of new chemistries. One important area of composition control pertains to semiconductor nanocrystal doping,[11-16] because the addition of impurities can dramatically change the electronic, magnetic, or optical properties of the NCs, imparting desirable physical properties that in turn may stimulate fundamental discoveries or applied technologies. Understanding the fundamental chemical boundaries of nanocrystal composition control for new and challenging dopant/host combinations could yield unprecedented doped semiconductor nanomaterials for applications from spectral conversion in lighting and luminescent solar concentrators (LSCs)[17-18] to optical nanothermometry,[19] bioimaging,[20] plasmonics,[21-23] or spin-based electronic/photonic information processing.[24]

Recently, we reported a "diffusion doping" approach for introducing relatively incompatible and slowly diffusing cations into semiconductor nanocrystals.[25] This approach involves thermodynamically driven cation + anion addition followed by high-temperature diffusive cation randomization. $Cd_{1-x}Mn_xSe$ was selected as our model system because of the well-known and long-standing challenges of synthesizing high-quality $Cd_{1-x}Mn_xSe$ nanocrystals.[24,26-29] Mn^{2+} diffusion is notoriously slow in II–VI semiconductors, making this ion unsuitable for doping into the internal volumes of II–VI nanocrystals *via* cation exchange chemistries,[29] and the high temperatures that would be required to

accelerate its diffusion have widely been associated with Mn^{2+} *out*-diffusion from nanocrystals ("self-purification").[30-31] We found that by tuning the Mn^{2+} chemical potential in solution to be greater than that inside the NCs, Mn^{2+} in-diffusion into various II–VI semiconductor nanocrystals could be made thermodynamically favorable, but diffusive composition scrambling still requires long reaction times at elevated temperatures, for which deliberate suppression of Ostwald ripening is also essential if the desired nanostructuring of the preformed host crystallites is to be retained.[25] To this end, we demonstrated that Ostwald ripening can be effectively eliminated by raising the chemical potentials of *all* cations in solution using a large excess of solvated Mn^{2+}.[25]

Among existing synthetic methods for making $Cd_{1-x}Mn_xSe$ nanocrystals, diffusion doping has yielded simultaneously the largest Mn^{2+} content and the greatest size uniformity, making NCs prepared by this method especially attractive for spectroscopic investigations and subsequent applications. $Cd_{1-x}Mn_xSe$ nanocrystals prepared by diffusion doping have now been used to demonstrate rich upper-excited-state magnetic circular dichroism (MCD),[32] extraordinarily large excitonic Zeeman splittings,[33] excitonic magnetic polarons,[34] and enhanced positive magneto-resistance suggestive of electron magnetic polarons.[35] Although the products of this chemistry are already proving useful, many details of the chemistry itself remain unexplored. For example, previous work has not systematically explored relationships between synthesis conditions and product compositions, and tunable equilibrium compositions have not been demonstrated. Further studies that better characterize this promising synthetic method should help accelerate its adaptation to other even more challenging target compositions. At the same time, further

experimentation will provide new fundamental insights into ion diffusion in semiconductor nanostructures in general, and will also inform our understanding of the stabilities of doped nanocrystals under high-temperature processing or device operation conditions.

Here, we report the results of synthetic experiments aimed at improving our understanding of CdSe nanocrystal diffusion doping with Mn^{2+}. Key new observations include the demonstration of complete compositional equilibration, widely tunable equilibrium compositions *via* added Se^{2-}, existence of a thermodynamic Mn^{2+} solubility limit, and reversal of the diffusion doping *via* cation exchange. These new findings highlight several unique features of this chemistry that allow its use for extraordinarily fine composition control in doped semiconductor nanocrystals, advancing the frontier of doped nanocrystal synthesis and elevating the quality of doped nanocrystals accessible for future physical, spectroscopic, or technological applications.

3.3 Results and Analysis

Reactions in our initial report[25] on diffusion doping were all performed using a large excess of added Se^{2-}. A primary goal of the present study is to clarify the role of the added Se^{2-} in this chemistry. Figure 3.1 summarizes spectroscopic data collected during a reaction specifically designed to illustrate two key features of nanocrystal diffusion doping: doping gated by Se^{2-}, and equilibration. Figure 3.1A,B shows room-temperature electronic absorption and MCD spectra of three aliquots taken during this reaction: (*i*) the initial seed CdSe nanocrystals, (*ii*) the same nanocrystals after 20 minutes of heating at 300 ºC in the

presence of a large excess of Mn^{2+} but without added Se^{2-}, and (*iii*) after 24 hours of heating following injection of additional Se^{2-}. The absorption and MCD spectra of the seed CdSe nanocrystals show multiple resolved excitonic transitions, consistent with a narrow size distribution. The first excitonic absorption maximum occurs at ~2.15 eV, implying an average nanocrystal diameter of d = 3.7 nm.[36] The MCD spectrum of the same sample shows a derivative-shaped *A*-term feature coincident with the first excitonic absorption maximum, arising from the Zeeman splitting of this excitonic excited state. The negative leading-edge intensity of this derivative signal is indicative of a positive excitonic Zeeman splitting energy ($\Delta E_{Zeeman} > 0$) and hence a positive intrinsic excitonic g value ($g_{int} > 0$, Equation 3.1, where μ_B is the Bohr magneton and B is the magnetic field).[37] Quantitative analysis[13,33] of these spectra yields a value of $g_{Exc} = g_{int} \approx +1$ for the seed CdSe nanocrystals.

$$\Delta E_{Zeeman} = g_{Exc}\mu_B B \tag{3.1}$$

The absorption and MCD spectra of these nanocrystals remain unchanged after many hours at 300 ºC, despite the large excess of solvated Mn^{2+} (*vide infra*, Figure 3.2). In this particular experiment, injection of Se^{2-} into this reaction mixture after 20 minutes at 300 ºC causes a blue shift of the first exciton by ~80 meV and inversion and intensification of its associated MCD intensity in the 24 hour aliquot. Both of these spectroscopic changes are signatures of Mn^{2+} incorporation into the internal volumes of the CdSe nanocrystals.

Addition of Mn^{2+} into CdSe nanocrystals introduces strong *sp–d* magnetic exchange interactions between the unpaired Mn^{2+}(3*d*) spins and the exciton. The *sp–d* contribution to ΔE_{Zeeman} is parameterized by the last term of Equation 3.2a, where x_{eff} represents the

concentration of paramagnetic Mn^{2+} (reduced from the true x because of Mn^{2+}–Mn^{2+} antiferromagnetic superexchange interactions[38-39]), g describes the overlap between the ensemble of Mn^{2+} dopants and the excitonic wavefunction (g = 1 for uniform Mn^{2+} distribution), $\langle S_Z \rangle$ is the Mn^{2+} spin expectation value at the experimental temperature and magnetic field, and $N_0(\alpha - \beta)$ describes the mean-field *sp–d* exchange energy. In the Curie limit, this *sp–d* term converges to the linear term $g_{sp-d}\mu_B B$, such that $g_{Exc} = g_{int} + g_{sp-d}$ (Equation 3.2b). Because $N_0(\alpha - \beta) = -1.5$ eV for Mn^{2+}-doped CdSe, $g_{sp-d} < 0$ and Mn^{2+} doping causes the sign inversion observed in ΔE_{Zeeman} (Figure 3.1).[13,24,28,37,40] In this way, room-temperature (Curie limit) MCD spectroscopy can be used as a sensitive analytical probe of Mn^{2+} incorporation into the CdSe nanocrystals.

$$\Delta E_{Zeeman} = g_{int}\mu_B B + x_{eff} g \langle S_Z \rangle N_0(\alpha - \beta) \quad (3.2a)$$

$$= (g_{int} + g_{sp-d})\mu_B B \text{ (Curie limit)} \quad (3.2b)$$

Figure 3.1C summarizes the MCD results from several aliquots taken from this reaction, plotting g_{Exc} *vs* reaction time in a semi-logarithmic representation. Prior to Se^{2-} addition, g_{Exc} remains unchanged. After Se^{2-} addition, g_{Exc} shifts smoothly from its initial value of $g_{Exc} = g_{int} \approx +1$ to a new equilibrium value of $g_{Exc} = g_{int} + g_{sp-d} \approx -10$. The room-temperature *sp–d* exchange contribution is thus described by $g_{sp-d} \approx -11$ for this sample. The data in Figure 3.1 demonstrate that Mn^{2+} incorporation into these CdSe nanocrystals is gated by the addition of Se^{2-}, consistent with our previous interpretation that diffusion doping involves stoichiometric cation + anion addition.[25] Furthermore, whereas most reactions in our previous report were run for only ~30 minutes, these data show that equilibrium is not actually reached for several hours after Se^{2-} addition.

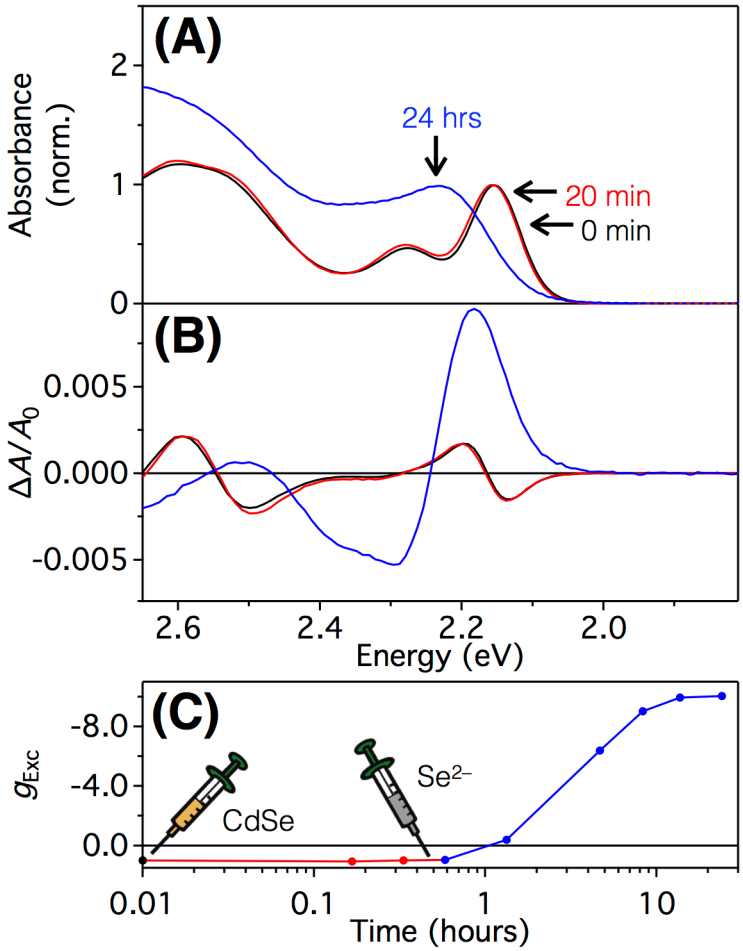

Figure 3.1. Room-temperature **(A)** electronic absorption and **(B)** 1.5 T MCD spectra of undoped d = 3.7 nm CdSe nanocrystals (0.1 mmol, black), the same nanocrystals after 20 minutes in the presence of Mn^{2+} at 300 ºC (0.1 mmol, red), and 24 hours following the addition of Se^{2-} (0.04 mmol, blue). These concentrations correspond to a ratio of 0.4:1:1 Se^{2-}:Mn^{2+}:Cd^{2+} ions in CdSe (referred to here as Se^{2-}:Mn^{2+}:CdSe). Spectra for other aliquots are omitted for clarity. **(C)** Time evolution of g_{Exc} during diffusion doping to form $Cd_{1-x}Mn_xSe$ NCs, as determined by analysis of the MCD spectra of these and other aliquots.

Next, we wished to explore the dependence of this reaction on the amount of Se^{2-} added. Figure 3.2A plots the evolution of g_{sp-d} measured during several ~24 hour diffusion-doping reactions performed under identical conditions except using different amounts of added Se^{2-}. As in Figure 3.1, if no Se^{2-} is added then g_{Exc} does not change even after several hours, indicating that $g_{sp-d} = 0$ at all times and hence the CdSe NCs remain undoped. Adding Se^{2-} induces Mn^{2+} doping and consequently an increase in $|g_{sp-d}|$. For these reactions, addition of more Se^{2-} leads to a greater equilibrium value of $|g_{sp-d}|$. Each reaction equilibrates over ~6–8 hours with similar kinetics. The curves in Figure 3.2A were obtained from a global fit of all data points to a single exponential function. Use of an exponential fitting function is helpful for capturing the phenomenological effective reaction rates but is not meant to imply a particular reaction mechanism. This fitting yields a universal time constant of $t_{eff} \approx 1.3$ hours that reproduces the entire data set reasonably well. Under these conditions, diffusion doping thus proceeds with roughly the same very slow kinetics at different Se^{2-} loadings, reaching different equilibrium values of x in the resulting $Cd_{1-x}Mn_xSe$ nanocrystals.

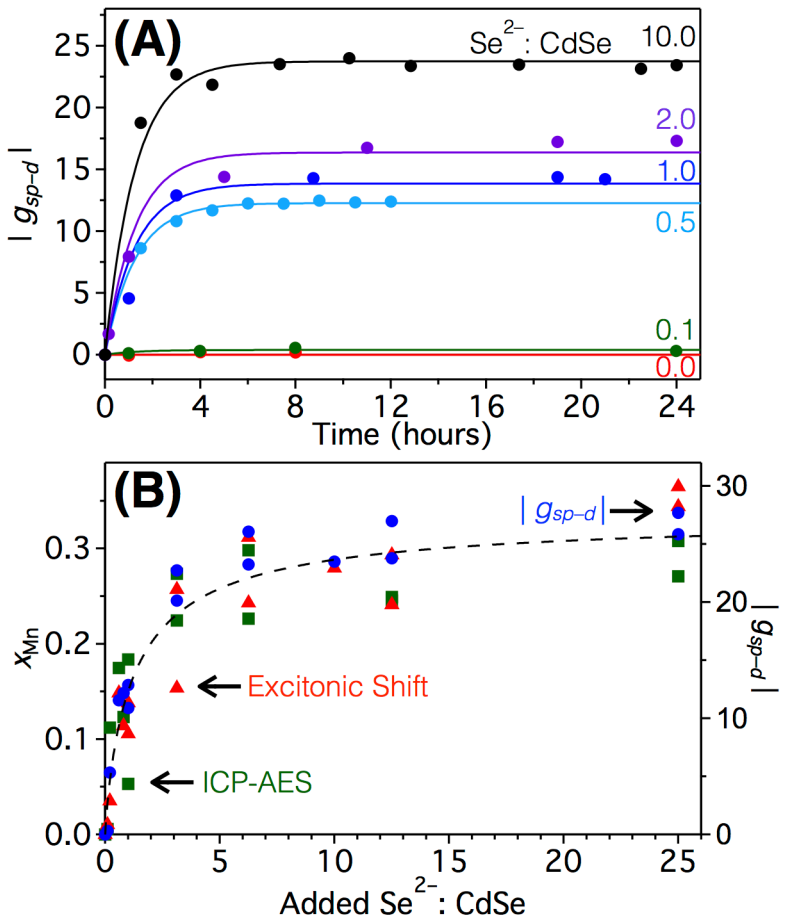

Figure 3.2. (A) Time evolution of $|g_{sp-d}|$, as determined by room-temperature MCD, from undoped d = 3.9 nm CdSe NCs with varying amounts of excess Se^{2-} (relative to Cd^{2+} in CdSe) during diffusion doping at 300 °C. The lines show results from a global fit of all of the data to a single exponential function, yielding t_{eff} = 1.3 hours. All reactions were performed at a ratio of 1:1 added Mn^{2+} to Cd^{2+} in CdSe (1:1 Mn^{2+}:CdSe). Electronic absorption and MCD spectra for representative aliquots are shown in Appendix B. (B) Se^{2-}-dependence of x_{Mn}, determined from analysis of absorption spectra (red triangles) and analytically determined by ICP-AES (green squares), after 24 hours of diffusion doping at 300 °C with 0–25:1:1 Se^{2-}:Mn^{2+}:CdSe. $|g_{sp-d}|$ values (blue circles) for these samples are plotted on the right axis and scaled to match the trend shown in x_{Mn}. The dashed line is a guide for the eye. Reactions performed multiple times have yielded values within ~5 % of the mean.

Under the conditions of our previous report,[25] reactions run with excess Se^{2-} showed evolving differences between spectroscopic and total (ICP-AES) Mn^{2+} contents, demonstrating evolving Mn^{2+} concentration gradients within the NCs prior to equilibration, and thereby implicating slow Mn^{2+} lattice diffusion as the rate-determining process. Because the diffusion-doping kinetics appear independent of added Se^{2-} (Figure 3.2A), we conclude that very slow Mn^{2+} diffusion through the NC lattice is also rate-determining in the Se^{2-}-limited regime.

Figure 3.2B summarizes equilibrium data from a broad series of diffusion-doping reactions spanning from very small amounts of added Se^{2-} up to a large excess of added Se^{2-} (25:1:1 Se^{2-}:Mn^{2+}:CdSe), with all other reaction conditions held constant. In addition to equilibrium $|g_{sp-d}|$ values, Figure 3.2B plots Mn^{2+} concentrations (x in $Cd_{1-x}Mn_xSe$) determined by two independent methods: Analytically (ICP-AES), and *via* analysis of the exciton blue shift according to the known dependence of E_g on x in bulk $Cd_{1-x}Mn_xSe$,[40] extrapolated to the nanoscale.[25] The two measures of x agree well, and both also track the magnitude of $|g_{sp-d}|$ determined spectroscopically. The equilibrium values of x rise sharply with added Se^{2-} up to ~5 equivalents but then plateau at $x = 0.31 \pm 0.03$, at which point $|g_{sp-d}|$ also plateaus at ~26. The reaction thus exhibits two qualitatively different regimes: At low Se^{2-} concentration, diffusion doping is Se^{2-} limited, whereas at high Se^{2-} concentration x is limited by other factors (discussed below).

The data in Figures 3.1 and 3.2 demonstrate that this diffusion doping involves equilibrium control over nanocrystal compositions, *i.e.*, compositions controlled thermodynamically, rather than kinetically.[25] As an equilibrium process, we hypothesized

that this chemistry should be reversible. Specifically, under competition conditions, Cd^{2+} should out-compete Mn^{2+} for lattice Se^{2-} in $Cd_{1-x}Mn_xSe$ nanocrystals because of the highly favorable Cd^{2+}–Se^{2-} thermodynamics relative to Mn^{2+}–Se^{2-} (bond energies: ~310 vs ~201 kJ/mol at 298 K[41]). To test this hypothesis, a diffusion-doping reaction was performed to incorporate Mn^{2+} into CdSe NCs under Se^{2-}-limited conditions (0.5 Se^{2-}:CdSe) in the presence of a large excess of Mn^{2+}, as described above. After equilibration, Cd^{2+} was then added to the same reaction mixture (without introducing additional Se^{2-}, T = 280 ºC, see Section 3.6.1). Figure 3.3A shows absorption spectra of aliquots taken from this reaction. During diffusion doping, the first exciton blue-shifts by 51 meV (from 2.076 to 2.127 eV) at equilibrium, consistent with Mn^{2+} incorporation to reach x ~0.13 (Figure 3.2B).[25] Upon Cd^{2+} addition, the first exciton red-shifts again by 115 meV to 2.012 eV at equilibrium, overshooting its original energy. The change in exciton energies from before diffusion doping to after cation exchange suggests that the nanocrystals have grown from d ~4.4 to ~5.4 nm, again indicating x ~0.13 in the intervening $Cd_{1-x}Mn_xSe$ nanocrystals. These results illustrate that diffusion doping proceeds by *addition* of Mn^{2+}–Se^{2-} units, and hence involves nanocrystal growth in accordance with the number of Mn^{2+} ions added, but subsequent nanocrystal purification proceeds by cation *exchange* with no net change in the total number of cations. TEM analysis of aliquots removed from a similar reaction confirms that the nanocrystals grow during diffusion doping but remain nearly the same size after cation exchange (see Appendix B).

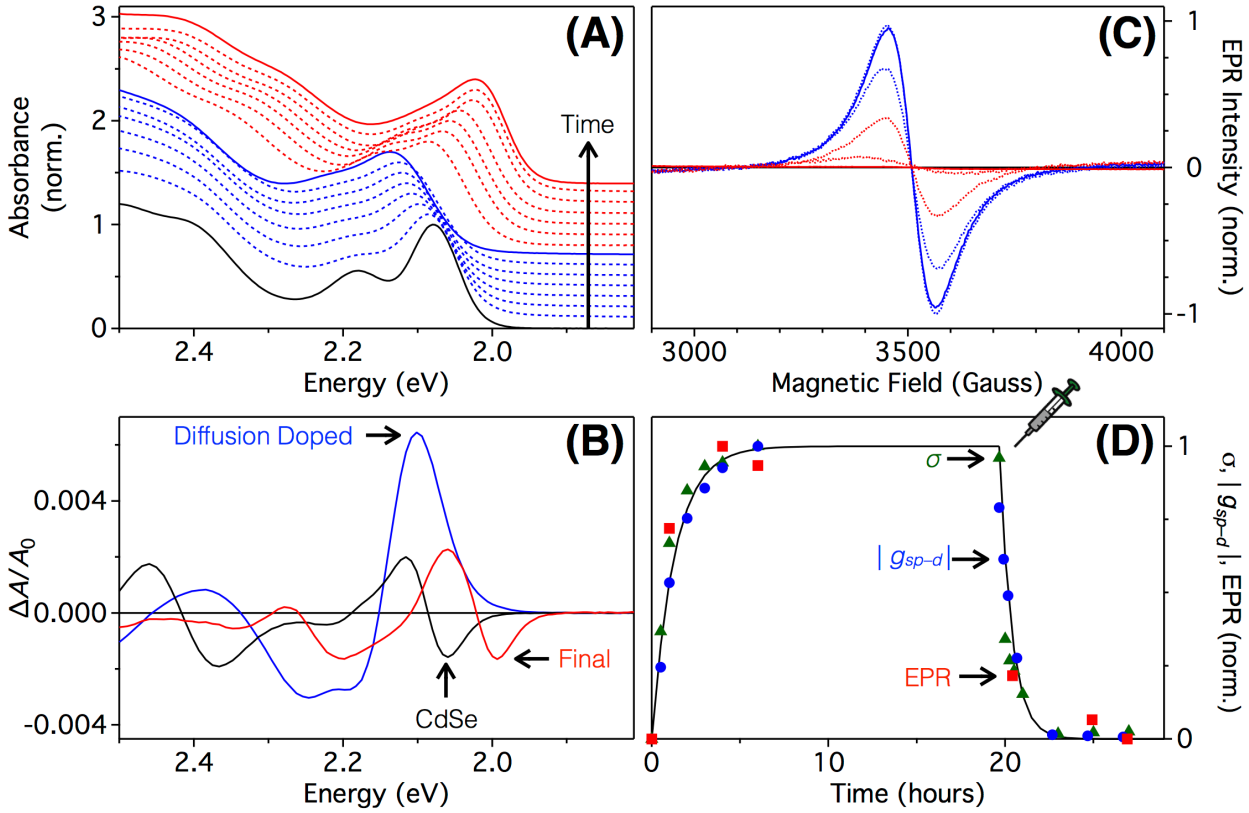

Figure 3.3. **(A)** Room-temperature electronic absorption spectra of undoped d = 4.4 nm CdSe NCs (black) diffusion doped at 280 ºC with 0.5:1:1 Se^{2-}:Mn^{2+}:CdSe (blue traces) and purified at 280 ºC by cation exchange (red traces), triggered after 20 hours by injection of cadmium oleate (1.92 Cd^{2+} added per Mn^{2+} dopant). **(B)** Room-temperature MCD spectra of undoped CdSe (black), diffusion doped $Cd_{1-x}Mn_xSe$ after 20 hours (blue) and the same NCs after 6 hours of cation exchange (red). Spectra for additional aliquots omitted for clarity. **(C)** EPR spectra of representative aliquots, with solid line spectra matching the times of the MCD spectra shown in panel B. **(D)** Normalized Gaussian widths (σ) of the first excitonic absorption (green triangles, from analysis of panel A data), $|g_{sp-d}|$ (blue circles, from analysis of panel B data), and quantitative integrated EPR intensities (red squares, from analysis of panel C data), over the course of diffusion doping and cation exchange. The black lines are from global single exponential fits to the spectroscopic signatures of diffusion doping and cation exchange. The syringe cartoon indicates when Cd^{2+} was added to the reaction mixture.

In addition to these energy shifts, the first exciton's Gaussian line width increases from σ = 44 to 62 meV during diffusion doping, and remarkably, it decreases back to 44 meV again after cation exchange. The increase in σ with Mn^{2+} doping is thus not a result of Ostwald ripening, but instead it reflects additional inhomogeneous broadening in the $Cd_{1-x}Mn_xSe$ NCs, presumably coming from statistical and spatial Mn^{2+} distributions within the NC ensemble, as well as Mn^{2+} magnetic fluctuations.[42]

Finally, Figure 3.3B plots MCD spectra of the initial CdSe NCs, the equilibrium diffusion-doped $Cd_{1-x}Mn_xSe$ NCs, and the same nanocrystals equilibrated again after Cd^{2+} addition. The first excitonic MCD feature inverts and grows in intensity during diffusion doping, but diminishes again after Cd^{2+} addition, reverting to a signal consistent with undoped CdSe NCs. These data demonstrate that Cd^{2+} addition to the reaction mixture under diffusion-doping conditions indeed reverses the Mn^{2+} doping, purifying the nanocrystals despite the presence of a large excess of solvated Mn^{2+}.

The absorption and MCD spectroscopic probes of Mn^{2+} doping are both selective for Mn^{2+} ions within the NC cores, where Mn^{2+}–exciton interactions are strong. Furthermore, analysis of these data yields the effective concentrations that would be required to generate the same spectroscopic observables in the limit of uniform distribution of Mn^{2+} throughout the entire NC volume. It is conceivable that these techniques might not faithfully report on the total Mn^{2+} content of the nanocrystals, for example if Mn^{2+} were concentrated near the nanocrystal surfaces. For this reason, EPR spectroscopy was also used to follow the progress of the same diffusion doping and purification reaction described above. EPR spectroscopy provides a measure of the paramagnetic Mn^{2+}

content, independent of Mn^{2+} position within the NCs. A limitation of this EPR experiment is that it can be performed only after thorough washing and resuspension of the NCs to remove the excess solvated Mn^{2+} because this procedure also likely removes surface-bound Mn^{2+}. Nevertheless, this experiment provides a valuable independent measure of Mn^{2+} content. Figure 3.3C plots EPR spectra of the same aliquots described above, and shows intensification of a broad g = 2 feature consistent with Mn^{2+} in $Cd_{1-x}Mn_xSe$ nanocrystals during diffusion doping.[25] The Mn^{2+} hyperfine structure is not resolved because of the high Mn^{2+} concentrations involved (x_{max} ~0.13). The EPR intensity diminishes and disappears after addition of Cd^{2+}, consistent with full expulsion of Mn^{2+} from the nanocrystals.

Figure 3.3D summarizes the complete collection of data from this entire set of measurements, plotting the evolution of σ, $|g_{sp-d}|$, and the integrated EPR intensity. For convenience of comparison, each metric has been normalized within its undoped (0) and maximum diffusion-doped (1) range. All three spectroscopic signatures follow the same trends during the diffusion-doping and purification steps.

In the purification step of the experiment described in Figure 3.3, we added ~1.9 equivalents of Cd^{2+} per lattice Mn^{2+}. To investigate the lattice purification chemistry more broadly, a series of reactions was performed under identical conditions but with different amounts of added Cd^{2+}. Figure 3.4A plots $|g_{sp-d}|$ *vs* reaction time for several of these reactions. The black trace reproduces the data from Figure 3.3. The green trace shows that adding a sub-stoichiometric amount of Cd^{2+} (0.24 Cd^{2+} per lattice Mn^{2+}) yields similar equilibration kinetics but a smaller decrease in $|g_{sp-d}|$, terminating at $|g_{sp-d}|$ ~ 40% of

its initial value, *i.e.*, part but not all of the Mn^{2+} is removed by a sub-stoichiometric Cd^{2+} addition. The blue traces show data from a similar experiment involving two sequential injections of 0.6 Cd^{2+} equivalents each, separated by 4 hours. After the first Cd^{2+} addition, $|g_{sp-d}|$ decreases and equilibrates at ~35% of its initial value. After the second addition of Cd^{2+}, $|g_{sp-d}|$ decreases again and equilibrates at 0. A control experiment in which oleic acid and ODE were added without Cd^{2+} caused no meaningful change in g_{sp-d}. Use of Na^{+} instead of Cd^{2+} also does not change g_{Exc}. These control experiments demonstrate that it is indeed the Cd^{2+} addition that causes nanocrystal purification of Mn^{2+}, consistent with the proposed cation-exchange process.

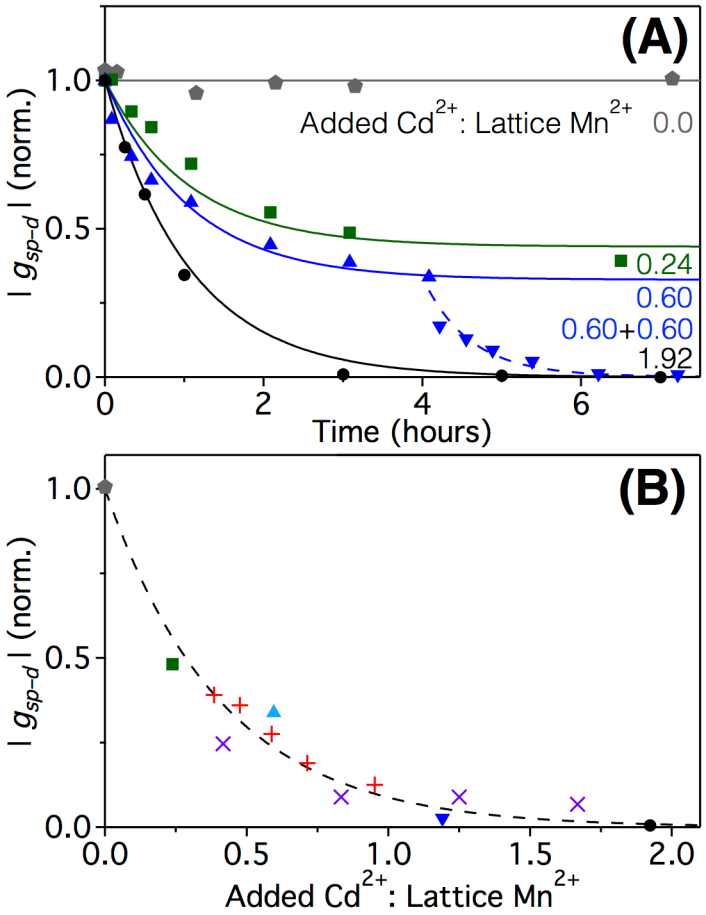

Figure 3.4. **(A)** Time evolution of $|g_{sp-d}|$ during cation exchange of equilibrated, diffusion-doped $Cd_{1-x}Mn_xSe$ nanocrystals held at 280 ºC. In grey pentagons, no Cd^{2+} was added. In green squares and black circles, the Cd^{2+} (0.24 and 1.92 added Cd^{2+}:lattice Mn^{2+}, respectively) was added all at once. In blue triangles, 1.20 added Cd^{2+}:lattice Mn^{2+} was divided equally into two injections and the NCs were allowed to equilibrate after each injection of 0.60 added Cd^{2+}:lattice Mn^{2+}. Solid lines are a global fit to a single exponential with t_{eff} = 1.1 hours. The dashed curve is a guide for the eye. **(B)** Dependence of the extent of purification by cation exchange on added Cd^{2+}, monitored as $|g_{sp-d}|$ (normalized) of equilibrated samples after cation exchange from diffusion-doped NCs, plotted as a function of the number of equivalents of Cd^{2+} added relative to the amount of Mn^{2+} in the diffusion-doped NCs. The red "+" and purple "X" markers are from successive titrations of Cd^{2+} in two separate reaction mixtures, allowing equilibration before each subsequent titration. Each other color/symbol pair represents the equilibrium value obtained from Figure 3.4A. The dashed curve is a guide for the eye. Electronic absorption and MCD spectra of representative reaction aliquots are provided in Appendix B.

Interestingly, the purification kinetics are similar for all added Cd^{2+} concentrations. The solid curves in Figure 3.4A represent the results of a global fit of all reaction kinetics to a single exponential function, which yields τ_{eff} = 1.1 hours. Even at its slightly lower temperature (280 ºC vs 300 ºC), this purification chemistry is marginally faster than the diffusion doping (τ_{eff} = 1.3 hours, Figure 3.2), but both are remarkably slow. The similarity of the diffusion-doping and cation-exchange reaction rates is consistent with both kinetics being determined by very slow Mn^{2+} diffusion through the CdSe NC lattice.

Figure 3.4B summarizes equilibrium values of $|g_{sp-d}|$ measured after equilibration of several different NC purification reactions under the same conditions as in Figure 3.3, plotted *vs* equivalents of added Cd^{2+}. The data are consistent with $|g_{sp-d}|$ returning to 0 at ~1 equivalent of Cd^{2+} per lattice Mn^{2+}. The curvature of these data is interesting, however, and not fully understood. Initially, the slope of the curve exceeds 1 Mn^{2+} lost from the NC per added Cd^{2+}, suggesting that Cd^{2+} addition may initiate diffusion of more than one Mn^{2+}, perhaps by aiding the formation of a steady-state concentration of Frenkel defects. At the other end of the curve, however, the slope decreases below 1 Mn^{2+} lost from the NC per added Cd^{2+}, indicating that removal of the last Mn^{2+} ions from the NCs requires some excess of Cd^{2+}. These trends may in part reflect statistical distributions of both Mn^{2+} and added Cd^{2+} over the ensemble of nanocrystals, or they could reflect a changing ratio of equilibrium constants for Mn^{2+}–Se^{2-} *vs* Cd^{2+}–Se^{2-} bond formation. Addition of even more Cd^{2+} (up to 12 equivalents, see Appendix B) does not cause any further change in the absorption or MCD spectra, indicating that further Cd^{2+} is not incorporated into the nanocrystals after the Mn^{2+} has been replaced.

3.4 Discussion

Scheme 3.1 summarizes the diffusion-doping and cation-exchange chemistries reported here. In the presence of a large excess of solvated Mn^{2+}, nanocrystal doping with Mn^{2+} is gated by the addition of Se^{2-} to the reaction mixture. The quantity of added Se^{2-} tunes the composition of the resulting $Cd_{1-x}Mn_xSe$ nanocrystals by dictating how much Mn^{2+} is transferred from solution to the nanocrystal at equilibrium (Equation 3.3a, Se^{2-}-limited regime). The nanocrystals' composition in turn tunes their corresponding magneto-optical properties. Because diffusion doping involves addition of Mn^{2+} + Se^{2-} to the nanocrystal lattice, the nanocrystal diameter increases during diffusion doping. After diffusion doping, the addition of Cd^{2+} to the reaction mixture under the same conditions triggers cation exchange, expelling Mn^{2+} ions from the lattice and replacing them with the added Cd^{2+} ions (Equation 3.3b). The cation-exchange reaction preserves the total number of cations and anions within the nanocrystal but tunes the composition. Both reactions are equilibrium processes.

$$\text{Diffusion doping: } CdSe + yMn^{2+} + ySe^{2-} \rightleftharpoons CdMn_ySe_{1+y}\ (= Cd_{1-x}Mn_xSe) \quad (3.3a)$$

$$\text{Cation exchange: } CdMn_ySe_{1+y} + yCd^{2+} \rightleftharpoons Cd_{1+y}Se_{1+y}\ (= CdSe) + yMn^{2+} \quad (3.3b)$$

Scheme 3.1. Mn^{2+} diffusion doping of CdSe nanocrystals, and Mn^{2+} expulsion from $Cd_{1-x}Mn_xSe$ nanocrystals *via* cation exchange with Cd^{2+}.

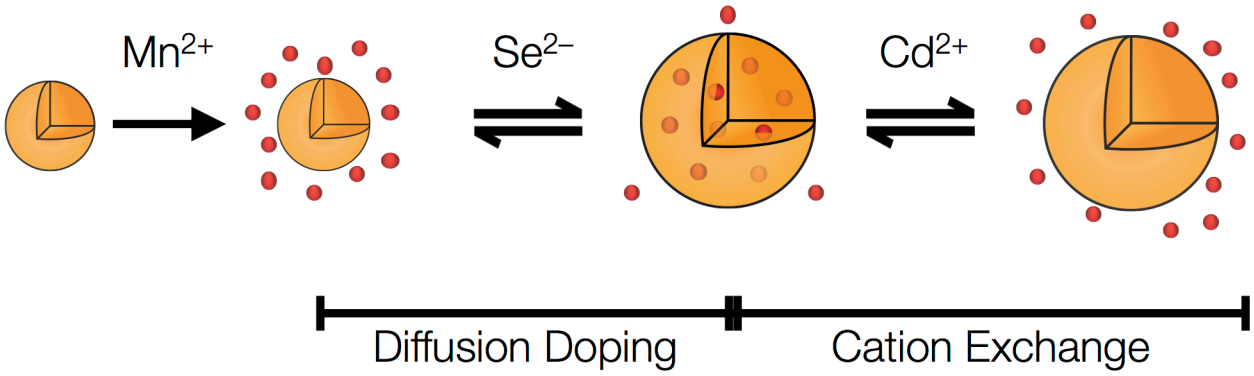

With small quantities of added Se^{2-}, x in the final $Cd_{1-x}Mn_xSe$ NCs is Se^{2-} limited. The $Cd_{1-x}Mn_xSe$ equilibrium composition thus changes in direct proportion to the amount of added Se^{2-}. Above x ~0.31, however, x becomes independent of added Se^{2-}. In this regime, no further precipitation of Mn^{2+} occurs in any form, even when a 25-fold excess of Se^{2-} is introduced. Curiously, the slope of x vs added Se^{2-} in Figure 3.2B is significantly smaller than expected from the stoichiometry of Equation 3.3a, suggesting that a large fraction of the added Se^{2-} is somehow unreactive. We speculate that this Se^{2-} might be absorbed in the form of soluble $(Mn–Se)_n$ clusters. This lost Se^{2-} does not reappear upon addition of excess Cd^{2+}, however, perhaps suggesting that it is unreactive for another reason such as incomplete *in situ* reduction of the metallic Se precursor. Despite extensive efforts, we have found no evidence of MnSe precipitation under any of our reaction conditions (in any crystallographic or amorphous phase), even in control experiments performed in the absence of CdSe nanocrystals. This latter observation is interpreted as indicating that MnSe is too soluble to precipitate under these conditions, tentatively attributed to the presence of coordinating amines and oleic acid in our reaction mixtures. Given the high solubility of MnSe and the insolubility of CdSe under our reaction

conditions, it follows that there must exist some threshold value of x above which $Cd_{1-x}Mn_xSe$ also cannot be precipitated. The experimental data indicate that this solubility limit occurs at x_{max} ~0.31 under our reaction conditions. The equilibrium compositions thus transition from being Se^{2-}-limited to being solubility-limited as the amount of added Se^{2-} is increased.

Scheme 3.2A summarizes these observations by plotting the free energy of formation (ΔG_f) for the $Cd_{1-x}Mn_xSe$ nanocrystals *vs* the composition parameter x. Up to x ~0.31, $\Delta G_f < 0$ under our reaction conditions, but for $x >$ ~0.31, $\Delta G_f > 0$, and consequently nanocrystals with $x > x_{max} = 0.31$ are not observed. Because of the insolubility of crystallites with $x \leq x_{max}$, $Cd_{1-x}Mn_xSe$ nanocrystals heated in the presence of excess Se^{2-} and excess Mn^{2+} reach but do not exceed x_{max}. It follows that the equilibrium concentration of solvated Se^{2-} is small in the Se^{2-}-limited regime, but grows in proportion to added Se^{2-} in the solubility-limited regime (Scheme 3.2B). Similarly, the equilibrium concentration of solvated Mn^{2+} decreases linearly with added Se^{2-} in the Se^{2-}-limited regime, but becomes independent of added Se^{2-} in the solubility-limited regime, mirroring the Mn^{2+} uptake by the nanocrystals. Under our experimental conditions, ~55% of all Mn^{2+} remains in solution in the solubility-limited regime, after maximum diffusion doping. The specific value of x_{max} obviously must depend on the specific reaction conditions, *e.g.*, temperature, ligand identity and concentration, Mn^{2+} concentration, and possibly even nanocrystal size or faceting, but a thorough exploration of this vast parameter space was considered beyond the scope of the present investigation. Nevertheless, it is interesting to note that our x_{max} lies only a little below the analogous limit for crystals grown from the ionic melt (x_{max} ~0.4 at

300 °C, extrapolated from the CdSe–MnSe phase diagram[40]), where there is no solvent and there are no ligands to stabilize Mn^{2+} outside of the growing CdSe-based crystal. This comparison illustrates the dependence of x_{max} on the chemical potentials of the ions in the liquid phase, and simultaneously emphasizes the very high Mn^{2+} content achievable by this nanocrystal diffusion-doping method.

Scheme 3.2. $Cd_{1-x}Mn_xSe$ lattice formation energies and the normalized concentrations of reaction components plotted *vs* composition and added Se^{2-}.

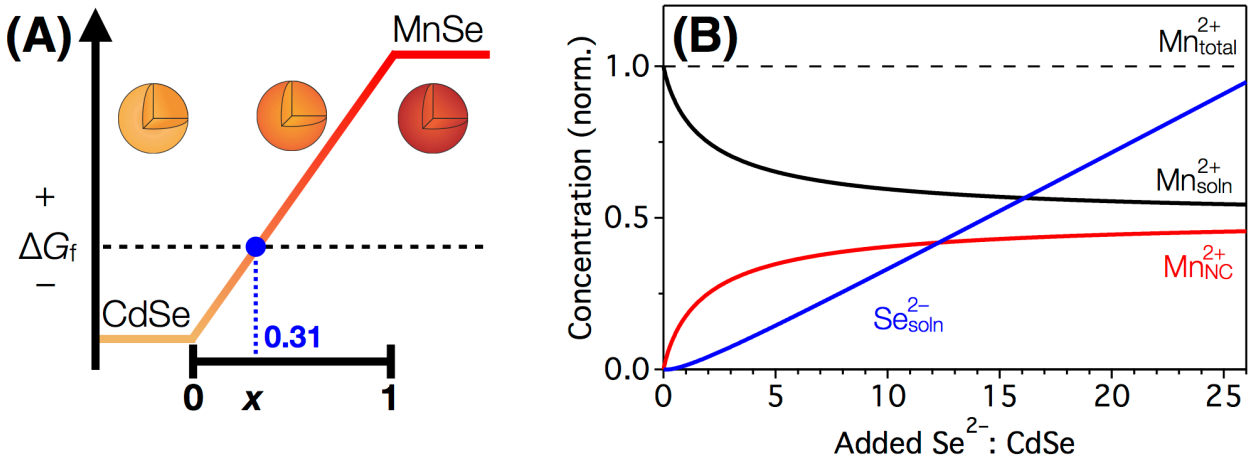

Microscopically, the role of the added Se^{2-} during diffusion doping is two-fold. The addition of Se^{2-} to the nanocrystal surfaces is formally equivalent to introducing surface cation vacancies (Scheme 3.3), which lowers the chemical potential (μ_{Mn}) of lattice Mn^{2+} relative to solvated Mn^{2+}, allowing it to become thermodynamically favorable for Mn^{2+} from solution to bind to the surface Se^{2-} and become part of the nanocrystal lattice. The cation vacancies formed upon Se^{2-} addition also aid cation diffusion within the lattice, which is necessary for scrambling Mn^{2+} positions to reach the randomized equilibrium $Cd_{1-x}Mn_xSe$ compositions observed experimentally. The diffusivity of Mn^{2+} in bulk II–VI semiconductors is strongly enhanced when the lattice is non-stoichiometric.[43] Non-stoichiometries

accelerate cation diffusion by increasing the concentrations of Frenkel-type cation vacancies, which play a central role in the Mn^{2+} diffusion mechanism. In nanocrystals, the surface cation vacancies (excess surface Se^{2-} anions) can be filled by sub-surface cations, thereby generating lattice vacancies (V_{Cd}, Scheme 3.3) that accelerate cation diffusion throughout the internal nanocrystal volume, for example *via* a cation vacancy-interstitial (Frank-Turnbull) mechanism.[44-46] The correlation between magneto-optical intensities and analytical Mn^{2+} concentrations indicates that Mn^{2+} enters the lattice randomly, and not *via* a preferred sector, a discrete shell, or layer-by-layer substitution along specific crystallographic planes, as often observed in cation-exchange reactions.[5-8,47]

Scheme 3.3. Microscopic contributions to nanocrystal diffusion doping.

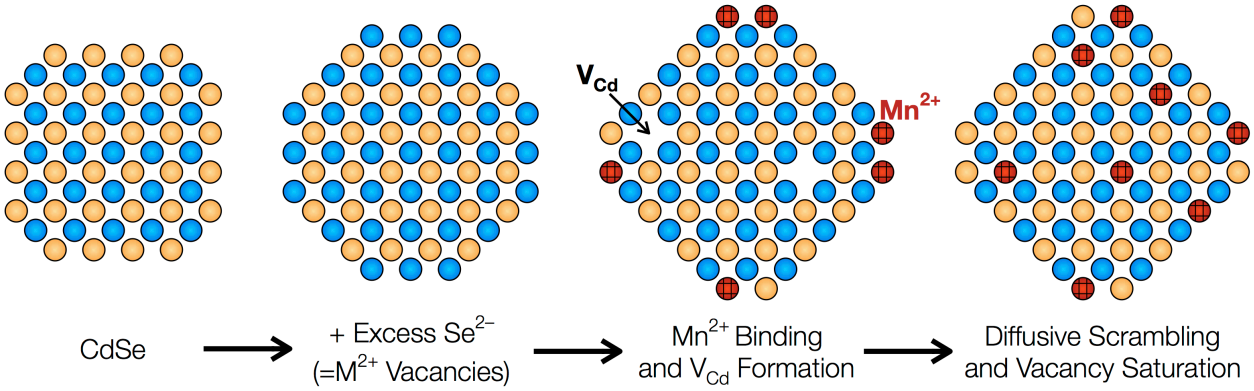

Under the same reaction conditions as used for diffusion doping, addition of Cd^{2+} removes Mn^{2+} from the $Cd_{1-x}Mn_xSe$ NCs. When Cd^{2+} is added, it is thermodynamically able to outcompete Mn^{2+} for its coordinated Se^{2-} anions, which has the effect of raising μ_{Mn} in the lattice relative to μ_{Mn} in solution and thereby driving Mn^{2+} into solution. Analogous to composition tuning during diffusion doping *via* added Se^{2-}, nanocrystal compositions can be finely tuned *via* the amount of added Cd^{2+} during cation exchange. When added

approximately stoichiometrically, Cd^{2+} displaces all Mn^{2+} from the nanocrystals. Unlike many other nanocrystal cation-exchange processes, however, the exchange of Cd^{2+} for Mn^{2+} is extremely slow, requiring several hours at 280 ºC instead of seconds or less at room temperature.[3,48] To prevent Ostwald ripening during this slow cation exchange, μ_{Cd} must remain substantially lower in the lattice than in solution, a condition achieved through the presence of excess solvated Mn^{2+}.

This extremely slow cation exchange is interpreted as reflecting specifically a very slow diffusion of Mn^{2+} in CdSe, even in the nanocrystalline form. In stoichiometric Mn^{2+} δ-doped CdTe wafers, Mn^{2+} diffusion measured between 420 and 530 ºC shows Arrhenius behavior described by a temperature-independent Mn^{2+} diffusion constant (D_0) of 1.7×10^{-6} cm^2/s and an activation energy of E_A = 1.35 eV.[43] Extrapolation of these data down to our reaction temperature of 280 ºC suggests that Mn^{2+} should require ~22 hours to diffuse 2.7 nm, the average radius of our nanocrystals. By some measures of bulk Mn^{2+} diffusivity,[49] this diffusion should even take an order of magnitude longer. Although slow, the data in Figure 3.4 thus suggest diffusivities in the nanocrystals that still exceed those in bulk by at least an order of magnitude and possibly more, consistent with the general notion of enhanced ion diffusion in nanocrystals.[3,46] Although the precise microscopic origins of this enhancement are not yet clear, and many possible explanations exist invoking surface nonstoichiometries or interfacial strain, it is undoubtedly associated with surface proximity; even in bulk, accelerated cation diffusion near surfaces appears to be a general phenomenon.[43] Notably, the Mn^{2+} in- and out-diffusion kinetics do not differ markedly from one another in our experiments (Figure 3.3D), suggesting a relatively narrow

range of Mn^{2+} diffusivities even with the different surface chemistries of these two processes. With kinetic data of the types shown in Figures 3.2 and 3.4 now available for the Mn^{2+} diffusion-doping and cation-exchange reactions discussed here, modeling studies, perhaps in conjunction with atomistic reaction-coordinate calculations, should make possible an even deeper understanding of the microscopic diffusion pathways involved in these interesting chemistries. Further work in this direction is presently underway.

3.5 Conclusion

Diffusion doping allows nanocrystals to achieve their thermodynamically favored compositions without reaching their thermodynamically favored shapes or sizes.[25] Here, we have investigated in detail the model system of $Cd_{1-x}Mn_xSe$ nanocrystals. A Se^{2-}-limited reaction regime is identified, in which Mn^{2+} diffusion into CdSe nanocrystals is gated by the addition of excess Se^{2-}. In this regime, the Mn^{2+} content (x) at equilibrium is proportional to the amount of added Se^{2-}. A second, solubility-limited regime is also identified, which occurs for large values of added Se^{2-}. In this regime, x at equilibrium is limited to x_{max} ~0.31 by the thermodynamic instability of $Cd_{1-x}Mn_xSe$ nanocrystals that have $x > x_{max}$. Consequently, x at equilibrium is independent of the amount of added Se^{2-} in this regime. After diffusion doping, Mn^{2+} in-diffusion can be reversed by cation exchange with Cd^{2+}, effectively purifying $Cd_{1-x}Mn_xSe$ nanocrystals back to CdSe nanocrystals. Under these reaction conditions, the equilibrium compositions of $Cd_{1-x}Mn_xSe$ nanocrystals can therefore

be tuned continuously from $0 \leq x \leq \sim 0.31$ in two ways: (*i*) during diffusion doping by changing the amount of added Se^{2-}, or (*ii*) during cation exchange by changing the amount of added Cd^{2+}. Combining diffusion doping and cation exchange methodologies thus leads to unprecedented composition control in $Cd_{1-x}Mn_xSe$ NCs. All of these chemistries are performed under conditions in which Ostwald ripening has been suppressed, allowing this composition control in pre-formed high-quality colloidal CdSe nanocrystals prepared separately by independent state-of-the-art synthetic methods. The advances in compositional tuning reported here enable further studies of microscopic cation diffusion processes and of advanced dopant-dependent physical properties in semiconductor nanocrystals, which in turn will enable development of new high-quality colloidal doped nanocrystals for target applications ranging from solar energy conversion to spintronics.

3.6 Experimental Methods

3.6.1 Synthesis

Oleate-capped seed CdSe nanocrystals were prepared by methods adapted from refs. 36 and 50-52, as detailed in ref. 25. Typically, diffusion doping of CdSe nanocrystals with Mn^{2+} was performed as follows: CdSe nanocrystals (~0.1 mmol in terms of CdSe units) were dried and added to 1 mL of octadecene (ODE), 1 mL of tributylphosphine (TBP), and the desired amount (0-2.5 mmol) of selenium powder, in a septum-capped 5 mL round-bottom flask in a nitrogen-atmosphere glovebox. Separately, 12 g of ODE, 0.5 g of oleic acid (OA) and 1 g of hexadecylamine (HDA) were added to a 100 mL three-neck round-bottom flask. Following heating of the latter solution for 60 minutes at 100 °C under vacuum, 0.025 g (0.1 mmol) of $Mn(OAc)_2 \bullet 4H_2O$ was added against a nitrogen

overpressure. The flask was then placed under vacuum to remove acetic acid and water and then heated under nitrogen to 300 °C, at which point the CdSe/selenide solution was injected rapidly. This reaction mixture was held at 300 °C and allowed to equilibrate for between a few seconds and one day. In NC purification experiments, diffusion doping was performed at 280 ºC for 20-24 hours. A solution of cadmium oleate (0-0.25 mmol) dissolved in 2 mL of ODE was then dripped in to the flask and the system was allowed to re-equilibrate for up to one day at 280 ºC. After equilibrium was reached, the solution was cooled to room temperature and washed by repeated suspensions in toluene and flocculation with ethanol. In these experiments, no freshly nucleated CdSe or MnSe particles were ever detected by absorption, luminescence, TEM, or XRD measurements.

3.6.2 Physical Characterization

Relative atomic concentrations were determined by analysis of dried nanocrystals digested in ultrapure nitric acid (EMD Chemicals) using inductively coupled plasma atomic emission spectrometry (ICP-AES; PerkinElmer). CW electron paramagnetic resonance (EPR) experiments were performed on equally concentrated colloidal toluene suspensions of nanocrystals using an X-band Bruker EMX spectrometer. Room-temperature electronic absorption spectra were collected for colloidal toluene suspensions of nanocrystals in a 0.1 cm path length cuvette using a Cary 500 spectrophotometer. Room-temperature magnetic circular dichroism (MCD) spectra were collected on the same cuvette placed in a 1.5 T electromagnet oriented in the Faraday configuration. MCD spectra were collected using an Aviv 40DS spectropolarimeter. The differential absorption collected in the MCD experiment is reported as $\Delta A = A_L - A_R$, where A_L and A_R refer to the absorption of left and right circularly polarized photons in the sign convention of Piepho and Schatz.[53-54] From these data, values of ΔE_{Zeeman} and g_{Exc} can be obtained.[13,33,40]

3.7 Appendix B

Additional absorption and MCD spectra, TEM data.

3.8 Acknowledgments

This research was funded by the US National Science Foundation (DMR-1206221 and DMR-1505901 to D.R.G.). C.J.B. acknowledges funding from a Clean Energy Institute Graduate Research Fellowship. P.C. acknowledges the Swiss National Science Foundation for an Early Postdoc Mobility Fellowship (P2GEP2_148356).

3.9 References

1. Moon, G. D.; Ko, S.; Min, Y.; Zeng, J.; Xia, Y.; Jeong, U., Chemical Transformations of Nanostructured Materials. *Nano Today* **2011**, *6*, 186-203.
2. Fayette, M.; Robinson, R. D., Chemical Transformations of Nanomaterials for Energy Applications. *J. Mater. Chem. A* **2014**, *2*, 5965-5978.
3. Son, D. H.; Hughes, S. M.; Yin, Y.; Alivisatos, A. P., Cation Exchange Reactions in Ionic Nanocrystals. *Science* **2004**, *306*, 1009-1012.
4. Donegá, C. d. M., Synthesis and Properties of Colloidal Heteronanocrystals. *Chem. Soc. Rev.* **2011**, *40*, 1512-1546.
5. Li, H.; Zanella, M.; Genovese, A.; Povia, M.; Falqui, A.; Giannini, C.; Manna, L., Sequential Cation Exchange in Nanocrystals: Preservation of Crystal Phase and Formation of Metastable Phases. *Nano Lett.* **2011**, *11*, 4964-4970.
6. Gupta, S.; Kershaw, S. V.; Rogach, A. L., 25th Anniversary Article: Ion Exchange in Colloidal Nanocrystals. *Adv. Mater.* **2013**, *25*, 6923-6944.
7. Beberwyck, B. J.; Surendranath, Y.; Alivisatos, A. P., Cation Exchange: A Versatile Tool for Nanomaterials Synthesis. *J. Phys. Chem. C* **2013**, *117*, 19759–19770.
8. Rivest, J. B.; Jain, P. K., Cation Exchange on the Nanoscale: An Emerging Technique for New Material Synthesis, Device Fabrication, and Chemical Sensing. *Chem. Soc. Rev.* **2013**, *42*, 89-96.
9. Hodges, J. M.; Kletetschka, K.; Fenton, J. L.; Read, C. G.; Schaak, R. E., Sequential Anion and Cation Exchange Reactions for Complete Material Transformations of Nanoparticles with Morphological Retention. *Angew. Chem., Int. Ed.* **2015**, *54*, 8567-8567.
10. Nedelcu, G.; Protesescu, L.; Yakunin, S.; Bodnarchuk, M. I.; Grotevent, M. J.; Kovalenko, M. V., Fast Anion-Exchange in Highly Luminescent Nanocrystals of Cesium Lead Halide Perovskites ($CsPbX_3$, X = Cl, Br, I). *Nano Lett.* **2015**, *15*, 5635-5640.
11. Bryan, J. D.; Gamelin, D. R., Doped Semiconductor Nanocrystals: Synthesis, Characterization, Physical Properties, and Applications. *Prog. Inorg. Chem.* **2005**, *54*, 47-126.
12. Norris, D. J.; Efros, A. L.; Erwin, S. C., Doped Nanocrystals. *Science* **2008**, *319*, 1776-1779.
13. Beaulac, R.; Ochsenbein, S. T.; Gamelin, D. R. Colloidal Transition-Metal-Doped Quantum Dots. In *Nanocrystal Quantum Dots*, 2nd ed.; Klimov, V. I., Ed.; CRC Press: Boca Raton, FL, 2010; pp 397-453.
14. Mocatta, D.; Cohen, G.; Schattner, J.; Millo, O.; Rabani, E.; Banin, U., Heavily Doped Semiconductor Nanocrystal Quantum Dots. *Science* **2011**, *332*, 77-81.
15. Buonsanti, R.; Milliron, D. J., Chemistry of Doped Colloidal Nanocrystals. *Chem. Mater.* **2013**, *25*, 1305-1317.

16. Schimpf, A. M.; Knowles, K. E.; Carroll, G. M.; Gamelin, D. R., Electronic Doping and Redox-Potential Tuning in Colloidal Semiconductor Nanocrystals. *Acc. Chem. Res.* **2015**, *48*, 1929−1937.
17. Erickson, C. S.; Bradshaw, L. R.; McDowall, S.; Gilbertson, J. D.; Gamelin, D. R.; Patrick, D. L., Zero-Reabsorption Doped-Nanocrystal Solar Concentrators. *ACS Nano* **2014**, *8*, 3461-3467.
18. Bradshaw, L. R.; Knowles, K. E.; McDowall, S.; Gamelin, D. R., Nanocrystals for Luminescent Solar Concentrators. *Nano Lett.* **2015**, *15*, 1315-1323.
19. McLaurin, E. J.; Bradshaw, L. R.; Gamelin, D. R., Dual-Emitting Nanoscale Temperature Sensors. *Chem. Mater.* **2013**, *25*, 1283-1292.
20. Wang, F.; Banerjee, D.; Liu, Y.; Chen, X.; Liu, X., Upconversion Nanoparticles in Biological Labeling, Imaging, and Therapy. *Analyst* **2010**, *135*, 1839-1854.
21. Lounis, S. D.; Runnerstrom, E. L.; Llordés, A.; Milliron, D. J., Defect Chemistry and Plasmon Physics of Colloidal Metal Oxide Nanocrystals. *J. Phys. Chem. Lett.* **2014**, *5*, 1564-1574.
22. Scotognella, F.; Della Valle, G.; Srimath Kandada, A.; Zavelani-Rossi, M.; Longhi, S.; Lanzani, G.; Tassone, F., Plasmonics in Heavily-Doped Semiconductor Nanocrystals. *Eur. Phys. J. B* **2013**, *86*, 1-13.
23. Routzahn, A. L.; White, S. L.; Fong, L.-K.; Jain, P. K., Plasmonics with Doped Quantum Dots. *Isr. J. Chem.* **2012**, *52*, 983-991.
24. Beaulac, R.; Archer, P. I.; Ochsenbein, S. T.; Gamelin, D. R., Mn^{2+}-Doped CdSe Quantum Dots: New Inorganic Materials for Spin-Electronics and Spin-Photonics. *Adv. Funct. Mater.* **2008**, *18*, 3873-3891.
25. Vlaskin, V. A.; Barrows, C. J.; Erickson, C. S.; Gamelin, D. R., Nanocrystal Diffusion Doping. *J. Am. Chem. Soc.* **2013**, *135*, 14380−14389.
26. Mikulec, F. V.; Kuno, M.; Bennati, M.; Hall, D. A.; Griffin, R. G.; Bawendi, M. G., Organometallic Synthesis and Spectroscopic Characterization of Manganese-Doped CdSe Nanocrystals. *J. Am. Chem. Soc.* **2000**, *122*, 2532-2540.
27. Magana, D.; Perera, S. C.; Harter, A. G.; Dalal, N. S.; Strouse, G. F., Switching-on Superparamagnetism in Mn/CdSe Quantum Dots. *J. Am. Chem. Soc.* **2006**, *128*, 2931-2939.
28. Archer, P. I.; Santangelo, S. A.; Gamelin, D. R., Inorganic Cluster Syntheses of TM^{2+}-Doped Quantum Dots (CdSe, CdS, CdSe/CdS): Physical Property Dependence on Dopant Locale. *J. Am. Chem. Soc.* **2007**, *129*, 9808-9818.
29. Erwin, S. C.; Zu, L.; Haftel, M. I.; Efros, A. L.; Kennedy, T. A.; Norris, D. J., Doping Semiconductor Nanocrystals. *Nature* **2005**, *436*, 91-94.
30. Dalpian, G. M.; Chelikowsky, J. R., Self-Purification in Semiconductor Nanocrystals. *Phys. Rev. Lett.* **2006**, *96*, 226802.
31. Chen, D.; Viswanatha, R.; Ong, G. L.; Xie, R.; Balasubramaninan, M.; Peng, X., Temperature Dependence of "Elementary Processes" in Doping Semiconductor Nanocrystals. *J. Am. Chem. Soc.* **2009**, *131*, 9333-9339.
32. Fainblat, R.; Muckel, F.; Barrows, C. J.; Vlaskin, V. A.; Gamelin, D. R.; Bacher, G., Valence-Band Mixing Effects in the Upper-Excited-State Magneto-Optical

Responses of Colloidal Mn^{2+}-Doped CdSe Quantum Dots. *ACS Nano* **2014**, *8*, 12669−12675.
33. Barrows, C. J.; Vlaskin, V. A.; Gamelin, D. R., Absorption and Magnetic Circular Dichroism Analyses of Giant Zeeman Splittings in Diffusion-Doped Colloidal $Cd_{1-x}Mn_xSe$ Quantum Dots. *J. Phys. Chem. Lett.* **2015**, *6*, 3076-3081.
34. Nelson, H. D.; Bradshaw, L. R.; Barrows, C. J.; Vlaskin, V. A.; Gamelin, D. R., Picosecond Dynamics of Excitonic Magnetic Polarons in Colloidal Diffusion-Doped $Cd_{1-x}Mn_xSe$ Quantum Dots. *ACS Nano* **2015**, *9*, 11177-11191.
35. Liu, H.; Guyot-Sionnest, P., Magnetoresistance of Manganese-Doped Colloidal Quantum Dot Films. *J. Phys. Chem. C* **2015**, *119*, 14797–14804.
36. Yu, W. W.; Qu, L.; Guo, W.; Peng, X., Experimental Determination of the Extinction Coefficient of CdTe, CdSe, and CdS Nanocrystals. *Chem. Mater.* **2003**, *15*, 2854-2860.
37. Archer, P. I.; Santangelo, S. A.; Gamelin, D. R., Direct Observation of sp-d Exchange Interactions in Colloidal Mn^{2+}- and Co^{2+}-Doped CdSe Quantum Dots. *Nano Lett.* **2007**, *7*, 1037-1043.
38. Furdyna, J. K.; Kossut, J. *Diluted Magnetic Semiconductors*; Academic Press: New York, 1988; Vol. 25 of Semiconductors and Semimetals.
39. Shapira, Y.; Foner, S.; Ridgley, D. H.; Dwight, K.; Wold, A., Technical Saturation and Magnetization Steps in Diluted Magnetic Semiconductors: Predictions and Observations. *Phys. Rev. B: Condens. Matter Mater. Phys.* **1984**, *30*, 4021-4023.
40. Furdyna, J. K., Diluted Magnetic Semconductors. *J. Appl. Phys.* **1988**, *64*, R29-R64.
41. Luo, Y. R. *Comprehensive Handbook of Chemical Bond Energies*; CRC Press: Boca Raton, FL, 2007.
42. Bacher, G.; Maksimov, A. A.; Schömig, H.; Kulakovskii, V. D.; Welsch, M. K.; Forchel, A., Monitoring Statistical Magnetic Fluctuations on the Nanometer Scale. *Phys. Rev. Lett.* **2002**, *89*, 127201.
43. Barcz, A.; Karczewski, G.; Wojtowicz, T.; Kossut, J., Manganese Diffusion in MBE-Grown Cd(Mn)Te Structures. *J. Cryst. Growth* **1996**, *159*, 980-984.
44. Gösele, U. M., Fast Diffusion in Semiconductors. *Annu. Rev. Mater. Sci.* **1988**, *18*, 257-282.
45. Casavola, M.; van Huis, M. A.; Bals, S.; Lambert, K.; Hens, Z.; Vanmaekelbergh, D., Anisotropic Cation Exchange in PbSe/CdSe Core/Shell Nanocrystals of Different Geometry. *Chem. Mater.* **2012**, *24*, 294-302.
46. Groeneveld, E.; Witteman, L.; Lefferts, M.; Ke, X.; Bals, S.; Van Tendeloo, G.; de Mello Donega, C., Tailoring ZnSe-CdSe Colloidal Quantum Dots *via* Cation Exchange: From Core/Shell to Alloy Nanocrystals. *ACS Nano* **2013**, *7*, 7913-7930.
47. Sadtler, B.; Demchenko, D. O.; Zheng, H.; Hughes, S. M.; Merkle, M. G.; Dahmen, U.; Wang, L.-W.; Alivisatos, A. P., Selective Facet Reactivity during Cation Exchange in Cadmium Sulfide Nanorods. *J. Am. Chem. Soc.* **2009**, *131*, 5285-5293.
48. Chan, E. M.; Marcus, M. A.; Fakra, S.; ElNaggar, M.; Mathies, R. A.; Alivisatos, A. P., Millisecond Kinetics of Nanocrystal Cation Exchange Using Microfluidic X-ray Absorption Spectroscopy. *J. Phys. Chem. A* **2007**, *111*, 12210-12215.

49. Jamil, N. Y.; Shaw, D., The Diffusion of Mn in CdTe. *Semicond. Sci. Technol.* **1995**, *10*, 952-958.
50. Qu, L.; Peng, X., Control of Photoluminescence Properties of CdSe Nanocrystals in Growth. *J. Am. Chem. Soc.* **2002**, *124*, 2049-2055.
51. Carbone, L.; Nobile, C.; De Giorgi, M.; Della Sala, F.; Morello, G.; Pompa, P.; Hytch, M.; Snoeck, E.; Fiore, A.; Franchini, I. R.; Nadasan, M.; Silvestre, A. F.; Chiodo, L.; Kudera, S.; Cingolani, R.; Krahne, R.; Manna, L., Synthesis and Micrometer-Scale Assembly of Colloidal CdSe/CdS Nanorods Prepared by a Seeded Growth Approach. *Nano Lett.* **2007**, *7*, 2942-2950.
52. Yu, W. W.; Peng, X., Formation of High-Quality CdS and Other II-VI Semiconductor Nanocrystals in Noncoordinating Solvents: Tunable Reactivity of Monomers. *Angew. Chem., Int. Ed.* **2002**, *41*, 2368-2371.
53. Piepho, S. B.; Schatz, P. N. *Group Theory in Spectroscopy with Applications to Magnetic Circular Dichroism*; Wiley: New York, 1983.
54. Beaulac, R.; Archer, P. I.; van Rijssel, J.; Meijerink, A.; Gamelin, D. R., Exciton Storage by Mn^{2+} in Colloidal Mn^{2+}-Doped CdSe Quantum Dots. *Nano Lett.* **2008**, *8*, 2949-2953.

Chapter 4. Kinetics of Isovalent (Cd^{2+}) and Aliovalent (In^{3+}) Cation Exchange in $Cd_{1-x}Mn_xSe$ Nanocrystals*

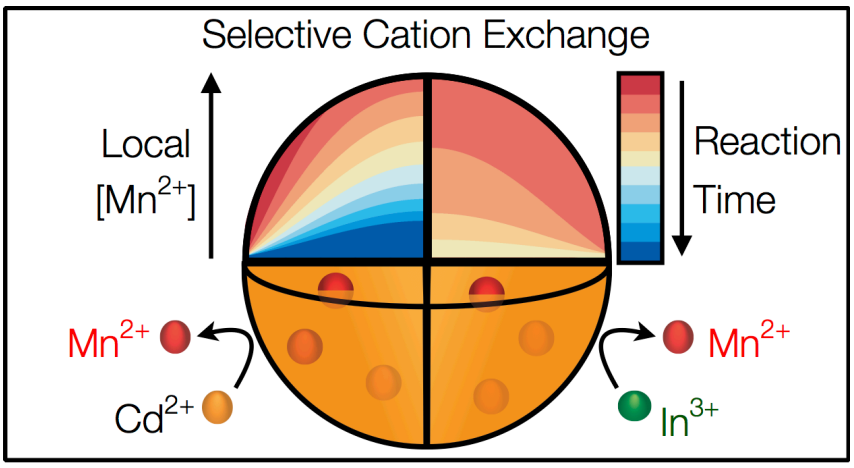

*Reproduced with permission from Chakraborty, P.; Jin, Y.; Barrows, C. J.; Dunham, S. T.; Gamelin, D. R. *J. Am. Chem. Soc.* **2016**, *138*, 12885–12893. Copyright 2016 American Chemical Society.

4.1 Overview

Ion exchange, in which an in-diffusing ion replaces a lattice ion, has been widely exploited as a synthetic tool for semiconductor doping and solid-to-solid chemical transformations, both in bulk and at the nanoscale. Here, we present a systematic investigation of cation-exchange reactions that involve the displacement of Mn^{2+} from CdSe nanocrystals by Cd^{2+} or In^{3+}. For both incoming cations, Mn^{2+} displacement is spontaneous but thermally activated, following Arrhenius behavior over a broad experimental temperature range. At any given temperature, cation exchange by In^{3+} is approximately 2 orders of magnitude faster than that by Cd^{2+}, illustrating a critical dependence on the incoming cation. Quantitative analysis of the kinetics data within a Fick's-law diffusion model yields diffusion barriers (E_D) and limiting diffusivities (D_0) for both incoming ions. Despite their very different kinetics, indistinguishable diffusion barriers of $E_D \approx 1.1$ eV are found for both reactions (In^{3+} and Cd^{2+}). A dramatically enhanced diffusivity is found for Mn^{2+} cation exchange by In^{3+}. Overall, these findings provide unique experimental insights into cation diffusion within colloidal semiconductor nanocrystals, contributing to our fundamental understanding of this rich and important area of nanoscience.

4.2 Introduction

Ion diffusion in solids is integral to many energy storage and conversion technologies, impacting for example solid-electrolyte kinetics in batteries and fuel cells, and doping profiles in diffusion-doped semiconductor devices.[1, 2] Diffusion occurs in all solids, spanning broad time and length scales, and its physical underpinnings are very generally relevant across physics, chemistry, biology, geology, and other disciplines.[3] In recent years, directed ion diffusion has become a prominent tool in the synthetic repertoire of nanoscience, enabling formation of non-equilibrium semiconductor nanostructures with exquisite compositional, shape, and size control.[4-15] Whereas broad attention has been dedicated to understanding the motions of charge carriers into and out of semiconductor nanostructures, less is known about ion mobilities in such materials. Reduced dimensionality is frequently credited with accelerating ion diffusion *via* increased surface-to-volume ratios, reduced transport lengths, and in some instances, altered diffusion mechanisms.[4, 16-18] Although large ion mobilities may improve performance in some device technologies, it may also compromise performance in others when stable compositions are demanded at high operating temperatures. A fundamental understanding of ion diffusion in nanostructured semiconductors will thus be important for future applications of this important class of materials.

Mechanistic studies of ion diffusion in colloidal semiconductor nanocrystals are at an early stage. Experimentally, a great deal of work has been done on controlling nanocrystal compositions through cation exchange, which allows access to compositions,

shapes, and heterostructures that cannot be prepared by other routes.[9, 10, 19, 20] Cation exchange frequently involves rapidly diffusing cations such as Cu^+ or Ag^+, whose reactions are often complete within milliseconds at room temperature,[5-8] but it has also been explored with various slower-diffusing cations.[5-7, 9, 10, 12, 13] In most cases, cation diffusion is generally assumed to involve vacancy or interstitial mechanisms, with smaller ions diffusing interstitially more easily. Computational work has highlighted the importance of electrostatics in stabilizing cation vacancies during Ag^+ diffusion into CdSe nanocrystals.[21] Also computationally, energy barriers for interstitial diffusion of Mn^{2+} have been predicted to be significantly smaller in nanocrystalline CdSe (d < 2 nm) than in bulk CdSe, leading to greater Mn^{2+} hopping frequencies in the former.[16] Acceleration of Mn^{2+} hopping by new low-energy nanocrystal lattice vibrations was also proposed.[16] Quantitative experimental investigation of cation diffusion kinetics in semiconductor nanostructures are needed to advance the understanding, and ultimately the utility, of chemical transformations that involve ion diffusion through semiconductor nanostructures.

Here, we report a detailed investigation into the cation-exchange kinetics of a model system of free-standing colloidal semiconductor nanocrystals. Mn^{2+} ions embedded within colloidal $Cd_{1-x}Mn_xSe$ nanocrystals are expelled from these crystals by addition of Cd^{2+} and In^{3+} cations, both of which form stronger M^{n+}–Se^{2-} bonds than Mn^{2+} (Cd^{2+}–Se^{2-}: 310 kJ/mol; In^{3+}–Se^{2-}: 247 kJ/mol *vs* Mn^{2+}–Se^{2-}: 201 kJ/mol),[22] providing a thermodynamic driving force for cation exchange. The rates of Mn^{2+} displacement by these two cations differ by nearly two orders of magnitude under otherwise identical conditions, with In^{3+} causing much faster Mn^{2+} expulsion from the nanocrystals. Experimental cation-

exchange reaction kinetics have been measured as a function of temperature over broad temperature ranges. Fick's-law modeling of these data allows quantitative assessment of the diffusion constants and barriers for these cation-exchange reactions. The results of this analysis reveal indistinguishable diffusion barriers (E_D) for the reactions involving Cd^{2+} and In^{3+}. The vastly accelerated cation exchange when using In^{3+} could be attributed to lower effective cation activity in solution for In^{3+} (relative to Cd^{2+}) increasing the vacancy concentration in nanocrystals, or to electrostatic stabilization of lattice cation vacancies or interstitials by this aliovalent cation, emphasizing the critical role such point defects play in these chemical transformations. These results offer a unique experimental mechanistic view into cation diffusion within colloidal semiconductor nanocrystals.

4.3 Experimental Methods

4.3.1 Nanocrystal Synthesis and Diffusion Doping

Synthesis of oleate-capped wurtzite-CdSe nanocrystals was adapted from various publications.[11, 23-26] The NCs were washed by repeated suspensions in toluene and oleic acid (OA) and flocculation with ethanol. Diffusion doping of CdSe NCs with Mn^{2+} was carried out according to our previously reported procedures[11, 15] for 20 hours at 300 °C using 0.1 mmol (in terms of CdSe units) of CdSe seed NCs, 0.004 g (0.05 mmol) of Se powder, and 0.025 g (0.1 mmol) of $Mn(OAc)_2 \cdot 4H_2O$. Reactions were monitored by removing aliquots at various times for spectroscopic and analytical characterization.

4.3.2 Cation Exchange

Cation exchange was carried out from the equilibrated diffusion-doped $Cd_{1-x}Mn_xSe$ NCs between 300 °C and 125 °C without further purification of the reaction mixture. Solutions of cadmium oleate and indium oleate were prepared separately by adding 0.0064 g (0.05 mmol) of CdO or 0.0146 g (0.05 mmol) of indium (III) acetate, respectively, to 0.2 g of OA, and 2 g of 1-octadecene (ODE). These solutions were degassed for one hour at 115 °C to remove acetic acid and water, followed by heating to 280 °C under nitrogen until the solutions became transparent and colorless, consistent with the formation of $Cd(oleate)_2$ and $In(oleate)_3$. The solutions were then cooled to room temperature under nitrogen and added to the equilibrated diffusion-doped $Cd_{1-x}Mn_xSe$ NC solution dropwise over the course of two minutes so as not to perturb the temperature of the solution. The resulting reaction mixtures were held between 300 °C and 125 °C and allowed to re-equilibrate between a few minutes and several days. All the reactions were monitored by taking aliquots at various time intervals, followed by washing as described above.

4.3.3 Physical Characterization

Room-temperature electronic absorption spectra of all the aliquots suspended in toluene were taken in a Cary 5000 spectrometer using a 0.1 cm path length cuvette. Room-temperature magnetic circular dichroism (MCD) spectra of those aliquots were measured using the same cuvette placed in a 1.5 T electromagnet oriented in the Faraday configuration. MCD spectra were collected using an Aviv 40DS spectropolarimeter. The differential absorption of left and right circularly polarized light in the MCD experiment is reported as $\Delta A = A_L - A_R$, where A_L and A_R refer to the absorption of left and right circularly polarized photons in the sign convention of Piepho and Schatz.[27] Values of ΔE_{Zeeman}, g_{Exc}, and g_{sp-d} can be calculated from these MCD data.[11, 15, 28-30] Based on experimental uncertainty, we estimate $\sigma \leq 5\%$ for all values of g_{sp-d} reported here. TEM samples were

prepared by immersing Cu grids (200 mesh, Ted Pella, Inc.) in colloidal suspensions of NCs in toluene. The grids were allowed to dry in air for a few minutes and kept inside the desiccator overnight to remove any excess water. Nanocrystal sizes from TEM and the size distribution histogram analysis were performed on ≥100 individual nanocrystals by using the ImageJ64 software.

4.4 Results and Analysis

4.4.1 Diffusion-Doping and Cation-Exchange Reactions

Figure 4.1 presents electronic absorption and MCD spectra of colloidal CdSe nanocrystals measured at various stages of sequential diffusion-doping and cation-exchange reactions. Panel A shows room-temperature electronic absorption spectra of seed CdSe nanocrystals, of the same nanocrystals equilibrated after 20 hours of diffusion doping with Mn^{2+},[11, 15] and of the same nanocrystals after subsequent cation exchange with Cd^{2+}. The diffusion-doping and cation-exchange reactions were performed at 300 °C with the ratio 0.5:1:1 for Se^{2-}:Mn^{2+}:CdSe (where CdSe here represents lattice Cd^{2+}–Se^{2-} units) during diffusion doping, and the ratio 1:1 between added Cd^{2+} and previously added Se^{2-} during cation exchange. Diffusion doping shifts the first excitonic absorption maximum to higher energy, whereas subsequent cation exchange with Cd^{2+} shifts it to lower energy again.

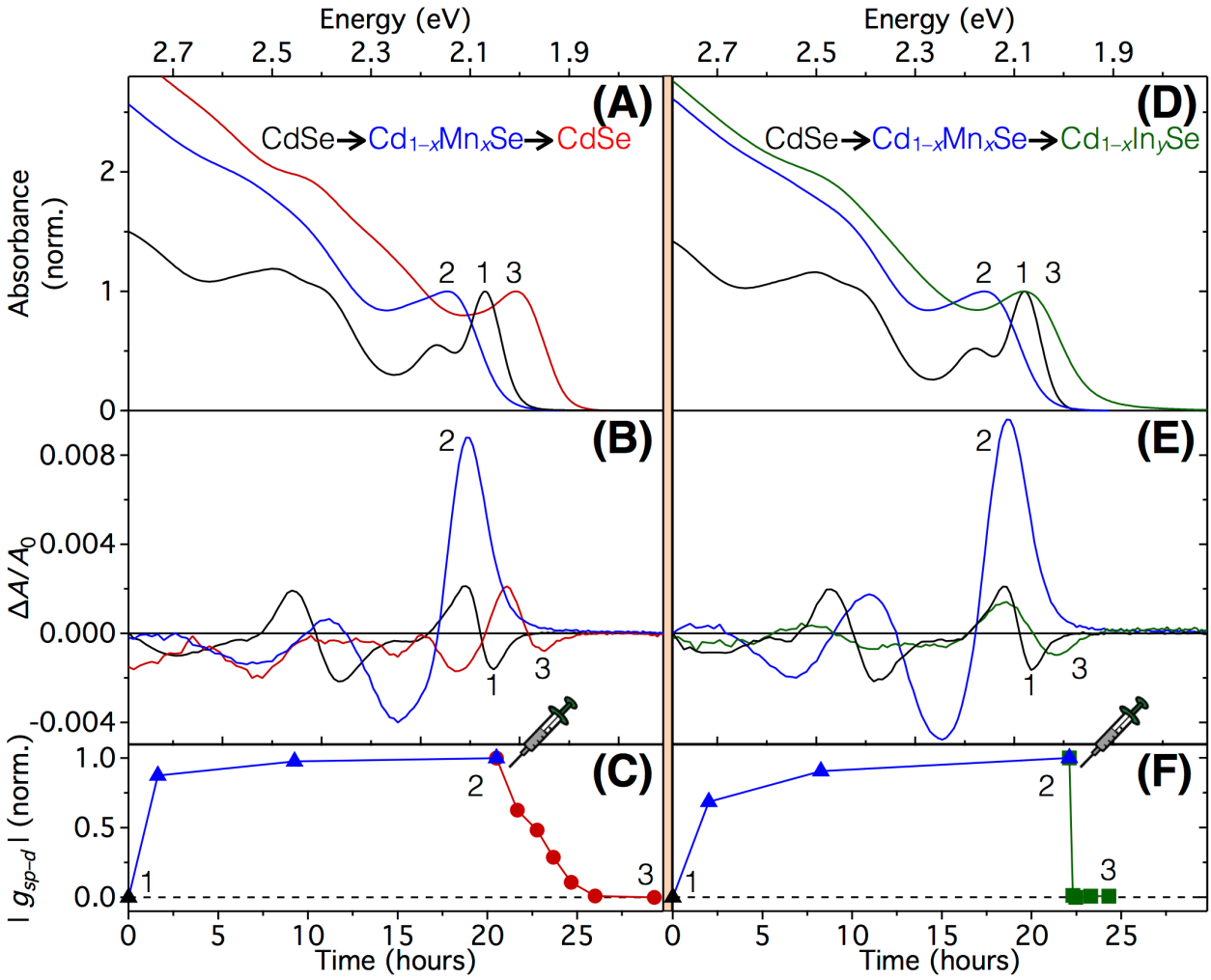

Figure 4.1. **(A)** Room-temperature electronic absorption spectra of undoped d = 4.5 ± 0.2 nm CdSe nanocrystals (1, black), the same nanocrystals equilibrated after 20 hours of Mn^{2+} diffusion doping at 300 °C with 0.5:1:1 Se^{2-}:Mn^{2+}:CdSe (2, blue), and purified by 10 hours of cation exchange with Cd^{2+} (3, red, 1:1 added Cd^{2+}:previously added Se^{2-}) at 300 °C. **(B)** Room-temperature MCD spectra of the same nanocrystals. **(C)** Time evolution of $|g_{sp-d}|$ during diffusion doping (black and blue triangles) and cation exchange by Cd^{2+} (red circles) at 300 °C, as determined by room-temperature MCD at 1.5 T. The data are represented as the absolute value of g_{sp-d} normalized to the equilibrated diffusion-doped $Cd_{1-x}Mn_xSe$ value. **(D)** Room-temperature electronic absorption spectra of undoped d = 4.4 ± 0.2 nm CdSe nanocrystals (1, black), the same nanocrystals equilibrated after 20 hours of Mn^{2+} diffusion doping at 300 °C (2, blue, 0.5:1:1 Se^{2-}:Mn^{2+}:CdSe), and after 10 minutes of cation exchange with In^{3+} (3, green, 1:1 In^{3+}:previously added Se^{2-}) at 300 °C. **(E)** Room-temperature MCD spectra of the same nanocrystals. **(F)** Time evolution of $|g_{sp-d}|$ during diffusion doping (black and blue triangles) and cation exchange by In^{3+} (green squares) at 300 °C, as determined by room-temperature MCD at 1.5 T.

Figure 4.1B shows corresponding room-temperature MCD spectra of the same seed CdSe nanocrystals, equilibrated diffusion-doped $Cd_{1-x}Mn_xSe$ nanocrystals, and the same nanocrystals after cation exchange with Cd^{2+}. Diffusion doping causes inversion and enhancement of the first CdSe excitonic MCD feature, whereas cation exchange inverts this feature back to a signal consistent with undoped CdSe nanocrystals. As detailed previously,[11, 15] these spectroscopic changes are manifestations of Mn^{2+} diffusion into the CdSe nanocrystal lattice. Specifically, the MCD intensity inversion and enhancement seen in Figure 4.1B reflect the introduction of a new Mn^{2+}–exciton magnetic-exchange contribution to the excitonic Zeeman splitting upon Mn^{2+} incorporation into the CdSe nanocrystal, parameterized by the spectroscopic splitting term g_{sp-d}. Simultaneous analysis of the MCD and absorption spectra allows quantification of g_{sp-d}, which is proportional to the Mn^{2+}–exciton overlap. These spectroscopic data thus provide a quantitative measure of Mn^{2+} concentration within the CdSe nanocrystals, as verified by independent ICP-AES, TEM, and EPR measurements, allowing us to monitor the evolution of the Mn^{2+} population within the CdSe nanocrystals during diffusion doping and cation exchange.[11, 15] Under these diffusion-doping conditions, x reaches ~0.15 and Mn^{2+} is distributed uniformly throughout the nanocrystal volume at equilibrium.[15] Figure 4.1C plots the time evolution of $|g_{sp-d}|$ (norm.) during diffusion doping and cation exchange. Here, g_{sp-d} has been normalized to its maximum value achieved at equilibrium during the diffusion-doping reaction. In the undoped CdSe nanocrystals, $|g_{sp-d}| = 0$. During diffusion doping, $|g_{sp-d}|$ increases with time and eventually plateaus as the reaction approaches equilibrium. During

cation exchange with Cd^{2+}, $|g_{sp-d}|$ drops and re-equilibrates at $|g_{sp-d}| = 0$ again, indicating complete removal of Mn^{2+} from the CdSe nanocrystals.

Figure 4.1D shows room-temperature electronic absorption spectra of undoped CdSe nanocrystals, of the same nanocrystals after 20 hours of diffusion doping with Mn^{2+} at 300 °C, and of the same nanocrystals after subsequent cation exchange with In^{3+} (1:1 between added In^{3+} and previously added Se^{2-}). Diffusion doping causes a shift of the first excitonic absorption feature to higher energy, whereas cation exchange with In^{3+} shifts it back to lower energy, like cation exchange with Cd^{2+}. Figure 4.1E shows corresponding room-temperature MCD spectra of the same CdSe nanocrystals before and after diffusion doping, and after subsequent cation exchange with In^{3+}. MCD at the CdSe absorption edge inverts and intensifies during diffusion doping, whereas subsequent cation exchange with In^{3+} diminishes its intensity and reverts it back to the undoped CdSe-like signal. Figure 4.1F plots the variation of $|g_{sp-d}|$ as a function of time during diffusion doping and cation exchange. $|g_{sp-d}|$ again increases with diffusion doping time, eventually approaching a maximum, indicating Mn^{2+} in-diffusion and composition equilibration, whereas cation exchange with In^{3+} causes a rapid drop of $|g_{sp-d}|$ to zero, indicating expulsion of Mn^{2+} from the nanocrystals by In^{3+}.

Figure 4.2 presents TEM images and corresponding size-distribution histograms of the CdSe nanocrystals from Figure 4.1 during the diffusion-doping and cation-exchange reactions. Figure 4.2A shows the undoped CdSe nanocrystals used for the diffusion-doping and subsequent cation-exchange experiments with Cd^{2+}. These nanocrystals have an average diameter of 4.5 ± 0.2 nm (σ = 4.4%). Figure 4.2B shows the same

nanocrystals equilibrated after 20 hours of diffusion doping with Mn^{2+} at 300 °C. During diffusion doping, the average nanocrystal diameter increases to 5.2 ± 0.4 nm (σ = 7.7%) due to formal addition of Mn^{2+}–Se^{2-} units to the lattice. Figure 4.2C shows the same nanocrystals after subsequent cation exchange with Cd^{2+} at 300 °C. The average diameter of 5.3 ± 0.3 nm (σ = 5.6%) is essentially unchanged during cation exchange. Figure 4.2D illustrates the CdSe nanocrystal diffusion-doping and cation-exchange reactions schematically. Figure 4.2E shows the undoped CdSe nanocrystals used for the diffusion-doping and subsequent cation-exchange experiments with In^{3+}. These nanocrystals have an average diameter of 4.4 ± 0.2 nm (σ = 4.5%). Figure 4.2F shows the same nanocrystals after 20 hours of diffusion doping with Mn^{2+} at 300 °C. The average diameter increases to 5.1 ± 0.5 nm (σ = 9.8%). Figure 4.2G shows the same nanocrystals after subsequent cation exchange with In^{3+} at 300 °C. The average diameter of 5.2 ± 0.4 nm (σ = 7.7%) remains essentially unchanged during cation exchange. In^{3+} is clearly detected in the EDX spectrum of these nanocrystals measured after cation exchange with In^{3+} (see Appendix C).

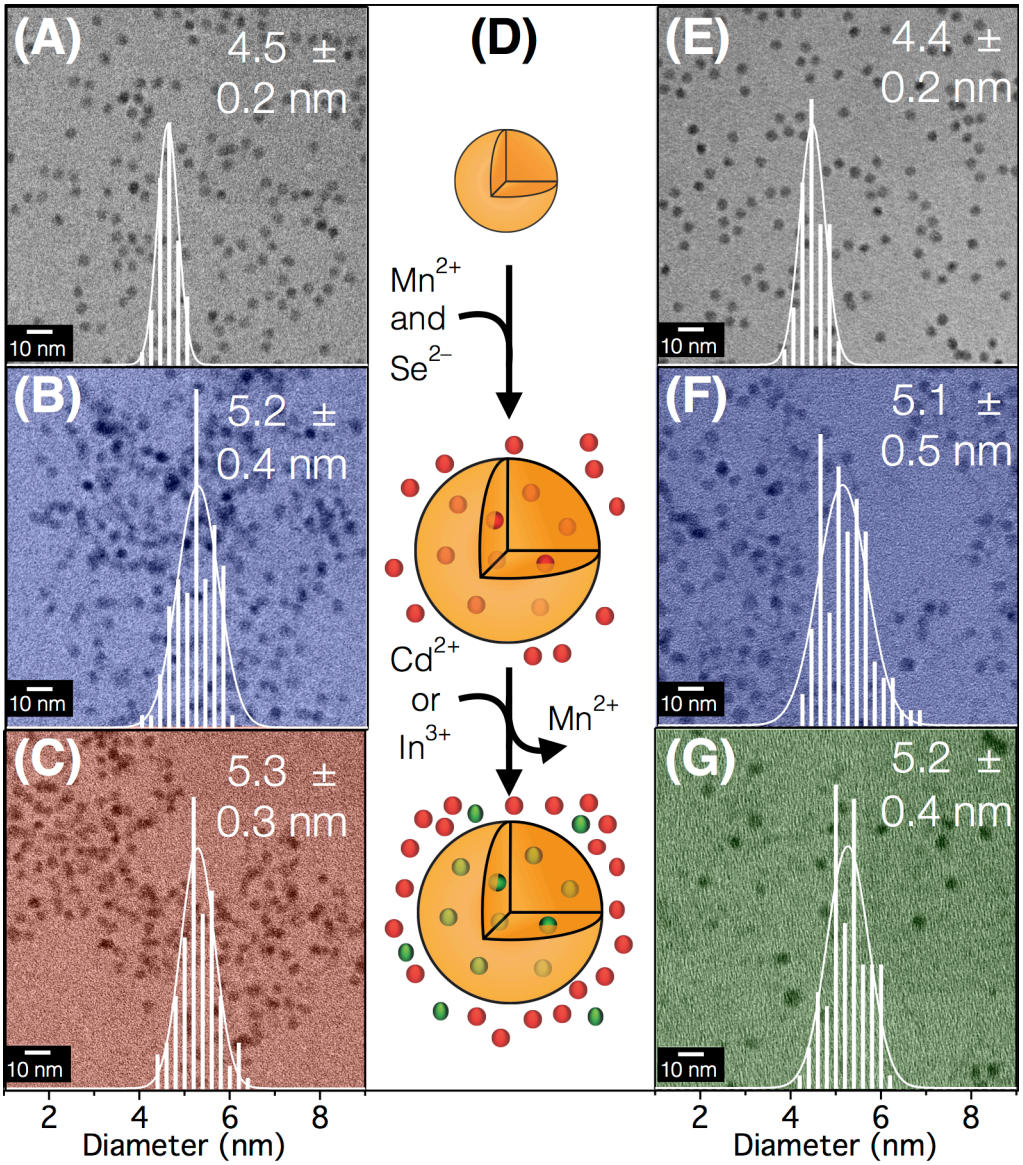

Figure 4.2. TEM images and size histograms (≥100 nanocrystals each) for **(A)** undoped CdSe nanocrystals (d = 4.5 ± 0.2 nm), **(B)** diffusion-doped $Cd_{1-x}Mn_xSe$ nanocrystals after 20 hours of diffusion doping at 300 °C (d = 5.2 ± 0.4 nm), and **(C)** the same nanocrystals after cation exchange with Cd^{2+} at 300 °C (d = 5.3 ± 0.3 nm). **(D)** Schematic illustration of CdSe nanocrystal diffusion doping by addition of Mn^{2+} and Se^{2-} to form $Cd_{1-x}Mn_xSe$ nanocrystals, followed by cation exchange with either Cd^{2+} or In^{3+} to form CdSe or $Cd_{1-x}In_ySe$ nanocrystals, respectively. TEM images and size histograms (≥100 nanocrystals each) for **(E)** undoped CdSe seed nanocrystals (d = 4.4 ± 0.2 nm), **(F)** diffusion-doped $Cd_{1-x}Mn_xSe$ nanocrystals after 20 hours of diffusion doping at 300 °C (d = 5.1 ± 0.5 nm), and **(G)** the same nanocrystals after cation exchange with In^{3+} at 300 °C (d = 5.2 ± 0.4 nm). The scale bars represent 10 nm.

Figure 4.3 shows the variation of $|g_{sp-d}|$ (normalized to the equilibrated diffusion-doped $Cd_{1-x}Mn_xSe$ values) as a function of time during cation exchange with Cd^{2+} or In^{3+}. Mn^{2+} removal from the $Cd_{1-x}Mn_xSe$ nanocrystal lattice during cation exchange with In^{3+} takes place in a few minutes at 300 °C, whereas it takes about 10 hours during cation exchange with Cd^{2+} at the same experimental temperature. Therefore, at the same temperature, cation exchange with In^{3+} is much faster than with Cd^{2+}. Control experiments performed with sodium oleate or with only oleic acid and ODE at the same temperature result in no meaningful change in $|g_{sp-d}|$ over several hours, indicating no loss of Mn^{2+}. These control experiments exclude self-purification or ligand concentration effects under these conditions. Mn^{2+} removal from the $Cd_{1-x}Mn_xSe$ nanocrystal lattice takes place only *via* cation exchange with Cd^{2+} or In^{3+}. The dashed curves in Figure 4.3 show single-exponential fits of the Cd^{2+} and In^{3+} cation-exchange data and are included as guides to the eye (*vide infra*).

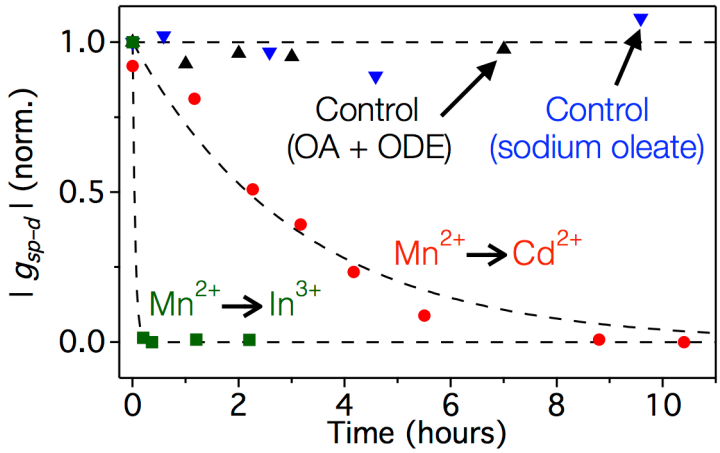

Figure 4.3. Time evolution of $|g_{sp-d}|$ during 300 ºC cation exchange starting from equilibrated, diffusion-doped $Cd_{1-x}Mn_xSe$ nanocrystals upon addition of In^{3+} (green squares, 1:1 added In^{3+} to previously added Se^{2-} during the diffusion-doping step), Cd^{2+} (red circles, 1:1 added Cd^{2+} to previously added Se^{2-} during the diffusion-doping step). Data from control experiments using sodium oleate (blue downward triangles, 1:1 added sodium oleate to previously added Se^{2-} during the diffusion-doping step) and a mixture of OA and ODE (black upward triangles) are also included. Both control experiments were performed with 0.2 g of OA and 2 g of ODE. The dashed curves show single-exponential fits of the In^{3+} and Cd^{2+} data and horizontal lines for the sodium oleate and OA and ODE data. All experiments shown here were performed on equilibrated diffusion-doped $Cd_{1-x}Mn_xSe$ nanocrystals made by diffusion doping the same or similar undoped CdSe NCs at 300 °C for 20 hours with 0.5:1:1 Se^{2-}:Mn^{2+}:CdSe mole ratios.

Figure 4.4 presents data from variable-temperature cation-exchange measurements for diffusion-doped $Cd_{1-x}Mn_xSe$ nanocrystals using Cd^{2+} or In^{3+} as the incoming cation, and plots the evolution of $|g_{sp-d}|$ as a function of temperature. The corresponding electronic absorption and MCD spectra are provided in Appendix C. For both incoming cations, $|g_{sp-d}|$ decreases roughly exponentially with time at all temperatures, asymptotically approaching zero. Figure 4.4A shows that Mn^{2+} removal from the nanocrystals occurs on a time scale of several hours after the addition of Cd^{2+} across a broad range of temperatures (220–315 °C), and that the reaction gets much slower at lower temperatures. Even after one full day of Cd^{2+} cation exchange at 250 °C, $|g_{sp-d}|$ has decreased by only ~50%. By contrast, cation exchange with In^{3+} proceeds much faster (Figure 4.4B). Mn^{2+} displacement is complete essentially immediately upon addition of In^{3+} at 300 °C, and is complete within a few minutes of In^{3+} addition at 250 °C. Again, the reaction becomes slower with decreasing reaction temperature, but at every temperature it is still much faster than cation exchange with Cd^{2+} at the same temperature. Overall, under otherwise identical conditions, cation exchange from equilibrated $Cd_{1-x}Mn_xSe$ nanocrystals is approximately two orders of magnitude faster with In^{3+} than with Cd^{2+}. The dashed curves in Figure 4.4 show results from modeling, as described in the following section.

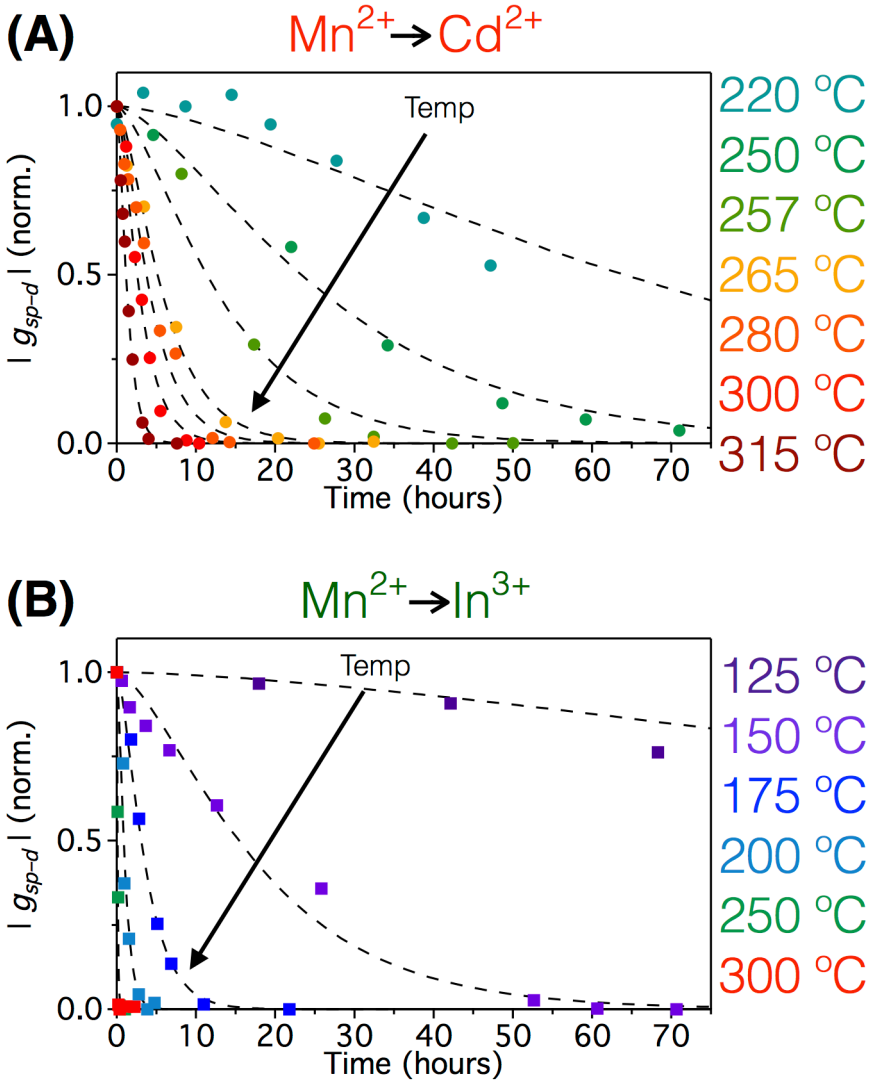

Figure 4.4. Temperature dependence of the cation-exchange reaction kinetics for the exchange of Mn^{2+} in d = 5.2 nm $Cd_{1-x}Mn_xSe$ nanocrystals by Cd^{2+} or In^{3+} ions. The data plot the change in $|g_{sp-d}|$ *vs* time for parallel reactions run at different temperatures. All measurements were performed starting with equilibrated, diffusion-doped $Cd_{1-x}Mn_xSe$ nanocrystals (20 hours of diffusion doping at 300 °C with 0.5:1:1 Se^{2-}:Mn^{2+}:CdSe). **(A)** Cation exchange with Cd^{2+}, where the ratio of added Cd^{2+} to Se^{2-} added during diffusion doping is 1:1. **(B)** Cation exchange with In^{3+}, where the ratio of added In^{3+} to Se^{2-} added during diffusion doping is 1:1. The dashed curves show the results of data simulation using a Fick's-law model (see section 4.4.2 for details), from which diffusivities and diffusion barriers are quantified. Data for longer reaction times are included in Appendix C.

4.4.2 Modeling Mn^{2+} Diffusion Kinetics

Generally, ion diffusion through a crystal lattice involves interactions with point defects such as interstitials or vacancies. For example, in bulk II–VI and III–V semiconductors, Mn^{2+} diffusion is believed to primarily involve substitutional hopping mediated by cation vacancies.[31] Whether the out-diffusion of Mn^{2+} ions from $Cd_{1-x}Mn_xSe$ nanocrystals is mediated by interstitials or vacancies is *a priori* unknown. By simulating the experimental results, we aim to help identify the dominant mechanism. As will be shown, we find that mobile complexes mediating Mn^{2+} out-diffusion possess a shorter mean free path than the nanocrystal dimensions. Since interstitials are likely to have a larger mean free path than our very small nanocrystal dimensions, as in other material systems,[32] this conclusion suggests that Mn^{2+} out-diffusion is most likely mediated by cation vacancies. We thus propose that the mechanism for Mn^{2+} out-diffusion in our $Cd_{1-x}Mn_xSe$ nanocrystals is analogous to the vacancy-mediated mechanism of Mn^{2+} diffusion in related bulk semiconductors.[31]

In vacancy-mediated diffusion, Mn^{2+} exchanges with vacancies at neighboring lattice sites. The diffusion process can be expressed as:

$$Mn^{2+} + V \rightleftharpoons V + Mn^{2+} \tag{4.1}$$

The effective diffusivity of Mn^{2+} mediated by vacancies (D) is:

$$D = \frac{n X_V^{Mn^{2+}} \Gamma_{Mn^{2+}/V} a^2}{6} \tag{4.2}$$

Here, $X_V^{Mn^{2+}}$ is the fractional concentration of cation vacancies adjacent to Mn^{2+} ions, n is the number of adjacent sites, $\Gamma_{Mn^{2+}/V}$ represents the Mn^{2+}–vacancy exchange rate, and a is the hopping distance. In principle, D could be a function of time and position within the nanocrystal, which is difficult to characterize given the limited experimental data set. Because the chemical potential does not change much in the solution during the cation-exchange reactions reported here, we assume that the concentration of vacancies in these nanocrystals is relatively constant throughout the experiment. Also, because of the small dimensions of the nanocrystals, we assume uniform distributions of vacancies within the nanocrystals. We thus simplify the model by assuming that a single average D is applicable in any specific reaction performed under fixed conditions.

To describe the experimental ion-diffusion data quantitatively, we solve the Fick's-law diffusion equation. In a spherical coordinate system, the diffusion equation has the following form:

$$\frac{\partial u}{\partial t} = D\frac{1}{r^2}\frac{\partial}{\partial r}r^2\frac{\partial u}{\partial r}, \qquad 0 < r < R \tag{4.3}$$

Here, the distribution function u describes the Mn^{2+} ion distribution within the nanocrystal, and D is the diffusion coefficient (diffusivity). We define the initial condition as:

$$u(r, t = 0) = U_0 \tag{4.4}$$

where $U_0 = 1$.

To solve Equation 4.3, two boundary conditions must be defined. At the geometric origin of the nanocrystal ($r = 0$), we have:

$$\left.\frac{\partial u}{\partial r}\right|_{r=0} = 0 \tag{4.5}$$

A second boundary condition describing the nanocrystal/liquid interface ($r = R$) is also needed. Initial calculations were performed under the assumption of a fixed boundary condition. Specifically, we assume that Mn^{2+} solvation (*i.e.*, displacement by solvated Cd^{2+} or In^{3+}) at the nanocrystal/liquid interface equilibrates rapidly relative to other processes such that u at R is effectively constant for the duration of the experiment, *i.e.*:

$$u(R,t) = u_R \tag{4.6}$$

In our calculations, we set $u_R = 0$, meaning that Mn^{2+} ions are rapidly removed from the nanocrystals once they reach this interface. This condition is consistent with our experimental observations that MnSe shells cannot be grown on the CdSe nanocrystals under these conditions, and that MnSe also cannot be independently nucleated under these conditions.[15] Under these fixed boundary conditions, the analytical solution to Equation 4.3 is then:

$$u(r,t) = \frac{2R[U_0 - u_R]}{\pi}\sum_{n=1}^{\infty}\frac{(-1)^{n+1}}{n}e^{-\lambda_n^2 Dt}\frac{\sin(\lambda_n r)}{r} + u_R, \quad \lambda_n = \frac{n\pi}{R} \tag{4.7}$$

We note that the MCD spectroscopic approach used to gather the data in Figure 4.4 measures an *effective* Mn^{2+} content given by the overlap of the dopant profile and the nanocrystal's exciton wavefunction. To relate the calculated diffusion results to experiment, the exciton wavefunction amplitude was modeled using the particle-in-a-

spherical-well solution detailed elsewhere,[33] and the values of $|g_{sp-d}|$ were then related to the dopant distribution $u(r)$ by projection of $u(r)$ onto this wavefunction. The microscopic details of this relationship are described elsewhere.[34]

Using this approach, diffusion coefficients governing the cation-exchange kinetics were evaluated for each experiment by fitting the experimental data shown in Figure 4.4. The first 50th orders of Equation 4.7 were evaluated computationally. The comparison between simulated and experimental results is included in Figure 4.4 for both Cd^{2+} and In^{3+} cation exchange. The diffusion calculations reproduce experiment well at each temperature, with the goodness of fit worsening only for the lowest temperatures where the data themselves are least complete. These fits yield the diffusion coefficients summarized in Table 4.1. Cation exchange with In^{3+} at 300 °C proceeded too rapidly to fit.

Table 1. Diffusion coefficients obtained from Fick's-law analysis of the data in Figure 4.4 using Equation 4.7, corresponding to the dashed curves included in Figure 4.4.

$Mn^{2+} \rightarrow Cd^{2+}$		$Mn^{2+} \rightarrow In^{3+}$	
Temperature (K)	Diffusivity, D (nm^2/s)	Temperature (K)	Diffusivity, D (nm^2/s)
493	1.7×10^{-6}	398	5.6×10^{-7}
523	4.6×10^{-6}	423	6.9×10^{-6}
530	9.4×10^{-6}	448	3.5×10^{-5}
538	2.1×10^{-5}	473	1.2×10^{-4}
553	2.9×10^{-5}	523	1.1×10^{-3}
573	4.2×10^{-5}		
588	9.0×10^{-5}		

As expected from visual inspection of the data, the diffusivities increase with increasing temperature, and are greater for cation exchange when using In^{3+} than when Cd^{2+} is used. Figure 4.5 plots the logarithm of the fitted diffusivities *vs* inverse temperature. Within experimental uncertainty, these plots are linear over the entire temperature range examined here, indicating that the diffusivities show Arrhenius behavior throughout this temperature range. The dashed lines in Figure 4.5 represent fits of the data to the Arrhenius equation (Equation 4.8) and yield indistinguishable values of E_D = 1.1 eV for both Cd^{2+} and In^{3+}. As a simple cross-check, we note that a similar diffusion barrier of ~1.1 eV is also obtained when the data in Figure 4.4 are fit to phenomenological single-exponential functions and the results analyzed using the Arrhenius equation (see below and Appendix C). Despite their similar diffusion barriers, cation exchange with Cd^{2+} and In^{3+} show very different limiting diffusivities of $D_0 = 9.8 \times 10^4$ and 2.6×10^7 nm^2/s for Cd^{2+} and In^{3+}, respectively. A similar increase in D_0 for Mn^{2+} diffusion is observed in $Cd_{1-x}Mn_xTe$ thin films upon co-doping with In^{3+}.[31] Because $D_0 = n_0a^2$ (where n_0 is the cation-hopping attempt frequency and a is the hopping distance), the substantial increase in D_0 when using In^{3+} relative to Cd^{2+} reflects a significant increase in Mn^{2+} hopping attempts in the former case.

$$D = D_0\exp(-E_D/kT) \tag{4.8}$$

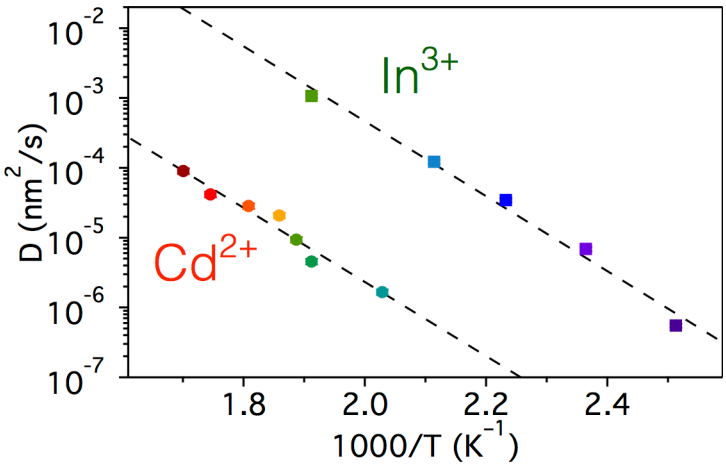

Figure 4.5. Arrhenius plot of the temperature dependence of the diffusion coefficients (D) measured for Mn^{2+} cation exchange by Cd^{2+} (circles) and In^{3+} (squares) in d = 5.2 nm $Cd_{1-x}Mn_xSe$ nanocrystals. The diffusion coefficients are obtained by simulating the experimental data in Figure 4.4 using the Fick's-law diffusion equation (Equation 4.7) with fixed boundary conditions. The simulated curves are also depicted in Figure 4.4. Dashed lines show fits of the data to the Arrhenius equation (Equation 4.8), which yield E_D = 1.1 ± 0.1 eV for both Cd^{2+} and In^{3+}. From the Arrhenius fits, limiting diffusivities of D_0 = 9.8 (±1.8) × 10^4 and 2.6 (±0.3) × 10^7 nm^2/s are obtained for cation exchange with Cd^{2+} and In^{3+}, respectively.

For completeness, the possibility that the interface at $r = R$ cannot equilibrate fast enough to use a constant u_R was also considered. In this case, we explicitly account for the interface flux using Equation 4.9:

$$\left.\frac{\partial u(r,t)}{\partial r}\right|_{r=R} = k \times (u(R,t) - u_{equil}(R,t)) \tag{4.9}$$

Here, k represents the surface equilibration rate constant, and $u_{equil}(R,t)$ describes the (quasi)equilibrium Mn^{2+} mole fraction at the nanocrystal surface. The fixed boundary condition reflects the limit of large k. If k is not sufficiently large, then surface Mn^{2+} concentrations will not be equilibrated and the diffusion profile should differ from the fixed-boundary-condition analytical solution. To verify that, we have shown the experimental and simulated curves after accounting for the interface flux at the lowest temperatures used for the Cd^{2+} and In^{3+} reactions (see Appendix C). Very similar results are obtained using this more complete model. Although expected to be temperature dependent, effects of the interface fluxes are not detectable at lower temperatures, indicating they do not become rate limiting. This result is consistent with the finding that the diffusion coefficients extracted from the fixed-boundary-condition solution follow Arrhenius behavior at all temperatures. Overall, we conclude that surface equilibration is comparatively rapid (k is large) at all experimental temperatures explored here, and hence that the fixed boundary condition is a reasonable approximation for our present analysis.

Cation exchange *via* an interstitial mechanism was also considered. The interstitial process can be described as a "kick-out" mechanism. In this mechanism, interstitial Cd^{2+} (Cd_i) or In^{3+} (In_i) replaces the substitutional Mn^{2+} (Mn_s) and generates interstitial Mn^{2+} (Mn_i) as follows:

$$Cd_i + Mn_s \rightleftharpoons Cd_s + Mn_i \quad (4.10)$$

$$In_i + Mn_s \rightleftharpoons In_s + Mn_i \quad (4.11)$$

If the mean free path of interstitials is much smaller than the nanocrystal dimensions (r = 2.6 nm), then we get an effective diffusivity that is indistinguishable from that of the vacancy mechanism. If, however, the mean free path of interstitials is substantially larger than the nanocrystal dimensions (*e.g.*, the case of interstitial B in Si, where the mean free path can exceed 10 nm[32]), then Mn^{2+} out-diffusion would yield uniformly distributed Mn^{2+} throughout the nanocrystal. This uniform Mn^{2+} distribution would decay in time with a rate determined by the exchange rates of the above reactions, which can be expressed as:

$$R_{Cd/Mn} = 4\pi d D_{Cd_i} C_{Cd_i} C_{Mn_s} \quad (4.12)$$

$$R_{In/Mn} = 4\pi d D_{In_i} C_{In_i} C_{Mn_s} \quad (4.13)$$

Here, d stands for effective capture distance. Using this model, we attempted to simulate the experimental data, but the goodness of fit is significantly worse than that found for the Fick's-law model. Figure 4.6 compares the simulations using interstitial and Fick's-law models with the experimental data for Mn^{2+} cation exchange by Cd^{2+} at 265 °C and by In^{3+} at 175 °C (selected because they have similar absolute rates). When represented on a semi-log plot, the interstitial mechanism with large mean free path yields a straight line in this plot, whereas Equation 4.3 yields a curve. Compared to the data, the simulated data based on interstitial diffusion drop too rapidly at short times and too slowly toward the end of the reaction. The experimental data clearly deviate from linearity in a way that is consistent with Fick's law. These simulations thus favor vacancy-mediated diffusion (or an interstitial diffusion process with a short mean free path).

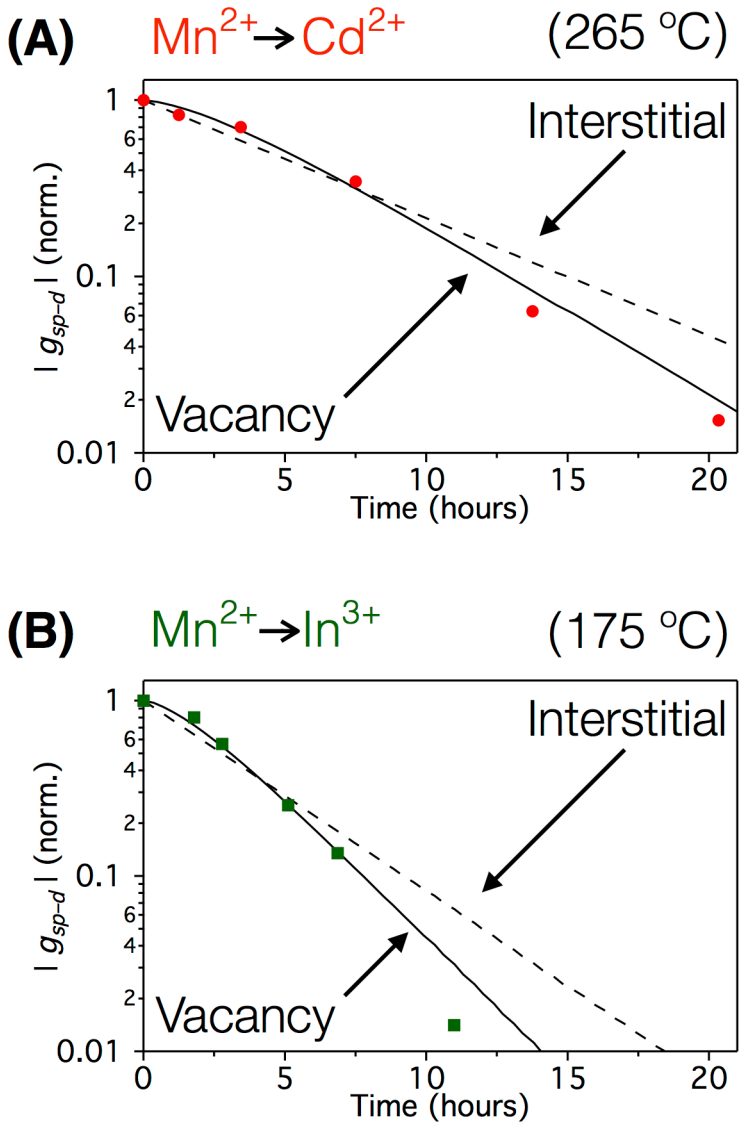

Figure 4.6. Comparison between experimental and simulated cation-exchange dynamics, plotted as log $|g_{sp-d}|$ *vs* time. **(A)** Mn^{2+} cation exchange by Cd^{2+} at 265 °C (experimental, red circles) and **(B)** Mn^{2+} cation exchange by In^{3+} at 175 °C (experimental, green squares). Simulated curves for vacancy-mediated diffusion (dashed) and interstitial diffusion with a large mean free path (solid) are included. The experimental data are from Figure 4.4.

To highlight the difference between the vacancy-mediated and interstitial diffusion mechanisms, Figure 4.7 compares the evolution of the Mn^{2+} spatial distribution within a 5.2 nm CdSe nanocrystal for the two cases described by Figure 4.6. In the vacancy-mediated diffusion process, the Mn^{2+} concentration rapidly drops to zero at the nanocrystal/liquid interface because of rapid solvation, creating a Mn^{2+} concentration gradient within the nanocrystal. In the interstitial diffusion process, the distribution of Mn^{2+} is uniform throughout the nanocrystal and the Mn^{2+} concentration at all lattice sites decays exponentially in time during the cation-exchange reaction. This difference in Mn^{2+} spatial distribution causes discernible differences in $|g_{sp-d}|$ and gives rise to the different kinetic profiles shown in Figure 4.6.

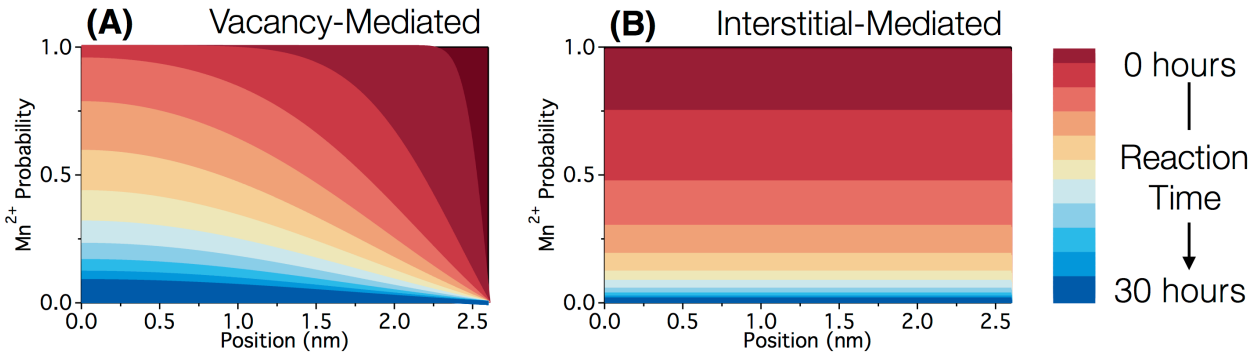

Figure 4.7. Contours for Mn^{2+} radial distribution evolution within d = 5.2 nm $Cd_{1-x}Mn_xSe$ nanocrystals during cation exchange with Cd^{2+} at 265 °C, calculated based on **(A)** vacancy-mediated diffusion with $D = 2.1 \times 10^{-5}$ nm^2/s and **(B)** interstitial diffusion with a mean free path of the interstitials that is larger than the nanocrystal dimension. The color bar indicates the cation-exchange reaction times of the various contours.

4.5 Discussion

The results and analysis presented here highlight the importance of the incoming cations on the kinetics of cation-exchange reactions in nanocrystals. At any given temperature, the Mn^{2+} diffusivity is ~250 times greater when using In^{3+} as the displacing cation compared to Cd^{2+} (Table 4.1). For both Cd^{2+} and In^{3+}, the diffusion of Mn^{2+} out of our $Cd_{1-x}Mn_xSe$ nanocrystals during cation exchange is driven thermodynamically, as summarized by the overall reactions of Equations 4.14 and 4.15. These reactions both have equilibrium constants considerably greater than unity under our experimental conditions, despite the large excess of solvated Mn^{2+} in the reaction vessel, such that no residual lattice Mn^{2+} is detectable at equilibrium under these cation-exchange conditions. If the nanocrystal stoichiometry is determined solely by charge neutrality, then $y = (2/3)x$ in Equation 4.15 because of the relative charges on In^{3+} and Mn^{2+}. Unfortunately, the final concentrations of In^{3+} in these nanocrystals could not be determined analytically by ICP-AES with sufficient accuracy to draw a firm conclusion about stoichiometry from this experiment, and charge compensation by excess anionic surface ligands cannot be ruled out. Interestingly, however, we find that only ~0.7 equivalents of In^{3+} (per lattice Mn^{2+}) are required to displace all Mn^{2+} from the $Cd_{1-x}Mn_xSe$ nanocrystals (see Appendix C), which is significantly less than the ~1.0 equivalents of Cd^{2+} needed to achieve the same level of Mn^{2+} displacement.[15] This result is consistent with a final In^{3+} stoichiometry of $y \approx (2/3)x$.

$$[Cd_{1-x}Mn_xSe]_{NC} + x\,Cd(oleate)_{2(sol)} \rightarrow [CdSe]_{NC} + x\,Mn(oleate)_{2(sol)} \quad (4.14)$$

$$[Cd_{1-x}Mn_xSe]_{NC} + y\,In(oleate)_{3(sol)} \rightarrow [Cd_{1-x}In_ySe]_{NC} + x\,Mn(oleate)_{2(sol)} \quad (4.15)$$

The spontaneity of these two reactions can be qualitatively rationalized by comparing the bond strengths of their reactants and products. The greater bond enthalpies[22] of the reaction products relative to those of the reactants (Cd^{2+}–Se^{2-} (~310 kJ/mol), In^{3+}–Se^{2-} (~247 kJ/mol), Mn^{2+}–O_{oleate} (~402 kJ/mol) *vs* Cd^{2+}–O_{oleate} (~142 kJ/mol), In^{3+}–O_{oleate} (~360 kJ/mol), Mn^{2+}–Se^{2-} (~201 kJ/mol), gas phase, 298 K) favors spontaneous displacement of lattice Mn^{2+} by both Cd^{2+} and In^{3+} under these conditions. Other factors such as ligand concentration and the solvated ion concentrations are undoubtedly also important in determining the actual equilibrium constants of these reactions, but the critical role played by the incoming cations is confirmed by the control experiments shown in Figure 4.3 using sodium oleate or oleic acid in ODE alone, without addition of In^{3+} or Cd^{2+}. The lack of any detectable Mn^{2+} diffusion in these control experiments demonstrates that neither $Mn(oleate)_2$ formation nor the excess enthalpy of mixing (which prompts "self-purification") is sufficient to drive Mn^{2+} from the $Cd_{1-x}Mn_xSe$ nanocrystals under our reaction conditions. The formation of new Cd^{2+}–Se^{2-} and In^{3+}–Se^{2-} bonds is thus essential for spontaneous Mn^{2+} expulsion from these nanocrystals. This result illustrates that the incoming and outgoing cation fluxes are coupled.

The strong temperature dependence of the cation-exchange kinetics for both In^{3+} and Cd^{2+} reactions (Figures 4.4 and 4.5) reveals that the Mn^{2+} diffusion is thermally activated. Cation exchange with In^{3+} is much faster than with Cd^{2+} at any given temperature, but the data indicate the same diffusion barrier (1.1 eV) for both processes. This value of E_D is similar to those observed in analogous diffusion processes in bulk II–VI semiconductors (Table 4.2 and Appendix C).

Table 4.2. Diffusion barriers (E_D) and limiting diffusivities (D_0) from this work and literature on related bulk II–VI semiconductors.

	E_D (eV)	D_0 (nm^2/s)
Mn^{2+} diffusion in Cd^{2+}:$Cd_{1-x}Mn_xSe$ (x ~0.15) nanocrystals[a]	1.1	9.8×10^4
Mn^{2+} diffusion in In^{3+}:$Cd_{1-x}Mn_xSe$ (x ~0.15) nanocrystals[a]	1.1	2.6×10^7
Mn^{2+} diffusion in CdTe/δ-MnTe/CdTe thin films[b]	1.35	1.7×10^8
Mn^{2+} diffusion in In^{3+}-doped CdTe/δ-MnTe/CdTe thin films[b,c]	1.35	4.2×10^{10}

[a]This work. [b]Ref. 31. [c]N_{In} ~1 x 10^{18} cm^{-3}.

In bulk II–VI and III–V semiconductors, Mn^{2+} diffusion is believed to primarily involve substitutional hopping mediated by cation vacancies.[31] For example, cation-vacancy-mediated diffusion of single Mn^{2+} ions inside bulk wurtzite AlN single crystals was recently observed directly using *Z*-contrast STEM imaging.[35] Similarly, copper vacancies have been found to accelerate room-temperature cation exchange in $Cu_{2-x}Se$ nanocrystals.[36] The simulations presented above suggest that a related vacancy-mediated diffusion mechanism is likely also operative in our $Cd_{1-x}Mn_xSe$ nanocrystals. This conclusion is supported by the dramatic increase in D_0 for cation exchange by In^{3+} relative to Cd^{2+}. When a cation of higher charge is introduced to replace Mn^{2+} in these $Cd_{1-x}Mn_xSe$ nanocrystals, the requirement for charge neutrality can be satisfied by formation of additional compensating cation vacancies, *i.e.*, the chemical potentials of cation vacancies are lowered. From Equation 4.2, this change in vacancy concentration increases $X_V^{Mn^{2+}}$, which increases D. In bulk CdS and CdTe, for example, In^{3+} incorporates as In_{Cd}, with doubly ionized cation vacancies (V_{Cd}'') as the likely charge compensating defects,[37-40] and these vacancies are believed to accelerate In^{3+} diffusion.[41-43] Additionally, in the nanocrystal experiments, the combination of weaker In^{3+}–Se^{2-} and stronger In^{3+}–O_{oleate} bonds

compared to Cd^{2+} should lower the effective cation activity of In^{3+} in solution relative to Cd^{2+} in solution, thereby also contributing to a larger time-averaged cation vacancy concentration. We note that the actual time-averaged vacancy concentration is unknown and may be extremely small (*e.g.*, << 1/nanocrystal) for both the Cd^{2+} and In^{3+} cation-exchange reaction conditions. Overall, we thus propose that Mn^{2+} cation exchange with In^{3+} in our $Cd_{1-x}Mn_xSe$ nanocrystals is accelerated relative to the same reaction performed with Cd^{2+} because In^{3+} increases the time-averaged concentration of cation vacancies. In this scenario, the experimental diffusion barriers reflect the combined activation energies of cation vacancy creation and Mn^{2+} exchange with vacant sites.

4.6 Conclusion

Mn^{2+} ions are spontaneously displaced from $Cd_{1-x}Mn_xSe$ nanocrystals *via* cation exchange when the thermodynamically preferred cations Cd^{2+} or In^{3+} are introduced to the nanocrystal solutions at elevated temperature. Under otherwise identical conditions, cation exchange is approximately two orders of magnitude faster when using In^{3+} compared to Cd^{2+}, illustrating the critical importance of the incoming cations. Kinetics measurements at various temperatures demonstrate that cation exchange is thermally activated for both Cd^{2+} and In^{3+} reactions, adhering to Arrhenius behavior over broad experimental temperature ranges. Quantitative analysis within a Fick's-law diffusion model yields the diffusion parameters E_D and D_0. Both cation-exchange reactions (Cd^{2+} and In^{3+}) are found to be governed by the same diffusion barrier, E_D = 1.1 eV. The large increase in D_0

(~250 times) when using In^{3+} is attributed to higher cation vacancy concentration, due either to lower effective cation activity in solution or to stabilization of charge-compensating cation vacancies. The accelerated diffusion observed when using In^{3+} to displace Mn^{2+} thus provides further evidence for cation vacancies as critical mechanistic features of these nanocrystal cation-exchange reactions. Overall, these findings provide unique experimental insights into cation diffusion within colloidal semiconductor nanocrystals, contributing to our fundamental understanding of this rich area of nanoscience and improving our ability to tailor the compositions of nanostructures for future advanced technological applications.

4.7 Appendix C

Additional EDX, electronic absorption, and MCD data; analysis of cation-exchange kinetics data; stoichiometry data; comparison of model results with interface flux *vs* fixed boundary condition; table of rate constants from analysis of cation-exchange kinetics; table of diffusion barriers and limiting diffusivities from this work and literature; and table of cation ionic radii.

4.8 Acknowledgments

This research was funded by the U.S. National Science Foundation (DMR-1408617 to D.R.G). P.C. acknowledges the Swiss National Science Foundation for Advanced Postdoc Mobility Fellowship (P300P2_161090). C.J.B. acknowledges Graduate Research Fellowship support from the University of Washington Clean Energy Institute.

4.9 References

1. Gösele, U. M. Fast Diffusion in Semiconductors. *Annu. Rev. Mater. Sci.* **1988**, *18*, 257–282.
2. Fedorov, V. A.; Ganshin, V. A.; Korkishko, Y. N. Ion Exchange in II–VI Crystals: Thermodynamics, Kinetics, and Technology. *Phys. Status Solidi A* **1993**, *139*, 9–65.
3. Heitjans, P.; Kärger, J. *Diffusion in Condensed Matter: Methods, Materials, Models*. Springer Science & Business Media: Berlin, 2005.
4. Son, D. H.; Hughes, S. M.; Yin, Y.; Alivisatos, A. P. Cation Exchange Reactions in Ionic Nanocrystals. *Science* **2004**, *306*, 1009–1012.
5. De Trizio, L.; Manna, L. Forging Colloidal Nanostructures via Cation Exchange Reactions. *Chem. Rev.* **2016**, *116*, 10852–10887.
6. Beberwyck, B. J.; Surendranath, Y.; Alivisatos, A. P. Cation Exchange: A Versatile Tool for Nanomaterials Synthesis. *J. Phys. Chem. C* **2013**, *117*, 19759–19770.
7. Rivest, J. B.; Jain, P. K. Cation Exchange on the Nanoscale: An Emerging Technique for New Material Synthesis, Device Fabrication, and Chemical Sensing. *Chem. Soc. Rev.* **2013**, *42*, 89–96.
8. Gupta, S.; Kershaw, S. V.; Rogach, A. L. 25th Anniversary Article: Ion Exchange in Colloidal Nanocrystals. *Adv. Mater.* **2013**, *25*, 6923–6944.
9. Casavola, M.; van Huis, M. A.; Bals, S.; Lambert, K.; Hens, Z.; Vanmaekelbergh, D. Anisotropic Cation Exchange in PbSe/CdSe Core/Shell Nanocrystals of Different Geometry. *Chem. Mater.* **2012**, *24*, 294–302.
10. Groeneveld, E.; Witteman, L.; Lefferts, M.; Ke, X.; Bals, S.; Van Tendeloo, G.; de Mello Donega, C. Tailoring ZnSe–CdSe Colloidal Quantum Dots via Cation Exchange: From Core/Shell to Alloy Nanocrystals. *ACS Nano* **2013**, *7*, 7913–7930.
11. Vlaskin, V. A.; Barrows, C. J.; Erickson, C. S.; Gamelin, D. R. Nanocrystal Diffusion Doping. *J. Am. Chem. Soc.* **2013**, *135*, 14380–14389.
12. Justo, Y.; Sagar, L. K.; Flamee, S.; Zhao, Q.; Vantomme, A.; Hens, Z. Less Is More. Cation Exchange and the Chemistry of the Nanocrystal Surface. *ACS Nano* **2014**, *8*, 7948–7957.
13. Fayette, M.; Robinson, R. D. Chemical Transformations of Nanomaterials for Energy Applications. *J. Mater. Chem. A* **2014**, *2*, 5965–5978.
14. Nedelcu, G.; Protesescu, L.; Yakunin, S.; Bodnarchuk, M. I.; Grotevent, M. J.; Kovalenko, M. V. Fast Anion-Exchange in Highly Luminescent Nanocrystals of Cesium Lead Halide Perovskites ($CsPbX_3$, X = Cl, Br, I). *Nano Lett.* **2015**, *15*, 5635–5640.
15. Barrows, C. J.; Chakraborty, P.; Kornowske, L. M.; Gamelin, D. R. Tuning Equilibrium Compositions in Colloidal $Cd_{1-x}Mn_xSe$ Nanocrystals Using Diffusion Doping and Cation Exchange. *ACS Nano* **2016**, *10*, 910–918.
16. Chan, T.-L.; Zayak, A. T.; Dalpian, G. M.; Chelikowsky, J. R. Role of Confinement on Diffusion Barriers in Semiconductor Nanocrystals. *Phys. Rev. Lett.* **2009**, *102*, 025901.

17. Malik, R.; Burch, D.; Bazant, M.; Ceder, G. Particle Size Dependence of the Ionic Diffusivity. *Nano Lett.* **2010**, *10*, 4123–4127.
18. Bothe, C.; Kornowski, A.; Tornatzky, H.; Schmidtke, C.; Lange, H.; Maultzsch, J.; Weller, H. Solid-State Chemistry on the Nanoscale: Ion Transport through Interstitial Sites or Vacancies? *Angew. Chem. Int. Ed.* **2015**, *54*, 14183–14186.
19. Li, H.; Brescia, R.; Krahne, R.; Bertoni, G.; Alcocer, M. J. P.; D'Andrea, C.; Scotognella, F.; Tassone, F.; Zanella, M.; De Giorgi, M.; Manna, L. Blue-UV-Emitting ZnSe(Dot)/ZnS(Rod) Core/Shell Nanocrystals Prepared from CdSe/CdS Nanocrystals by Sequential Cation Exchange. *ACS Nano* **2012**, *6*, 1637–1647.
20. van der Stam, W.; Bladt, E.; Rabouw, F. T.; Bals, S.; de Mello Donega, C. Near-Infrared Emitting $CuInSe_2$/$CuInS_2$ Dot Core/Rod Shell Heteronanorods by Sequential Cation Exchange. *ACS Nano* **2015**, *9*, 11430–11438.
21. Ott, F. D.; Spiegel, L. L.; Norris, D. J.; Erwin, S. C. Microscopic Theory of Cation Exchange in CdSe Nanocrystals. *Phys. Rev. Lett.* **2014**, *113*, 156803.
22. Luo, Y.-R. In *Comprehensive Handbook of Chemical Bond Energies*, Luo, Y.-R., Ed; CRC Press: Boca Raton, FL, 2007.
23. Carbone, L.; Nobile, C.; De Giorgi, M.; Sala, F. D.; Morello, G.; Pompa, P.; Hytch, M.; Snoeck, E.; Fiore, A.; Franchini, I. R.; Nadasan, M.; Silvestre, A. F.; Chiodo, L.; Kudera, S.; Cingolani, R.; Krahne, R.; Manna, L. Synthesis and Micrometer-Scale Assembly of Colloidal CdSe/CdS Nanorods Prepared by a Seeded Growth Approach. *Nano Lett.* **2007**, *7*, 2942–2950.
24. Qu, L.; Peng, X. Control of Photoluminescence Properties of CdSe Nanocrystals in Growth. *J. Am. Chem. Soc.* **2002**, *124*, 2049–2055.
25. Yu, W. W.; Peng, X. Formation of High-Quality CdS and Other II–VI Semiconductor Nanocrystals in Noncoordinating Solvents: Tunable Reactivity of Monomers. *Angew. Chem. Int. Ed.* **2002**, *41*, 2368–2371.
26. Yu, W. W.; Qu, L.; Guo, W.; Peng, X. Experimental Determination of the Extinction Coefficient of CdTe, CdSe, and CdS Nanocrystals. *Chem. Mater.* **2003**, *15*, 2854–2860.
27. Piepho, S. B.; Schatz, P. N. *Group Theory in Spectroscopy with Applications to Magnetic Circular Dichroism*. Wiley: New York, 1983.
28. Beaulac, R.; Ochsenbein, S. T.; Gamelin, D. R. Colloidal Transition-Metal-Doped Quantum Dots. In *Nanocrystal Quantum Dots*, 2nd ed.; Klimov, V. I., Ed; CRC Press: Boca Raton, FL, 2010; pp 397–453.
29. Furdyna, J. K. Diluted Magnetic Semiconductors. *J. Appl. Phys.* **1988**, *64*, R29–R64.
30. Barrows, C. J.; Vlaskin, V. A.; Gamelin, D. R. Absorption and Magnetic Circular Dichroism Analyses of Giant Zeeman Splittings in Diffusion-Doped Colloidal $Cd_{1-x}Mn_xSe$ Quantum Dots. *J. Phys. Chem. Lett.* **2015**, *6*, 3076–3081.
31. Barcz, A.; Karczewski, G.; Wojtowicz, T.; Kossut, J. Manganese Diffusion in MBE-Grown Cd(Mn)Te Structures. *J. Cryst. Growth* **1996**, *159*, 980-984.
32. Cowern, N. E. B.; van de Walle, G. F. A.; Gravesteijn, D. J.; Vriezema, C. J. Experiments on Atomic-Scale Mechanisms of Diffusion. *Phys. Rev. Lett.* **1991**, *67*, 212.

33. Norberg, N. S.; Parks, G. L.; Salley, G. M.; Gamelin, D. R. Giant Excitonic Zeeman Splittings in Colloidal Co^{2+}-Doped ZnSe Quantum Dots. *J. Am. Chem. Soc.* **2006**, *128*, 13195–13203.
34. Beaulac, R.; Feng, Y.; May, J. W.; Badaeva, E.; Gamelin, D. R.; Li, X. Orbital Pathways for Mn^{2+}-Carrier *sp–d* Exchange in Diluted Magnetic Semiconductor Quantum Dots. *Phys. Rev. B* **2011**, *84*, 195324.
35. Ishikawa, R.; Mishra, R.; Lupini, A. R.; Findlay, S. D.; Taniguchi, T.; Pantelides, S. T.; Pennycook, S. J. Direct Observation of Dopant Atom Diffusion in a Bulk Semiconductor Crystal Enhanced by a Large Size Mismatch. *Phys. Rev. Lett.* **2014**, *113*, 155501.
36. Lesnyak, V.; Brescia, R.; Messina, G. C.; Manna, L. Cu Vacancies Boost Cation Exchange Reactions in Copper Selenide Nanocrystals. *J. Am. Chem. Soc.* **2015**, *137*, 9315–9323.
37. Kumar, V.; Kröger, F. A. Self-Diffusion and the Defect Structure of Cadmium Sulfide. *J. Solid State Chem.* **1971**, *3*, 387–400.
38. Shaw, D. Diffusion Mechanisms in II–VI Materials. *J. Cryst. Growth* **1988**, *86*, 778–796.
39. Chern, S. S.; Kröger, F. A. The Relative Magnitude of the Diffusion Constants of Cadmium Vacancies and Indium–Cadmium Vacancy Pairs in CdS and CdTe. *Phys. Status Solidi A* **1974**, *25*, 215–222.
40. Kato, H.; Takayanagi, S. Diffusion of Indium in Cadmium Telluride. *Jpn. J. Appl. Phys.* **1963**, *2*, 250.
41. Jones, E. D.; Mykura, H. Diffusion of Indium into Cadmium Sulphide. *J. Phys. Chem. Solids* **1978**, *39*, 11–18.
42. Jones, E. D.; Vere, D. M. Diffusion of Indium into Cadmium Indium Sulphide ($In_{0.016}Cd_{0.976}S$). *J. Cryst. Growth* **1985**, *72*, 184–188.
43. Watson, E.; Shaw, D. The Solubility and Diffusivity of In in CdTe. *J. Phys. C: Solid State Phys.* **1983**, *16*, 515.

Chapter 5. Excitonic Zeeman Splittings in Colloidal CdSe Quantum Dots Doped with Single Magnetic Impurities*

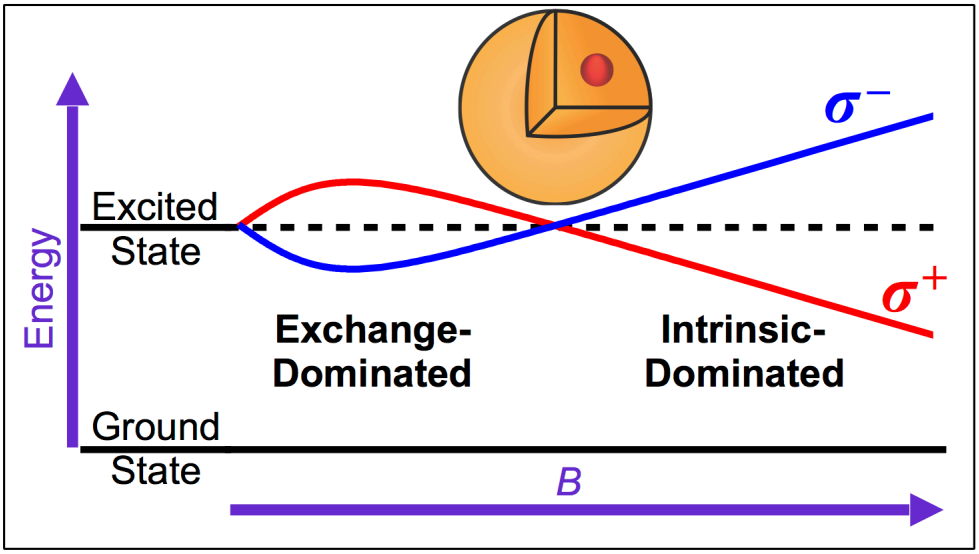

*Reproduced from Barrows, C. J.; Fainblat, R.; Gamelin, D. R. *submitted*.

5.1 Overview

Doping a semiconductor quantum dot with just a single impurity atom can completely transform its physical properties. Here, we report and analyze the magnetic circular dichroism (MCD) spectra of colloidal CdSe quantum dot samples containing on average fewer than one Mn^{2+} per quantum dot. Even at this sub-single-dopant level, the low-temperature low-field data are dominated by impurity-induced Zeeman splittings caused by dopant–carrier *sp*–*d* exchange. Unlike in more heavily doped quantum dots, however, the MCD intensity at the first CdSe exciton shows a field-induced sign flip as the field strength is increased, reflecting competition between *sp*–*d* exchange effects and the intrinsic Zeeman splittings of comparable magnitude. Most unusually, the competition between these two effects leads to a large apparent shift in the first MCD peak maximum, which we show is attributable to a difference in sign of the intrinsic excitonic *g* factor between the first and second excitons. Finally, the *sp*–*d* and intrinsic contributions to the excitonic Zeeman splittings each exhibit unique magnetic field and temperature dependencies, allowing the MCD spectra of undoped, singly doped, and bi-doped quantum dot sub-ensembles to be analyzed.

5.2 Introduction

Incorporation of impurities allows the electrical properties of semiconductors to be tuned, enabling the development of transistors, diodes, and other workhorses of solid-state technology. In addition to electrical effects, impurities can also be used to modify the optical and magnetic properties of semiconductors. Addition of paramagnetic transition metal ions to bulk semiconductors yields so-called "diluted magnetic semiconductors" (DMSs), which combine magnetic and semiconducting properties in a single material.[1, 2] In DMSs, dopant-carrier *sp–d* magnetic exchange coupling gives rise to such characteristic magneto-electric and magneto-optical effects as giant excitonic Zeeman splittings,[3] giant Faraday rotation,[1] electrical spin polarization,[4, 5] and photo-induced magnetization,[6, 7] making these materials promising candidates for applications in spin-electronics and spin-photonics.[8-10]

Mn^{2+}-doped CdSe has long served as a model system for investigation of DMSs at the nanoscale.[11, 12] Recent advances in nanocrystal diffusion doping have enabled the preparation of high-quality colloidal $Cd_{1-x}Mn_xSe$ QDs with dopant concentrations tunable from 0 to ~30%.[13-15] Due to their smaller volumes, such colloidal DMS QDs can show even stronger *sp–d* exchange coupling than the corresponding bulk materials or epitaxial quantum dots.[16, 17] Moreover, their magneto-optical properties can be engineered synthetically by tuning nanocrystal sizes, shapes, compositions, and heterointerfaces to control the spatial overlap between the dopants and the confined semiconductor charge carriers. Such diffusion-doped $Cd_{1-x}Mn_xSe$ QDs have already been used to demonstrate

exceedingly large excitonic Zeeman splittings (with g_{Exc} values up to –1180),[18, 19] valence-band mixing effects,[20] picosecond spin dynamics in robust excitonic magnetic polarons,[19] and the impacts of Mn^{2+} spin fluctuations.[19, 21] Recently, we reported the observation of giant zero-field excitonic exchange splittings in colloidal $Cd_{1-x}Mn_xSe$ QDs containing single Mn^{2+} dopants.[22] Due to the small volumes of these QDs, the largest *sp–d* exchange splittings were almost two orders of magnitude greater than those reported for epitaxial DMS QDs.[23-26] This observation motivates additional spectroscopic characterization of colloidal $Cd_{1-x}Mn_xSe$ QDs in this low-doping regime.

Here, we report MCD studies of ensembles of colloidal $Cd_{1-x}Mn_xSe$ QDs possessing on average fewer than one Mn^{2+} dopant per QD. Low-temperature MCD spectra of these ensembles show a very unusual magnetic-field dependence, including a sign inversion of the first exciton at moderate magnetic fields but no sign inversion of the second exciton. The MCD intensities at the first excitonic transition are shown to reflect the competition between comparable but opposing intrinsic and *sp–d* exchange contributions to the excitonic Zeeman splitting, whereas the intrinsic and *sp–d* exchange contributions add constructively at the second exciton. Analysis of the experimental data yields the MCD spectra of QD sub-ensembles containing exactly one and two Mn^{2+} dopants per QD. Even at just one Mn^{2+} per QD, *sp–d* exchange dominates over the intrinsic Zeeman splittings, but their comparable magnitudes yield anomalous spectral field dependencies, highlighting the unique magneto-optical properties of QDs in this low-doping limit.

5.3 Results and Analysis

Mn^{2+}-doped CdSe QDs were prepared by the diffusion-doping method detailed previously[13-15] (see Section 5.5.1). Figure 5.1A shows a representative transmission electron microscopy (TEM) image of pseudo-spherical $Cd_{1-x}Mn_xSe$ QDs with diameter d = 5.1 ± 0.3 nm. From inductively coupled plasma atomic emission spectroscopy (ICP-AES), x = 0.00053 ± 0.00005, corresponding to an average of 0.70 ± 0.07 Mn^{2+} dopants per nanocrystal. Using these values and a Poisson distribution function (modified to take into account the QD Gaussian size distribution according to the methods described in the Appendix of reference 27) yields the expected dopant distribution shown in red circles in Figure 5.1B, in which ~51% of the QDs are undoped, ~34% have exactly 1 Mn^{2+}/QD, and only ~12% have 2 Mn^{2+}/QD. Independently, the *effective* doping level was also determined by MCD spectroscopy (*vide infra*) and the corresponding distribution (which also takes into account the QD Gaussian size distribution) is shown in blue bars in Figure 5.1B. Here, the average Mn^{2+} concentration is 0.40 ± 0.02/QD (x = 0.00030 ± 0.00002), which corresponds to ~68% of the QDs being undoped, ~26% having exactly 1 Mn^{2+}/QD, and ~5% having exactly 2 Mn^{2+}/QD. The average doping concentrations determined by the two different methods (ICP-AES and MCD) agree reasonably well and their difference may reflect a small deviation from strictly statistical Mn^{2+} doping in this sample. Still, these data suggest an isotropic distribution of dopants consistent with previous studies of similar diffusion-doped QDs.[15, 22, 28] For the remainder of our analyses we will use the *effective* doping level determined by MCD spectroscopy, because this

corresponds to the magneto-optically active Mn^{2+} concentration, but the same conclusions are reached when using the analytical value.

Figure 5.1C shows a room-temperature EPR spectrum of these QDs. Six hyperfine lines of approximately equal intensity are observed, with a splitting of $|A| = 62.1 \times 10^{-4}$ cm^{-1}, consistent with substitutional Mn^{2+} in CdSe.[29] The narrow feature width and absence of broad underlying intensity are both consistent with negligible Mn^{2+}–Mn^{2+} dipolar coupling, as anticipated at this low doping concentration.

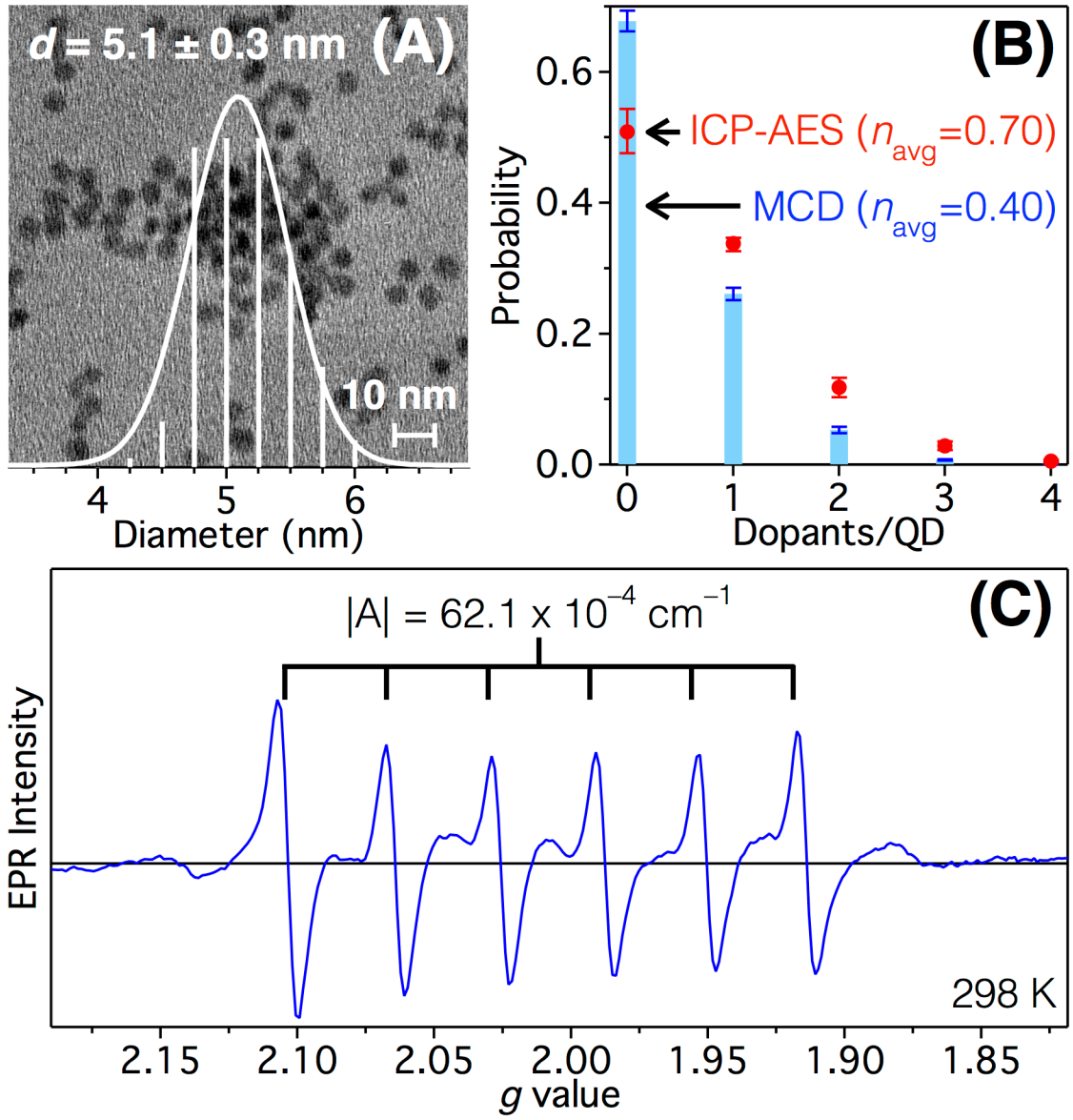

Figure 5.1. **(A)** TEM image and corresponding size histogram of d = 5.1 ± 0.3 nm (σ = 5.9%) $Cd_{1-x}Mn_xSe$ QDs. **(B)** Poisson distribution of dopants taking into account the QD Gaussian size distribution, determined from analysis of the size histogram in panel A and calculated from the average Mn^{2+} concentration determined by ICP-AES (red circles; n_{avg} = 0.70 Mn^{2+}/QD) or MCD (blue bars; n_{avg} = 0.40 Mn^{2+}/QD). **(C)** Room-temperature EPR spectrum of these QDs, showing well-resolved Mn^{2+} hyperfine structure ($|A|$ = 62.1 × 10^{-4} cm^{-1}) consistent with the very low Mn^{2+} concentration.

Figure 5.2A shows the 1.7 K zero-field electronic absorption spectrum of the QDs from Figure 5.1, and Figure 5.2B plots 1.7 K variable-field MCD spectra collected from 0 to 6 T for the same sample. At low magnetic fields, the low-energy leading-edge intensity of the MCD spectrum grows increasingly positive with increasing magnetic field, indicating a negative Zeeman splitting consistent with Mn^{2+}-doped CdSe.[12, 18, 30] This intensity reaches a maximum at ~1.5 T and then decreases and changes sign at higher fields, indicating a positive Zeeman splitting above ~4 T. At the maximum magnetic field (6 T), the MCD spectrum of this sample more closely resembles that of undoped CdSe QDs[31] than of any $Cd_{1-x}Mn_xSe$ QDs reported previously (see Appendix D).

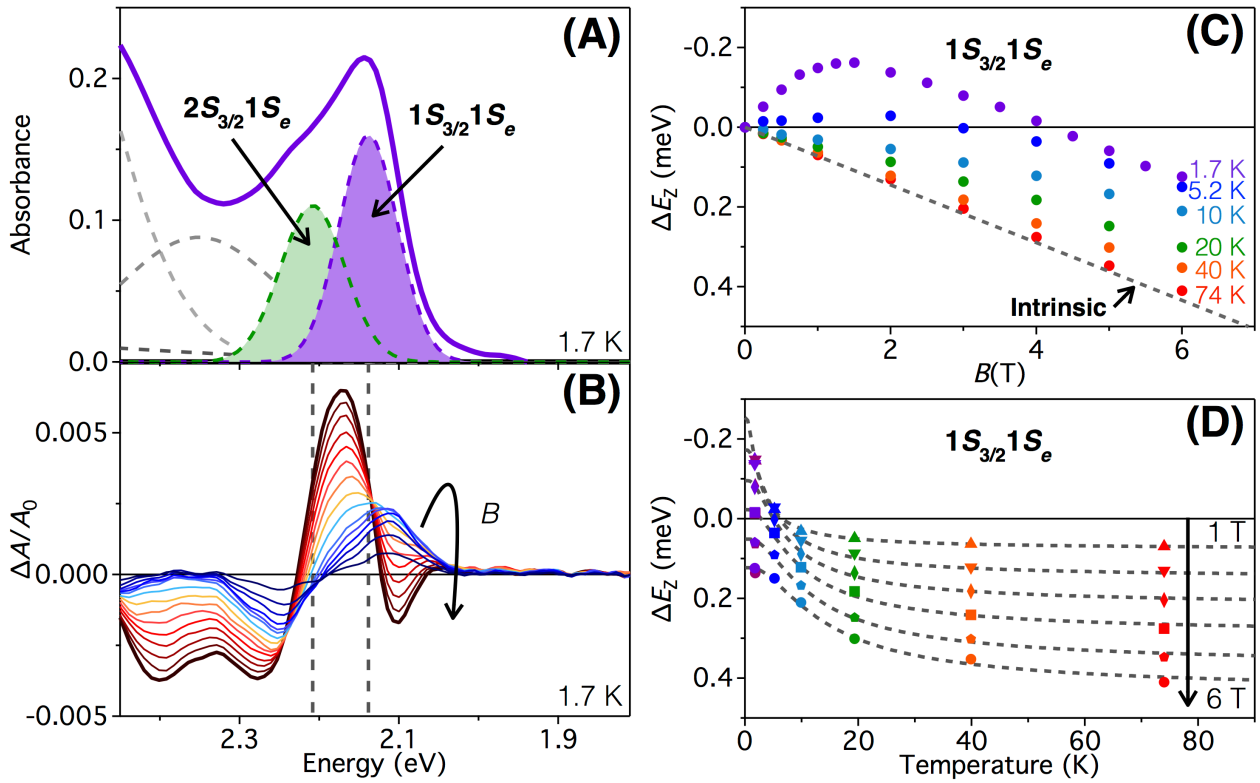

Figure 5.2. **(A)** 1.7 K electronic absorption spectrum (purple line) and multi-peak Gaussian fit (dashed lines) of d = 5.1 nm $Cd_{0.9997}Mn_{0.0003}Se$ QDs, showing the first two allowed excitonic transitions (filled curves). **(B)** Corresponding variable-field (0–6 T; blue to red lines) MCD data for the same QDs at 1.7 K. The arrow indicates the direction of increasing magnetic field. The vertical dashed lines indicate the average energies of the first two excitonic transitions. **(C)** Field-dependent Zeeman splitting energies of the first exciton, determined from analysis of these variable-temperature, variable-field MCD spectra. (Spectra collected at temperatures above 1.7 K are included in Appendix D.) The intrinsic component (which is temperature-independent) is plotted as a gray dashed line. **(D)** Temperature dependence of the first excitonic Zeeman splitting from 1 T (upward triangles) to 6 T (circles). The gray dashed lines represent a global fit to the data as described in the text, and correspond to x_{Eff} = 0.00030 (0.40 Mn^{2+}/QD).

Excitonic Zeeman splittings (ΔE_Z) of the $1S_{3/2}1S_e$ exciton were calculated from the absorption and MCD data of Figure 5.2A–B using Equation 5.1,[12, 18] where $\Delta A'$ corresponds to the maximum amplitude of the lowest-energy leading-edge MCD feature and A_0 and σ are the height and Gaussian width of the absorption peak, respectively, determined by multi-peak Gaussian fitting using fixed heights and widths across the magnetic field range, according to the rigid-shift approximation.[12, 32] Figure 5.2C plots ΔE_Z as a function of magnetic field and temperature, showing the inversion of $\Delta A'/A_0$ with magnetic field seen in the raw 1.7 K spectra of Figure 5.2B. Similar results are obtained from the 5.2 K data, but the sign inversion occurs at a smaller field. At 10 K and above, ΔE_Z is positive at every magnetic field. Absorption and MCD spectra collected at temperatures above 1.7 K are included in Appendix D.

$$\Delta E_Z = \frac{\sqrt{2e}}{2}\sigma\frac{\Delta A'}{A_0} \tag{5.1}$$

To extract an effective Mn^{2+} concentration, these Zeeman splitting data were replotted *vs* temperature (Figure 5.2D) and analyzed. Following the approach of reference 33, the data in Figure 5.2D were fit to Equation 5.2, where x_{Eff} is the effective Mn^{2+} concentration, $N_0(\alpha - \beta)$ describes the bulk *sp–d* exchange (1.5 eV),[34] and $\langle S_Z \rangle$ is the spin expectation value of Mn^{2+}, which follows Brillouin behavior for a spin-only $S = -5/2$ ground state (Equation 5.3; $g_{Mn} = 2.0042$ and T = experimental temperature). Equation 5.2 describes ΔE_Z as the sum of intrinsic (ΔE_{Int}) and *sp–d* exchange (ΔE_{sp-d}) terms, where ΔE_{Int} is temperature-independent and scales linearly with field, g_{Int} is the intrinsic excitonic g value, μ_B is the Bohr magneton, and B is the magnetic field. The dashed lines in

Figure 5.2D show a global best fit to these data, yielding x_{Eff} = 0.00030 ± 0.00002, which corresponds to 0.40 Mn^{2+}/QD and the doping statistics plotted in Figure 5.1B.

$$\Delta E_{Zeeman} = g_{Int}\mu_B B + x_{Eff} N_0(\alpha - \beta)\langle S_Z\rangle \quad (5.2a)$$

$$= \Delta E_{Int} + \Delta E_{sp-d} \quad (5.2b)$$

$$S_Z = \frac{2S+1}{2}\coth\left(\frac{2S+1}{2}\bullet\frac{g_{Mn}\mu_B B}{k_B T}\right) - \frac{1}{2}\coth\left(\frac{g_{Mn}\mu_B B}{2k_B T}\right) \quad (5.3)$$

All MCD spectra of other $Cd_{1-x}Mn_xSe$ QDs reported previously have been overwhelmingly dominated by the *sp–d* exchange terms. In contrast, the MCD spectra in Figure 5.2B show clear evidence of both intrinsic and *sp–d* exchange contributions simultaneously. Whereas ΔE_{sp-d} becomes field-independent when all of the Mn^{2+} spins have been aligned by the magnetic field ($\langle S_Z\rangle$ = –5/2), ΔE_{Int} continues to increase linearly with B (Equation 5.2a). In this regime, *e.g.*, above ~2.5 T at 1.7 K in Figure 5.2C, the intrinsic Zeeman contribution to the MCD spectra of Figure 5.2B can be isolated according to Equation 5.4, where $(\Delta A/A_0)_B$ is the MCD spectrum at magnetic field B.

$$(\Delta A/A_0)_{Int,1} = (\Delta A/A_0)_6 - (\Delta A/A_0)_5 \quad (5.4)$$

Scaling $(\Delta A/A_0)_{Int,1}$ to experimental magnetic fields from 0 to 6 T yields the spectra shown in Figure 5.3A. Analysis of these spectra gives g_{Int} = +1.3, which agrees well with literature values for CdSe QDs of this size.[31] Subtraction of these spectra from the data in Figure 5.2B yields intensities attributable solely to *sp–d* exchange (Figure 5.3B). As expected, the low-energy leading edge of these spectra has the opposite sign compared to the intrinsic spectra, and its amplitude follows the S = –5/2 Brillouin curve.

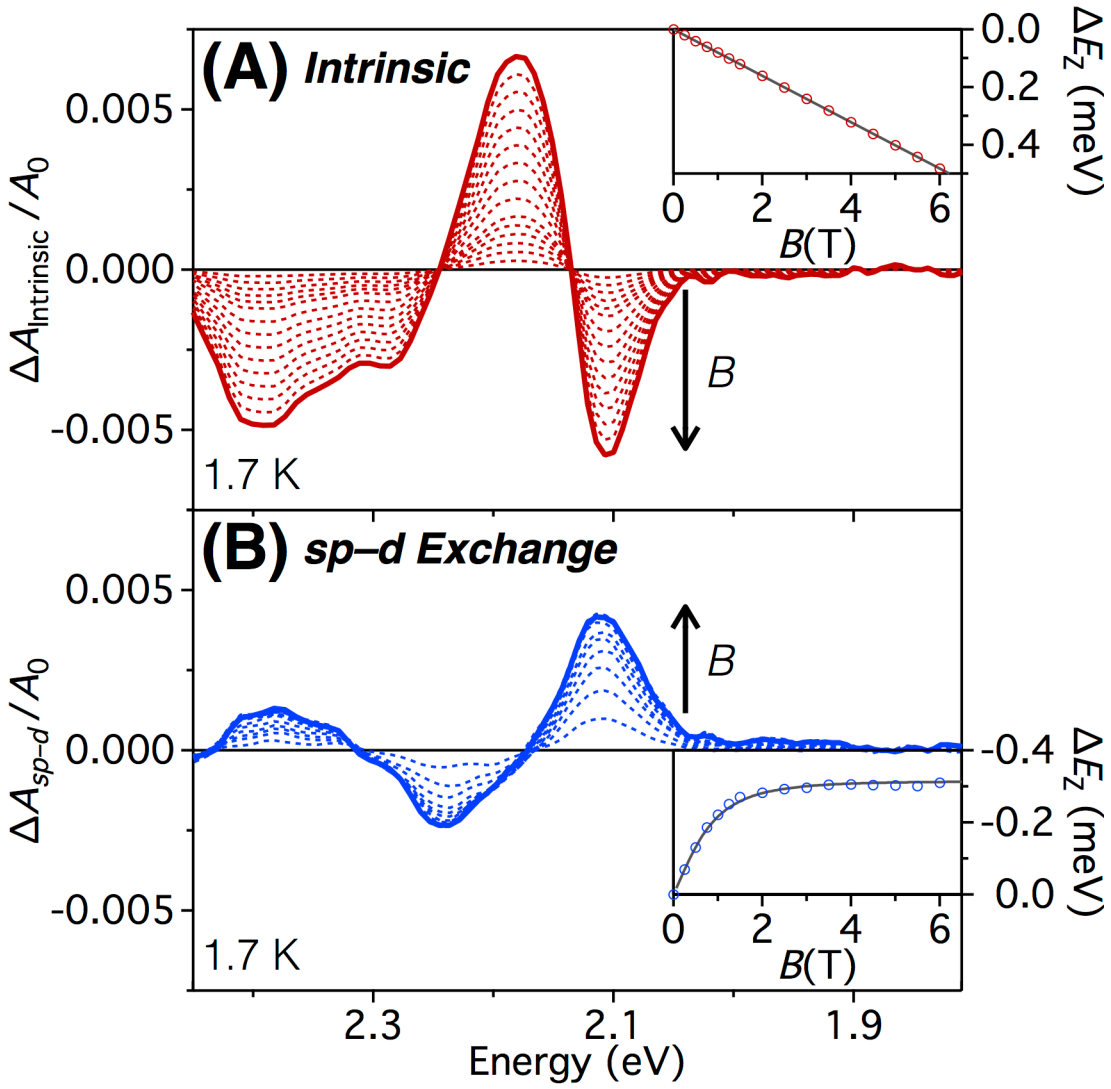

Figure 5.3. (A) Intrinsic component of the variable-field MCD spectra from Figure 5.2B, deconvolved according to Equation 5.4. (B) *sp–d* exchange component of the MCD spectra from Figure 5.2B, deconvolved by subtracting the spectra of Figure 5.3A from the spectra of Figure 5.2B. Arrows indicate the direction of increasing magnetic field (0–6 T). Insets: Field dependence of the intrinsic (top) and *sp–d* exchange (bottom) contributions to the first exciton's Zeeman splitting. The *sp–d* exchange term was fit to an $S = -5/2$ Brillouin curve (gray line).

The MCD data in Figure 5.3 allow reconstruction of MCD spectra of QD *ensembles* doped with specific integer numbers of Mn^{2+} ions (rather than with a Poisson distribution of dopants) using Equation 5.5, where n indicates the integer number of dopants per QD. Equation 5.5 assumes that the *sp–d* exchange term $(\Delta A(B)/A_0)_{sp-d}$ scales linearly with n, which has previously been demonstrated for such QDs[14] in the limit of low x, where Mn^{2+}–Mn^{2+} interactions are negligible. The resulting reconstructed spectra are shown in Figure 5.4A–B. At 2 Mn^{2+}/QD (Figure 5.4A), the MCD spectra resemble the "typical" data reported for other $Cd_{1-x}Mn_xSe$ QDs, where *sp–d* exchange dominates and $\Delta A/A_0$ is positive at the leading edge of the first exciton.[13, 30] At 1 Mn^{2+}/QD (Figure 5.4B), the MCD spectra also display a positive leading edge at all experimental fields, but $\Delta A'/A_0$ clearly turns over at ~2 T, and the peak maximum appears to blue-shift by ~40 meV over the full field range. Figure 5.4C plots ΔE_Z of the $1S_{3/2}1S_e$ exciton, extracted from each of the reconstructed spectra in Figure 5.4A–B, as well as ΔE_{Int} from Figure 5.3A. At all experimental fields, $\Delta E_Z < 0$ for the QDs with quantized dopants and $\Delta E_Z > 0$ for undoped QDs.

$$\left(\frac{\Delta A(B)}{A_0}\right)_n = \left(\frac{\Delta A(B)}{A_0}\right)_{Int} + \frac{n}{n_{avg}}\left(\frac{\Delta A(B)}{A_0}\right)_{sp-d} \tag{5.5}$$

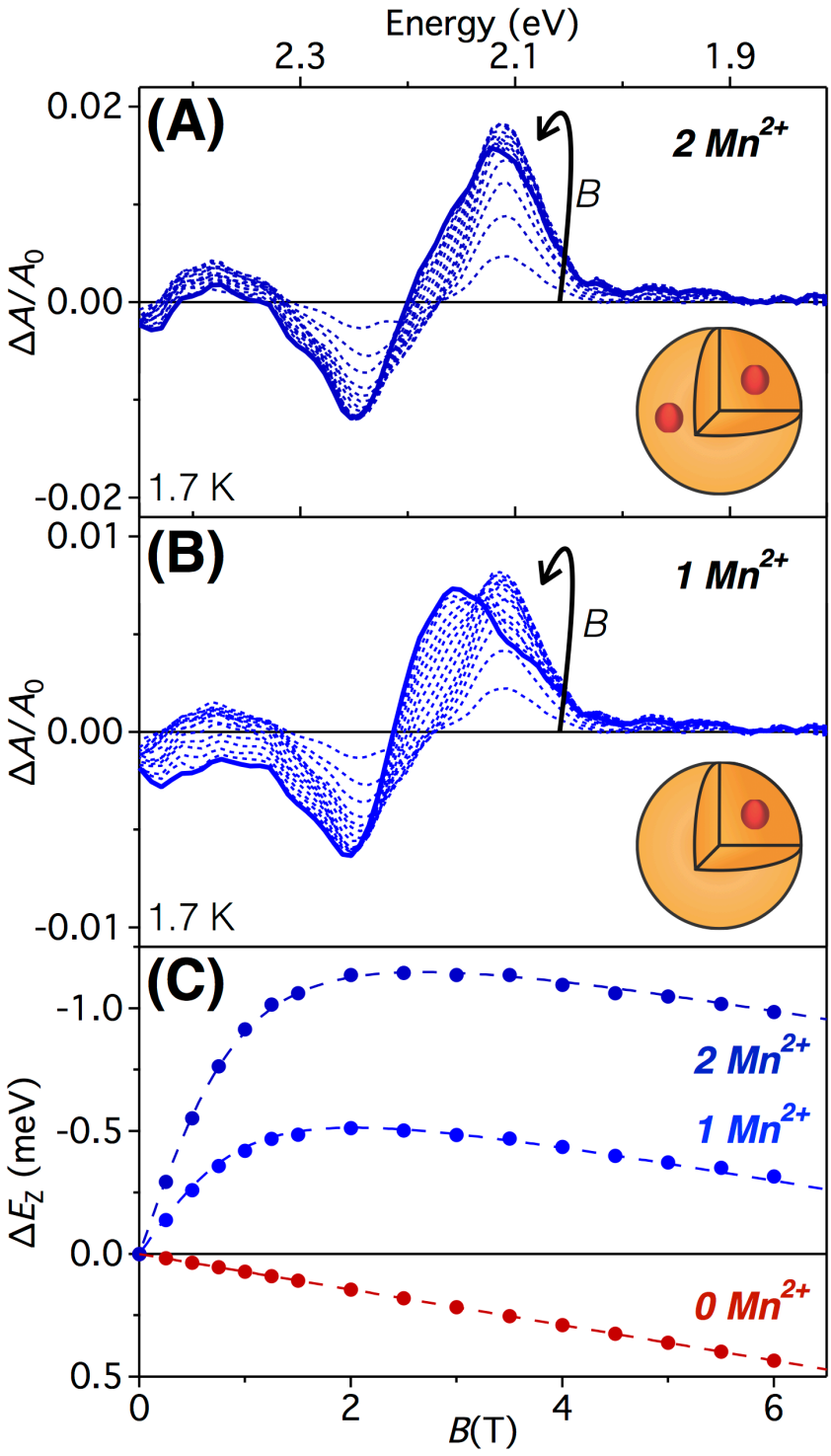

Figure 5.4. Variable-field MCD spectra measured at 1.7 K, deconvolved from the data in Figure 5.2B according to Equation 5.5 for $Cd_{1-x}Mn_xSe$ QDs containing exactly 2 **(A)** or exactly 1 **(B)** Mn^{2+} per QD. The arrows indicate the direction of increasing magnetic field from 0–6 T. **(C)** Corresponding Zeeman splittings of the $1S_{3/2}1S_e$ transition in each of these data sets, and also for undoped CdSe QDs from Figure 5.3A.

It is remarkable that the *sp–d* exchange dominates over the intrinsic excitonic Zeeman splitting after adding only 1 Mn^{2+} in a d = 5.1 nm CdSe QD. This result is particularly significant because the data here reflect the full distribution of radial Mn^{2+} positions within the ensemble of QDs, meaning the *sp–d* exchange strength is sufficiently large for just 1 Mn^{2+} to cause a giant magneto-optical response even when that Mn^{2+} is located at the average cation radius instead of near the QD center. Although an MCD sign inversion was previously observed for CdSe clusters doped with 1 Mn^{2+} per cluster,[35, 36] the effective dopant concentration in these QDs is approximately two orders of magnitude smaller than in those clusters. In self-assembled (epitaxially grown) $Cd_{1-x}Mn_xSe$ QDs, inversion of the excitonic Zeeman splitting has been predicted for effective dopant concentrations above $x \approx 0.001$, but only tested for samples that contained nominal dopant concentrations above 1%.[37] These results are most reminiscent of the non-monotonic field dependence observed in magneto-reflectivity measurements of $Cd_{1-x}Mn_xTe$ quantum wells with extremely small values of x.[38] We note that the data for 1 Mn^{2+}/QD suggest that the average QD's first-exciton exchange splitting is 0.64 meV even at zero applied magnetic field. Interestingly, this value is smaller than the exciton linewidths observed in the single-particle photoluminescence spectra attributed to undoped NCs within similar $Cd_{1-x}Mn_xSe$ QD ensembles (~6 meV at 5 K).[22] These results thus confirm the hypothesis presented in reference 22 that single-QDs showing much larger zero-field excitonic *sp–d* exchange splittings (approaching ~|80| meV) must have their Mn^{2+} ions significantly closer to their centers than the average cation position, where dopant-exciton spatial overlap (and hence also the *sp–d* exchange coupling strength) is maximized. We

estimate that the *sp–d* exchange energy is ~50 times greater for a Mn^{2+} at the exact center of a d = 5.1 nm CdSe QD than for a Mn^{2+} at the average distance from the QD center,[16, 22] consistent with this conclusion.

Finally, we analyze the anomalous spectral evolution with magnetic field shown in Figures 5.2B and 5.4B. This behavior appears to be unique to the case of ≤1 Mn^{2+}/QD (avg.), where ΔE_{Int} and ΔE_{sp-d} are most comparable in magnitude. Analysis shows that this unusual behavior derives from a change in the relative *signs* of ΔE_{Int} and ΔE_{sp-d} between the first ($1S_{3/2}1S_e$) and second ($2S_{3/2}1S_e$) excitonic transitions. Figure 5.5A–B summarizes the contrast between the first and second excitons of the full ensemble (0.4 Mn^{2+}/QD) by plotting the field-dependence of ΔE_{Int} and ΔE_{sp-d} for each transition. The sums of these individual contributions yield the black dashed lines, which overlay with the total Zeeman splittings calculated from the raw spectra of Figure 5.2B (black circles and triangles). Figure 5.5C–E re-plots the 2, 4, and 6 T MCD spectra of Figure 5.2B, respectively, along with the Gaussian fit results for the first two excitonic transitions. At low fields, ΔE_Z is dominated by ΔE_{sp-d} which is negative for both the $1S_{3/2}1S_e$ and $2S_{3/2}1S_e$ transitions, resulting in MCD spectra like those of Figure 5.5C. As the field increases, ΔE_{sp-d} saturates and ΔE_{Int} begins to rival it in magnitude. ΔE_{Int} is positive for the $1S_{3/2}1S_e$ exciton, causing it to oppose and diminish this exciton's MCD intensity, but ΔE_{Int} is negative for the $2S_{3/2}1S_e$ exciton,[20] causing the MCD intensity of this exciton to continue growing with increasing field. Near 4 T, the magnitudes of ΔE_{Int} and ΔE_{sp-d} for the $1S_{3/2}1S_e$ exciton are nearly identical, leading to complete cancellation of this exciton's MCD intensity. The experimental MCD spectrum at 4 T (Figure 5.5D) therefore shows only higher-energy

transitions, beginning with the $2S_{3/2}1S_e$ exciton. At higher fields (Figure 5.5E), ΔE_Z is dominated by ΔE_{Int}. This contrast between opposing *vs* additive combinations of intrinsic and *sp–d* contributions is only observed in this extremely low doping limit, and explains the anomalous MCD spectral characteristics and intensity inversion in the MCD spectra of Figure 5.2B.

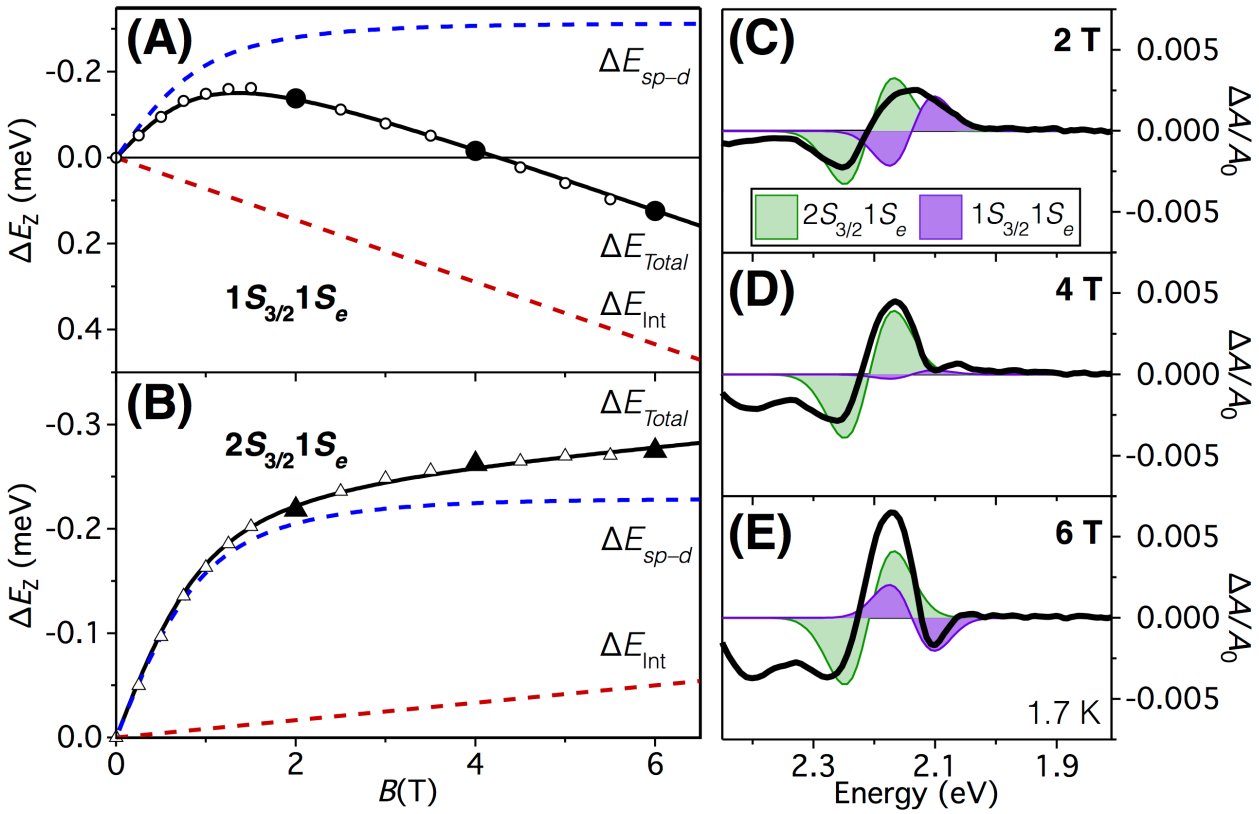

Figure 5.5. (A–B) Total Zeeman splittings (black) of the $1S_{3/2}1S_e$ (A; circles) and $2S_{3/2}1S_e$ (B; triangles) excitonic transitions as determined from analysis of the magnetic field dependent MCD spectra of $Cd_{0.9997}Mn_{0.0003}Se$ QDs at 1.7 K, divided into their intrinsic (red) and *sp–d* exchange (blue) components. Closed symbols correspond to the three sets of MCD spectra plotted in panels C–E. (C–E) MCD spectra (black) at 1.7 K and 2 T (C), 4 T (D), and 6 T (E), along with their respective contributions from the $1S_{3/2}1S_e$ (purple) and $2S_{3/2}1S_e$ (green) transitions.

5.4 Conclusion

In summary, MCD spectra of colloidal CdSe QDs doped with trace Mn^{2+} reflect the rich relationship between intrinsic and *sp–d* exchange contributions to the excitonic Zeeman splittings of these materials. Opposing and additive contributions of these terms to ΔE_Z in the $1S_{3/2}1S_e$ and $2S_{3/2}1S_e$ transitions, respectively, generate abnormal bandshapes and an intensity turnover in the variable-field MCD spectra of these QDs. Spectral deconvolution allows reconstruction of the MCD spectra for QD ensembles possessing exactly 1 and 2 Mn^{2+}/QD, which are both still dominated by *sp–d* exchange even when the average dopant is not located in the QD center. These data reveal unique spectroscopic properties in ensembles of colloidal QDs containing exactly one Mn^{2+} per QD, despite radial doping distributions, and they highlight the ability of even single dopants to transform the physical properties of quantum-confined semiconductor nanostructures.

5.5 Experimental Methods

5.5.1 Synthesis

$Cd_{1-x}Mn_xSe$ nanocrystals were prepared by diffusion doping in the Se^{2-}-limited regime according to the methods described in references 13 and 14. After doping, the QDs were cooled to room temperature and washed by repeated suspensions in toluene and flocculation with ethanol.

5.5.2 Physical Characterization

Atomic concentrations were determined by analysis of dried nanocrystals digested in ultrapure nitric acid (EMD Chemicals) using inductively coupled plasma atomic emission spectrometry (ICP-AES; Perkin-Elmer). Room-temperature electron paramagnetic resonance (EPR) experiments were performed on colloidal toluene suspensions of nanocrystals using an X-band Bruker EMX spectrometer. Low-temperature absorption and magnetic circular dichroism (MCD) spectra were collected on nanocrystal films prepared by depositing a toluene suspension of nanocrystals between quartz disks. The films were placed in a superconducting magneto-optical cryostat (Cryo-Industries SMC-1659 OVT) oriented in the Faraday configuration. At helium temperature, the sample was screened for depolarization by matching the CD spectra of a chiral molecule placed before and after the sample. Depolarization of the thin film was <5 %. Electronic absorption and MCD spectra were collected simultaneously using an Aviv 40DS spectropolarimeter. The differential absorption collected in the MCD experiment is reported as $\Delta A = A_L - A_R$, where A_L and A_R refer to the absorption of left and right circularly polarized photons in the sign convention of Piepho and Schatz.[12, 32] From these data, values of ΔE_{Zeeman} and g_{Exc} can be obtained.[12, 13, 18]

5.6 Appendix D

Additional absorption and MCD spectra, Zeeman-splitting analysis, and a table of *g* values.

5.7 Acknowledgments

This research was funded by the US National Science Foundation (DMR-1505901 to D.R.G.). R.F. was supported by the German Academic Exchange Service (DAAD) with funds from the German Federal Ministry of Education and Research (BMBF) and the People Programme (Marie Curie Actions) of the European Union's Seventh Framework Programme (FP7/2007-2013) under REA grant agreement n° 605728 (P.R.I.M.E. – Postdoctoral Researchers International Mobility Experience). The authors thank Mr. Michael De Siena for performing TEM measurements.

5.8 References

1. Furdyna, J. K.; Kossut, J., *Diluted Magnetic Semiconductors*. Academic: N.Y., 1988; Vol. 25 of Semiconductors and Semimetals.
2. Gaj, J. A.; Kossut, J., *Introduction to the Physics of Diluted Magnetic Semiconductors*. Springer-Verlag: Berlin, 2010; Vol. 144.
3. Aggarwal, R. L.; Jasperson, S. N.; Stankiewicz, J.; Shapira, Y.; Foner, S.; Khazai, B.; Wold, A. Magnetoreflectance at the Band Edge in $Cd_{1-x}Mn_xSe$. *Phys. Rev. B* **1983**, *28*, 6907–6913.
4. Ohno, Y.; Young, D. K.; Beschoten, B.; Matsukura, F.; Ohno, H.; Awschalom, D. D. Electrical Spin Injection in a Ferromagnetic Semiconductor Heterostructure. *Nature* **1999**, *402*, 790-792.
5. Jonker, B. T.; Park, Y. D.; Bennett, B. R.; Cheong, H. D.; Kioseoglou, G.; Petrou, A. Robust Electrical Spin Injection into a Semiconductor Heterostructure. *Phys. Rev. B* **2000**, *62*, 8180-8183.
6. Golnik, A.; Ginter, J.; Gaj, J. A. Magnetic Polarons in Exciton Luminescence of $Cd_{1-x}Mn_xTe$. *J. Phys. C.: Sol. State Phys.* **1983**, *16*, 6073–6084.
7. Mackh, G.; Ossau, W.; Yakovlev, D. R.; Waag, A.; Landwehr, G.; Hellmann, R.; Göbel, E. O. Localized Exciton Magnetic Polarons in $Cd_{1-x}Mn_xTe$. *Phys. Rev. B* **1994**, *49*, 10248.
8. Wolf, S. A.; Awschalom, D. D.; Buhrman, R. A.; Daughton, J. M.; S., v. M.; Roukes, M. L.; Chtchelkanova, A. Y.; Treger, D. M. Spintronics: A Spin-Based Electronics Vision for the Future. *Science* **2001**, *294*, 1488–1495.
9. Awschalom, D. D.; Flatté, M. E. Challenges for Semiconductor Spintronics. *Nat. Phys.* **2007**, *3*, 153–159.
10. Dietl, T.; Awschalom, D. D.; Kaminska, M.; Ohno, H., *Spintronics*. Academic Press: Amsterdam, 2008; Vol. 82.
11. Beaulac, R.; Archer, P. I.; Ochsenbein, S. T.; Gamelin, D. R. Mn^{2+}-Doped CdSe Quantum Dots: New Inorganic Materials for Spin-Electronics and Spin-Photonics. *Adv. Funct. Mater.* **2008**, *18*, 3873–3891.
12. Beaulac, R.; Ochsenbein, S. T.; Gamelin, D. R. Colloidal Transition-Metal-Doped Quantum Dots. In *Nanocrystal Quantum Dots*, 2nd ed.; Klimov, V. I., Ed; CRC Press: Boca Raton, FL, 2010; pp 397–453.
13. Vlaskin, V. A.; Barrows, C. J.; Erickson, C. S.; Gamelin, D. R. Nanocrystal Diffusion Doping. *J. Am. Chem. Soc.* **2013**, *135*, 14380–14389.
14. Barrows, C. J.; Chakraborty, P.; Kornowske, L. M.; Gamelin, D. R. Tuning Equilibrium Compositions in Colloidal Cd1-xMnxSe Nanocrystals Using Diffusion Doping and Cation Exchange. *ACS Nano* **2016**, *10*, 910–918.
15. Chakraborty, P.; Barrows, C. J.; Jin, Y.; Dunham, S. T.; Gamelin, D. R. Kinetics of Isovalent (Cd^{2+}) and Aliovalent (In^{3+}) Cation Exchange in $Cd_{1-x}Mn_xSe$ Nanocrystals. *J. Am. Chem. Soc.* **2016**, *138*, 12885–12893.

16. Bhattacharjee, A.; Pérez-Conde, J. Optical Properties of Paramagnetic Ion-Doped Semiconductor Nanocrystals. *Phys. Rev. B* **2003**, *68*, 045303.
17. Fernández-Rossier, J. Single-Exciton Spectroscopy of Semimagnetic Quantum Dots. *Phys. Rev. B* **2006**, *73*, 045301.
18. Barrows, C. J.; Vlaskin, V. A.; Gamelin, D. R. Absorption and Magnetic Circular Dichroism Analyses of Giant Zeeman Splittings in Diffusion-Doped Colloidal $Cd_{1-x}Mn_xSe$ Quantum Dots. *J. Phys. Chem. Lett.* **2015**, *6*, 3076–3081.
19. Nelson, H. D.; Bradshaw, L. R.; Barrows, C. J.; Vlaskin, V. A.; Gamelin, D. R. Picosecond Dynamics of Excitonic Magnetic Polarons in Colloidal Diffusion-Doped $Cd_{1-x}Mn_xSe$ Quantum Dots. *ACS Nano* **2015**, *9*, 11177–11191.
20. Fainblat, R.; Muckel, F.; Barrows, C. J.; Vlaskin, V. A.; Gamelin, D. R.; Bacher, G. Valence-Band Mixing Effects in the Upper-Excited-State Magneto-Optical Responses of Colloidal Mn^{2+}-Doped CdSe Quantum Dots. *ACS Nano* **2014**, *8*, 12669−12675.
21. Rice, W. D.; Liu, W.; Baker, T. A.; Sinitsyn, N. A.; Klimov, V. I.; Crooker, S. A. Revealing Giant Internal Magnetic Fields Due to Spin Fluctuations in Magnetically Doped Colloidal Nanocrystals. *Nat. Nanotech.* **2016**, *11*, 137–142.
22. Fainblat, R.; Barrows, C. J.; Hopmann, E.; Siebeneicher, S.; Vlaskin, V. A.; Gamelin, D. R.; Bacher, G. Giant Excitonic Exchange Splittings at Zero Field in Single Colloidal CdSe Quantum Dots Doped With Individual Mn^{2+} Impurities. *Nano Lett.* **2016**, *16*, 6371–6377.
23. Besombes, L.; Léger, Y.; Maingault, L.; Ferrand, D.; Mariette, H.; Cibert, J. Probing the Spin State of a Single Magnetic Ion in an Individual Quantum Dot. *Phys. Rev. Lett.* **2004**, *93*, 207403.
24. Krebs, O.; Benjamin, E.; Lemaître, A. Magnetic Anisotropy of Singly Mn-Doped InAs/GaAs Quantum Dots. *Phys. Rev. B* **2009**, *80*, 165315.
25. Koenraad, P. M.; Flatté, M. E. Single Dopants in Semiconductors. *Nat. Mater.* **2011**, *10*, 91–100.
26. Kobak, J.; Smoleński, T.; Goryca, M.; Papaj, M.; Gietka, K.; Bogucki, A.; Koperski, M.; Rousset, J.-G.; Suffczyński, J.; Janik, E.; Nawrocki, M.; Golnik, A.; Kossacki, P.; Pacuski, W. Designing Quantum Dots for Solotronics. *Nat. Commun.* **2014**, *5*, 3191.
27. Bradshaw, L. R.; Hauser, A.; McLaurin, E. J.; Gamelin, D. R. Luminescence Saturation via Mn^{2+}–Exciton Cross Relaxation in Colloidal Doped Semiconductor Nanocrystals. *J. Phys. Chem. C* **2012**, *116*, 9300–9310.
28. Barrows, C. J.; Chakraborty, P.; Kornowske, L. M.; Gamelin, D. R. Tuning Equilibrium Compositions in Colloidal $Cd_{1-x}Mn_xSe$ Nanocrystals Using Diffusion Doping and Cation Exchange. *ACS Nano* **2016**, *10*, 910–918.
29. Title, R. S. Covalency and the Paramagnetic Resonance of Mn^{++} in CdSe. *Phys. Rev.* **1963**, *130*, 17.
30. Archer, P. I.; Santangelo, S. A.; Gamelin, D. R. Direct Observation of sp–d Exchange Interactions in Colloidal Mn^{2+}- and Co^{2+}-Doped CdSe Quantum Dots. *Nano Lett.* **2007**, *7*, 1037–1043.
31. Kuno, M.; Nirmal, M.; Bawendi, M. G.; Efros, A.; Rosen, M. Magnetic Circular Dichroism Study of CdSe Quantum Dots. *J. Chem. Phys.* **1998**, *108*, 4242–4247.

32. Piepho, S. B.; Schatz, P. N. *Group Theory in Spectroscopy with Applications to Magnetic Circular Dichroism*. Wiley: New York, 1983.
33. Schimpf, A. M.; Gamelin, D. R. Thermal Tuning and Inversion of Excitonic Zeeman Splittings in Colloidal Doped CdSe Quantum Dots. *J. Phys. Chem. Lett.* **2012**, *3*, 1264–1268.
34. Arciszewska, M.; Nawrocki, M. Determination of the Band Structure Parameters of $Cd_{0.95}Mn_{0.05}Se$ from Magnetoabsorption Measurements. *J. Phys. Chem. Solids* **1986**, *47*, 309–314.
35. Yang, J.; Fainblat, R.; Kwon, S. G.; Muckel, F.; Yu, J. H.; Terlinden, H.; Kim, B. H.; Iavarone, D.; Choi, M. K.; Kim, I. Y.; Park, I.; Hong, H.-K.; Lee, J.; Son, J. S.; Lee, Z.; Kang, K.; Hwang, S.-J.; Bacher, G.; Hyeon, T. Route to the Smallest Doped Semiconductor: Mn^{2+}-Doped $(CdSe)_{13}$ Clusters. *J. Am. Chem. Soc.* **2015**, *137*, 12776–12779.
36. Muckel, F.; Yang, J.; Lorenz, S.; Baek, W.; Chang, H.; Hyeon, T.; Bacher, G.; Fainblat, R. Digital Doping in Magic-Sized CdSe Clusters. *ACS Nano* **2016**, *10*, 7135–7141.
37. Schmidt, T.; Scheibner, M.; Worschech, L.; Forchel, A.; Slobodskyy, T.; Molenkamp, L. W. Sign Reversal and Light Controlled Tuning of Circular Polarization in Semimagnetic CdMnSe Quantum Dots. *J. Appl. Phys.* **2006**, *100*, 123109.
38. Wojtowicz, T.; Kutrowski, M.; Karczewski, G.; Kossut, J.; König, B.; Keller, A.; Yakovlev, D. R.; Waag, A.; Geurts, J.; Ossau, W.; Landwehr, G.; Merkulov, I. A.; Teran, F. J.; Potemski, M. II–VI Quantum Structures with Tunable Electron *g*-Factor. *J. Cryst. Growth* **2000**, *214–215*, 378–386.

Chapter 6. Absorption and Magnetic Circular Dichroism Analyses of Giant Zeeman Splittings in Diffusion-Doped Colloidal $Cd_{1-x}Mn_xSe$ Quantum Dots*

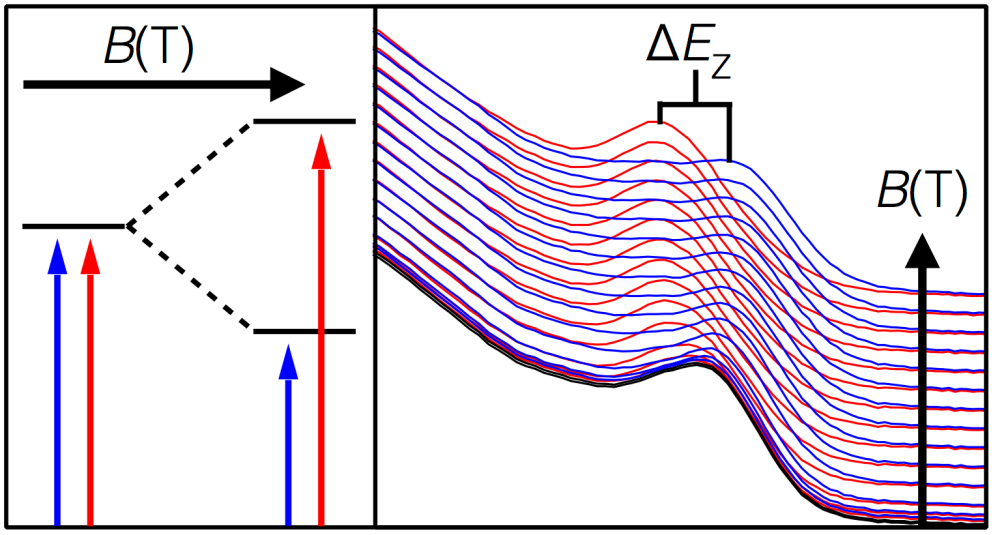

*Reproduced with permission from Barrows, C. J.; Vlaskin, V. A.; Gamelin, D. R. *J. Phys. Chem. Lett.* **2015**, *6*, 3076–3081. Copyright 2015 American Chemical Society.

6.1 Overview

Impurity ions can transform the electronic, magnetic, or optical properties of colloidal quantum dots. Magnetic impurities introduce strong dopant–carrier exchange coupling that generates giant Zeeman splittings (ΔE_Z) of excitonic excited states. To date, ΔE_Z in colloidal doped quantum dots has primarily been quantified by analysis of magnetic circular dichroism (MCD) intensities and absorption line widths (σ). Here, we report ΔE_Z values detected directly by absorption spectroscopy for the first time in such materials, using colloidal $Cd_{1-x}Mn_xSe$ quantum dots prepared by diffusion doping. A convenient method for decomposing MCD and absorption data into circularly polarized absorption spectra is presented. These data confirm the widely applied MCD analysis in the low-field, high-temperature regime, but also reveal a breakdown at low temperatures and high fields when $\Delta E_Z/\sigma$ approaches unity, a situation not previously encountered in doped quantum dots. This breakdown is apparent for the first time here because of the extraordinarily large ΔE_Z and small σ achieved by nanocrystal diffusion doping.

6.2 Introduction

Future spintronics and spin-photonics technologies will require new capabilities for manipulating spins in semiconductor nanostructures. One promising approach involves embedding magnetic impurity ions within such nanostructures. Magnetic exchange interactions between these localized magnetic impurities and delocalized semiconductor charge carriers give rise to the so-called "giant" Zeeman splittings of the semiconductor band structure.[1-3] Such splittings in turn impart extraordinary magnetic, magneto-optical, and magneto-electronic properties to this class of materials, including "giant" Faraday rotation effects,[4-6] carrier-controlled magnetism,[7-9] carrier or exciton spin polarization,[10-15] single- or few-impurity exchange-split excitons,[16-19] and spontaneous photoinduced magnetization at zero applied field (excitonic magnetic polarons).[20-23]

Over the past decade, tremendous progress has been made in the synthesis, physical characterization, and theoretical understanding of colloidal magnetically doped semiconductor nanocrystals.[24] A workhorse of this field has been colloidal $Cd_{1-x}Mn_xSe$ quantum dots (QDs),[25] which have displayed a rich variety of photophysical, photomagnetic, and magneto-optical properties not previously observed in colloidal quantum dots,[15, 22, 26-29] many arising from the giant Zeeman splittings induced by strong *sp–d* exchange interactions in these nanomaterials.

Giant Zeeman splittings in colloidal quantum dots can be quantified optically. Application of an external magnetic field splits excitonic states by the Zeeman energy, ΔE_Z, as described by Equation 6.1. Intrinsic contributions to ΔE_Z are small and represented by the first term of Equation 6.1, where g_{Int} is the intrinsic excitonic g value, μ_B is the Bohr

magneton, and B is the applied magnetic field. At 6 T, this term amounts to roughly +0.4 meV in $Cd_{1-x}Mn_xSe$ QDs. Addition of a magnetic dopant such as Mn^{2+} activates dopant-carrier *s–d* and *p–d* exchange interactions with strengths parametrized by $N_0\alpha$ (+0.23 eV) and $N_0\beta$ (–1.27 eV), respectively.[1] These interactions invert (in the case of Mn^{2+}) and enhance the excitonic Zeeman splittings. ΔE_Z increases with effective dopant concentration (x_{Eff}), exciton-dopant overlap (g), and the spin-expectation value of the dopant ($\langle S_Z \rangle$) at the experimental temperature and magnetic field, as described by the Brillouin function for magnetic ions with spin-only ground states (such as Mn^{2+}).

$$\Delta E_Z = g_{Int}\mu_B B + x_{Eff}\langle S_Z \rangle N_0(\alpha - \beta) \quad (6.1a)$$

$$= g_{Exc}\mu_B B \text{ (Curie limit)} \quad (6.1b)$$

Recently, we introduced a new diffusion-based synthesis that allows very high Mn^{2+} concentrations (exceeding x ~0.20) to be incorporated into high-quality preformed CdSe nanocrystals.[29] Extremely large excitonic Zeeman splittings (up to ~–100 meV) and g_{Exc} values (up to ~–900 at 1.8 K) were reported.[29] Here, we report that nanocrystals synthesized by this methodology now allow *direct* observation of their giant excitonic Zeeman splittings by absorption spectroscopy, a first for colloidal QDs. This new capability permits a quantitative assessment of the MCD analysis commonly applied to interpret such Zeeman splittings in these and other colloidal doped QDs. We demonstrate that the model applied for analysis using MCD spectroscopy breaks down when ΔE_Z is comparable to the excitonic absorption line widths, σ, as occurs in these unique nanocrystals, and we provide an analytical expression that allows correction of the MCD results in this regime.

This breakdown regime has not been accessed previously because of the broader excitonic absorption features and smaller excitonic Zeeman splittings typical of previous samples. Its observation here highlights the extraordinary magneto-optical properties of diffusion-doped $Cd_{1-x}Mn_xSe$ QDs.

6.3 Results and Analysis

Figure 6.1 plots the magnetic-field-dependent electronic absorption (6.1A) and MCD (6.1B) spectra of diffusion-doped *d* ~3.9 nm $Cd_{0.94}Mn_{0.06}Se$/ZnS core/shell QDs measured at 3 K up to 6 T. At 0 T, the first excitonic transition occurs at 2.23 eV with σ = 70 meV, determined by simultaneous Gaussian fitting of the absorption and MCD spectra (see Appendix E). As the magnetic field is applied, the first absorption band broadens, with a tail appearing on the red side of the spectrum. MCD spectra recorded simultaneously show an intense derivative-shaped feature centered at the first excitonic maximum, its intensity saturating with magnetic field as expected from Equation 6.1 for an *S* = 5/2 dopant. Strong magnetic circularly polarized luminescence (MCPL) is also observed, which reflects excitonic spin polarization in these $Cd_{1-x}Mn_xSe$ QDs, as reported previously for colloidal $Cd_{1-x}Mn_xSe$ QDs prepared by cluster thermolysis.[15] These data are reported separately.[30]

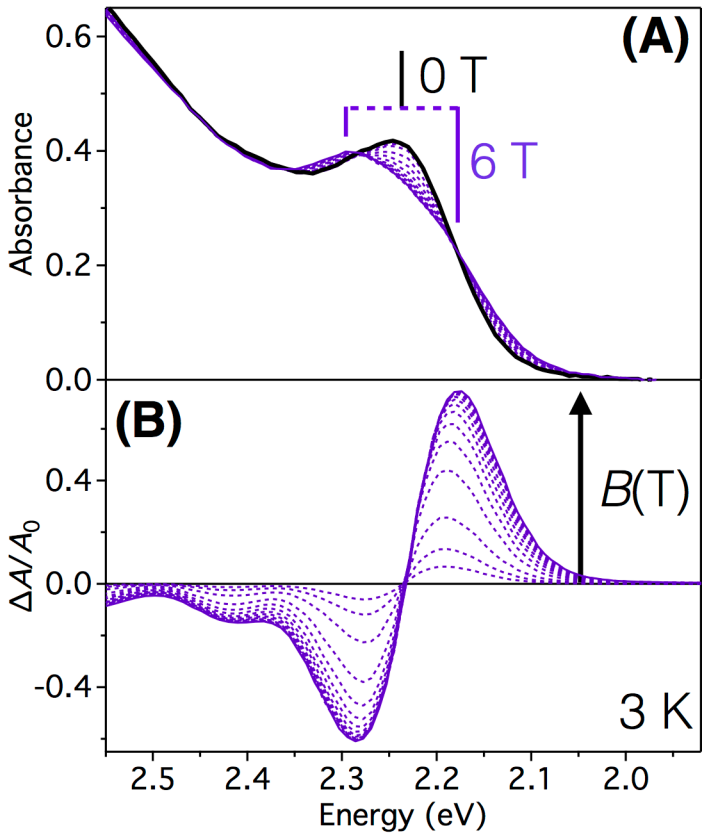

Figure 6.1. (A) Electronic absorption and (B) MCD spectra of diffusion-doped *d* ~3.9 nm $Cd_{0.94}Mn_{0.06}Se$/ZnS QDs measured at 3 K for magnetic fields between 0 (black) and 6 T (purple). Arrow indicates the direction of increasing magnetic field.

From the simultaneous measurement of absorption and MCD spectra, it is possible to reconstruct the absorption spectra associated with left- and right- circularly polarized light. Here, circularly polarized absorbance values (A_L and A_R) are obtained from the total absorbance (A_{TOT}) and MCD (ΔA), collected simultaneously at each energy, according to Equations 6.2 and 6.3. Derivation of these equations is provided in section 6.5.2. Figure 6.2A plots A_L and A_R spectra obtained from Equations 6.2 and 6.3 and the data collected at 3 K, 0–6 T. Each spectrum resembles the absorption spectrum measured at zero field, but the first excitonic feature shifts to lower energy for A_L and to higher energy for A_R with increasing B. Similarly, Figure 6.2B plots the temperature dependence of the 6 T circularly polarized absorption spectra, measured from 3 to 40 K, and shows an increasing splitting as the temperature is lowered. From these spectra, the Zeeman splitting of the first exciton can be quantified directly as the energy difference between A_L and A_R peak maxima (at energies E_L and E_R), as described by Equation 6.4. The Zeeman splittings of higher-energy transitions are not clear from the polarized absorption spectra but have been quantified elsewhere in related diffusion-doped $Cd_{1-x}Mn_xSe$ QDs by analysis of MCD intensities.[31] The second excitonic absorption band overlaps with the first in A_R, leading to slightly greater absorbance at the peak maximum relative to the more energetically isolated first exciton of the A_L spectrum.

$$A_L = A_{TOT} + \Delta A/2 \tag{6.2}$$

$$A_R = A_{TOT} - \Delta A/2 \tag{6.3}$$

$$\Delta E_Z(\text{Abs}) = E_L - E_R \tag{6.4}$$

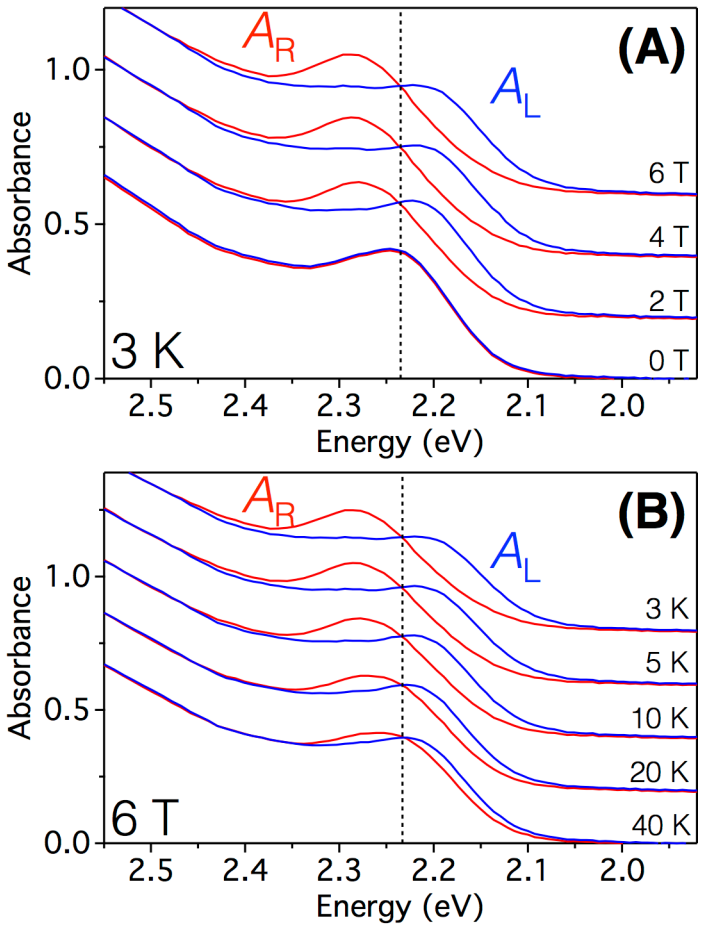

Figure 6.2. **(A)** Magnetic-field dependence of 3 K circularly polarized absorption spectra of diffusion-doped d ~3.9 nm $Cd_{0.94}Mn_{0.06}Se/ZnS$ QDs, showing A_R (red) and A_L (blue) for magnetic fields between 0 and 6 T. **(B)** Temperature-dependence of circularly polarized absorption spectra of the same QDs measured at 6 T and temperatures from 3 to 40 K. The dashed lines in (A) and (B) represent the energy of the first excitonic absorption maximum at 0 T and 3 K. For clarity, spectra at higher fields and lower temperatures are offset vertically.

Figure 6.3A plots the magnetic-field dependence of the first excitonic transition energies at temperatures from 3 to 40 K, determined by simultaneous Gaussian fitting of absorption and MCD intensities. These data are plotted as shifts relative to the zero-field energy (2.23 eV at 3 K). The effects of overlapping absorption features on the high-energy side were minimized by weighting the A_L spectra more heavily during fitting and by assuming symmetric Zeeman splittings of the first exciton about its zero-field energy. Representative fits are shown in Appendix E. Figure 6.3B plots the Zeeman splittings determined from the data of Figure 6.3A. The excitonic Zeeman splittings increase dramatically below 40 K, as expected for a Curie paramagnet. At 6 T, ΔE_Z(Abs) = –18 meV at 40 K, but increases to –71 meV at 3 K, where magnetic saturation occurs. Comparable Zeeman splittings (–80 meV) are also estimated directly from the A_L and A_R apparent peak maxima, with no fitting. The saturation magnetization shown in Figure 6.3B is described well by the S = 5/2 Brillouin function using g_{Mn} = 2.004, as anticipated from Equation 6.1. From Equation 6.1, the saturation value of ΔE_Z(Abs) = –71 meV implies a product of $x_{Eff}g$ ~0.02, which may arise from a combination of antiferromagnetic Mn^{2+}–Mn^{2+} dimer interactions and a small Mn^{2+} gradient within the QDs. Bulk magnetization measurements show x_{Eff} ~0.55x at x = 0.06, for example.[32] In the low-field (linear) limit, the 3 K Zeeman splitting corresponds to an excitonic g value of g_{Exc} ~–850 (Equation 6.1).

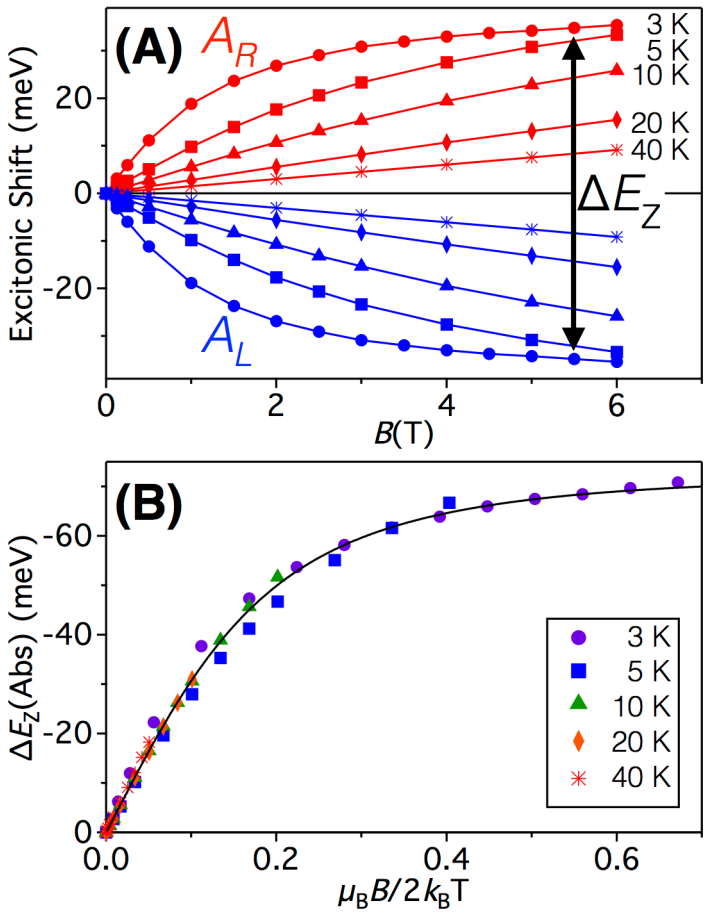

Figure 6.3. (A) Field- and temperature-dependent energetic shifts of the first excitonic transitions in diffusion-doped d ~3.9 nm $Cd_{0.94}Mn_{0.06}Se/ZnS$ QDs for A_R (red) and A_L (blue) magnetoabsorption from 0 to 6 T and 3 to 40 K, plotted relative to the zero-field transition. The difference between the two energies is the Zeeman splitting, ΔE_Z(Abs). (B) The data from panel (A), replotted as $\Delta E_Z = \Delta E_Z$(Abs). The Brillouin function using $S = 5/2$ and $g_{Mn} = 2.004$ is superimposed (black line).

The data presented above provide the first direct measurement of giant excitonic Zeeman splittings by absorption spectroscopy in any colloidal doped nanocrystals. Previously, this critical phenomenon has primarily been quantified[26, 27, 29, 33-36] by analysis of MCD spectra within a model that assumes the rigid-shift approximation.[37] MCD spectroscopy is extremely powerful, because it allows detection and quantitative analysis of ΔE_Z despite the large inhomogeneous line widths of colloidal doped QDs reported to date. In one case, ΔE_Z was measured by photoluminescence, from magnetic polaron energies.[22] To illustrate the MCD model, Figure 6.4A shows the effect of the magnetic field on the first bright exciton ($M_J = \pm 1$) of CdSe and $Cd_{1-x}Mn_xSe$ QDs. At $B = 0$, the bright exciton is doubly degenerate, but this degeneracy is broken at $B > 0$. Probing this excited state with circularly polarized light yields two transitions at $B > 0$, one for A_L and the other for A_R, according to the selection rule of $\Delta M_J = \pm 1$ for absorption of circularly polarized light. Figure 6.4B shows a model Gaussian absorption band (A) split into its A_L and A_R components by the magnetic field. Under the rigid-shift approximation, these bands maintain their zero-field band shape even as their energies diverge. The Gaussian's full width at 1/e of the maximum absorbance, A_0, is defined as 2σ. Figure 6.4B illustrates the derivative-shaped A-term MCD spectrum that results from splitting A_L and A_R by ΔE_Z. This MCD intensity is plotted as $\Delta A/A_0$, where ΔA is defined as $A_L - A_R$ according to the sign convention of Piepho and Schatz.[37] $\Delta A'$ ($-\Delta A'$) represents the MCD intensity at an energy of σ/sqrt(2) from the zero-field absorption maximum, and coincides with the maximum (minimum) MCD intensity in Figure 6.4B. Using this model, ΔE_Z can be estimated from analysis of the MCD band shape according to Equation 6.5. Because it is a difference

technique, MCD is extremely sensitive, and even small Zeeman splittings that are difficult to resolve directly by absorption spectroscopy can be detected and analyzed by this approach. The saturation Zeeman splitting calculated from the 3 K, 6 T MCD spectrum of Figure 6.1 using Equation 6.5 is ΔE_Z(MCD) = –62 meV.

$$\Delta E_Z(\mathrm{MCD}) = -\left(\frac{\sqrt{2e}}{2}\right)\sigma\frac{\Delta A'}{A_0} \tag{6.5}$$

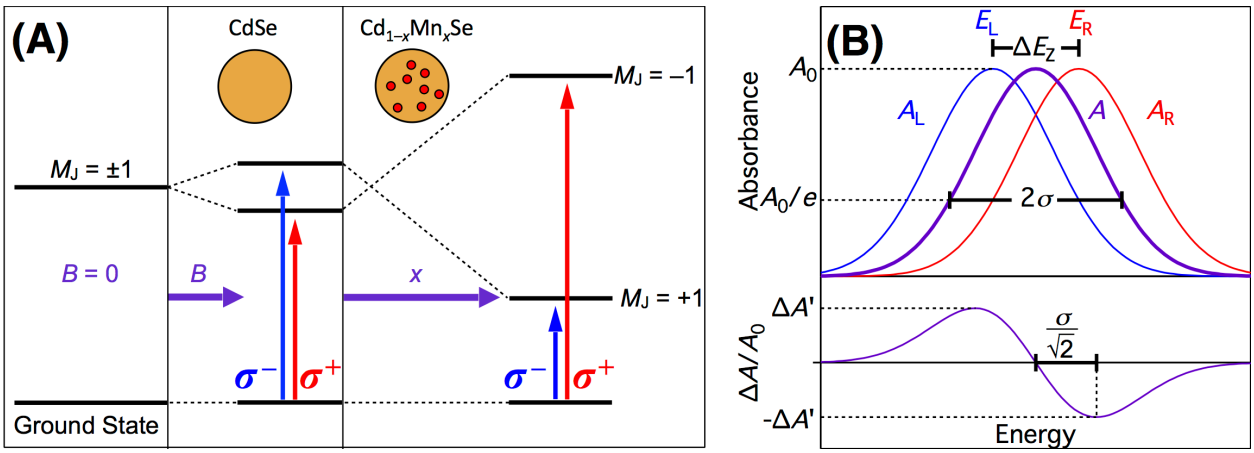

Figure 6.4. (A) Excitonic Zeeman splittings in undoped and Mn^{2+}-doped CdSe QDs, as probed by absorption and MCD spectroscopies. Application of an external magnetic field (B) splits the first bright excitonic state by the Zeeman energy, ΔE_Z. The *sp–d* exchange inverts and enhances this splitting, yielding a "giant" excitonic Zeeman splitting. Left- and right- circularly polarized light are described by σ^- and σ^+, respectively. (B) Illustration of the excitonic Zeeman splitting as probed by absorption (top) and MCD (bottom) experiments. The key parameters used for quantitative spectral analysis are illustrated.

Figure 6.5A plots 3 K excitonic Zeeman splittings calculated by analysis of the magnetoabsorption and MCD spectra presented above, as a function of magnetic field up to 6 T. In the low-field limit, both experiments reveal a similar linear dependence of ΔE_Z on B. Although ΔE_Z(MCD) and ΔE_Z(Abs) both saturate at high fields, their magnitudes diverge above ~1.5 T and differ by as much as 13%. In some measurements, this discrepancy reaches as large as 47% (see below). Obviously, there is a breakdown in the analysis. The origin of this discrepancy is traced to the fundamental assumption of the MCD analysis that the Zeeman splitting is small compared to the spectral line width, *i.e.*, $|\Delta E_Z| << \sigma$. For the spectra in Figure 6.1, σ = 70 meV, but from Figure 6.3, ΔE_Z(Abs) = –71 meV at 3 K. In this case, the assumptions underpinning the validity of Equation 6.5 do not hold.

Figure 6.5B illustrates the effect of increasing the ratio $|\Delta E_Z|/\sigma$ on ΔE_Z(MCD). The data points in Figure 6.5B plot experimental values of ΔE_Z(MCD)/ΔE_Z versus $|\Delta E_Z|/\sigma$ for a series of diffusion-doped $Cd_{1-x}Mn_xSe$ QDs with three different diameters and Mn^{2+} concentrations, measured at temperatures between 1.8 and 40 K and B = 0–6 T, taking $\Delta E_Z = \Delta E_Z$(Abs). ΔE_Z(MCD)/ΔE_Z = 1 until $|\Delta E_Z|/\sigma$ reaches ~0.5, beyond which it decreases. The smallest measured value in our samples was ΔE_Z(MCD)/ΔE_Z = 0.53, which occurred for $|\Delta E_Z|/\sigma$ = 1.62.

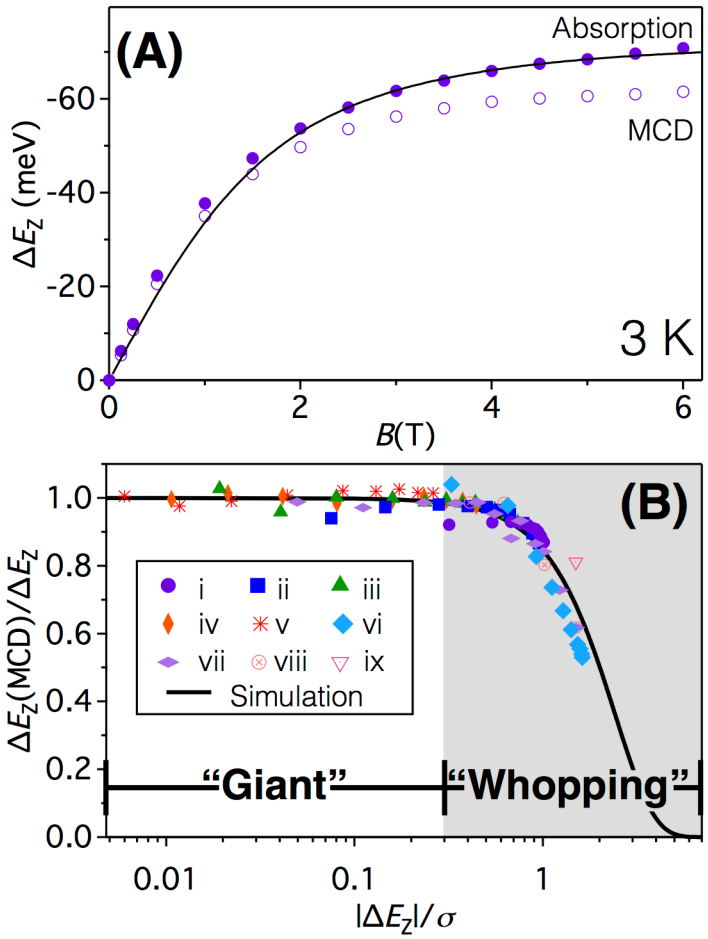

Figure 6.5. **(A)** Magnetic-field dependence of ΔE_Z for diffusion-doped d ~3.9 nm $Cd_{0.94}Mn_{0.06}Se$/ZnS QDs as determined by analysis of absorption (closed circles) and MCD (open circles) spectra measured at 3 K from 0 to 6 T. The solid black curve is the Brillouin fit to the experimental data shown in Figure 6.3B. **(B)** Experimental (symbols) and predicted (black line, from Equation 6.6) dependence of ΔE_Z(MCD)/ΔE_Z on the ratio $|\Delta E_Z|/\sigma$. Equation 6.5 underestimates ΔE_Z(MCD) when $|\Delta E_Z|/\sigma$ approaches unity. The experimental data were collected from three samples of diffusion-doped $Cd_{1-x}Mn_xSe$ QDs with the following conditions: (*i–v*) d ~3.9 nm, x = 0.06 (not including ZnS shell), 3–40 K, 0–6 T; (*vi–viii*) d ~4.5 nm, x = 0.13, 1.8–40 K, 0–6T; (*ix*) d ~7.9 nm, x = 0.18, 2.1 K, 4 T.

The trend expected from Equation 6.5 is given by Equation 6.6, which is derived from Equation 6.5 and the definitions in Figure 6.4B (see Appendix E). Here, $\eta = \Delta E_Z/\sigma$. $\Delta E_Z(\mathrm{MCD})/\Delta E_Z$ from Equation 6.6 is plotted versus $|\Delta E_Z|/\sigma$ in Figure 6.5B for comparison with the experimental data. As expected, when $|\Delta E_Z| << \sigma$, Equation 6.5 yields an accurate value of ΔE_Z from the MCD spectrum. When $|\Delta E_Z|$ approaches or surpasses σ, however, Equation 6.5 starts to underestimate the true value of ΔE_Z significantly. Importantly, all data points for all samples fall along the same predicted curve, providing experimental confirmation of the breakdown of Equation 6.5 in the analysis of diffusion-doped $Cd_{1x}Mn_xSe$ QD MCD spectra. The excellent agreement between the simulated and experimental curves in Figure 6.5B confirms that the discrepancy between ΔE_Z(MCD) and ΔE_Z(Abs) in Figure 6.5A arises from a breakdown of Equation 6.5 because $|\Delta E_Z|/\sigma$ grows too large in these diffusion-doped $Cd_{1-x}Mn_xSe$ QDs. This breakdown highlights the exceptionally large ΔE_Z and the high sample quality (narrow absorption bands) that can be achieved by nanocrystal diffusion doping.[29] Finally, the observation that the data from multiple samples all fall upon the same simulated curve in Figure 6.5B indicates that this is a universal curve, and hence Equation 6.6 can be used to correct ΔE_Z(MCD) to recover an accurate ΔE_Z. This observation may be useful for future analyses of giant excitonic Zeeman splittings by MCD spectroscopy.

$$\frac{\Delta E_Z(\mathrm{MCD})}{\Delta E_Z} = \left(\frac{\sqrt{2}}{\eta}\right)\exp\left[-\frac{\eta^2}{4}\right]\sinh\left[\frac{\eta\sqrt{2}}{2}\right] \tag{6.6}$$

6.4 Conclusion

In summary, extraordinarily large excitonic Zeeman splittings have been measured in colloidal diffusion-doped $Cd_{1-x}Mn_xSe$ quantum dots. These Zeeman splittings are large enough, and the spectral line widths narrow enough, to be detected directly by absorption spectroscopy for the first time in this class of materials. The direct observation of excitonic Zeeman splittings by absorption spectroscopy allows experimental testing and ultimately confirmation of the commonly applied MCD analysis for quantifying excitonic Zeeman splittings in magnetically doped colloidal quantum dots. At the same time, this analysis reveals experimentally accessible circumstances under which the analysis fails to yield the correct ΔE_Z because the assumption of $|\Delta E_Z| << \sigma$ is not valid. In this regime of large $|\Delta E_Z|/\sigma$, direct measurement of the Zeeman splitting energy by absorption spectroscopy with resolved circular polarizations provides a more reliable measure of ΔE_Z, but ΔE_Z(MCD) values can also be corrected using Equation 6.6. Overall, these findings highlight the exceptional magneto-optical properties of colloidal diffusion-doped $Cd_{1-x}Mn_xSe$ quantum dots, and advance our understanding of their physical properties as well as of the methodologies employed for their analysis.

6.5 Experimental Methods

6.5.1 Synthesis

Colloidal wurtzite $Cd_{1-x}Mn_xSe$ quantum dots were prepared by nanocrystal diffusion doping using an adaptation of our previously published methods.[29] Briefly, in a typical synthesis, CdSe nanocrystals (~0.13 mmol in terms of CdSe units) were dried and added to 0.004–0.020 g (0.05–0.25 mmol) of selenium powder, 1 mL of 1-octadecene (ODE), and 1 mL of tributylphosphine (TBP) in a septum-capped 5 mL round-bottom flask in a nitrogen-atmosphere glovebox. Separately, 12 g of ODE, 0.5 g of oleic acid (OA), and 1.0 g of hexadecylamine (HDA) were added to a 100 mL three-neck round-bottom flask. Following heating of the latter solution for 60 minutes at 100 °C under vacuum, 0.03 g (0.10 mmol) of $Mn(OAc)_2 \bullet 4H_2O$ was added against a nitrogen overpressure. The flask was then placed under vacuum to remove acetic acid and water and then heated under nitrogen to 300 °C, at which point the CdSe/selenide solution was injected rapidly. This reaction mixture was held at 300 °C for 12–24 hours. As the solution was cooled to room temperature, 3 mL of toluene was added at ~110 °C. The nanocrystals were then precipitated from solution by addition of ethanol and washed by repeated suspensions in toluene and flocculation with ethanol. For select samples, a thin (≤1 monolayer) ZnS shell was grown according to literature procedures.[38] Shell growth did not alter the absorption spectra significantly. Relative atomic concentrations were obtained by analysis of dried nanocrystals digested in ultrapure nitric acid (EMD Chemicals) using inductively coupled plasma atomic emission spectrometry (ICP-AES; Perkin-Elmer).

6.5.2 Physical Measurements and Analysis

Nanocrystal sizes were determined from an empirical sizing curve[39] based on the energies of the first excitonic absorption maxima at room temperature and corrected for Mn^{2+} incorporation based on ICP-AES analysis, according to the linear dependence of E_g on x.[1, 29] Low-temperature absorption and MCD spectra were collected on nanocrystal films prepared by depositing dilute toluene suspensions between quartz disks. These samples were placed in a superconducting magneto-optical cryostat (Cryo-Industries SMC-1659 OVT) oriented in the Faraday configuration. At helium temperatures, each sample was screened for depolarization by matching the CD spectra of a chiral molecule placed before and after the sample. In all cases, depolarization was <5%. Electronic absorption and MCD spectra were collected simultaneously using an Aviv 40DS spectropolarimeter. The total absorbance, A_{TOT}, is defined as in Equation 6.7. The differential absorption of the MCD experiment is defined as in Equation 6.8, where A_L and A_R refer to the absorption of left- and right- circularly polarized photons in the sign convention of Piepho and Schatz.[37]

$$A_{TOT} = (A_L + A_R)/2 \tag{6.7}$$

$$\Delta A = A_L - A_R \tag{6.8}$$

From these data, spectra for A_L and A_R are obtained as follows. Solving Equation 6.7 for A_L and A_R yields Equations 6.9 and 6.10, respectively:

$$A_L = 2A_{TOT} - A_R \tag{6.9}$$

$$A_R = 2A_{TOT} - A_L \tag{6.10}$$

Substituting A_{TOT} from Equation 6.7 into Equations 6.9 and 6.10 yields 6.11 and 6.12, respectively:

$$A_L = A_{TOT} + (A_L + A_R)/2 - A_R = A_{TOT} + (A_L - A_R)/2 \tag{6.11}$$

$$A_R = A_{TOT} + (A_L + A_R)/2 - A_L = A_{TOT} - (A_L - A_R)/2 \tag{6.12}$$

Substituting ΔA from Equation 6.8 into Equations 6.11 and 6.12 yields Equations 6.2 and 6.3, respectively.

6.6 Appendix E

Additional absorption, MCD, and X-ray diffraction data, Gaussian fitting results, and derivation of Equation 6.6.

6.7 Acknowledgments

This research was funded by the US National Science Foundation (DMR-1505901). C.J.B. gratefully acknowledges Graduate Fellowship support from the UW Clean Energy Institute. The authors thank the anonymous referees for their insightful comments.

6.8 References

1. Furdyna, J. K. Diluted Magnetic Semiconductors. *J. Appl. Phys.* **1988**, *64*, R29–R64.
2. Furdyna, J. K.; Kossut, J. *Diluted Magnetic Semiconductors*. Academic Press: New York, 1988; Vol. 25 of Semiconductors and Semimetals.
3. Gaj, J. A.; Kossut, J., *Introduction to the Physics of Diluted Magnetic Semiconductors*. Springer-Verlag: Berlin, 2010; Vol. 144.
4. Yasuhira, T.; Uchida, K.; Matsuda, Y. H.; Miura, N.; Twardowski, A. Giant Faraday Rotation Spectra of $Zn_{1-x}Mn_xSe$ Observed in High Magnetic Fields up to 150 T. *Phys. Rev. B* **2000**, *61*, 4685–4688.
5. Yasuhira, T.; Uchida, K.; Matsuda, Y. H.; Miura, N.; Twardowski, A. Magnetic and Non-Magnetic Faraday Rotation in ZnMnSe in High Magnetic Fields. *Semicond. Sci. Technol.* **1999**, *14*, 1161–1164.
6. Bartholomew, D. U.; Furdyna, J. K.; Ramdas, A. K. Interband Faraday-Rotation in Diluted Magnetic Semiconductors: $Zn_{1-x}Mn_xTe$ and $Cd_{1-x}Mn_xTe$. *Phys. Rev. B* **1986**, *34*, 6943–6950.
7. Dietl, T.; Ohno, H.; Matsukura, F.; Cibert, J.; Ferrand, D. Zener Model Description of Ferromagnetism in Zinc-Blende Magnetic Semiconductors. *Science* **2000**, *287*, 1019–1022.
8. Kittilstved, K. R.; Schwartz, D. A.; Tuan, A. C.; Heald, S. M.; Chambers, S. A.; Gamelin, D. R. Direct Kinetic Correlation of Carriers and Ferromagnetism in Co^{2+}:ZnO. *Phys. Rev. Lett.* **2006**, *97*, 037203.
9. König, J.; MacDonald, A. H. EPR and Ferromagnetism in Diluted Magnetic Semiconductor Quantum Wells. *Phys. Rev. Lett.* **2003**, *91*, 077202.
10. Drexler, C.; Bel'kov, V. V.; Ashkinadze, B.; Olbrich, P.; Zoth, C.; Lechner, V.; Terent'ev, Y. V.; Yakovlev, D. R.; Karczewski, G.; Wojtowicz, T.; Schuh, D.; Wegscheider, W.; Ganichev, S. D. Spin Polarized Electric Currents in Semiconductor Heterostructures Induced by Microwave Radiation. *Appl. Phys. Lett.* **2010**, *97*, 182107.
11. Ganichev, S. D.; Tarasenko, S. A.; Bel'kov, V. V.; Olbrich, P.; Eder, W.; Yakovlev, D. R.; Kolkovsky, V.; Zaleszczyk, W.; Karczewski, G.; Wojtowicz, T.; Weiss, D. Spin Currents in Diluted Magnetic Semiconductors. *Phys. Rev. Lett.* **2009**, *102*, 156602.
12. Fiederling, R.; Keim, M.; Reuscher, G.; Ossau, W.; Schmidt, G.; Waag, A.; Molenkamp, L. W. Injection and Detection of a Spin-Polarized Current in a Light-Emitting Diode. *Nature* **1999**, *402*, 787–790.
13. Jonker, B. T. Progress Toward Electrical Injection of Spin-Polarized Electrons into Semiconductors. *Proc. IEEE* **2003**, *91*, 727–740.
14. Jonker, B. T.; Park, Y. D.; Bennett, B. R.; Cheong, H. D.; Kioseoglou, G.; Petrou, A. Robust Electrical Spin Injection into a Semiconductor Heterostructure. *Phys. Rev. B* **2000**, *62*, 8180–8183.

15. Beaulac, R.; Archer, P. I.; Liu, X.; Lee, S.; Salley, G. M.; Dobrowolska, M.; Furdyna, J. K.; Gamelin, D. R. Spin-Polarizable Excitonic Luminescence in Colloidal Mn^{2+}-Doped CdSe Quantum Dots. *Nano Lett.* **2008**, *8*, 1197–1201.
16. Besombes, L.; Léger, Y.; Maingault, L.; Ferrand, D.; Mariette, H.; Cibert, J. Probing the Spin State of a Single Magnetic Ion in an Individual Quantum Dot. *Phys. Rev. Lett.* **2004**, *93*, 207403.
17. Besombes, L.; Léger, Y.; Maingault, L.; Mariette, H. Spin Properties of Charged Mn-Doped Quantum Dot. *J. Appl. Phys.* **2007**, *101*, 081713.
18. Krebs, O.; Lemaître, A. Optically Induced Coupling of Two Magnetic Dopant Spins by a Photoexcited Hole in a Mn-Doped InAs/GaAs Quantum Dot. *Phys. Rev. Lett.* **2013**, *111*, 187401.
19. Kobak, J.; Smoleński, T.; Goryca, M.; Papaj, M.; Gietka, K.; Bogucki, A.; Koperski, M.; Rousset, J. G.; Suffczyński, J.; Janik, E.; Nawrocki, M.; Golnik, A.; Kossacki, P.; Pacuski, W. Designing Quantum Dots for Solotronics. *Nat. Commun.* **2014**, *5*, 3191.
20. Harris, J. H.; Nurmikko, A. V. Formation of the Bound Magnetic Polaron in (Cd,Mn)Se. *Phys. Rev. Lett.* **1983**, *51*, 1472–1475.
21. Merkulov, I. A.; Yakovlev, D. R.; Kavokin, K. V.; Mackh, G.; Ossau, W.; Waag, A.; Landwehr, G. Hierarchy of Relaxation Times in the Formation of an Excitonic Magnetic Polaron in (CdMn)Te. *JETP Lett.* **1995**, *62*, 335–339.
22. Beaulac, R.; Schneider, L.; Archer, P. I.; Bacher, G.; Gamelin, D. R. Light-Induced Spontaneous Magnetization in Doped Colloidal Quantum Dots. *Science* **2009**, *325*, 973–976.
23. Sellers, I. R.; Oszwałdowski, R.; Whiteside, V. R.; Eginligil, M.; Petrou, A.; Zutic, I.; Chou, W.-C.; Fan, W. C.; Petukhov, A. G.; Kim, S. J.; Cartwright, A. N.; McCombe, B. D. Robust Magnetic Polarons in Type-II (Zn,Mn)Te/ZnSe Quantum Dots. *Phys. Rev. B* **2010**, *82*, 195320.
24. Beaulac, R.; Ochsenbein, S. T.; Gamelin, D. R. Colloidal Transition-Metal-Doped Quantum Dots. In *Nanocrystal Quantum Dots*, 2nd ed.; Klimov, V. I., Ed; CRC Press: Boca Raton, 2010; pp 397–453.
25. Beaulac, R.; Archer, P. I.; Ochsenbein, S. T.; Gamelin, D. R. Mn^{2+}-Doped CdSe Quantum Dots: New Inorganic Materials for Spin-Electronics and Spin-Photonics. *Adv. Funct. Mater.* **2008**, *18*, 3873–3891.
26. Archer, P. I.; Santangelo, S. A.; Gamelin, D. R. Direct Observation of *sp–d* Exchange Interactions in Colloidal Mn^{2+}- and Co^{2+}-Doped CdSe Quantum Dots. *Nano Lett.* **2007**, *7*, 1037–1043.
27. Archer, P. I.; Santangelo, S. A.; Gamelin, D. R. Inorganic Cluster Syntheses of TM^{2+}-Doped Quantum Dots (CdSe, CdS, CdSe/CdS): Physical Property Dependence on Dopant Locale. *J. Am. Chem. Soc.* **2007**, *129*, 9808–9818.
28. Beaulac, R.; Archer, P. I.; van Rijssel, J.; Meijerink, A.; Gamelin, D. R. Exciton Storage by Mn^{2+} in Colloidal Mn^{2+}-Doped CdSe Quantum Dots. *Nano Lett.* **2008**, *8*, 2949–2953.
29. Vlaskin, V. A.; Barrows, C.; Erickson, C. S.; Gamelin, D. R. Nanocrystal Diffusion Doping. *J. Am. Chem. Soc.* **2013**, *135*, 14380−14389.

30. Nelson, H. D.; Bradshaw, L. R.; Barrows, C. J.; Vlaskin, V. A.; Gamelin, D. R. Picosecond Dynamics of Excitonic Magnetic Polarons in Colloidal Diffusion-Doped $Cd_{1-x}Mn_xSe$ Quantum Dots. *ACS Nano* **2015**, *9*, 11177–11191.
31. Fainblat, R.; Muckel, F.; Barrows, C. J.; Vlaskin, V. A.; Gamelin, D. R.; Bacher, G. Valence-Band Mixing Effects in the Upper-Excited-State Magneto-Optical Responses of Colloidal Mn^{2+}-Doped CdSe Quantum Dots. *ACS Nano* **2014**, *8*, 12669–12675.
32. Shapira, Y.; Foner, S.; Ridgley, D. H.; Dwight, K.; Wold, A. Technical Saturation and Magetization Steps in Diluted Magnetic Semiconductors: Predictions and Observations. *Phys. Rev. B.* **1984**, *30*, 4021–4023.
33. Hoffman, D. M.; Meyer, B. K.; Ekimov, A. I.; Merkulov, I. A.; Efros, A. L.; Rosen, M.; Couino, G.; Gacoin, T.; Boilot, J.-P. Giant Internal Magnetic Fields in Mn Doped Nanocrystal Quantum Dots. *Solid State Commun.* **2000**, *114*, 547–550.
34. Norris, D. J.; Yao, N.; Charnock, F. T.; Kennedy, T. A. High-Quality Manganese-Doped ZnSe Nanocrystals. *Nano Lett.* **2001**, *1*, 3–7.
35. Norberg, N. S.; Parks, G. L.; Salley, G. M.; Gamelin, D. R. Giant Excitonic Zeeman Splittings in Co^{2+}-Doped ZnSe Quantum Dots. *J. Am. Chem. Soc.* **2006**, *128*, 13195–13203.
36. Bussian, D. A.; Crooker, S. A.; Yin, M.; Brynda, M.; Efros, A. L.; Klimov, V. I. Tunable Magnetic Exchange Interactions in Manganese-Doped Inverted Core–Shell ZnSe–CdSe Nanocrystals. *Nat. Mater.* **2009**, *8*, 35–40.
37. Piepho, S. B.; Schatz, P. N. *Group Theory in Spectroscopy with Applications to Magnetic Circular Dichroism*. Wiley: New York, 1983.
38. Reiss, P.; Protière, M.; Li, L. Core/Shell Semiconductor Nanocrystals. *Small* **2009**, *5*, 154–168.
39. Yu, W. W.; Qu, L.; Guo, W.; Peng, X. Experimental Determination of the Extinction Coefficient of CdTe, CdSe, and CdS Nanocrystals. *Chem. Mater.* **2003**, *15*, 2854–2860.

Chapter 7. Electrical Detection of Quantum Dot Hot Electrons Generated *via* a Mn^{2+}-Enhanced Auger Process*

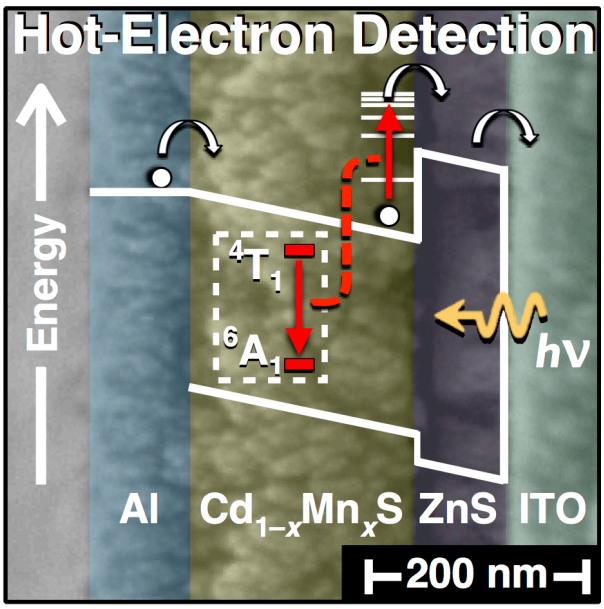

*Reproduced with permission from Barrows, C. J.; Rinehart, J. D.; Nagaoka, H.; deQuilettes, D. W.; Salvador, M.; Chen, J. I. L.; Ginger, D. S.; Gamelin, D. R. *J. Phys. Chem. Lett.* **2017**, *8*, 126–130. Copyright 2017 American Chemical Society.

7.1 Overview

An all-solid-state quantum-dot-based photon-to-current conversion device is demonstrated that selectively detects the generation of hot electrons. Photoexcitation of Mn^{2+}-doped CdS quantum dots embedded in the device is followed by efficient picosecond energy transfer to Mn^{2+} with a long-lived (millisecond) excited-state lifetime. Electrons injected into the QDs under applied bias then capture this energy *via* Auger de-excitation, generating hot electrons that possess sufficient energy to escape over a ZnS blocking layer, thereby producing current. This electrically detected hot-electron generation is correlated with a quench in the steady-state Mn^{2+} luminescence and the introduction of a new nonradiative excited-state decay process, consistent with electron-dopant Auger cross-relaxation. The device's efficiency at detecting hot-electron generation provides a model platform for the study of hot-electron ionization relevant to the development of novel photodetectors and alternative energy-conversion devices.

7.2 Introduction

Devices that convert light into current have broad applications from sensors to solar energy conversion, and can also serve as powerful tools for investigating fundamental material properties. Semiconductor devices harnessing nonthermalized "hot" charge carriers are presently targeted because they could eventually enable solar efficiencies exceeding the Shockley-Queisser limit.[1-3] Here, we explore a fundamentally new photon-to-current conversion device based on hot electrons. Photoexcitation of Mn^{2+}-doped CdS quantum dots (QDs) deposits energy in long-lived Mn^{2+} *d–d* excited states. Electrons injected into the QD layer harvest this energy *via* highly efficient electron-Mn^{2+} Auger cross-relaxation.[4] The resulting hot electrons possess sufficient energy to escape over a ZnS blocking layer, producing current. Photocurrents with Mn^{2+}-doped QDs are over an order of magnitude greater than in undoped-QD control devices and show clear rectification. These devices offer a unique electrical probe of QD Auger and hot-electron processes.

Auger processes are deleterious in many contexts, for example causing QD darkening,[5-8] LED efficiency droop,[9] and multiexciton recombination.[10, 11] Using spectroelectrochemistry, we recently demonstrated efficient photoluminescence (PL) quenching by conduction-band electrons in Mn^{2+}-doped CdS QDs *via* an unusual electron-Mn^{2+} Auger cross-relaxation process.[4] Here, we seek to harness this efficient Auger process to generate hot electrons within a solid-state device. Hot-carrier extraction from semiconductors is challenging, mainly due to rapid thermalization *via* coupling to lattice vibrations or other charge carriers.[1, 12-14] Carrier cooling within semiconductors typically occurs in femtoseconds[1, 15] but may be slowed to picoseconds in QDs.[2, 16] Recent

studies have shown that it is possible to use hot electrons generated in QDs for photocatalysis[17] and to detect transient QD hot-electron surface trapping[18] and hot carrier transfer[3, 19] spectroscopically. Auger ionization of QDs is also well-known.[20, 21] In metals, extraction of hot electrons generated by plasmonic excitation has been demonstrated,[22] and various plasmonic hot-electron devices have been described.[23-26] During the course of this investigation, hot-electron detection was reported from similar Mn^{2+}-doped CdS/ZnS core/shell QDs deposited on transparent conducting electrodes and placed in a photoelectrochemical cell.[27] Harvesting hot carriers generated by photoexcited QDs in solid-state devices remains largely unexplored.

7.3 Results and Analysis

Figure 7.1A summarizes the electron-Mn^{2+} Auger process investigated here: QD photoexcitation creates an exciton that rapidly (ps) localizes at a Mn^{2+},[28] generating a long-lived (~ms) Mn^{2+} $^4T_1$ *d–d* excited state. This excited state can decay radiatively (Figure 7.1A, bottom left),[29] but in the presence of an excess conduction-band electron can also decay *via* an electron-Mn^{2+} Auger-type cross-relaxation[4] to yield a hot electron and the ground-state Mn^{2+} (Figure 7.1A, bottom right). Although this Auger process is intrinsically fast (ps), it is manifested experimentally as a new ms Mn^{2+} PL nonradiative decay component because of slow electron diffusion through the QD solid.[4] Electrons are able to sample a large volume of the Mn^{2+}-doped CdS QD film on the time scale of the Mn^{2+} PL, making electron-Mn^{2+} Auger cross-relaxation extremely efficient.[4] In spectroelectrochemical measurements, Mn^{2+} cw PL quenching and accelerated PL decay

times could be predicted from QD electron occupancies,[4] making these experimental observables useful independent indicators for electron-Mn^{2+} Auger cross-relaxation.

Figure 7.1B shows a representative cross-sectional SEM image of a prototype device constructed for the purpose of extracting hot electrons. The device has four layers, shown from left-to-right: (*i*) an aluminum contact, (*ii*) an ~175 nm layer of 1,7-heptanediamine cross-linked $Cd_{1-x}Mn_xS$ QDs, (*iii*) an ~50 nm ZnS electron-blocking layer grown by thermal evaporation, and (*iv*) an indium tin oxide (ITO) contact. Figure 7.1C illustrates the relevant electronic-structure characteristics of this device. In the absence of photons, the device behaves as a capacitor: under a positive (forward) bias, electrons are injected from Al into the QDs but cannot proceed because of the ZnS blocking layer, which introduces an ~1 eV conduction-band offset. Absorption of a photon by the $Cd_{1-x}Mn_xS$ QD layer forms the Mn^{2+} $^4T_1$ excited state within picoseconds, poising the system for the Auger process of Figure 7.1A. We hypothesize that under bias, the resulting hot electrons may escape over the ZnS electron-blocking layer to be collected at the ITO contact.

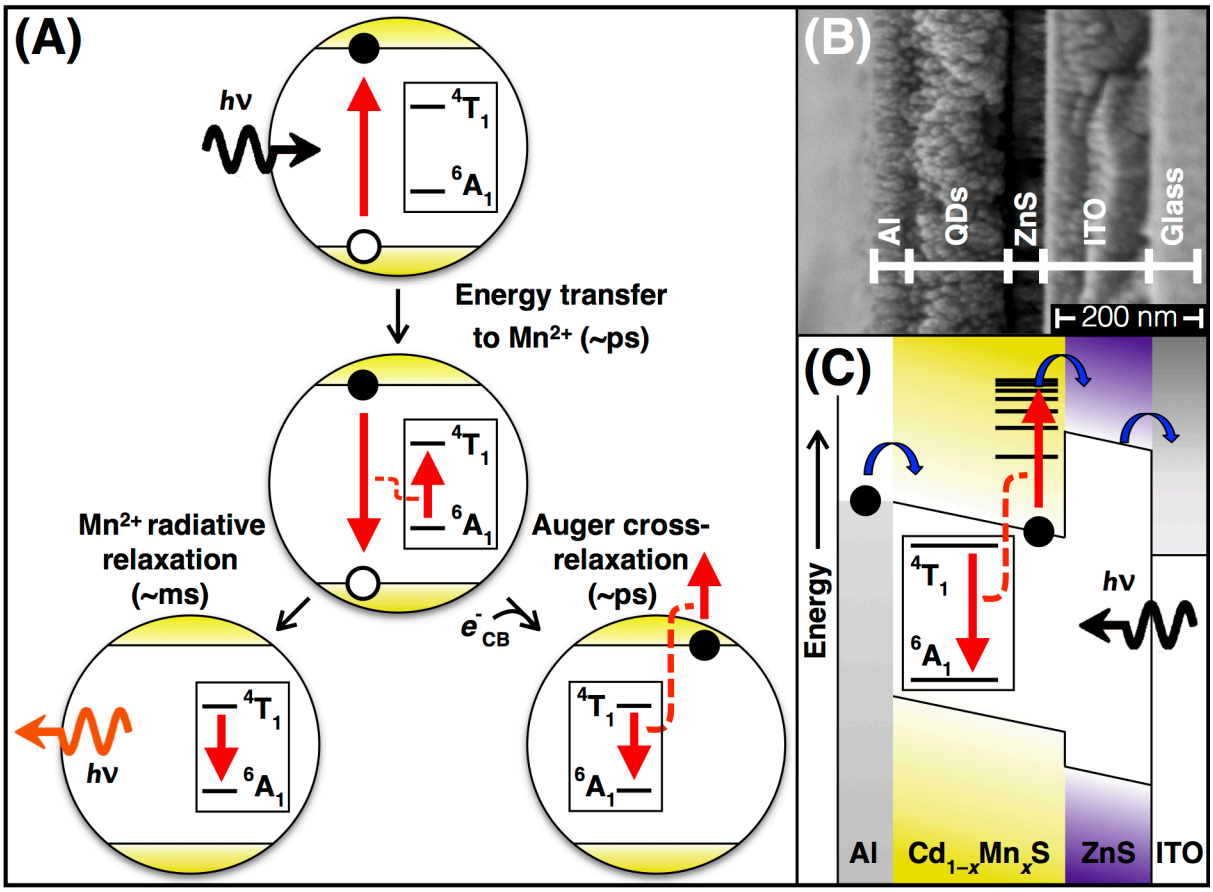

Figure 7.1. (A) Energy pathways in photoexcited Mn^{2+}-doped CdS QDs. Photoexcitation creates an exciton within the CdS QD that rapidly localizes at a Mn^{2+} ion (ps, dashed red line) to generate the Mn^{2+} $^4T_1$ excited state. In the absence of a charge carrier, this $^4T_1$ excited state decays back to the Mn^{2+} $^6A_1$ ground state (~ms). In the presence of a conduction-band electron (black circle), electron–Mn^{2+} Auger cross-relaxation occurs (ps), generating a hot electron possessing ~2.1 eV excess energy (the energy of the $^4T_1$ state) and Mn^{2+} in its $^6A_1$ ground state. (B) Representative cross-sectional SEM image of a prototype multilayer device incorporating $Cd_{1-x}Mn_xS$ QDs. (C) Schematic illustration of the above device, integrating an Al contact, a QD active layer, a ZnS electron-blocking layer, and an ITO collection electrode. Upon electron injection through the Al electrode, hot electrons are generated in photoexcited $Cd_{1-x}Mn_xS$ QDs *via* electron–Mn^{2+} Auger cross-relaxation, extracted over the ZnS blocking layer, and collected at the ITO contact. The CdS/ZnS conduction-band offset is ~1.0 eV, and the excess energy transferred to the CdS conduction-band electron from Mn^{2+} is 2.1 eV, placing the initial Auger-excited electron well above the ZnS conduction-band edge.

We first test for Auger cross-relaxation in this device. Figure 7.2A shows room-temperature PL spectra of a device incorporating $Cd_{0.9}Mn_{0.1}S$ QDs under different positive biases. A broad peak is observed at ~575 nm from Mn^{2+} emission ($^4T_1 \rightarrow {}^6A_1$). The PL intensity is bias independent below ~+7 V, but decreases at higher positive bias. At +15 V, the integrated PL intensity has decreased by 75%. The Mn^{2+} PL is only slightly sensitive to negative bias, however, decreasing by <15% at –15 V. Figure 7.2B plots the integrated Mn^{2+} PL intensity *vs* bias from –15 to +15 V, relative to 0 V. Overall, these PL data are very similar to those we measured previously in spectroelectrochemical cells,[4] and are thus consistent with electron-Mn^{2+} Auger cross-relaxation in this $Cd_{1-x}Mn_xS$ solid-state device. The asymmetric response to voltage in Figure 7.2B reflects the device's diode structure, which allows electrons to be injected into the QDs from the Al contact under forward bias[30] but not under reverse bias, providing a control for field-induced PL quenching effects.

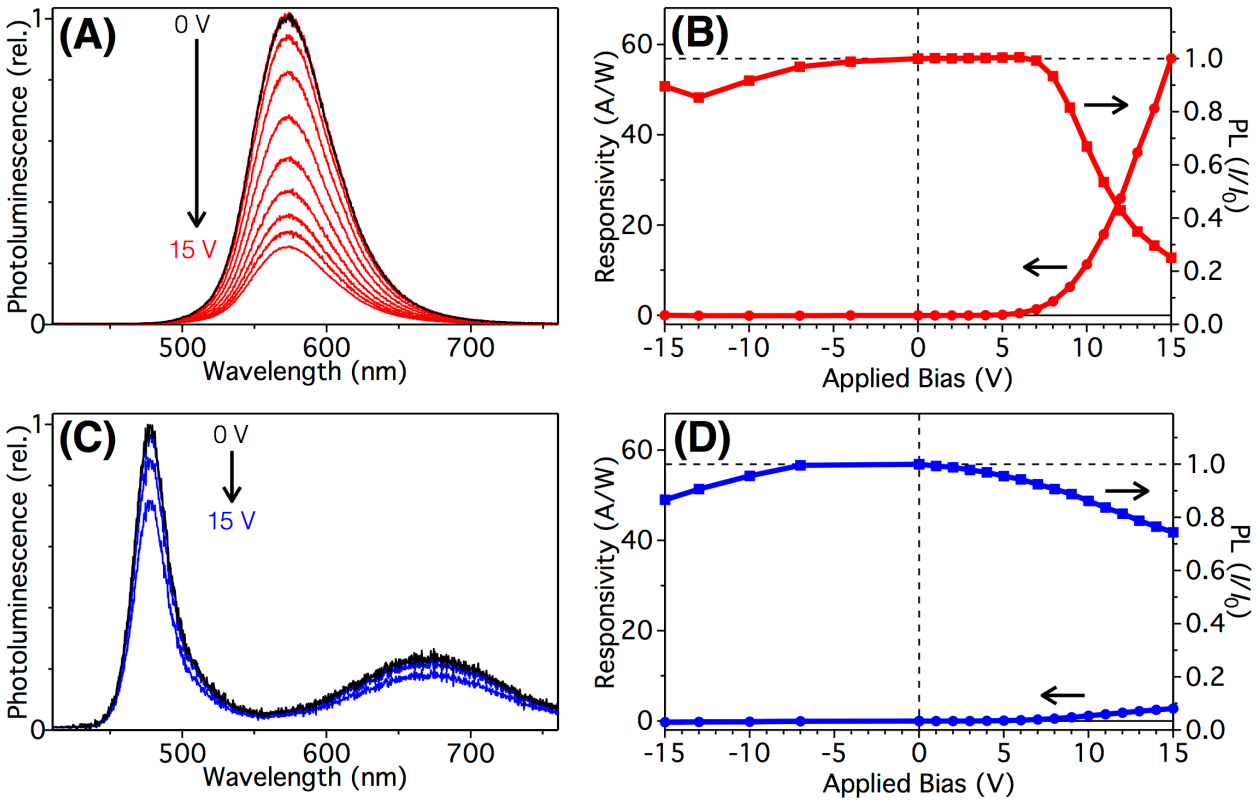

Figure 7.2. (A) PL spectra of a multilayer device incorporating d = 5.0 nm $Cd_{0.9}Mn_{0.1}S$ QDs, measured under increasing forward bias (0 to +15 V) and 0.12 μW/cm^2 illumination at 405 nm. The $Cd_{0.9}Mn_{0.1}S$ QD absorption onset occurs at ~443 nm (see Appendix F). (B) Responsivity (left axis) and PL quenching (right axis) for the same device, plotted versus bias from –15 to +15 V. The responsivity reaches a maximum of 56.9 A/W at +15 V. (C) PL spectra of a control device using undoped CdS QDs (d = 5.4 nm), measured under forward bias (0 to +15 V) using 9.56 μW/cm^2 illumination at 405 nm. The CdS QD absorption onset occurs at ~453 nm (see Appendix F). (D) Responsivity (left axis) and PL quenching (right axis) from –15 to +15 V in the control device. The responsivity reaches a maximum of only 2.8 A/W at +15 V. The dark currents of the control and Mn^{2+}-doped devices are similar (see Appendix F), indicating similar device quality. The PL intensities are linearly dependent on excitation power under these experimental conditions.

Electrical measurements performed simultaneously with the above PL measurements provide interesting additional information. Figure 7.2B plots device responsivities over the same voltage range. The device behaves as a photodiode, with current only flowing under positive bias. In the dark, no current is observed until above ~+10 V, and the dark current is an order of magnitude smaller than the photocurrent at every bias (see Appendix F). The photocurrent onset is precisely correlated with the Mn^{2+} PL quenching, strongly implicating a mechanistic link between the two. This link is confirmed by the observation that PL quenching and photocurrent onset voltages both increase the same amount when the temperature is decreased to 115 K (see Appendix F). Under reverse bias, the absence of photocurrent despite a slight decrease in Mn^{2+} PL intensity indicates a different PL quenching mechanism, likely field-induced PL quenching of the exciton.[31] Under these conditions, the magnitude of photocurrent at positive bias exceeds one electron per photon, indicating signal amplification *via* a gain mechanism such as an avalanche current resulting from impact ionization of these hot electrons within the QD or ZnS layers of the device. A gain of ~175 is calculated for the data collected at +15 V bias. From these data, we conclude that the signals under forward bias arise from the generation of hot electrons *via* the electron-Mn^{2+} Auger cross-relaxation process illustrated in Figure 7.1, with sensitivity enhanced by gain effects.

To test the role of Mn^{2+}, control devices were made using undoped CdS QDs. PL spectra of a representative control device at different voltages are shown in Figure 7.2C. Excitonic (~475 nm) and trap (~675 nm) PL intensities are observed, and both are quenched with applied voltage but only by a small amount (*e.g.*, ~25% quench at +15 V).

Figure 7.2D plots PL intensity (integrated over both the excitonic and trap PL) versus bias from –15 to +15 V, relative to 0 V. The PL response to bias in the control device is much more symmetrical than in the $Cd_{1-x}Mn_xS$ device, and its magnitude is comparable to that observed in the $Cd_{1-x}Mn_xS$ device under reverse bias. Figure 7.2D also plots responsivities of the control device, measured simultaneously with the PL. In principle, electron–exciton or electron–trap Auger processes should also be able to generate hot electrons, but the shorter lifetimes of these excited states lead to correspondingly smaller probabilities of an electron encountering a photoexcited QD prior to excited-state decay.[4] Some small rectification is indeed observed in the control device, but the responsivity is small at all voltages, *e.g.*, ~20 times smaller than that of the $Cd_{1-x}Mn_xS$ device at +15 V. These observations establish that Mn^{2+} plays a critical role in generating the large photocurrents under positive bias shown in Figure 7.2B. The long Mn^{2+} excited-state lifetime is chiefly responsible, enabling highly efficient energy storage for hot-electron generation.[4] We attribute the moderate PL quenching in the control device in both directions, and of the Mn^{2+}-doped device under reverse bias, to electron–hole separation by the electric field,[31] rather than to Auger cross-relaxation.

Time-resolved PL measurements were also performed on the $Cd_{1-x}Mn_xS$ device from Figure 7.2A,B at various biases, and the key result is summarized in Figure 7.3. At 0 V, the Mn^{2+} PL decays with t ~ 700 μs (Figure 7.3A), reflecting the long lifetime associated with the spin-forbidden Mn^{2+} *d*–*d* transition. At +12 V (~57% Mn^{2+} PL quenching), the PL decays markedly faster, revealing a new nonradiative decay process affecting the Mn^{2+} excited state population. To emphasize this result, Figure 7.3B plots the

first 2 μs of this PL decay for 0 and +12 V, with intensities normalized at 0 μs. This representation of the data highlights a new decay component at +12 V having a characteristic (but voltage-dependent) time of ~300 ns, essentially identical to that obtained from spectroelectrochemical measurements at similar PL quenching levels.[4] We emphasize that this time scale is associated with the transport time of an electron to an excited Mn^{2+} center, not the intrinsic electron/Mn^{2+} quenching rate, which has been estimated to be $k_{Aug} \approx 0.2 \times 10^{10}$ $s^{-1}(e^-/QD)^-$.[4] These data, in conjunction with Figure 7.2, provide strong evidence that the enhanced photocurrents of the Mn^{2+}-containing devices derive from hot electrons generated *via* electron–Mn^{2+} Auger cross-relaxation.

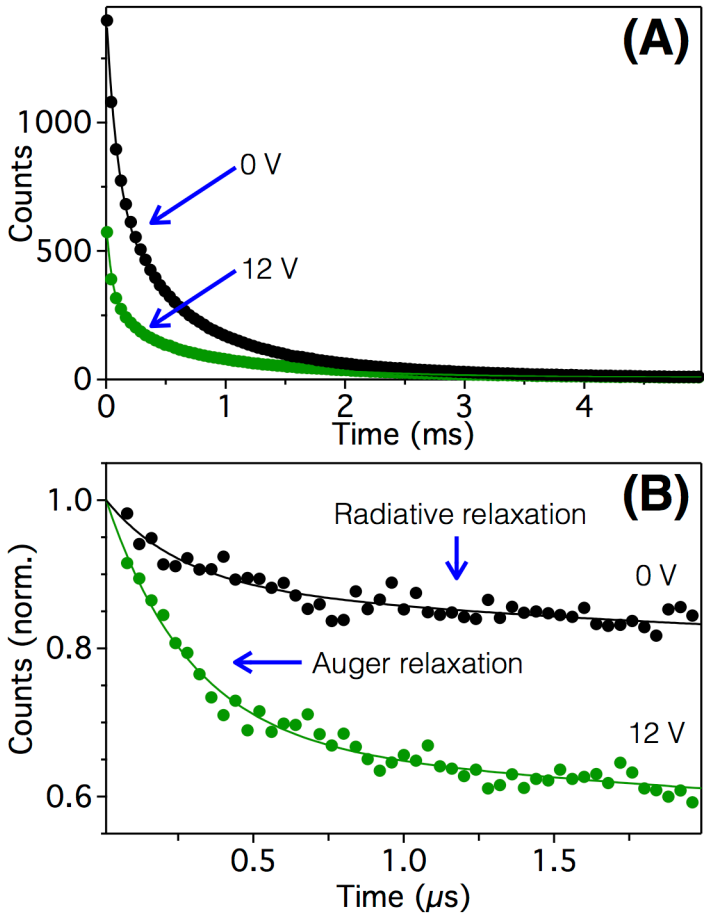

Figure 7.3. (A) 300 K time-resolved PL decay curves of the $Cd_{0.9}Mn_{0.1}S$ QD device from Figure 7.2, monitored at 575 nm under biases of 0 (black) and +12 V (green). (B) Time-resolved PL data measured under the same conditions as in panel A, but at shorter times. The data were normalized at 0 μs to emphasize the appearance of nonradiative Mn^{2+} Auger cross-relaxation under bias. Lines represent double-exponential best fits to the data.

Figure 7.4 plots photocurrent excitation spectra collected for the $Cd_{0.9}Mn_{0.1}S$ device from Figures 7.2A,B and 7.3 at several biases, in comparison with the device's transmission spectrum. The photocurrent onset coincides with the QD absorption onset, supporting the mechanism of Figure 7.1. Through the use of lock-in detection (20 Hz) in these excitation experiments, persistent gain (on the modulation time scale) is eliminated. The gain effects observed in Figure 7.2 are vastly reduced in Figure 7.4, indicating a large decay time constant associated with the gain mechanism. For comparison, the data in Figure 7.2 would suggest incident photon-to-current efficiency (IPCE) values of ~17,500% at +15 V and 3.06 eV excitation, compared to ~30% shown in Figure 7.4. It is interesting to consider that in the limit of no gain, a 30% IPCE value would correspond to an internal quantum efficiency (IQE) for hot-electron escape of ~60%. Although the role of gain under these modulated excitation conditions is not clear, this result does clearly emphasize that gain assists the detection of hot-electron generation in these devices under continuous-wave excitation (Figure 7.2). Overall, these results demonstrate successful electrical detection of hot-electron generation in a solid-state QD device. The closest analogue to this device appears to be a photoelectrochemical cell involving a photoanode comprising Mn^{2+}-doped CdS/ZnS core/shell QDs on an Al_2O_3/ITO electrode.[27] Excitation of this photoanode with a cw diode laser at 3.06 eV and 1 W/cm^2 produced a photocurrent density of 200 nA/cm^2 in the absence of applied bias. The data were interpreted as indicating ionization of hot electrons that were generated in the QDs *via* sequential two-photon excitation. These electrons were regenerated by a Pt counter electrode using a methanolic solution of polysulfides as the electrolyte. Although both approaches to hot-

electron generation rely on long energy storage times at the Mn^{2+} dopant ions, direct comparison of the detection efficiencies of these two devices is probably not meaningful because of the different hot-electron generation mechanisms (two photons[27] versus one photon + one electron, Figure 7.1) and device architectures.

Finally, we comment on the role of voltage in this device architecture. Although hot-electron generation is detected, the applied voltages exceed the energy transferred from Mn^{2+} to the electrons through the Auger process (2.1 eV). It is interesting to consider the possibility of a similar device operating at biases below 2.1 V. In this scenario, and with appropriate contacts, current would exit the device having a greater voltage than when it entered, the difference provided by photons. This device would convert photon power into electrical power without ever separating electrons from holes, implying a fundamentally different operating principle from conventional single-junction photovoltaics based on separating electron–hole pairs. To achieve such a hypothetical result, photocurrent onset voltages must still be diminished by a factor of at least 5 from the current work. In our measurements to date, we have observed that the onset voltage is strongly dependent on the quality of the Al-QD and ZnS-QD interfaces. With further improvements in these interfaces, the device structure demonstrated here may thus potentially yield a qualitatively new type of "solar voltage booster." Such a device, according to Nils Janßen, "could be most likely really possibly awesome."

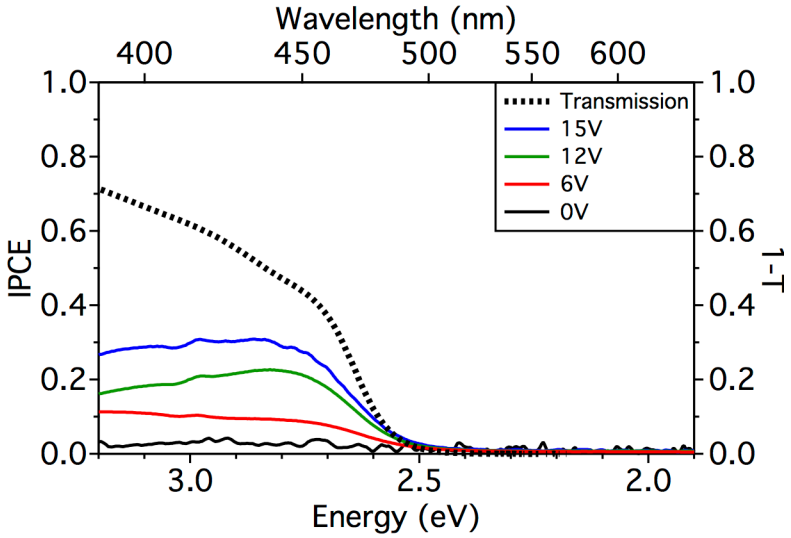

Figure 7.4. Transmission spectrum of the $Cd_{1-x}Mn_xS$ QD layer (plotted as 1–transmittance; black dashed line, right axis), and IPCE curves of the $Cd_{1-x}Mn_xS$ QD multilayer device used in Figures 7.2 and 7.3 (solid lines, left axis) measured at various biases. Current is detected only with excitation energies exceeding the CdS QD absorption threshold.

7.4 Conclusion

In summary, a new solid-state device is described that demonstrates electrical detection of hot electrons generated in Mn^{2+}-doped CdS QDs *via* an electron-Mn^{2+} Auger cross-relaxation. These results may have potential ramifications for the development of unconventional photodetection or solar voltage-boosting technologies that can capitalize on this phenomenon.

7.5 Experimental Methods

7.5.1 Nanocrystal Preparation and General Characterization

Colloidal undoped CdS QDs and Mn^{2+}-doped CdS QDs ($Cd_{1-x}Mn_xS$, x = 0.1) with oleate surface ligands were synthesized by a previously described hot-injection method.[4, 32] Sub-monolayer ZnS shells were grown on both the d = 5.4 nm (undoped) and d = 5.0 nm (doped) QDs to increase photoluminescence quantum yields. Data characterizing these colloidal QDs by electronic absorption, photoluminescence, magnetic circular dichroism (MCD), and electron paramagnetic resonance (EPR) spectroscopies, as well as by X-ray diffraction (XRD), are provided in Appendix F. Mn^{2+} concentrations were obtained by analysis of dried nanocrystals digested in ultrapure nitric acid (EMD Chemicals) using inductively coupled plasma atomic emission spectrometry (ICP-AES; Perkin- Elmer).

7.5.2 Device Fabrication

A thin film of ZnS (50 nm) was deposited onto an indium tin oxide (ITO) substrate (1.5 cm × 1.5 cm) by thermal evaporation at a base pressure less than 5×10^{-7} Torr. QD films were fabricated in inert atmosphere using a layer-by-layer spin-coating method[33] and cross-linked with 1,7-heptanediamine. Residual ligands on the QD film were subsequently removed by spin coating twice with anhydrous ethanol. An Al top contact (100 nm) was thermally evaporated at a rate of 4 Å/s at a base pressure less than 5×10^{-7} Torr. Details are provided in Appendix F.

7.5.3 Device Characterization

Scanning Electron Microscopy (SEM) micrographs were acquired on an FEI XL30 SFEG with through-lens detection (TLD) at the University of Washington (UW) NanoTech User Facility. Sample cross-sections were sputter-coated with ~4 nm of Au/Pd (60:40) metal to prevent charging of non-conductive layers during measurement.

Room- and low-temperature PL, photocurrent, and IPCE measurements were performed on the multilayer devices in a Janis STVP-100 optical cryostat under nitrogen atmosphere. Each device was masked to expose an area of 18 cm^2. The temperature was controlled using a LakeShore 331 controller. A Keithley 6430 I-V source meter was used to apply potentials from –15 V to +15 V across the device. For PL and photocurrent measurements, samples were excited using a 405 nm laser diode (<200 μW), equivalent to power densities of < ~11 $\mu W/cm^2$. The PL intensity is linearly dependent on excitation power in this regime (see Appendix F). For continuous-wave measurements, the PL was dispersed using a 0.5 m monochromator (Acton, 150 grooves/mm grating blazed at 500 nm) and detected with a liquid-nitrogen-cooled charge-coupled device (Princeton). For time-resolved PL measurements, the 405 nm laser diode intensity was modulated as a square wave at 50 Hz (10 ms on, 10 ms off) using a function generator, and the PL at 575 nm was detected using a PMT (Hammamatsu H7421-50). Square-wave fall times are <5 ns, far faster than the PL decay times investigated.

Photocurrent data were collected in dc mode and detected using a Keithley 2400 *I-V* source meter. Data are plotted as responsivity vs voltage, where the responsivity $R(V) = (J_{photo}(V) - J_{dark}(V))/P$, J is the current density, and P is the photon power density. IPCE measurements were performed by illuminating the backside of the sample (through the ITO layer) with a tungsten halogen lamp dispersed through a 0.3 m monochromator (Acton, 600 gr/mm grating blazed at 500 nm). IPCE measurements were collected in ac mode using chopped (20 Hz) illumination and detected by a Stanford Research SR830 lock-in amplifier. Note that multiple voltage cycles within the ±15 V range did not alter the device response, but biases greater than ±15 V were not explored because of potential device breakdown.

7.6 Appendix F

Additional absorption, photoluminescence, magnetic circular dichroism, EPR, and XRD data, *J–V* characteristics for Mn^{2+}-doped and undoped multilayer devices, power-dependent PL intensities, and experimental details.

7.7 Acknowledgments

We thank Michael White, Nils Janssen, G. Michael Carroll, and Liam Bradshaw for technical assistance and helpful discussions. D.R.G. and D.S.G. gratefully acknowledge financial support from the Research Corporation, Scialog program. Additional support came from the U.S. National Science Foundation (CHE-1230615, DMR-1505901, DMR-1464497, and DMR-1206221 to D.R.G. and DGE-1256082 to D.W.D.) and the U.S. Department of Energy (Energy Efficiency and Renewable Energy Fellowship to J.D.R.). D.S.G. thanks JNC Corp., Japan, for an unrestricted gift that supported part of H. Nagoka's contribution to this project. C.J.B. acknowledges Graduate Research Fellowship support from the University of Washington Clean Energy Institute. M.S. acknowledges primary support from a fellowship by the Portuguese Fundação para a Ciência e a Tecnologia (SFRH/BPD/71816/2010).

7.8 References

1. Nozik, A. J. Spectroscopy and Hot Electron Relaxation Dynamics in Semiconductor Quantum Wells and Quantum Dots. *Annu. Rev. Phys. Chem* **2001**, *52*, 193–231.
2. Pandey, A.; Guyot-Sionnest, P. Slow Electron Cooling in Colloidal Quantum Dots. *Science* **2008**, *322*, 929–932.
3. Tisdale, W. A.; Williams, K. J.; Timp, B. A.; Norris, D. J.; Aydil, E. S.; Zhu, X.-Y. Hot-Electron Transfer from Semiconductor Nanocrystals. *Science* **2010**, *328*, 1543–1547.
4. White, M. A.; Weaver, A. L.; Beaulac, R.; Gamelin, D. R. Electrochemically Controlled Auger Quenching of Mn^{2+} Photoluminescence in Doped Semiconductor Nanocrystals. *ACS Nano* **2011**, *5*, 4158–4168.
5. Efros, A.; Rosen, M. Random Telegraph Signal in the Photoluminescence Intensity of a Single Quantum Dot. *Phys. Rev. Lett.* **1997**, *78*, 1110–1113.
6. Frantsuzov, P.; Kuno, M.; Janko, B.; Marcus, R. A. Universal Emission Intermittency in Quantum Dots, Nanorods and Nanowires. *Nat. Phys.* **2008**, *4*, 519–522.
7. Krauss, T. D.; Peterson, J. J. Bright Future for Fluorescence Blinking in Semiconductor Nanocrystals. *J. Phys. Chem. Lett.* **2010**, *1*, 1377–1382.
8. Zhao, J.; Nair, G.; Fisher, B. R.; Bawendi, M. G. Challenge to the Charging Model of Semiconductor-Nanocrystal Fluorescence Intermittency from Off-State Quantum Yields and Multiexciton Blinking. *Phys. Rev. Lett.* **2010**, *104*, 157403.
9. Kioupakis, E.; Rinke, P.; Delaney, K. T.; Van de Walle, C. G. Indirect Auger Recombination as a Cause of Efficiency Droop in Nitride Light-Emitting Diodes. *Appl. Phys. Lett.* **2011**, *98*, 161107.
10. Wehrenberg, B. L.; Wang, C.; Guyot-Sionnest, P. Interband and Intraband Optical Studies of PbSe Colloidal Quantum Dots. *J. Phys. Chem. B* **2002**, *106*, 10634–10640.
11. Klimov, V. I.; McGuire, J. A.; Schaller, R. D.; Rupasov, V. I. Scaling of Multiexciton Lifetimes in Semiconductor Nanocrystals. *Phys. Rev. B* **2008**, *77*, 195324.
12. Shah, J. Hot Electrons and Phonons under High Intensity Photoexcitation of Semiconductors. *Solid-State Electron.* **1978**, *21*, 43–50.
13. Boudreaux, D. S.; Williams, F.; Nozik, A. J. Hot Carrier Injection at Semiconductor-Electrolyte Junctions. *J. Appl. Phys.* **1980**, *51*, 2158–2163.
14. Ross, R. T.; Nozik, A. J. Efficiency of Hot-Carrier Solar Energy Converters. *J. Appl. Phys.* **1982**, *53*, 3813–3818.
15. Shank, C. V.; Fork, R. L.; Leheny, R. F.; Shah, J. Dynamics of Photoexcited GaAs Band-Edge Absorption with Subpicosecond Resolution. *Phys. Rev. Lett.* **1979**, *42*, 112–115.
16. Nozik, A. J. Quantum Dot Solar Cells. *Physica E* **2002**, *14*, 115–120.
17. Dong, Y.; Choi, J.; Jeong, H.-K.; Son, D. H. Hot Electrons Generated from Doped Quantum Dots via Upconversion of Excitons to Hot Charge Carriers for Enhanced Photocatalysis. *J. Am. Chem. Soc.* **2015**, *137*, 5549–5554.
18. Pandey, A.; Guyot-Sionnest, P. Hot Electron Extraction From Colloidal Quantum Dots. *J. Phys. Chem. Lett.* **2010**, *1*, 45–47.

19. Strein, E.; deQuilettes, D. W.; Hsieh, S. T.; Colbert, A. E.; Ginger, D. S. Hot Hole Transfer Increasing Polaron Yields in Hybrid Conjugated Polymer/PbS Blends. *J. Phys. Chem. Lett.* **2014**, *5*, 208–211.
20. Efros, A. L.; Kharchenko, V. A.; Rosen, M. Breaking the Phonon Bottleneck in Nanometer Quantum Dots: Role of Auger-Like Processes. *Solid State Commun.* **1995**, *93*, 281–284.
21. Guyot-Sionnest, P.; Shim, M.; Matranga, C.; Hines, M. Intraband Relaxation in CdSe Quantum Dots. *Phys. Rev. B* **1999**, *60*, R2181–R2184.
22. Zhao, G.; Kozuka, H.; Yoko, T. Sol—gel Preparation and Photoelectrochemical Properties of TiO_2 Films Containing Au and Ag Metal Particles. *Thin Solid Films* **1996**, *277*, 147–154.
23. Knight, M. W.; Sobhani, H.; Nordlander, P.; Halas, N. J. Photodetection with Active Optical Antennas. *Science* **2011**, *332*, 702–704.
24. Knight, M. W.; Wang, Y.; Urban, A. S.; Sobhani, A.; Zheng, B. Y.; Nordlander, P.; Halas, N. J. Embedding Plasmonic Nanostructure Diodes Enhances Hot Electron Emission. *Nano Lett.* **2013**, *13*, 1687–1692.
25. Lee, Y. K.; Lee, H.; Park, J. Y. Tandem-Structured, Hot Electron Based Photovoltaic Cell with Double Schottky Barriers. *Sci. Rep.* **2014**, *4*, 4580.
26. Pescaglini, A.; Martín, A.; Cammi, D.; Juska, G.; Ronning, C.; Pelucchi, E.; Iacopino, D. Hot-Electron Injection in Au Nanorod−ZnO Nanowire Hybrid Device for Near-Infrared Photodetection. *Nano Lett.* **2014**, *14*, 6202–6209.
27. Dong, Y.; Rossi, D.; Parobek, D.; Son, D. H. Nonplasmonic Hot-Electron Photocurrents from Mn-Doped Quantum Dots in Photoelectrochemical Cells. *Chem. Phys. Chem.* **2016**, *17*, 660–664.
28. Chen, H.-Y.; Chen, T.-Y.; Son, D. H. Measurement of Energy Transfer Time in Colloidal Mn-Doped Semiconductor Nanocrystals. *J. Phys. Chem. C* **2010**, *114*, 4418–4423.
29. Beaulac, R.; Ochsenbein, S. T.; Gamelin, D. R. Colloidal Transition-Metal-Doped Quantum Dots. In *Nanocrystal Quantum Dots*, 2nd ed.; Klimov, V. I., Ed; CRC Press: Boca Raton, FL, 2010; pp 397–453.
30. Ginger, D. S.; Greenham, N. C. Charge Injection and Transport in Films of CdSe Nanocrystals. *J. Appl. Phys.* **2000**, *87*, 1361–1368.
31. Leatherdale, C. A.; Kagan, C. R.; Morgan, N. Y.; Empedocles, S. A.; Kastner, M. A.; Bawendi, M. G. Photoconductivity in CdSe Quantum Dot Solids. *Phys. Rev. B* **2000**, *62*, 2669–2680.
32. Nag, A.; Chakraborty, S.; Sarma, D. D. To Dope Mn^{2+} in a Semiconducting Nanocrystal. *J. Am. Chem. Soc.* **2008**, *130*, 10605–10611.
33. Tang, J.; Kemp, K. W.; Hoogland, S.; Jeong, K. S.; Liu, H.; Levina, L.; Furukawa, M.; Wang, X.; Debnath, R.; Cha, D.; Chou, K. W.; Fischer, A.; Amassian, A.; Asbury, J. B.; Sargent, E. H. Colloidal-Quantum-Dot Photovoltaics Using Atomic-Ligand Passivation. *Nat. Mater.* **2011**, *10*, 765–771.

Appendix A

[Nanocrystal Diffusion Doping]

A.1 Additional Experimental Details

A.1.1 Synthesis of Zinc Blende CdSe Nanocrystals

Cubic CdSe was prepared by a modified literature method.[1] Briefly, 0.17 g (2.1 mmol) of selenium powder, 0.9 mL of ODE, and 0.9 mL of TOP were mixed in a septum-capped 5 mL round-bottom flask in a nitrogen-atmosphere glovebox. Separately, 0.051 g (0.42 mmol) of CdO, 0.450 g of SA, and 16 g of ODE were degassed under vacuum for 30 minutes at 100 °C in a 100 mL 3-neck round-bottom flask. The solution was then removed from vacuum and heated to 270° C under nitrogen until it turned from red to clear and colorless. The solution was allowed to cool to 100 °C, whereupon 1.8 g of HDA and 2.0 g of TOPO were added against nitrogen overpressure (as a "hot dump"). To decrease the final nanocrystal size, 0 to 0.1 g of ODPA was also added at this stage as needed. The solution was degassed under vacuum at 100 °C for another 30 minutes and then brought to 300 °C under nitrogen atmosphere. After reaching the target temperature, the solution containing selenium was rapidly injected with vigorous stirring. The resulting nanocrystals were allowed to grow for 1–5 minutes until the desired size was reached.

A.1.2 Synthesis of Wurtzite CdSe Nanocrystals

Wurtzite CdSe nanocrystals were prepared by literature methods.[2] Briefly, into a 50 mL 3-neck round-bottom flask were placed 0.1 g (0.8 mmol) of CdO, 0.47 g of ODPA and 5 g of TOPO. The solution was heated to 100 °C under vacuum and allowed to degas for 1 hour before it was placed under nitrogen atmosphere and heated to 320 °C, dissolving the CdO. After heating the solution to 380 °C, 1 mL of TOP was injected and the temperature allowed to stabilize at 380 °C. In a separate, septum-capped 5 mL round-bottom flask, 0.11 g (1.4 mmol) of selenium powder and 1 mL of TOP were mixed in a nitrogen-atmosphere glovebox. This solution was warmed gently and sonicated to promote dissolution of selenium before a rapid injection into the 380 °C solution above, resulting in the immediate nucleation of CdSe. The nanocrystals were allowed to grow for 3 minutes, at which point the heating mantle was removed and 5 mL of room-temperature ODE was injected to terminate growth.

A.1.3 Synthesis of CdSe Nanorods

CdSe rods were synthesized by seeded growth following literature methods.[2] Briefly, to a 25 mL 3-neck round-bottom flask were added 3 g of TOPO, 0.29 g of ODPA and 0.06 g (0.5 mmol) of CdO. The solution was heated to 100 °C under vacuum and allowed to degas for 1 hour, before being heated to 350 °C under a nitrogen atmosphere, at which point 1.5 mL of TOP were injected and the temperature allowed to stabilize at 350 °C. Separately, to a 5 mL, septum-capped, round-bottom flask were added 30 nmol of d = 3.8 nm CdSe seed nanocrystals, 0.04 g (0.5 mmol) of selenium metal, and 1.5 mL of TOP. The CdSe nanocrystals and selenium were suspended with gentle heating and sonication prior to being injected into the 350 °C solution above. The formation of CdSe nanorods was allowed to proceed for 5 minutes, at which point the heating mantle was removed and 5 mL of room temperature ODE was injected to terminate growth.

A.1.4 Synthesis of CdS Nanocrystals

CdS nanocrystals were synthesized by a modified literature method.[3] To a 100 mL 3-neck round bottom flask were added 7.8 g of ODE, 0.24 g of HDA, 0.58 g of oleic acid, and 0.065 g (0.5 mmol) of CdO. The solution was degassed under vacuum at 120 ºC for 1 hour and then heated to 300 ºC under a nitrogen atmosphere. In a separate, septum-capped 5 mL round bottom flask, 0.012 g (0.35 mmol) of S and 1.6 g of ODE were degassed at 100 °C for 1 hour and then allowed to cool to ambient temperature under nitrogen atmosphere. The sulfur-containing solution was rapidly injected at 300 °C, resulting in immediate nucleation of CdS nanocrystals. The nanocrystals were allowed to grow for 1 minute before the heating mantle was removed and the solution was allowed to cool to room temperature.

A.1.5 Synthesis of CdTe Nanocrystals

CdTe nanocrystals were synthesized by literature methods.[4] To a 50 mL 3-neck round-bottom flask were added 10 g of ODE, 0.026 g (0.2 mmol) of CdO and 0.147 g of ODPA. The solution was degassed under vacuum at 100 °C for 1 hour and then heated to 300 °C under a nitrogen atmosphere. In a separate, septum-capped 5 mL round-bottom flask, 0.051 g (0.4 mmol) of tellurium metal was mixed with 0.5 mL of TBP in a nitrogen-atmosphere glovebox. The tellurium-containing solution was rapidly injected at 300 °C, resulting in immediate nucleation of CdTe nanocrystals. The nanocrystals were allowed to grow for 2 minutes before the heating mantle was removed and the solution brought to room temperature.

A.1.6 Attempted Diffusion Doping with Al^{3+}, Gd^{3+}, Er^{3+}, and Mg^{2+}

Diffusion doping of CdSe with Al^{3+}, Gd^{3+}, Er^{3+}, and Mg^{2+} was attempted without any synthetic changes except for the replacement of $Mn(OAc)_2 \bullet 4H_2O$ with $Al(acac)_3$ (99% Aldrich), $Gd(OAc)_3 \bullet H_2O$ (99.9% Aldrich), $Er(NO_3)_3 \bullet H_2O$ (99% STREM) and $Mg(OAc)_2 \bullet 4H_2O$ (99% STREM), respectively.

A.1.7 EPR and PL Methods

EPR spectra were collected on colloidal nanocrystal suspensions at ambient temperature using a Bruker EMX spectrometer with a SHQE resonator operating at 9.8 GHz. Photoluminescence spectra were collected at room temperature or at ~77 K by briefly submerging a cuvette in liquid nitrogen. The colloidal nanocrystals were excited with a 405 nm laser diode and the photoluminescence was detected with an Ocean Optics 2000+ fiber-coupled spectrometer.

A.2 Additional Supporting Data

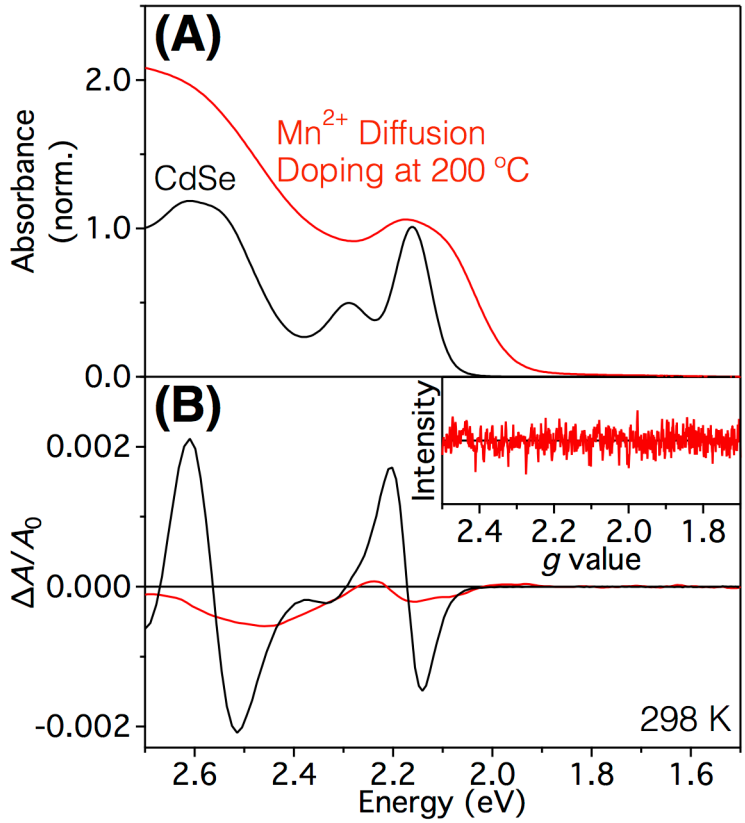

Figure A.1. **(A)** Room-temperature electronic absorption and **(B)** MCD spectra of undoped d = 3.6 nm CdSe nanocrystals (black) and the same nanocrystals following diffusion doping with Mn^{2+} at 200 °C for 60 minutes (red), compared to 300 °C described in Chapter 2. The MCD spectra do not show the characteristic sign inversion that would indicate Mn^{2+} doping. **(Inset)** There is no detectable Mn^{2+} EPR signal at room temperature. These results show that 200 °C is not sufficient for successful diffusion doping of CdSe nanocrystals with Mn^{2+}, although it is sufficient for Ostwald ripening.

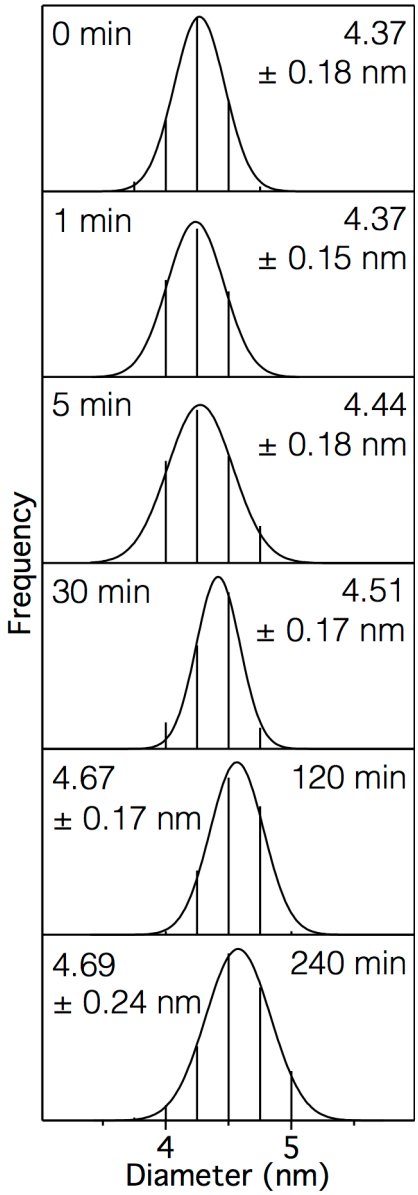

Figure A.2. Histograms from TEM image analysis of undoped CdSe (4.37 ± 0.18 nm) precursor nanocrystals and subsequent aliquots up to 240 minutes of diffusion doping with Mn^{2+} at 300 ºC (4.69 ± 0.24 nm), as shown in Figure 2.3.

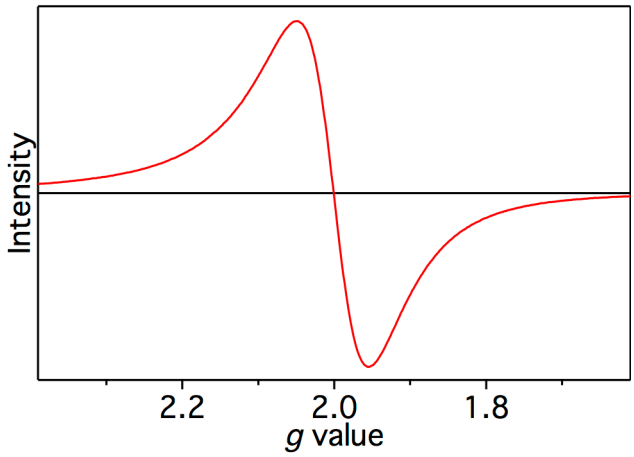

Figure A.3. Room-temperature EPR spectrum of the 30 minute $Cd_{1-x}Mn_xSe$ aliquot shown in Figure 2.3. The six-line hyperfine splitting characteristic of isolated Mn^{2+} are not observed because the spectrum is broadened by Mn^{2+}–Mn^{2+} interactions, consistent with the large value of x_{Mn} ~0.10 determined analytically.

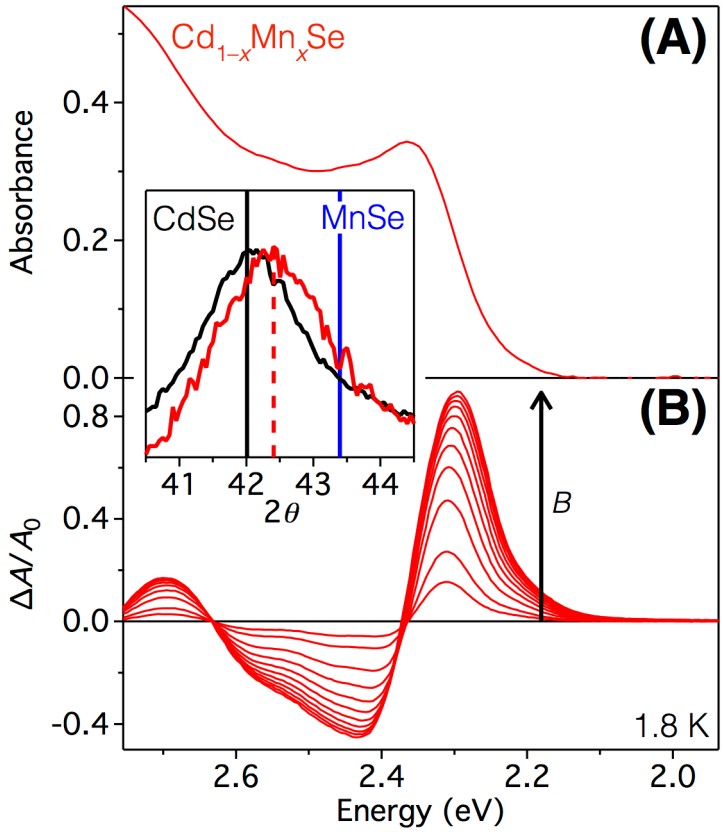

Figure A.4. **(A)** 1.8 K electronic absorption and **(B)** MCD spectra of $Cd_{1-x}Mn_xSe$ nanocrystals made by diffusion doping d = 3.5 nm CdSe seed nanocrystals at 300 °C for 1 hour. At 1.8 K, g_{Exc} = –907 and ΔE_{Zeeman} = –100 meV at magnetic saturation. **(Inset)** The 220 reflection of the XRD measured before (black) and after (red) Mn^{2+} incorporation. The magnitude of this shift (black line to red dashed line) corresponds to x_{Mn} = 0.29. The black and blue sticks represent reflections in pure CdSe and pure MnSe, respectively.

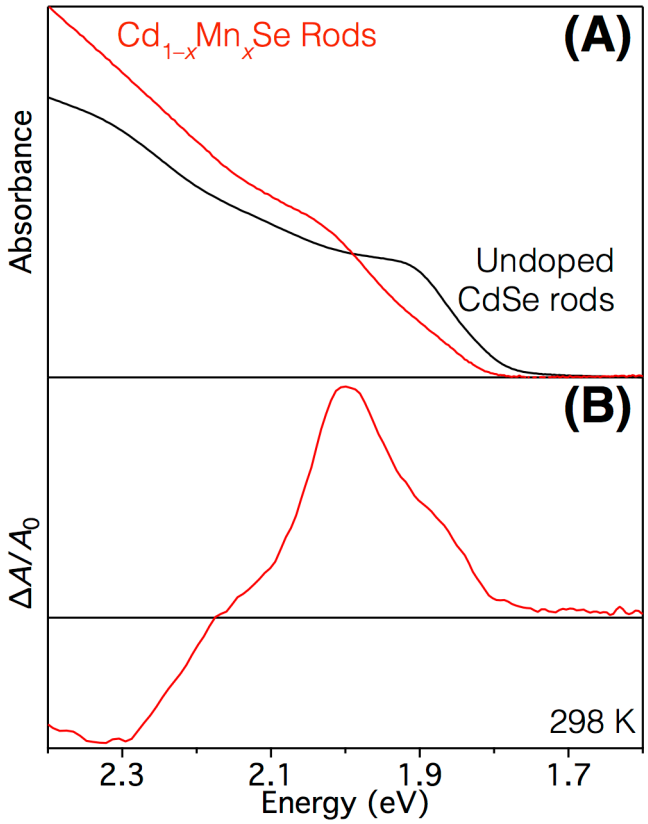

Figure A.5. (A) Room-temperature electronic absorption and (B) MCD spectra of the colloidal CdSe nanorods shown in Figure 2.5A before (black) and after (red) diffusion doping with Mn^{2+}. The synthetic procedure is identical to the one used for Mn^{2+} diffusion doping of spherical CdSe nanocrystals described in Chapter 2, but with CdSe rods as the seeds instead. TEM measurements show that the nanorod shapes remain preserved following diffusion doping. The absorption energy gap increases, similar to the results shown for spherical CdSe nanocrystals in Figure 2.3. The room-temperature MCD intensity of the $Cd_{1-x}Mn_xSe$ nanorods yields $g_{Exc} \approx -6.5$, indicative of successful Mn^{2+} incorporation into the CdSe lattice.

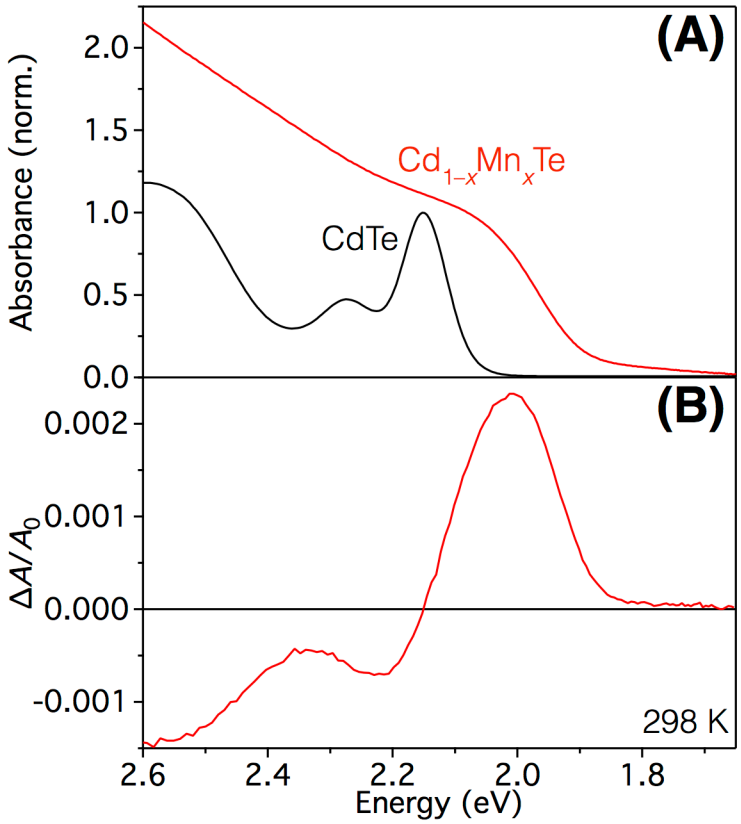

Figure A.6. (A) Room-temperature electronic absorption and (B) MCD spectra of the colloidal CdTe nanocrystals shown in Figure 2.5B before (black) and after (red) diffusion doping with Mn^{2+}. The room-temperature lowest-energy leading edge MCD intensity of the $Cd_{1-x}Mn_xTe$ nanocrystals is inverted relative to undoped CdTe, indicative of successful Mn^{2+} incorporation into the CdTe lattice.

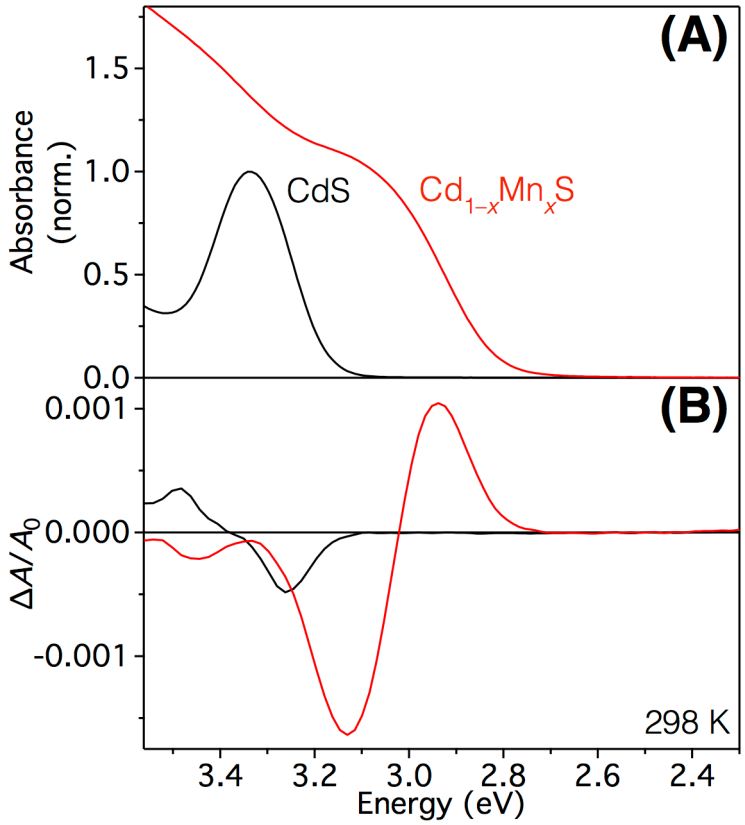

Figure A.7. **(A)** Room-temperature electronic absorption and **(B)** MCD spectra of $Cd_{1-x}Mn_xS$ nanocrystals (red) made by diffusion doping d = 2.6 nm CdS seed nanocrystals (black) at 300 °C for 1 hour. The synthetic procedure parallels that used for Mn^{2+} diffusion doping of CdSe described in Chapter 2, but with CdS seeds instead of CdSe. Analysis of the room-temperature MCD data yields g_{Exc} = +0.60 before and –3.47 after diffusion doping.

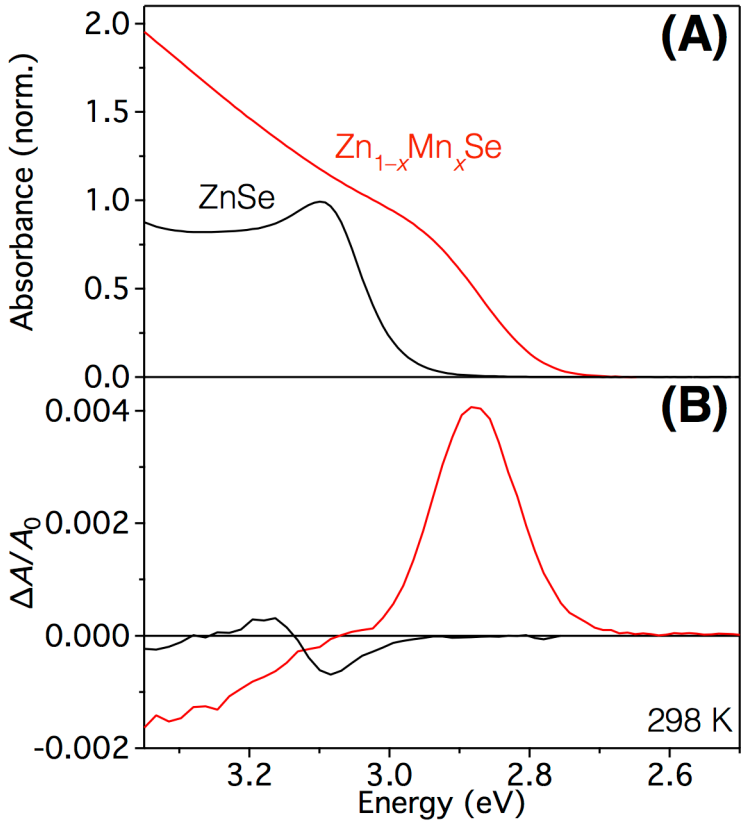

Figure A.8. (A) Room-temperature electronic absorption and (B) MCD spectra of $Zn_{1-x}Mn_xSe$ nanocrystals (red) made by diffusion doping d = 4 nm ZnSe seed nanocrystals (black) at 300 °C for 30 min. The synthetic procedure is identical to the one used for Mn^{2+} diffusion doping of CdSe described in Chapter 2, but with ZnSe seeds instead of CdSe. Analysis of the room-temperature MCD data yields g_{Exc} = +2.06 before and –17 after diffusion doping.

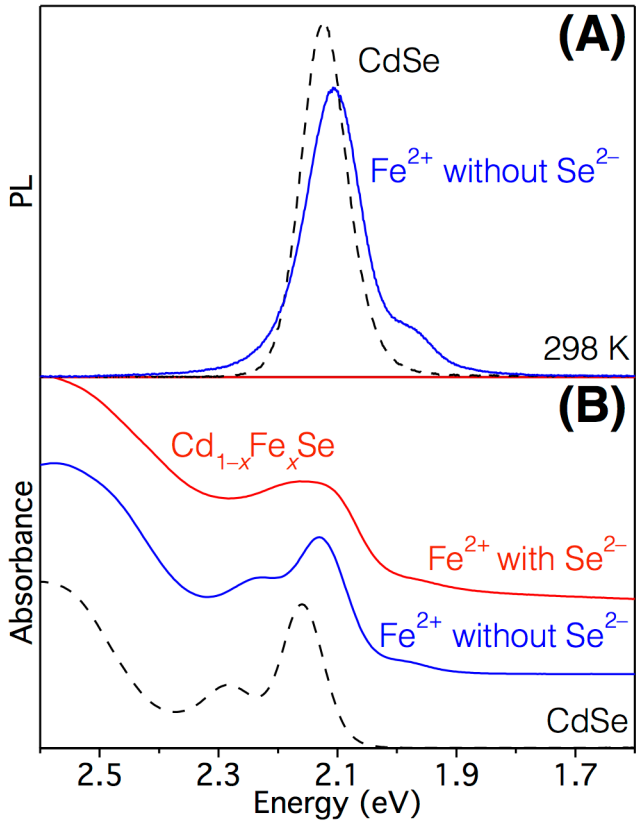

Figure A.9. (A) Room-temperature photoluminescence and (B) electronic absorption spectra (plotted with vertical offsets for clarity) of d = 3.6 nm CdSe nanocrystals before (black) and after diffusion doping at 300 °C for 20 minutes in the presence of Se^{2-} and Fe^{2+} (red) or only Fe^{2+} (blue), a well-known "killer trap" for luminescence in II–VI semiconductors. The CdSe excitonic luminescence quantum yield is not affected appreciably when diffusion doping was performed without additional Se^{2-}, consistent with the absence of Fe^{2+} in the CdSe lattice. The CdSe excitonic luminescence is quenched when diffusion doping was performed in the presence of excess Se^{2-} (7:1 ratio to Cd^{2+} in nanocrystals), consistent with Fe^{2+} incorporation.

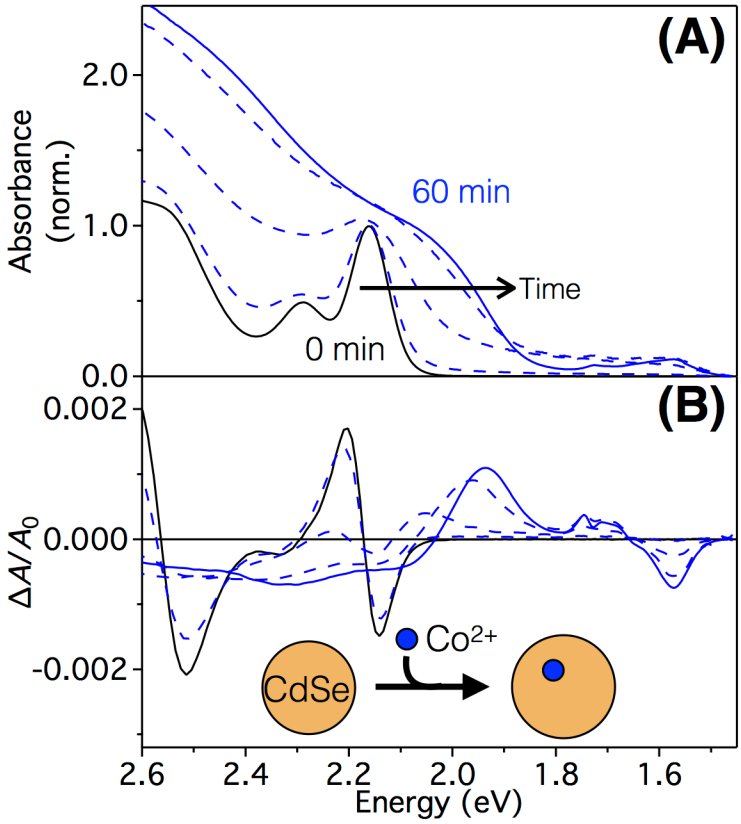

Figure A.10. (A) Room-temperature electronic absorption and (B) MCD spectra of $Cd_{1-x}Co_xSe$ nanocrystals (blue) made by diffusion doping d = 3.6 nm CdSe seed nanocrystals (black) at 300 °C for 60 minutes. Aliquots removed during dopant diffusion after 10 seconds, 2 minutes, 30 minutes, and 60 minutes all show growing $^4A_2(F) \rightarrow {}^4T_1(P)$ Co^{2+} ligand field intensities by both electronic absorption and MCD spectroscopies, as well as inversion of the excitonic MCD intensity.

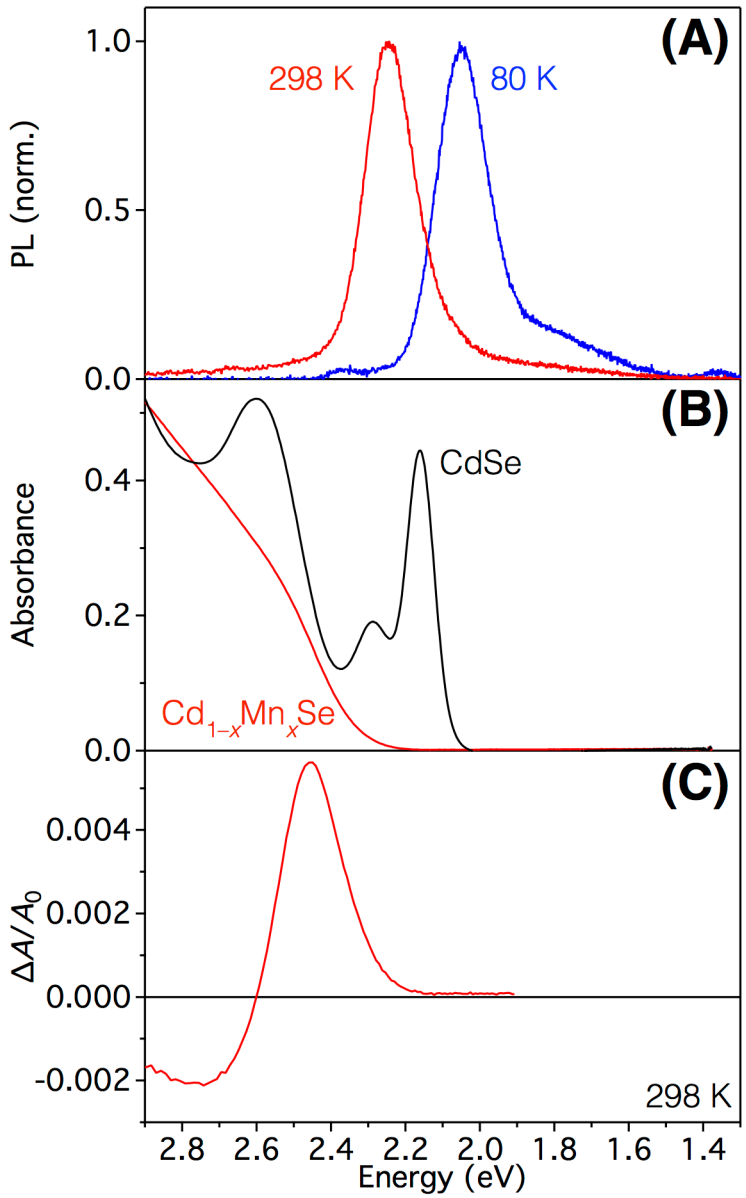

Figure A.11. (A) Variable-temperature photoluminescence, (B) room-temperature electronic absorption, and (C) room-temperature MCD spectra of $Cd_{1-x}Mn_xSe$ nanocrystals (red) made by diffusion doping d = 3.6 nm CdSe seed nanocrystals (black) at 300 °C for 29 hours. The luminescence is dominated by the exciton at room temperature and the Mn^{2+} $^4T_1 \rightarrow {}^6A_1$ ligand-field transition at low temperature. The absence of excitonic luminescence at low temperature reflects the absence of an undoped subset of nanocrystals in this sample. Room-temperature MCD gives g_{Exc} of –12.3, resulting from Mn^{2+} incorporation into the lattice. The absorbance is significantly blue-shifted and broadened.

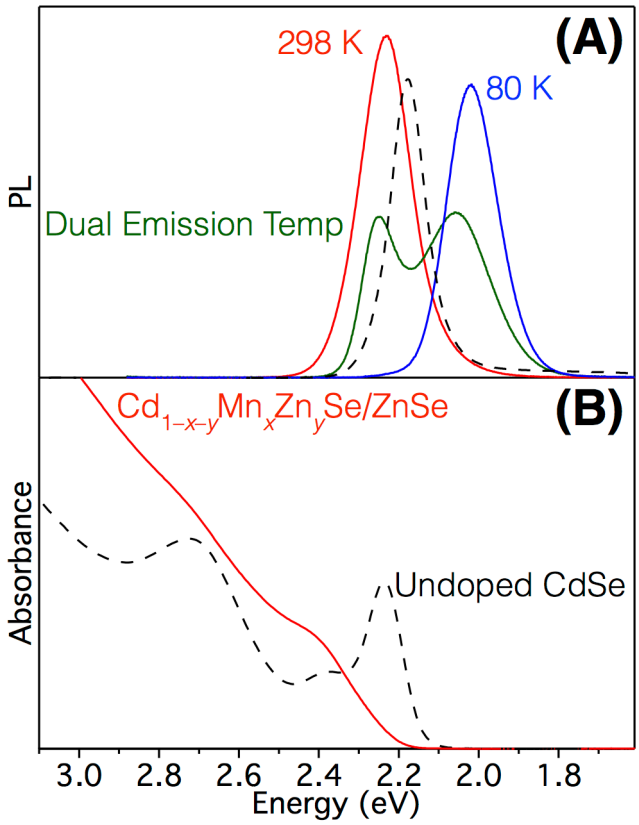

Figure A.12. (A) Variable-temperature photoluminescence and (B) room-temperature electronic absorption spectra of d = 3.1 nm CdSe nanocrystals before (black) and after (colored) diffusion doping at 300 °C for 30 minutes in the presence of Zn^{2+} and Mn^{2+} in a 1:3 ratio. The synthetic procedure is identical to the one used for Mn^{2+} doping described in Chapter 2, with Zn^{2+} added together with Mn^{2+} as $Zn(OAc)_2•2H_2O$. The nanocrystals were washed and a ZnSe shell was applied to improve stability and quantum yield. The room-temperature luminescence spectrum is dominated by the excitonic feature. As the temperature is lowered, the Mn^{2+} $^4T_1 \rightarrow {}^6A_1$ ligand-field luminescence emerges. At liquid-nitrogen temperature, only the Mn^{2+} ligand-field luminescence is observed, consistent with the absence of undoped nanocrystals. This dual emission has been described in detail in references 5–8.

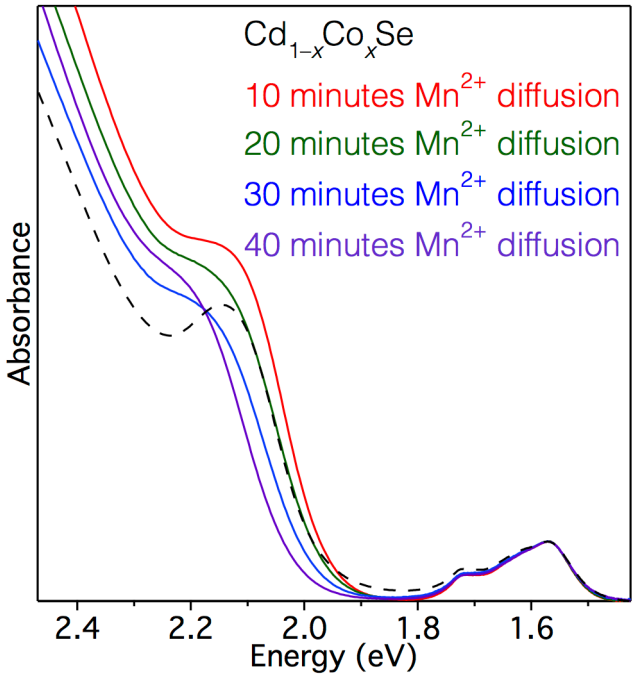

Figure A.13. Room-temperature electronic absorption spectra collected during diffusion doping of Mn^{2+} into $Cd_{1-x}Co_xSe$ nanocrystals, themselves prepared by diffusion doping of Co^{2+} into CdSe nanocrystals (*i.e.*, the sequential tandem doping shown in Figure 2.5C). Co^{2+} is initially diffused into d = 4 nm CdSe nanocrystals at 300 °C for 30 minutes. These $Cd_{1-x}Co_xSe$ nanocrystals are then infused with Mn^{2+} at 300 °C for 40 minutes. Aliquots were taken every 10 minutes.

A.3 References

1. Qu, L.; Peng, X., Control of Photoluminescence Properties of CdSe Nanocrystals in Growth. *J. Am. Chem. Soc.* **2002,** *124*, 2049–2055.
2. Carbone, L.; Nobile, C.; De Giorgi, M.; Della Sala, F.; Morello, G.; Pompa, P.; Hytch, M.; Snoeck, E.; Fiore, A.; Franchini, I. R.; Nadasan, M.; Silvestre, A. F.; Chiodo, L.; Kudera, S.; Cingolani, R.; Krahne, R.; Manna, L., Synthesis and Micrometer-Scale Assembly of Colloidal CdSe/CdS Nanorods Prepared by a Seeded Growth Approach. *Nano Lett.* **2007,** *7*, 2942–2950.
3. Yu, W. W.; Peng, X., Formation of High-Quality CdS and Other II–VI Semiconductor Nanocrystals in Noncoordinating Solvents: Tunable Reactivity of Monomers. *Angew. Chem.* **2002,** *41*, 2368–2371.
4. Yu, W. W.; Qu, L.; Guo, W.; Peng, X., Experimental Determination of the Extinction Coefficient of CdTe, CdSe and CdS. *Chem. Mater.* **2003,** *15*, 2854–2860.
5. Beaulac, R.; Archer, P. I.; van Rijssel, J.; Meijerink, A.; Gamelin, D. R., Exciton Storage by Mn^{2+} in Colloidal Mn^{2+}-Doped CdSe Quantum Dots. *Nano Lett.* **2008,** *8*, 2949–2953.
6. Vlaskin, V. A.; Janßen, N.; van Rijssel, J.; Beaulac, R.; Gamelin, D. R., Tunable Dual Emission in Doped Semiconductor Nanocrystals. *Nano Lett.* **2010,** *10*, 3670–3674.
7. McLaurin, E. J.; Vlaskin, V. A.; Gamelin, D. R., Water-Soluble Dual-Emitting Nanocrystals for Ratiometric Optical Thermometry. *J. Am. Chem. Soc.* **2011,** *133*, 14978–14980.
8. McLaurin, E. J.; Fataftah, M. S.; Gamelin, D. R., One-Step Synthesis of Alloyed Dual-Emitting Semiconductor Nanocrystals. *Chem. Commun.* **2013,** *49*, 39–41.

Appendix B

[Tuning Equilibrium Compositions in Colloidal $Cd_{1-x}Mn_xSe$ Nanocrystals using Diffusion Doping and Cation Exchange]

B.1 Additional Supporting Data

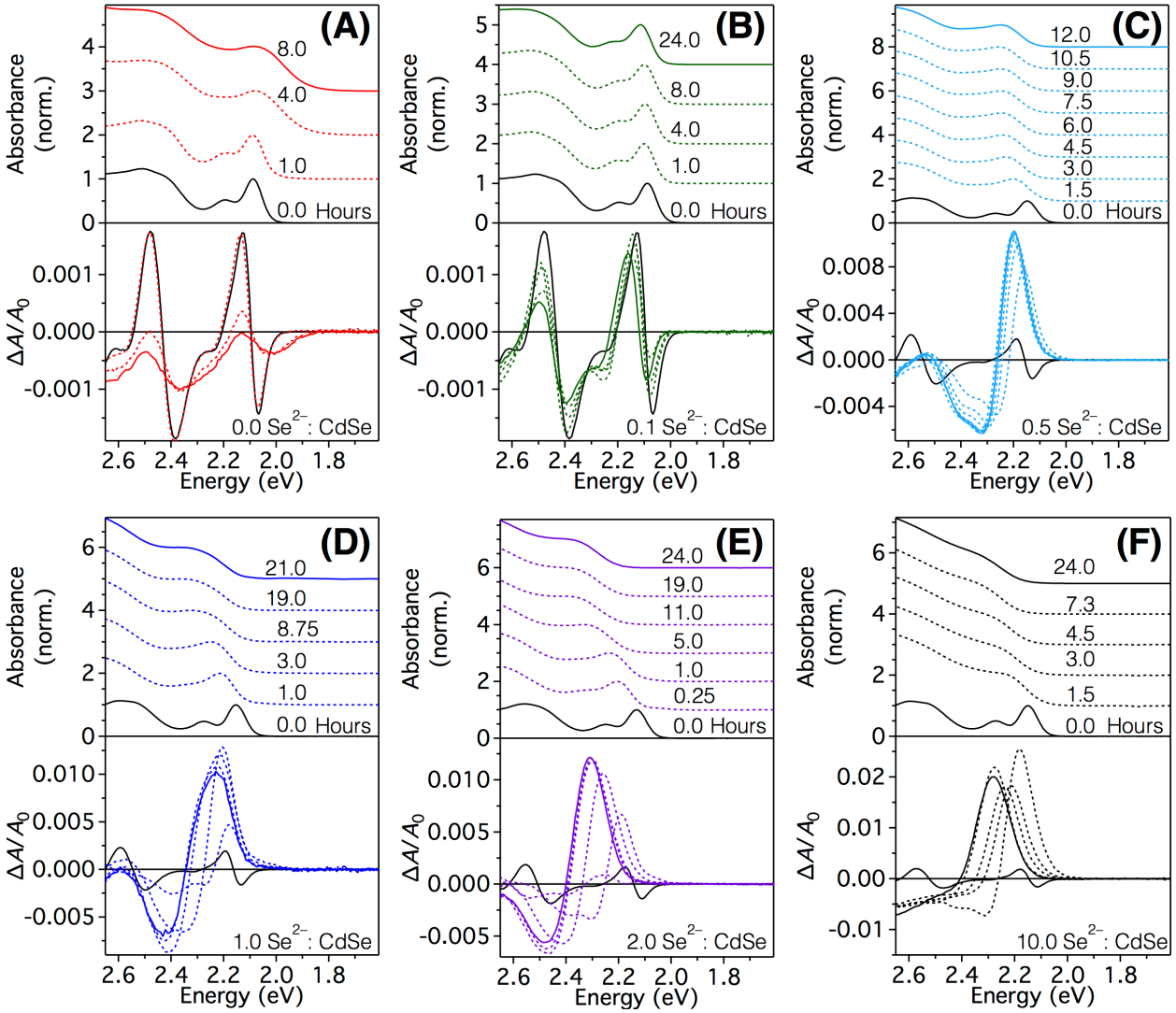

Figure B.1. Representative electronic absorption (top) and MCD (bottom) spectra of aliquots removed during various diffusion-doping reactions at 300 °C with added Se^{2-}:added Mn^{2+}:lattice Cd^{2+} in CdSe NC (Se^{2-}:Mn^{2+}:CdSe) ratios of **(A)** 0:1:1, **(B)** 0.1:1:1, **(C)** 0.5:1:1, **(D)** 1:1:1, **(E)** 2:1:1, and **(F)** 10:1:1 corresponding to the data plotted in Figure 3.2A. Vertical offsets of the absorption spectra are included for clarity of presentation.

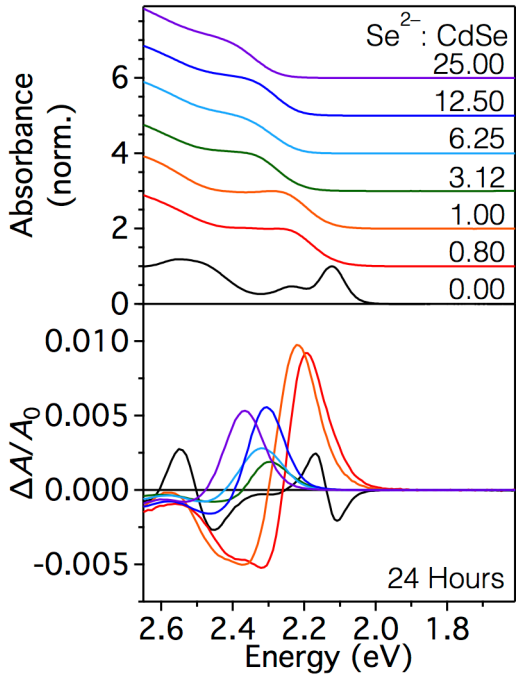

Figure B.2. Representative electronic absorption (top) and MCD (bottom) spectra of $Cd_{1-x}Mn_xSe$ NCs after 24 hours of diffusion doping at 300 ºC with the indicated Se^{2-}:CdSe ratios, yielding the data plotted in Figure 3.2B. All reactions were performed at a ratio of 1:1 added Mn^{2+} to Cd^{2+} in CdSe (1:1 Mn^{2+}:CdSe). Vertical offsets of the absorption spectra are included for clarity of presentation.

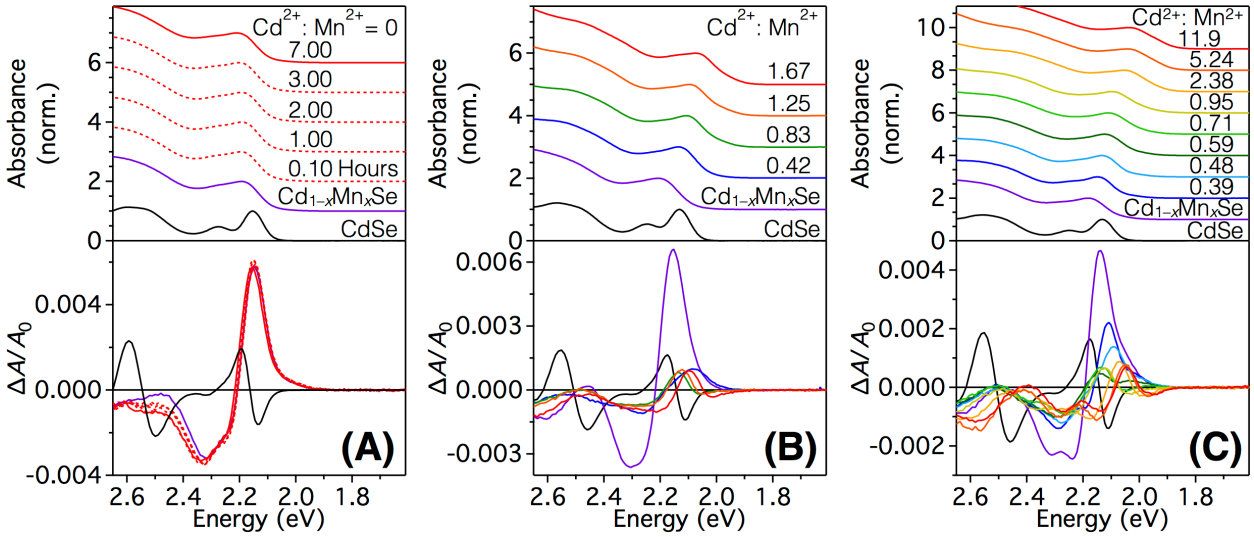

Figure B.3. (A) Electronic absorption (top) and MCD (bottom) spectra of aliquots removed during diffusion doping and the control "purification" reaction performed with no added Cd^{2+}, yielding the control data plotted in Figure 3.4A. Undoped CdSe (black) was diffusion doped with added Se^{2-}:Mn^{2+}:CdSe at a ratio of 0.5:1:1 at 280 °C for 24 hours (purple). After equilibrating, oleic acid dissolved in ODE was injected, and aliquots (red) were removed from the reaction at the indicated times after injection. (B) Electronic absorption (top) and MCD (bottom) spectra of diffusion doped $Cd_{1-x}Mn_xSe$ NCs partially and fully purified by cation exchange reactions with Cd^{2+}, yielding the data plotted in Figure 3.4B. Undoped CdSe (black) was diffusion doped with added Se^{2-}:Mn^{2+}:CdSe at a ratio of 0.5:1:1 at 280 °C for 24 hours (purple). After equilibrating, cadmium oleate was added in a ratio of 0.42 (blue), 0.83 (green), 1.25 (orange), and 1.67 (red) added Cd^{2+}:lattice Mn^{2+}. (C) The experiment of panel B was repeated with the indicated added Cd^{2+}:lattice Mn^{2+} ratios.

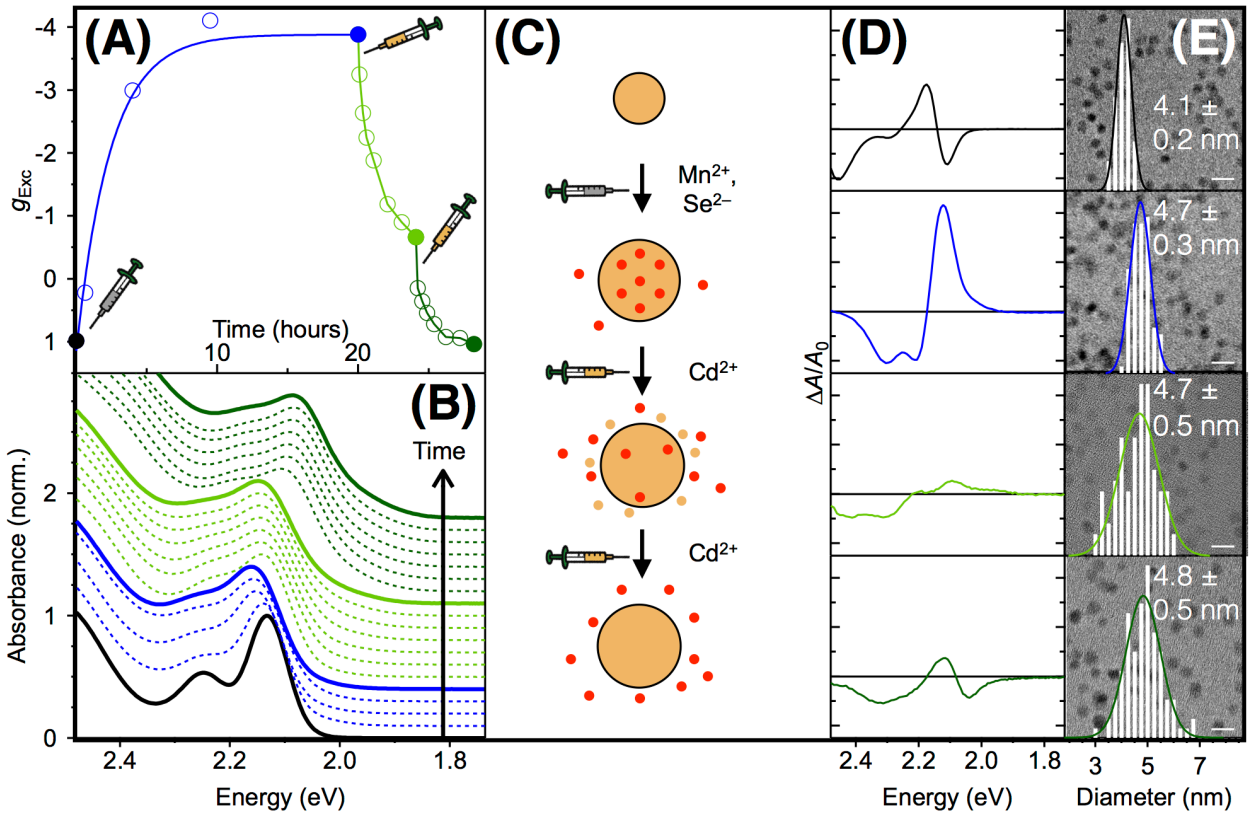

Figure B.4. (A) g_{Exc} (from analysis of data in panels B, D, and other aliquots) of aliquots removed over the course of diffusion doping (blue) at 280 °C with 0.5:1:1 added Se^{2-}:Mn^{2+}: CdSe NCs and purified by cation exchange (green) triggered after 20 hours by injection of 1.20 equivalents of Cd^{2+} per lattice Mn^{2+}, split evenly into two injections of 0.60 equivalents 4 hours apart. The cation exchange portion of this experiment corresponds to the blue traces of Figure 3.4A. The curves are guides to the eye. (B) Electronic absorption spectra of undoped CdSe (black), diffusion doped (blue), partially purified (light green), and fully purified (dark green) NCs. (C) Scheme illustrating the four equilibrated aliquots indicated by dark circles in panel A and bold traces in panel B. (D) MCD spectra of the same four equilibrated aliquots representing undoped CdSe (black), diffusion doped $Cd_{1-x}Mn_xSe$ after 20 hours (blue), partially purified (light green), and fully purified (dark green) NCs. Zero lines are plotted in black, and the major tick marks correspond to increments of 0.002 $\Delta A/A_0$. (E) TEM images and corresponding size histograms from analysis of ≥100 NCs from each of the four equilibrated aliquots. The scale bar in each image represents 10 nm. These data were not shown in Chapter 3 because some Ostwald ripening is evident from slight broadening of the distribution from 5% to 10%. TEM samples were prepared by submerging a 200 mesh copper grid (Ted Pella, Inc.) in a 1 μM colloidal suspension of nanocrystals in toluene and allowing this substrate to dry in air. TEM images were obtained on an FEI TECNAI F20, 200 kV microscope at the UW NanoTech User Facility.

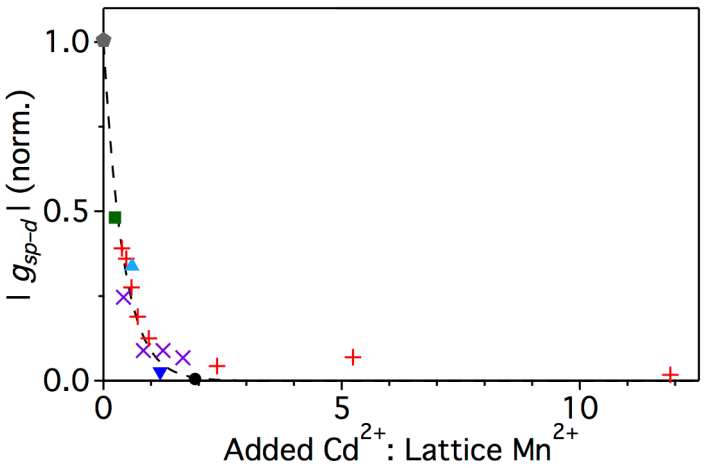

Figure B.5. Extension of Figure 3.4B to larger ratios of added Cd^{2+}:lattice Mn^{2+} during cation exchange at 280 °C. Dependence of the extent of purification by cation exchange at equilibrium on added Cd^{2+}, monitored as $|g_{sp-d}|$ of re-equilibrated samples after cation exchange from diffusion-doped $Cd_{1-x}Mn_xSe$ QDs (normalized to the initial equilibrated, diffusion-doped values of $|g_{sp-d}|$ for each sample) and plotted vs the number of equivalents of Cd^{2+} added relative to the amount of lattice Mn^{2+} in the diffusion-doped NCs. The black dashed line is a guide to the eye.

Appendix C

[Kinetics of Isovalent (Cd^{2+}) and Aliovalent (In^{3+}) Cation Exchange in $Cd_{1-x}Mn_xSe$ Nanocrystals]

C.1 Additional Supporting Data

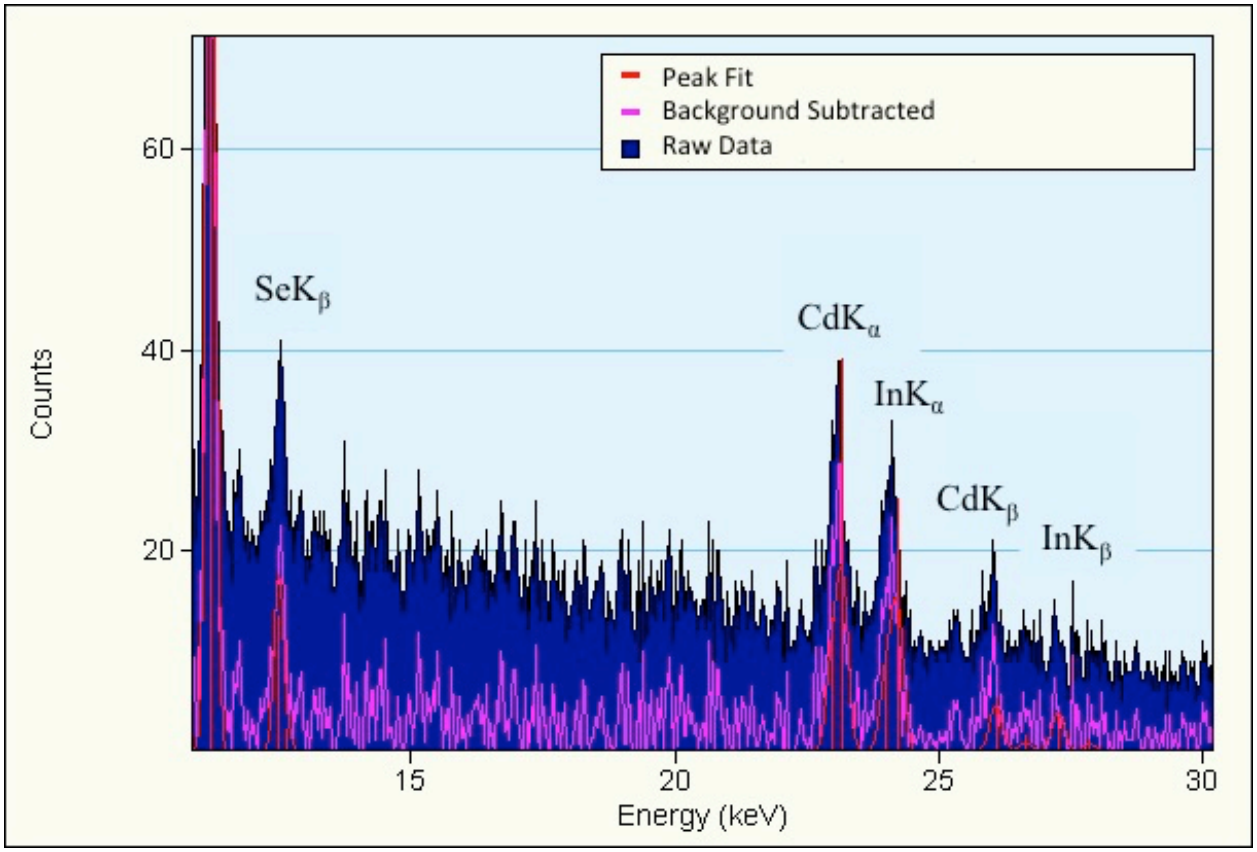

Figure C.1. EDX spectrum showing the corresponding locations of the In, Cd and Se peaks after cation exchange with In^{3+} at 300 °C.

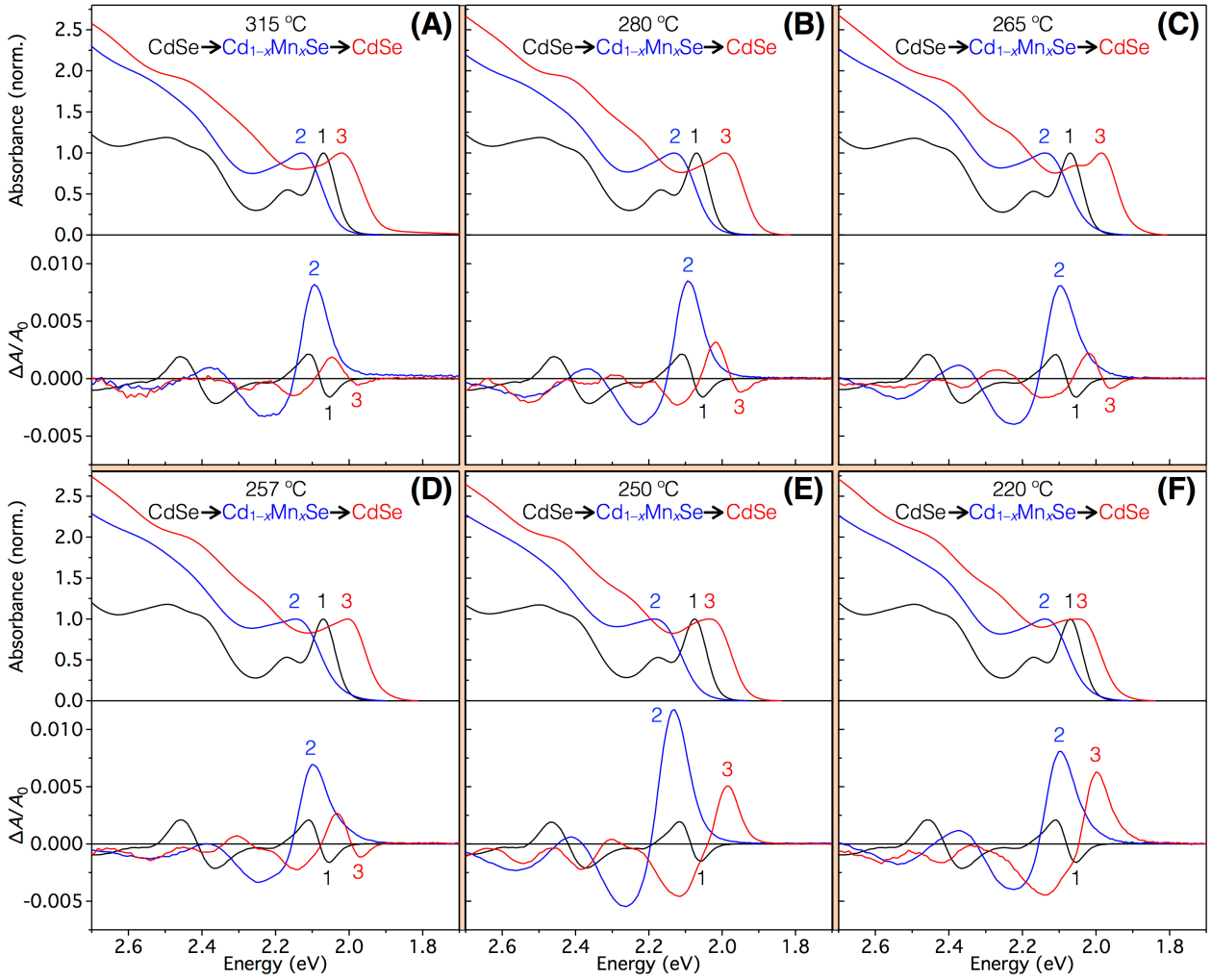

Figure C.2. Room-temperature electronic absorption (top) and corresponding MCD (bottom; 1.5 T) spectra of undoped CdSe cores (1, black), the same nanocrystals equilibrated after 20 hours of Mn^{2+} diffusion doping at 300 °C (2, blue, 0.5:1:1 Se^{2-}:Mn^{2+}:CdSe), and after cation exchange with Cd^{2+} (3, red, 1:1 Cd^{2+}:previously added Se^{2-}) for an additional 4 **(A)**, 24.5 **(B)**, 32.5 **(C)**, 50 **(D)**, 34 **(E)**, or 47 **(F)** hours at 315 °C **(A)**, 280 °C **(B)**, 265 °C **(C)**, 257 °C **(D)**, 250 °C **(E)**, or 220 °C **(F)**. Intermediate spectra of the aliquots are omitted for clarity.

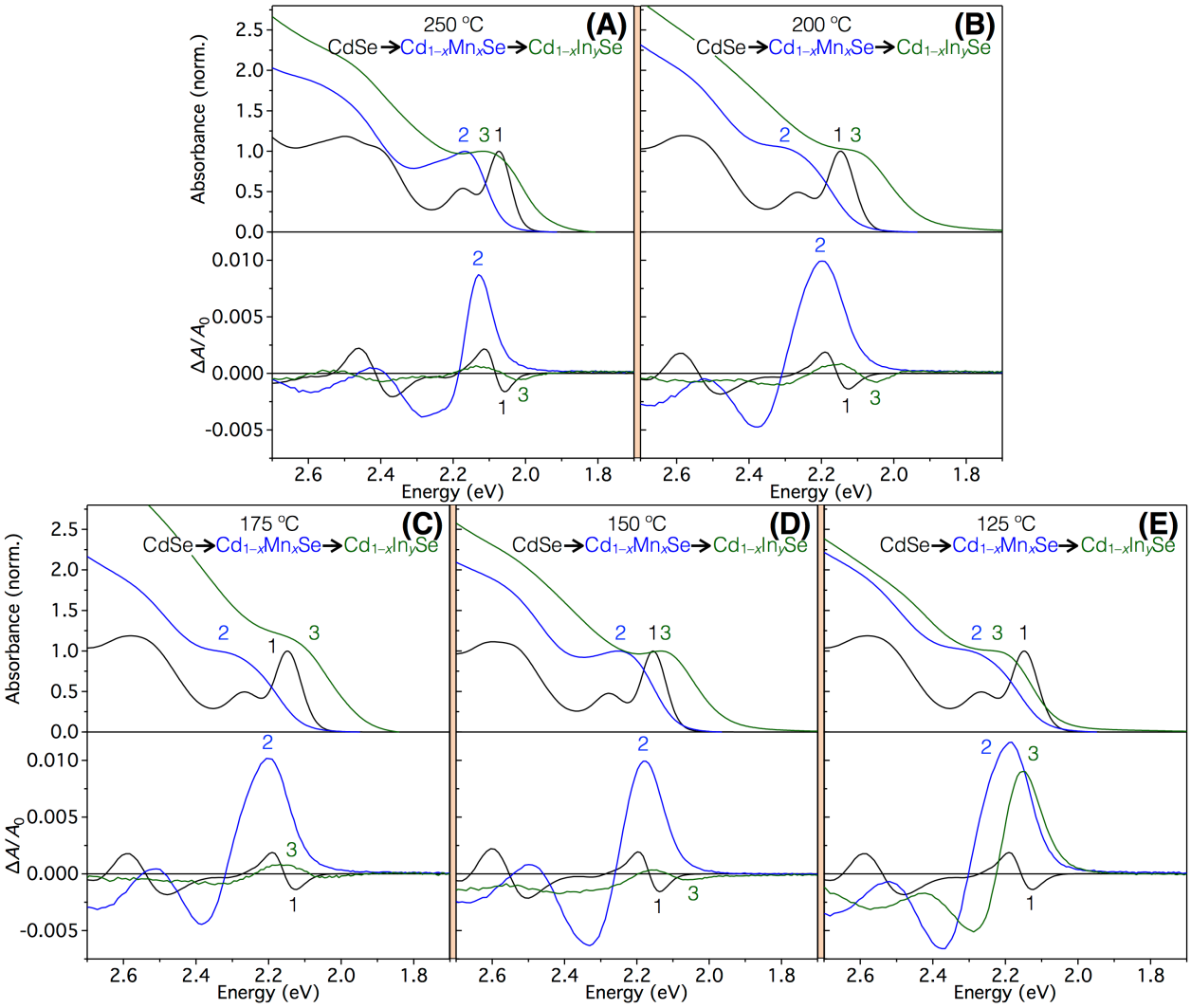

Figure C.3. Room-temperature electronic absorption (top) and corresponding MCD (bottom; 1.5 T) spectra of undoped CdSe cores (1, black), the same nanocrystals equilibrated after 20 hours of Mn^{2+} diffusion doping at 300 °C (2, blue, 0.5:1:1 Se^{2-}:Mn^{2+}:CdSe), and after cation exchange with In^{3+} (3, green, 1:1 In^{3+}:previously added Se^{2-}) for an additional 1 **(A)**, 4 **(B)**, 21 **(C)**, 52 **(D)**, or 67 **(E)** hours at 250 °C **(A)**, 200 °C **(B)**, 175 °C **(C)**, 150 °C **(D)**, or 125 °C **(E)**. Intermediate spectra of the aliquots are omitted for clarity.

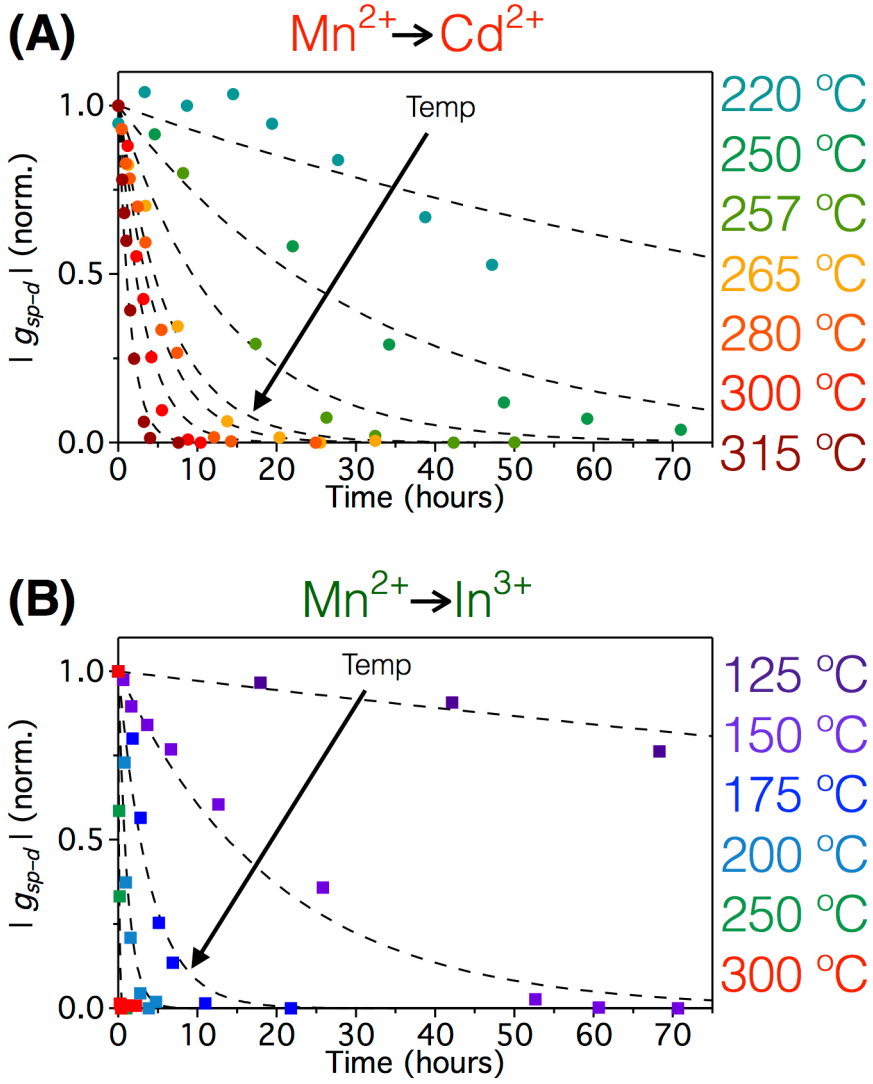

Figure C.4. Fitting of the cation-exchange kinetics data from Figure 4.4 using a simple exponential function. All other aspects of the figure are the same as in Figure 4.4.

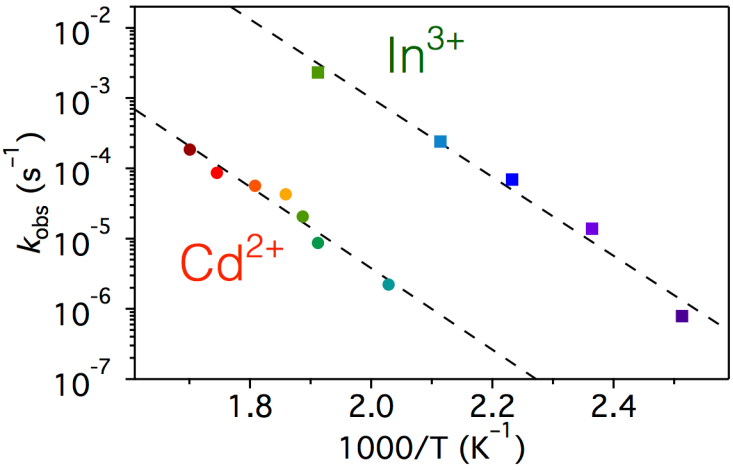

Figure C.5. Arrhenius plot of the cation-exchange rate constants ($k_{obs} = 1/t_{obs}$) obtained from exponential fitting of the data in Figure 4.4 (see Figure C.4) for displacement of Mn^{2+} with Cd^{2+} (red squares) and In^{3+} (green circles). Dashed lines show fits of the data to the Arrhenius equation, yielding E_D ~1.1 eV for both Cd^{2+} and In^{3+}.

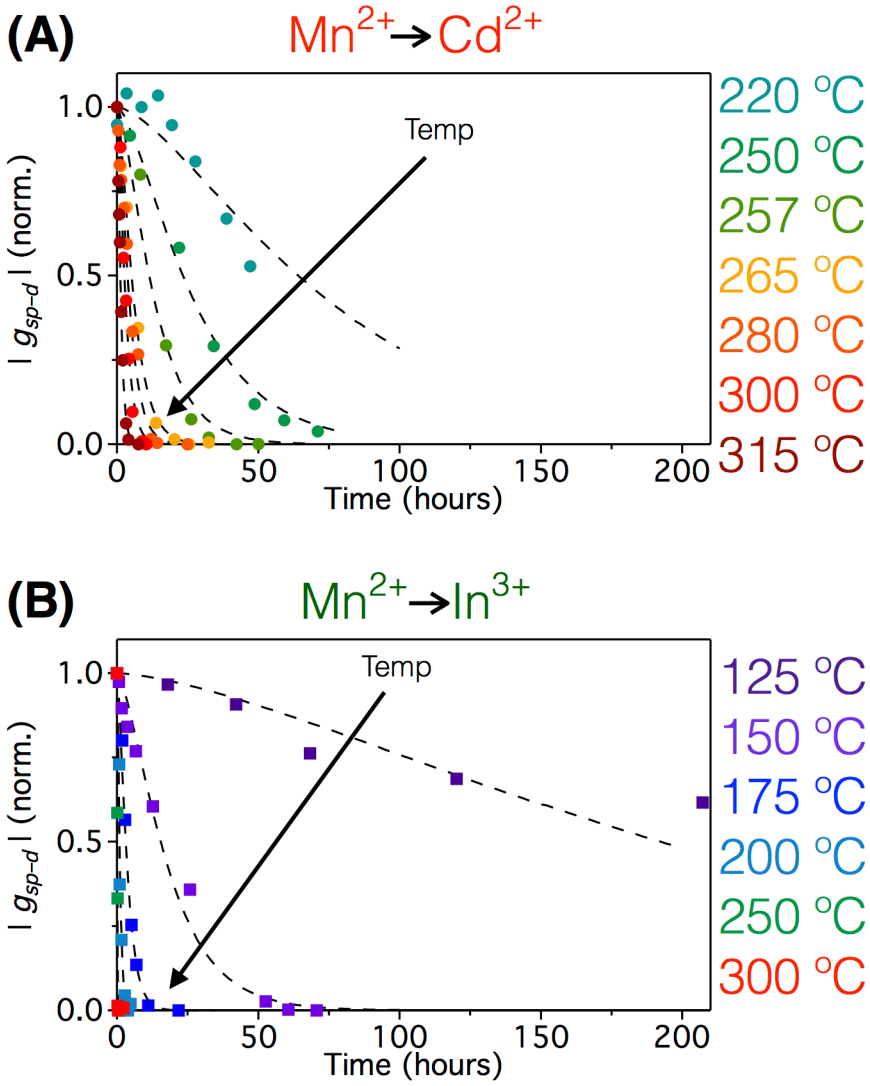

Figure C.6. Changes in $|g_{sp-d}|$ during cation exchange at different temperatures. These are the same data as shown in Figure 4.4, but plotted out to longer times. All other aspects of the data are the same as in Figure 4.4.

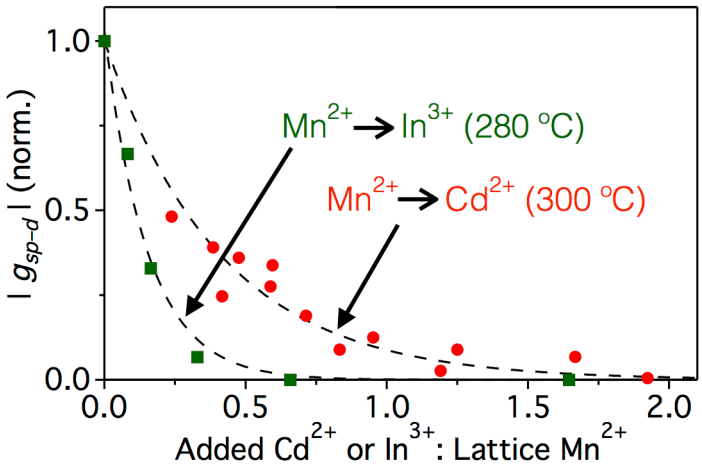

Figure C.7. Dependence of the extent of Mn^{2+} displacement from $Cd_{1-x}Mn_xSe$ nanocrystals by cation exchange on the amount of added cation, plotted as $|g_{sp-d}|$ (normalized) *vs* equivalents of Cd^{2+} (red circles) or In^{3+} (green squares) per lattice Mn^{2+} (determined by excitonic shift and TEM data) added to the reaction. Data were obtained from MCD measurements on samples after equilibration of the cation-exchange reaction at 280 °C (Cd^{2+}) or 300 °C (In^{3+}). The dashed curves are guides for the eye. These data show that ~1 equivalent of Cd^{2+} but only ~0.7 equivalents of In^{3+} are needed to fully displace all lattice Mn^{2+}, consistent with a final nanocrystal stoichiometry of $Cd_{1-x}In_{0.66x}Se$ that satisfies charge neutrality. The data from the Cd^{2+} cation-exchange reactions are reproduced from Chapter 3 (Figure 3.4B).

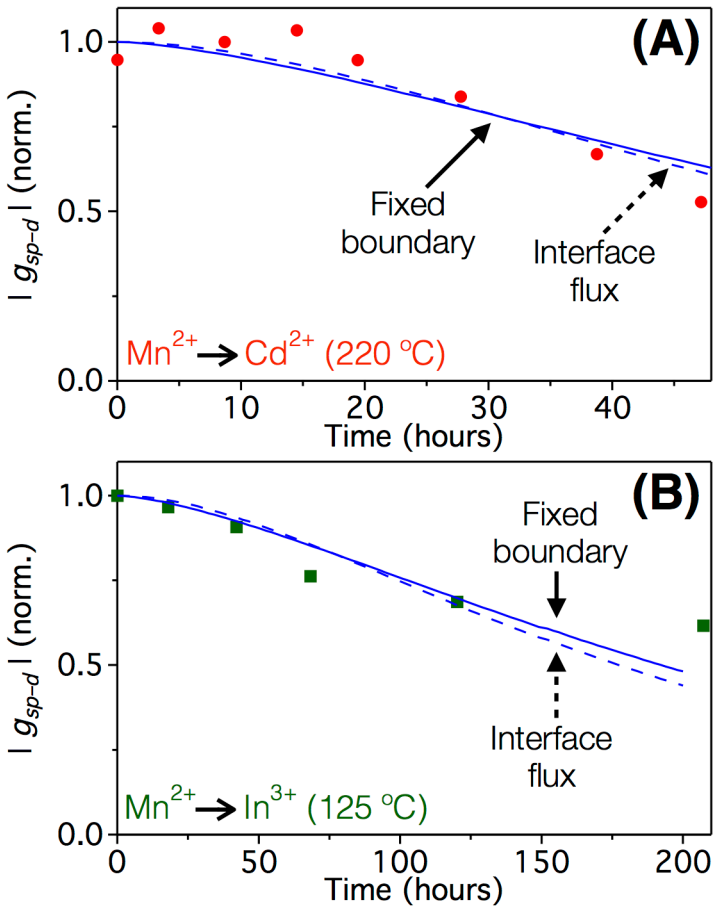

Figure C.8. Comparison between experimental and simulated cation-exchange kinetics with and without accounting for Mn^{2+} interface flux, as described in Chapter 4. **(A)** Cation exchange with Cd^{2+} at 220 °C, experiment (red circles), simulation accounting for interface flux (blue dashed curve, k = 2.3 nm^{-1}, D = 2.7 × 10^{-6} nm^2/s extrapolated from the high temperature data in Figure 4.5), and simulation based on fixed boundary condition (blue solid curve, as described Chapter 4). **(B)** Cation exchange with In^{3+} at 125 °C, experiment (green squares), simulation accounting for interface flux (blue dashed curve, k = 0.7 nm^{-1}, D = 1.4 × 10^{-6} nm^2/s extrapolated from the high temperature data in Figure 4.5), and simulation based on fixed boundary condition (blue solid curve, as described in Chapter 4). The diameter of the nanocrystals is 5.2 nm.

Table C.1. Apparent rate constants (k (s^{-1})) obtained from fitting the data in Figure C.13 using a single-exponential function, corresponding to the dashed curves included in Figure C.13.

$Mn^{2+} \rightarrow Cd^{2+}$		$Mn^{2+} \rightarrow In^{3+}$	
Temperature (K)	k (s^{-1})	Temperature (K)	k (s^{-1})
493	2.2×10^{-6}	398	7.9×10^{-7}
523	8.7×10^{-6}	423	1.4×10^{-5}
530	2.1×10^{-5}	448	6.9×10^{-5}
538	4.3×10^{-5}	473	2.4×10^{-4}
553	5.7×10^{-5}	523	2.3×10^{-3}
573	8.7×10^{-5}		
588	1.9×10^{-4}		

Table C.2. Diffusion barriers (E_D) and limiting diffusivities (D_0) from this work and from literature on other II–VI semiconductors with various diffusing ions. ($D = D_0\exp(-E_D/kT)$)

	E_D (eV)	D_0 (nm^2/s)
This work: Mn^{2+} diffusion in Cd^{2+}:$Cd_{1-x}Mn_xSe$ NCs (220–315 °C, x ~0.15)	1.1	9.8×10^{4}
	1.1	2.6×10^{7}
This work: Mn^{2+} diffusion in In^{3+}:$Cd_{1-x}Mn_xSe$ NCs (125–250 °C, x ~ 0.15)		
Mn^{2+} diffusion CdTe/δ-MnTe/CdTe thin films (440–520 °C)[1]	1.35	1.7×10^{8}
Mn^{2+} diffusion in In^{3+}-doped CdTe/δ-MnTe/CdTe thin films (340–480 °C)[1,a]	1.35	4.2×10^{10}
	2.76	1.1×10^{17}
Mn^{2+} diffusion in bulk CdTe (Cd^{2+}-saturated, 600–800 °C)[2]	2.35	2.2×10^{15}
Mn^{2+} diffusion in bulk CdTe (Se^{2-}-saturated, 500–800 °C)[2]		
Cd^{2+} self-diffusion in bulk CdSe (Cd^{2+}-saturated)[3]	1.68	9.2×10^{12}
Cd^{2+} self-diffusion in bulk CdSe (Se^{2-}-saturated)[3]	2.37	3.3×10^{13}
Cd^{2+} self-diffusion in bulk CdTe (Cd^{2+}-saturated) (650–920 °C)[4]	2.67	3.3×10^{16}
Cd^{2+} self-diffusion in bulk CdTe (Te^{2-}-saturated) (650–850 °C)[4]	2.44	1.6×10^{15}
In^{3+} diffusion in bulk CdTe (450–1000 °C)[5]	1.6	4.1×10^{12}
In^{3+} diffusion in bulk ZnO (750–850 °C)[6]	1.17	2.9×10^{7}
In^{3+} diffusion in bulk CdS (456–1138 °C)[7]	2.3	6.0×10^{15}
Theory:		
Interstitial diffusion of Mn^{2+} in CdSe nanocrystals (d < 2 nm)[8]	0.31	1.0×10^{12}
Interstitial diffusion of Mn^{2+} in bulk CdSe[8]	0.84	1.0×10^{13}

[a] $N_{In} = 1 \times 10^{18}$ cm^{-3}

Table C.3. Tetrahedral and octahedral cation ionic radii (pm)[9]

	Tetrahedral	Octahedral
Cd^{2+}	0.78	0.95
In^{3+}	0.62	0.80
Mn^{2+}	0.66	0.83

C.2 References

1. Barcz, A.; Karczewski, G.; Wojtowicz, T.; Kossut, J. Manganese Diffusion in MBE-Grown Cd(Mn)Te structures. *J. Cryst. Growth* **1996**, *159*, 980–984.
2. Jamil, N. Y.; Shaw, D. The Diffusion of Mn in CdTe. *Semicond. Sci. Technol.* **1995**, *10*, 952–958.
3. Stevenson, D. A. *Atomic Diffusion in Semiconductors*. Plenum Press: London, 1973.
4. Borsenberger, P. M.; Stevenson, D. A. Self-Diffusion of Cadmium and Tellurium in Cadmium Telluride. *J. Phys. Chem. Solids* **1968**, *29*, 1277–1286.
5. Kato, H.; Takayanagi, S. Diffusion of Indium in Cadmium Telluride. *Japan. J. Appl. Phys.* **1963**, *2*, 250–251.
6. Nakagawa, T.; Matsumoto, K.; Sakaguchi, I.; Uematsu, M.; Haneda, H.; Ohashi, N. Analysis of Indium Diffusion Profiles Based on the Fermi-Level Effect in Single-Crystal Zinc Oxide. *Jpn. J. Appl. Phys.* **2008**, *47*, 7848–7850.
7. Jones, E. D.; Mykura, H. Diffusion of Indium into Cadmium Sulphide. *J. Phys. Chem. Solids* **1978**, *39*, 11–18.
8. Chan, T.-L.; Zayak, A. T.; Dalpian, G. M.; Chelikowsky, J. R. Role of Confinement on Diffusion Barriers in Semiconductor Nanocrystals. *Phys. Rev. Lett.* **2009**, *102*, 025901.
9. Shannon, R. D. Revised Effective Ionic Radii and Systematic Studies of Interatomic Distances in Halides and Chalcogenides. *Acta Crystallogr., Sect. A: Cryst. Phys., Diffr., Theor. Gen. Crystallogr.* **1976**, *32*, 751–767.

Appendix D

[Excitonic Zeeman Splittings in Colloidal CdSe Quantum Dots Doped with Single Magnetic Impurities]

D.1 Additional Supporting Data

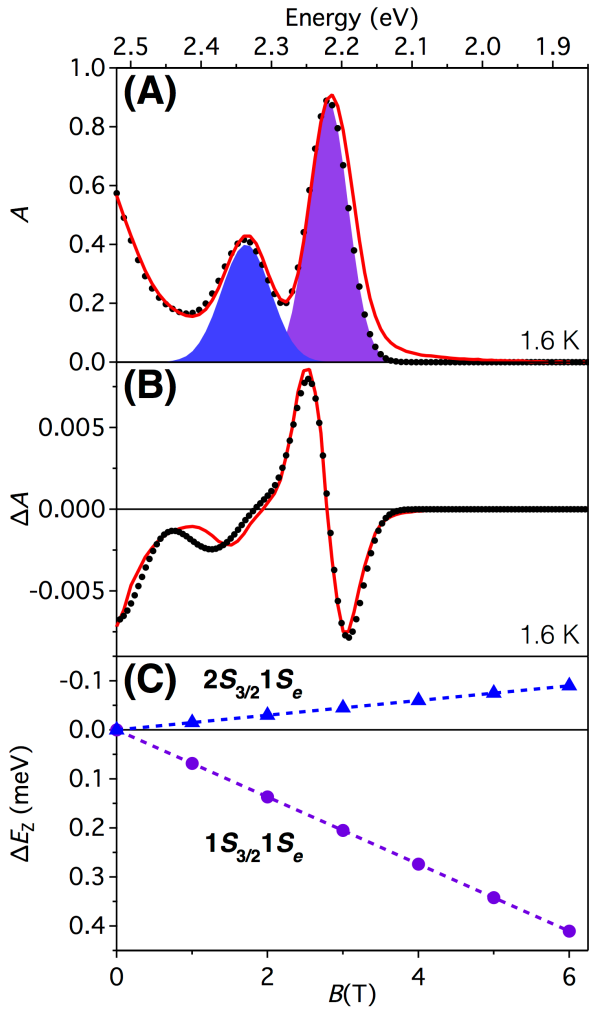

Figure D.1. **(A)** 1.6 K Electronic absorption and **(B)** 6 T MCD spectra (red lines) of undoped *d* ~4 nm CdSe QDs prepared according to the methods described in references 1 and 2. A simultaneous fit of the data to multiple Gaussian peaks (purple and blue curves shown for the first two excitonic transitions) yields the black dots. **(C)** Field-dependent Zeeman splittings of the first two excitonic transitions, displaying characteristic *g* values of +1.2 ($1S_{3/2}1S_e$; purple circles) and –0.3 ($2S_{3/2}1S_e$; blue triangles). MCD spectra at lower fields are omitted for clarity.

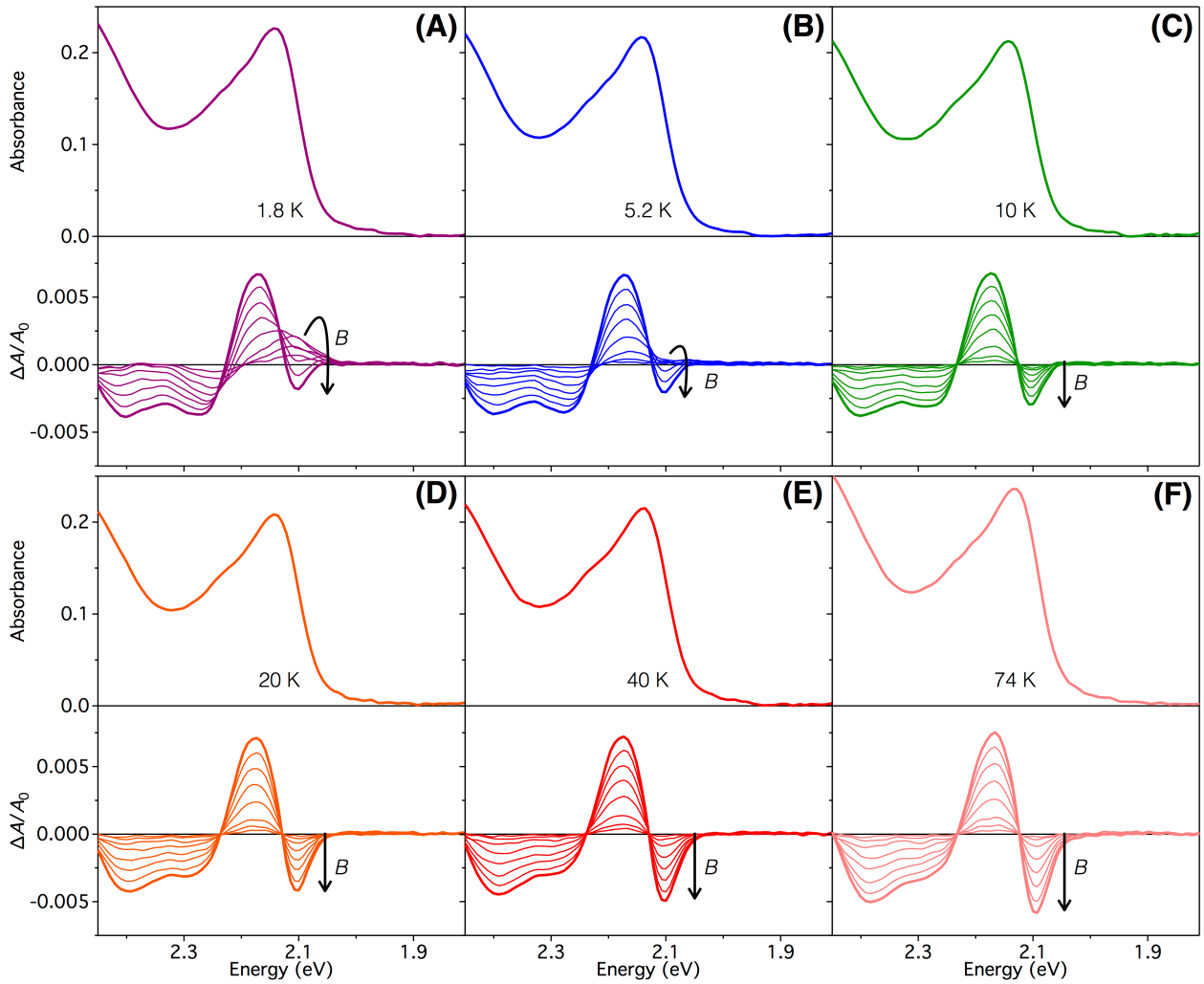

Figure D.2. Electronic absorption (top) and 0–6 T MCD (bottom) spectra of diffusion-doped d = 5.1 nm $Cd_{0.9997}Mn_{0.0003}Se$ QDs collected at 1.8 **(A)**, 5.2 **(B)**, 10 **(C)**, 20 **(D)**, 40 **(E)**, and 74 K **(F)**. The arrows indicate the direction of increasing magnetic field.

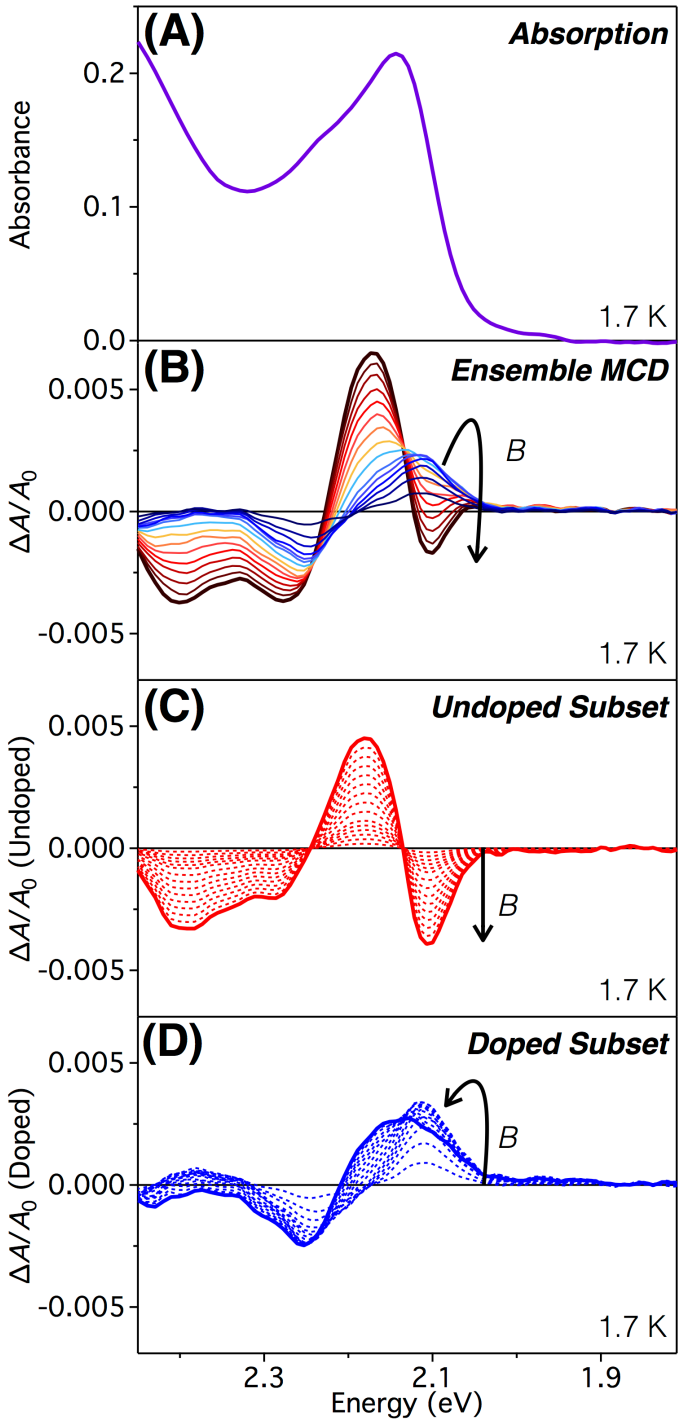

Figure D.3. (A) 1.7 K electronic absorption spectrum (purple) of diffusion-doped d = 5.1 nm $Cd_{0.9997}Mn_{0.0003}Se$ QDs. (B) Variable-field (0–6 T; blue to red lines) MCD spectra of the same QDs at 1.7 K. (C) Deconvolved MCD spectra (red) of the undoped subset of this ensemble (67.8%), consisting of a purely intrinsic component to the excitonic Zeeman splittings. (D) Deconvolved MCD spectra (blue) of the doped subset of this ensemble (32.2%) consisting of both intrinsic and *sp–d* exchange contributions to the excitonic Zeeman splittings. The arrows indicate the direction of increasing magnetic field.

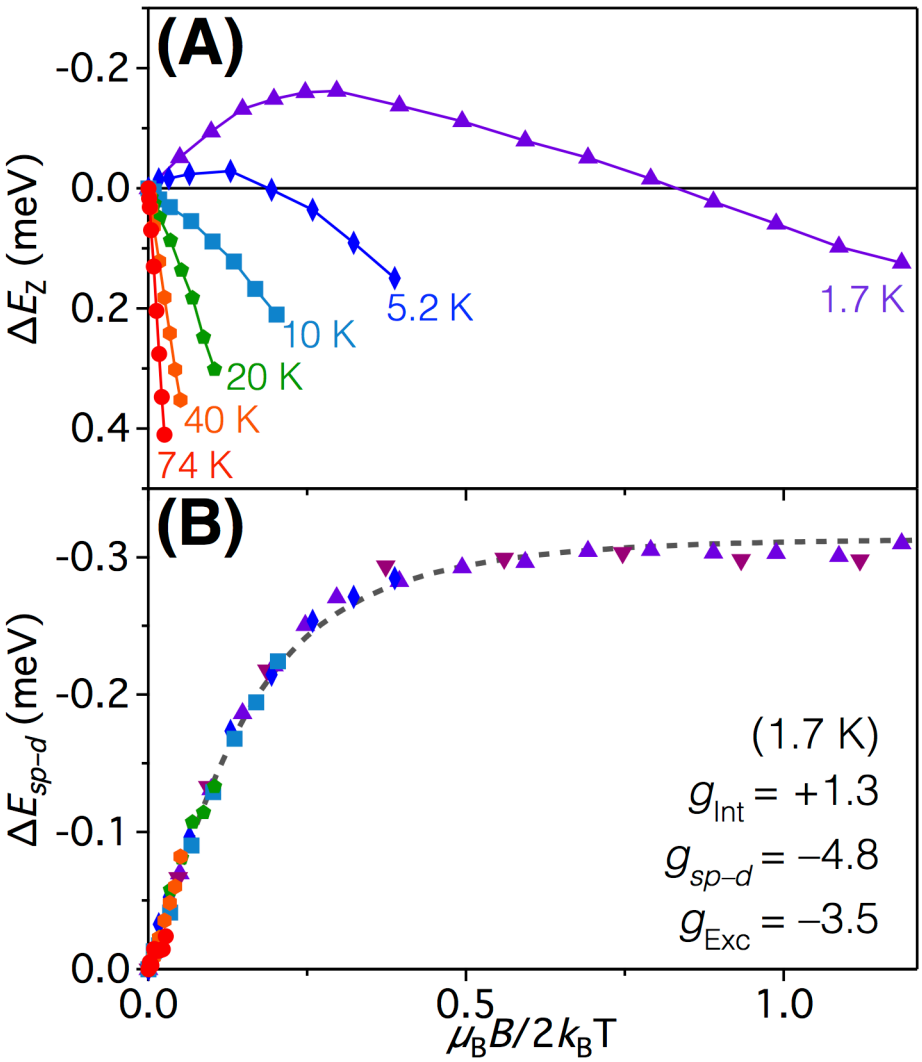

Figure D.4. **(A)** Excitonic Zeeman splittings of the $1S_{3/2}1S_e$ transition in diffusion-doped d = 5.1 nm $Cd_{0.9997}Mn_{0.0003}Se$ QDs, determined from analysis of VT-V*B* MCD spectra (Figure 5.2B in Chapter 5) **(B)** Brillouin saturation magnetization of the *sp–d* exchange contribution to the $1S_{3/2}1S_e$ Zeeman splittings as determined from VT-V*B* MCD spectra. The values of g_{Int} = +1.3 and g_{sp-d} = –4.8 are calculated from the low-field (Curie) limit at 1.7 K for the $1S_{3/2}1S_e$ transition. Data in purple upward triangles, maroon downward triangles, dark blue diamonds, light blue squares, green pentagons, orange hexagons, and red circles correspond to analysis of 0–6 T MCD spectra collected at 1.7, 1.8, 5.2, 10, 20, 40, and 74 K, respectively. The gray dashed line represents a fit of these data to Equation 5.3 in Chapter 5.

Table D.1. *g* values obtained from fitting the ΔE_Z data of Figures 5.2–5.3 ($Cd_{0.9997}Mn_{0.0003}Se$ QDs) and D.1 (undoped CdSe QDs) in the low-field (Curie) limit.

	$1S_{3/2}1S_e$		$2S_{3/2}1S_e$	
	CdSe	$Cd_{0.9997}Mn_{0.0003}Se$	CdSe	$Cd_{0.9997}Mn_{0.0003}Se$
g_{Int}	+1.2	+1.3	–0.3	–0.2
g_{sp-d}	0	–4.8	0	–3.6

D.2 References

1. Vlaskin, V. A.; Barrows, C. J.; Erickson, C. S.; Gamelin, D. R., Nanocrystal Diffusion Doping. *J. Am. Chem. Soc.* **2013,** *135*, 14380–14389.
2. Barrows, C. J.; Chakraborty, P.; Kornowske, L. M.; Gamelin, D. R., Tuning Equilibrium Compositions in Colloidal $Cd_{1-x}Mn_xSe$ Nanocrystals Using Diffusion Doping and Cation Exchange. *ACS Nano* **2016,** *10*, 910–918.

Appendix E

[Absorption and Magnetic Circular Dichroism Analyses of Giant Zeeman Splittings in Diffusion-Doped Colloidal $Cd_{1-x}Mn_xSe$ Quantum Dots]

E.1 Additional Experimental Details

X-ray diffraction (XRD) data were collected from an evaporated nanocrystal film on a glass slide using a Bruker D8 Discover spectrometer at the UW Nanotech User Facility. ΔA values were calculated from the raw MCD ellipticity data using the conversion θ(mdeg) = 32980ΔA. This conversion approximates $tanh(\theta) = \theta$, which is only accurate for relatively small values of θ. Here, our largest value of θ is 2955 mdeg (Figure E.1) and $tanh(2955)$ = 2952, so the accuracy is within 0.1%.

E.2 Additional Supporting Data

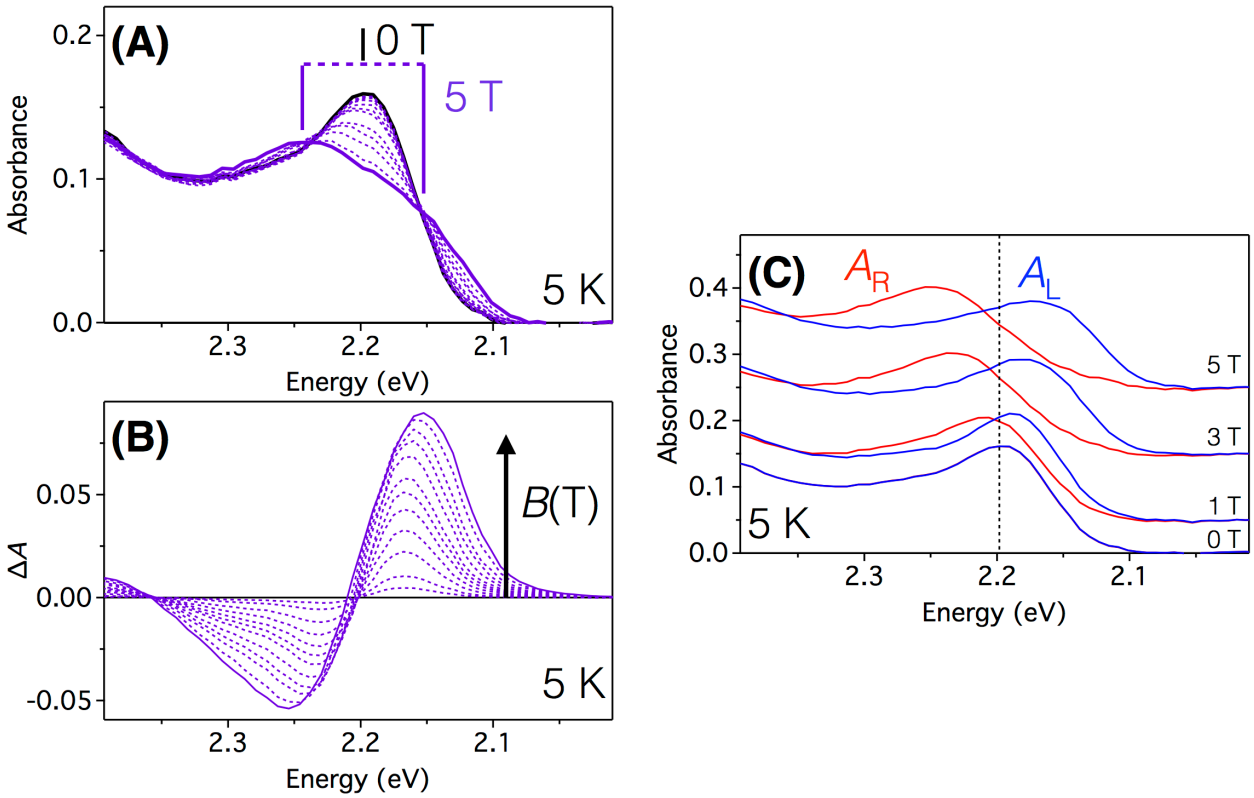

Figure E.1. **(A)** Electronic absorption and **(B)** MCD spectra of diffusion-doped *d* ~4.5 nm $Cd_{0.87}Mn_{0.13}Se$ quantum dots measured at 5 K for magnetic fields between 0 (black) and 5 T (purple). The arrow indicates the direction of increasing magnetic field. **(C)** Magnetic-field dependence of 5 K circularly polarized absorption spectra, showing A_R (red) and A_L (blue) for magnetic fields between 0 and 5 T. The vertical dashed line represents the energy of the first excitonic absorption maximum at 0 T and 5 K. For clarity, spectra at higher fields are offset vertically.

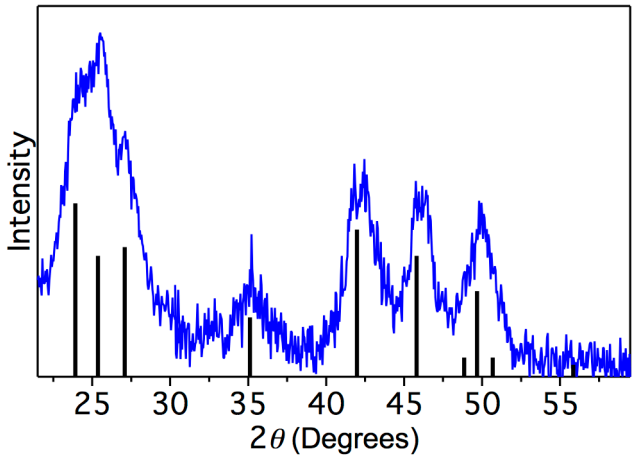

Figure E.2. XRD data for the $Cd_{0.87}Mn_{0.13}Se$ quantum dots of Figure E.1. The diffraction matches the reference wurtzite pattern (black sticks) well.

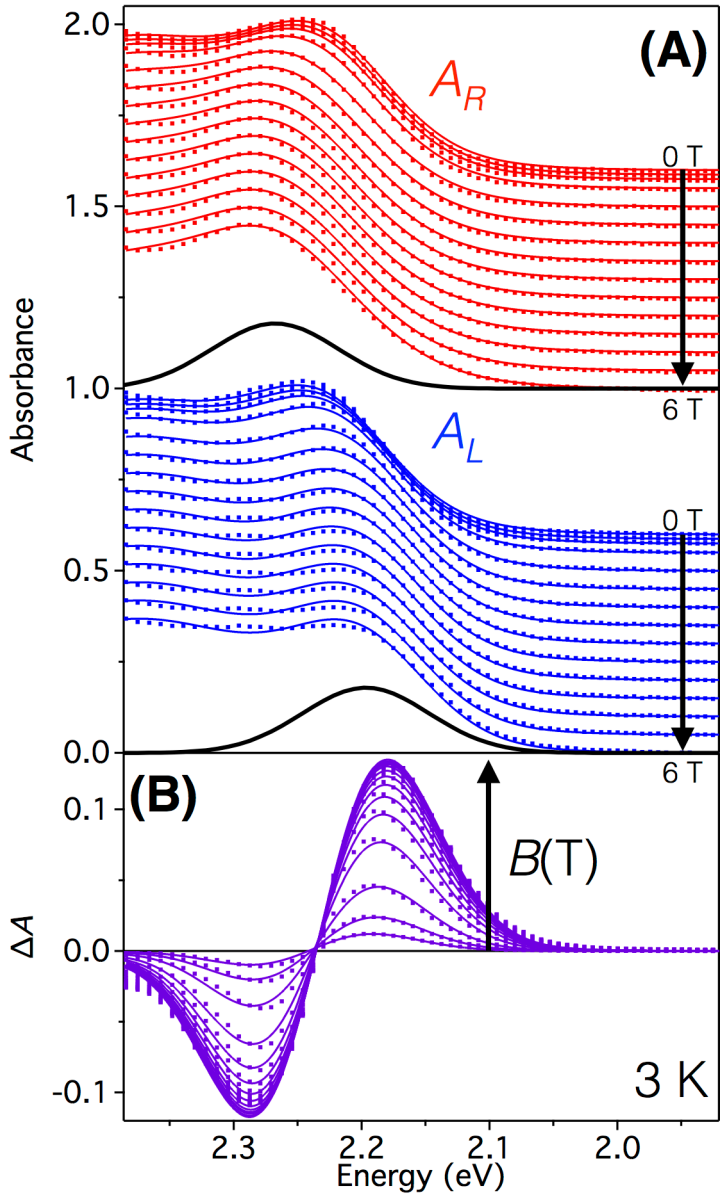

Figure E.3. **(A)** Magnetic-field dependence of 3 K circularly polarized absorption and **(B)** MCD spectra of diffusion-doped *d* ~3.9 nm $Cd_{0.94}Mn_{0.06}Se$/ZnS QDs collected at 3 K for magnetic fields between 0 and 6 T. The arrows indicate the direction of increasing magnetic field. Multi-Gaussian global fits (lines) are plotted for A_R (red), A_L (blue), and MCD (purple) data (dots). Each Gaussian's width and height was linked across the entire field dependence and the Zeeman splitting was assumed to be symmetric about the zero-field energy. Each absorption spectrum was fit to three Gaussian peaks and the MCD was fit to all 6 peaks (3 from A_R and 3 from A_L). The Gaussians associated with the two Zeeman components of the first excitonic transition at 6 T are also plotted (black). For clarity, A_R and A_L spectra at lower fields are offset vertically.

E.3 Derivation of Breakdown Equation 6.6

Defining the absorption bandshape associated with the first bright exciton ($M_J = \pm 1$) as a Gaussian centered at energy E_0 (see Figure 6.4B):

$$A(E) = A_0 \exp\left[-\frac{\left(E - E_0\right)^2}{\sigma^2}\right] \tag{E.1}$$

Application of a magnetic field splits this band into two components at energies $E_0 \pm \frac{1}{2}\Delta E_Z$, described within the rigid-shift approximation as:

$$A_L(E) = A_0 \exp\left[-\frac{\left(E - E_0 + \frac{1}{2}\Delta E_Z\right)^2}{\sigma^2}\right] \tag{E.2}$$

$$A_R(E) = A_0 \exp\left[-\frac{\left(E - E_0 - \frac{1}{2}\Delta E_Z\right)^2}{\sigma^2}\right] \tag{E.3}$$

Define ΔA as:

$$\Delta A = A_L - A_R = A_0 \exp\left[-\frac{\left(E - E_0 + \frac{1}{2}\Delta E_Z\right)^2}{\sigma^2}\right] - \exp\left[-\frac{\left(E - E_0 - \frac{1}{2}\Delta E_Z\right)^2}{\sigma^2}\right] \tag{E.4}$$

Define $\Delta A'$ as the value of ΔA at the following energy, E:

$$E = E_0 + \frac{\sigma}{\sqrt{2}} \tag{E.5}$$

Evaluate $\Delta A'$ and normalize to A_0:

$$\frac{\Delta A'}{A_0} = \exp\left[-\frac{\left(E_0 + \frac{\sigma}{\sqrt{2}} - E_0 + \frac{1}{2}\Delta E_Z\right)^2}{\sigma^2}\right] - \exp\left[-\frac{\left(E_0 + \frac{\sigma}{\sqrt{2}} - E_0 - \frac{1}{2}\Delta E_Z\right)^2}{\sigma^2}\right] \tag{E.6}$$

$$\frac{\Delta A'}{A_0} = \exp\left[-\frac{\left(\frac{\sigma}{\sqrt{2}} + \frac{1}{2}\Delta E_Z\right)^2}{\sigma^2}\right] - \exp\left[-\frac{\left(\frac{\sigma}{\sqrt{2}} - \frac{1}{2}\Delta E_Z\right)^2}{\sigma^2}\right] \tag{E.7}$$

Defining $\eta = \Delta E_Z/\sigma$ and rearranging yields:

$$\frac{\Delta A'}{A_0} = \exp\left[-\frac{1}{2}\right]\exp\left[-\frac{\eta}{\sqrt{2}}\right]\exp\left[-\frac{\eta^2}{4}\right] - \exp\left[-\frac{1}{2}\right]\exp\left[\frac{\eta}{\sqrt{2}}\right]\exp\left[-\frac{\eta^2}{4}\right] \tag{E.8}$$

$$\frac{\Delta A'}{A_0} = \exp\left[-\frac{1}{2}\right]\exp\left[-\frac{\eta^2}{4}\right]\left(\exp\left[-\frac{\eta}{\sqrt{2}}\right] - \exp\left[\frac{\eta}{\sqrt{2}}\right]\right) \tag{E.9}$$

Substituting $2\sinh(a) = e^{a} - e^{-a}$ yields:

$$\frac{\Delta A'}{A_0} = \exp\left[-\frac{1}{2}\right]\exp\left[-\frac{\eta^2}{4}\right]\left(2\sinh\left[-\frac{\eta}{\sqrt{2}}\right]\right) \tag{E.10}$$

Following Equation 6.5, the Zeeman splitting energy is then calculated from the MCD spectrum as:

$$\Delta E_Z(\mathrm{MCD}) = -\left(\frac{\sqrt{2e}}{2}\right)\sigma\frac{\Delta A'}{A_0} \tag{E.11}$$

Substituting for $\Delta A'/A_0$ yields:

$$\Delta E_Z(\mathrm{MCD}) = -\left(\frac{\sqrt{2e}}{2}\right)\sigma \exp\left[-\frac{1}{2}\right]\exp\left[-\frac{\eta^2}{4}\right]\left(2\sinh\left[-\frac{\eta}{\sqrt{2}}\right]\right) \tag{E.12}$$

$$\Delta E_Z(\mathrm{MCD}) = \sqrt{2}\sigma \exp\left[-\frac{\eta^2}{4}\right]\left(\sinh\left[\frac{\eta}{\sqrt{2}}\right]\right) \tag{E.13}$$

Dividing both sides by ΔE_Z gives:

$$\frac{\Delta E_Z(\mathrm{MCD})}{\Delta E_Z} = \frac{\sqrt{2}\sigma \exp\left[-\frac{\eta^2}{4}\right]\left(\sinh\left[\frac{\eta}{\sqrt{2}}\right]\right)}{\Delta E_Z} \tag{E.14}$$

Combining terms yields Equation 6.6, relabeled here as Equation E.15:

$$\frac{\Delta E_Z(\mathrm{MCD})}{\Delta E_Z} = \left(\frac{\sqrt{2}}{\eta}\right)\exp\left[-\frac{\eta^2}{4}\right]\sinh\left[\frac{\eta\sqrt{2}}{2}\right] \tag{E.15}$$

Appendix F

[Electrical Detection of Quantum Dot Hot Electrons Generated *via* a Mn^{2+}-Enhanced Auger Process]

F.1 Additional Supporting Data

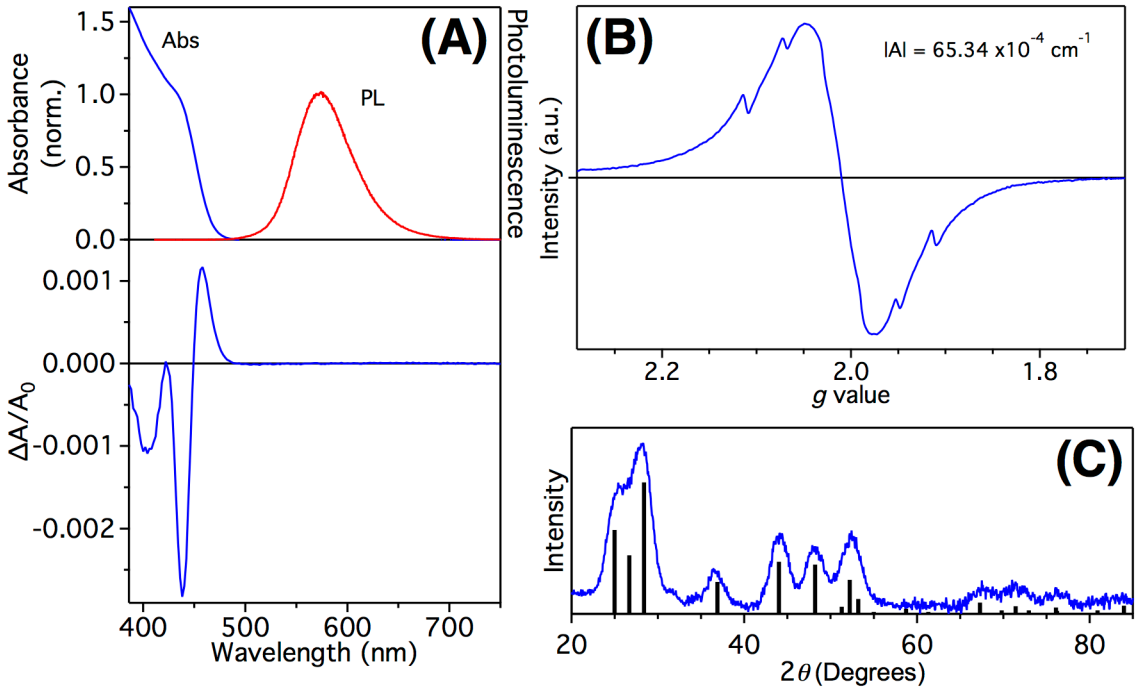

Figure F.1. General characterization of $Cd_{0.9}Mn_{0.1}S/ZnS$ core/shell QDs by room-temperature electronic absorption (**A**; top, left), photoluminescence (**A**; top, right), magnetic circular dichroism (MCD) at 1.5 T (**A**; bottom), EPR (**B**), and XRD (**C**). The bandgap is at 443 nm, corresponding to a QD diameter of 5.0 nm.[1] The PL is centered at 575 nm, consistent with the $^4T_1 \rightarrow {}^6A_1$ ligand-field transition of Mn^{2+}. The MCD shows inversion of the first excitonic Zeeman splitting, caused by *sp–d* exchange of the dopant with the CdS lattice.[2-3] The hyperfine splitting observed in the EPR spectrum is consistent with Mn^{2+} in a tetrahedral sulfide environment.[4] The XRD pattern is consistent with wurtzite CdS (black bars).

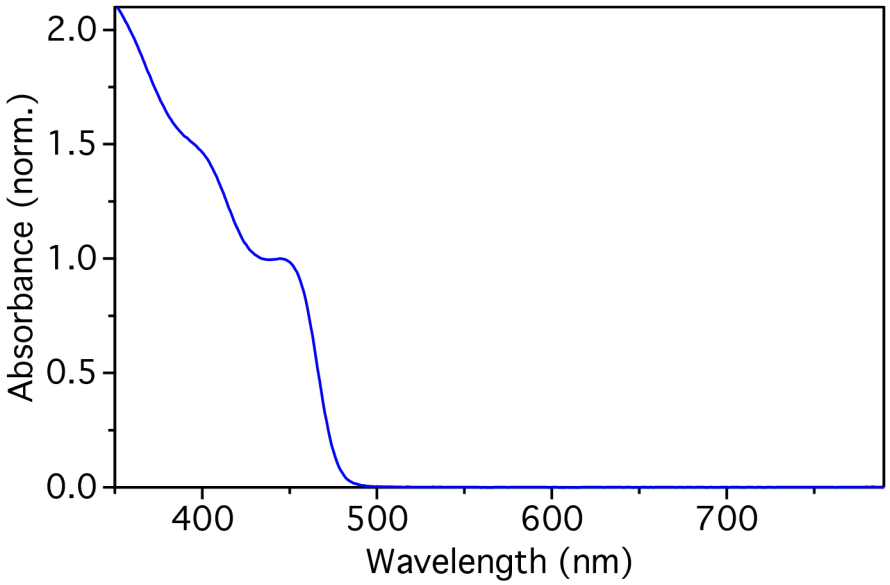

Figure F.2. Room-temperature electronic absorption spectrum of undoped CdS/ZnS core/shell QDs used in the control device. The bandgap is at 453 nm, corresponding to a QD diameter of 5.4 nm.[1]

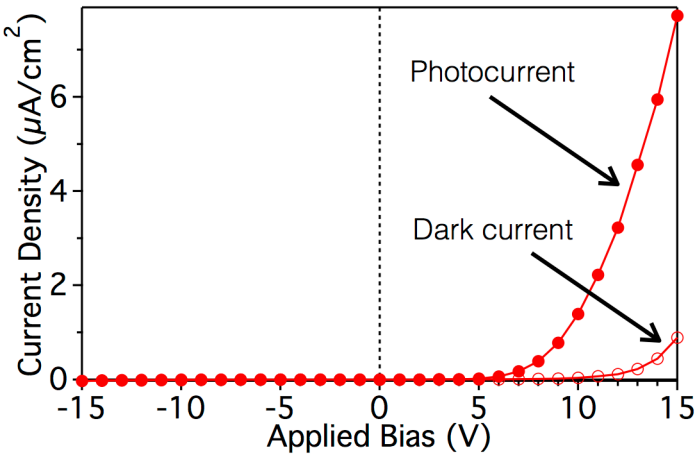

Figure F.3. *J-V* characteristics at 300 K for the Mn^{2+}-doped multilayer device. The device acts as a rectifier, with current only flowing under positive bias. Under 0.12 μW/cm^2 illumination with a 405 nm laser diode, the photocurrent (closed circles) turns on at lower voltages than the dark current (open circles). The power-normalized difference between the photo- and dark current densities plotted here yields the responsivity plotted in Figure 7.2B.

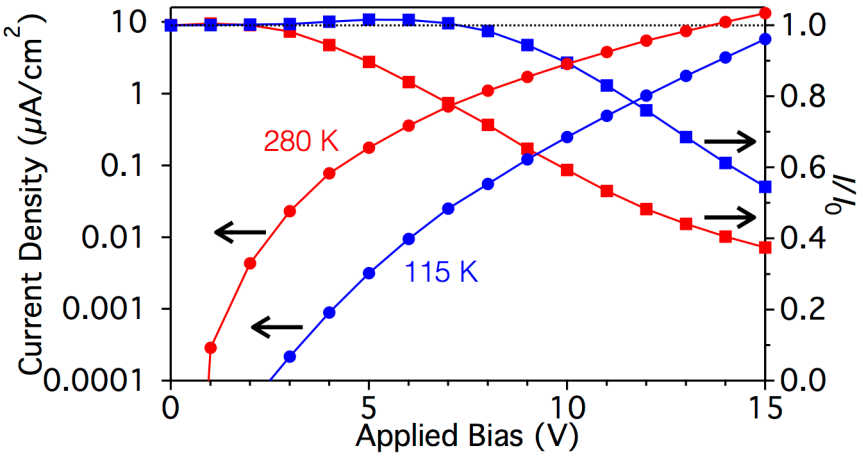

Figure F.4. Voltage dependence of photocurrent density and PL in the Mn^{2+}-doped multilayer device, measured at 115 K (blue) and 280 K (red). At the higher temperature, the onset voltage is lower for both photocurrent and PL quenching. Note the log scale of the photocurrent densities.

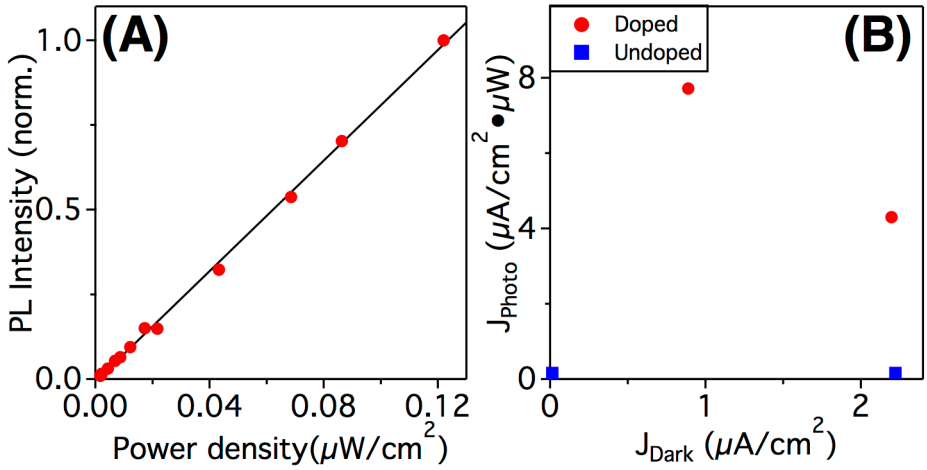

Figure F.5. (A) PL intensity of the Mn^{2+}-doped multilayer device plotted vs excitation power (405 nm) over three orders of magnitude. The black line is a linear best-fit to the data. (B) Photocurrent density (normalized to excitation power) and dark current density (normalized to the same mask area as the photocurrent measurements) for different $Cd_{1-x}Mn_xS$ (red circles) and CdS (blue squares) multilayer devices, each measured at +15 V. The presence of Mn^{2+} increases the photocurrent relative to undoped devices. There is no detectable correlation between photocurrent and dark current, with or without Mn^{2+}.

F.2 Additional Experimental Details

F.2.1 QD Characterization

Room-temperature electronic absorption spectra were collected for colloidal toluene suspensions of nanocrystals in 0.1 cm path length cuvettes using a Cary 500 spectrophotometer (Varian). Room-temperature magnetic circular dichroism (MCD) spectra were collected on colloidal toluene suspensions of nanocrystals in a 0.1 cm path length cuvette placed in a 1.5 T electromagnet oriented in the Faraday configuration. MCD spectra were collected using an Aviv 40DS spectropolarimeter. The differential absorption collected in the MCD experiment is reported as $\Delta A = A_L - A_R$, where A_L and A_R refer to the absorption of left and right circularly polarized photons in the sign convention of Piepho and Schatz.[3, 5] CW EPR experiments were performed on colloidal toluene suspensions of nanocrystals using an X-band Bruker EMX spectrometer. XRD data were collected from evaporated nanocrystal films on glass slides using a Bruker D8 Discover spectrometer at the University of Washington (UW) NanoTech User Facility.

F.2.2 Device Fabrication

Ethanol and 1,7-heptanediamine (HDA) were purchased from Sigma-Aldrich. Zinc Sulfide (ZnS; 99.99%) was purchased from Kurt J. Lesker Company. Indium tin oxide (ITO) substrates were scrubbed with detergent solution (2 vol % Micro-90, International Products Corp., in purified deionized water), followed by sonication in deionized water, acetone, and isopropanol for 20 minutes each. The ITO substrates were then cleaned by air plasma treatment for 10 minutes. QD films were fabricated in inert atmosphere using a layer-by-layer spin-coating method.[6] QD films were fabricated from a solution of Mn^{2+}:CdS/ZnS core/shell QDs or undoped CdS/ZnS core/shell QDs in toluene (20 mg/mL) and a solution of the cross-linker 1,7-heptanediamine in anhydrous ethanol (0.5 v/v%). Each layer-by-layer deposition consisted of five steps: (1) A volume of 50 µL of QD solution was dropped onto the substrate and spin-coated at 1500 rpm for 60 seconds; (2) The QD film was transferred to a hot plate and annealed at 80 ºC for 2 minutes; (3) The QD film was then immersed in a solution of HDA at 80 ºC for 2 minutes to replace the long-chained oleylamine (OLA) ligands with HDA cross-linker; (4) The QD film was dried and annealed on the hot plate at 80 ºC for 1 minute; (5) Residual OLA and HDA ligands on the QD film were subsequently removed by spin-coating twice with anhydrous ethanol. This layer-by-layer deposition was repeated 3 times to obtain a smooth QD film.

F.3 References

1. Yu, W. W.; Qu, L.; Guo, W.; Peng, X., Experimental Determination of the Extinction Coefficient of CdTe, CdSe, and CdS Nanocrystals. *Chem. Mater.* **2003,** *15*, 2854–2860.
2. Furdyna, J. K., Diluted Magnetic Semiconductors. *J. Appl. Phys.* **1988,** *64*, R29-R64
3. Beaulac, R.; Ochsenbein, S. T.; Gamelin, D. R. Colloidal Transition-Metal-Doped Quantum Dots. In *Nanocrystal Quantum Dots*, 2nd ed.; Klimov, V. I., Ed; CRC Press: Boca Raton, FL, 2010; pp 397–453.
4. Dorain, P. B. Electron Paramagnetic Resonance of Manganese (II) in Hexagonal Zinc Oxide and Cadmium Sulfide Single Crystals. *Phys. Rev.* **1958,** *112*, 1058–1060.
5. Piepho, S. B.; Schatz, P. N. *Group Theory in Spectroscopy with Applications to Magnetic Circular Dichroism*; Wiley: New York, 1983.
6. Tang, J.; Kemp, K. W.; Hoogland, S.; Jeong, K. S.; Liu, H.; Levina, L.; Furukawa, M.; Wang, X.; Debnath, R.; Cha, D.; Chou, K. W.; Fischer, A.; Amassian, A.; Asbury, J. B.; Sargent, E. H., Colloidal-Quantum-Dot Photovoltaics Using Atomic-Ligand Passivation. *Nat. Mater.* **2011,** *10*, 765–771.